Ice formation in the Arctic Ocean: Observed processes and climate feedbacks

by

A. C. Bradley

A.B., Dartmouth College, 2011

B.E., Thayer School of Engineering, 2011

M.S., University of Colorado Boulder, 2014

A thesis submitted to the
Faculty of the Graduate School of the
University of Colorado in partial fulfillment
of the requirements for the degree of
Doctor of Philosophy
Department of Aerospace Engineering Sciences
2016

This thesis entitled:
Ice formation in the Arctic Ocean: Observed processes and climate feedbacks
written by A. C. Bradley
has been approved for the Department of Aerospace Engineering Sciences

Dr. Scott Palo

Dr. James Maslanik

Date

The final copy of this thesis has been examined by the signatories, and we find that both the content and the form meet acceptable presentation standards of scholarly work in the above mentioned discipline.

Bradley, A. C. (Ph.D., Aerospace Engineering Sciences in Remote Sensing, Earth and Space Sciences)

Ice formation in the Arctic Ocean: Observed processes and climate feedbacks

Thesis directed by Prof. Dr. Scott Palo

The Arctic seasonal ice zone undergoes dramatic changes throughout the year. In the summer, ice cover melts off, leaving the ocean surface exposed to the atmosphere. Incident solar radiation warms the surface mixed layer. At the end of the summer season, the mixed layer must then cool to the freezing point in order for ice to form at the surface. This thesis explores the impact of that heat throughout the annual cycle, but especially on first-year ice growth. Through analysis of CTD profiles and buoy data, it is found that summer heat gets into the summer halocline, where it is trapped through the fall season cooling process. The mixed layer heat (estimated from an empirical relationship derived from direct measurements and atmospheric and geographic parameters along with sea surface temperatures) is well correlated with freeze-up date. The results presented herein suggest that delayed freeze-up does result in thinner ice cover at the end of the winter season, in part because the maximum ice growth rate is consistent (approximately 12 cm/day) between observations from Antarctic polynyas with exceptionally high ice production and the few observations that exist in the Arctic. Finally, from analysis of end-of-season first year ice thickness distributions, it is clear that the summer heat trapped in the summer halocline is released over the course of the winter, limiting ice growth in addition to that caused by the delay in freeze-up. In all, it is likely that as the Arctic becomes increasingly dominated by first-year ice, the thinning trend will continue though at a slower rate than in the current transition from multi- to first-year ice cover.

Acknowledgements

The notion that science is a solitary pursuit is disproved by the number of people who have been involved in my graduate work in one form or another.

Without the loving support of Allen Pope, completing this project certainly would have been a longer process. You have encouraged me to fly (in more ways than one) these last few years. Casey Gardiner is to thank for a continual dedication to sanity and perspective and for helping me keep long-term goals in mind even when the details seemed overwhelming. My parents, Dwight and Lauren Bradley, raised me to believe that a Ph.D. is both something to be proud of and just something you do. These parallel approaches have been critical for maintaining motivation through the process.

A remarkable number of researchers and faculty have helped along the way, both in support of my research and in support of my career. Scott Palo has been an excellent advisor, consistently supportive of all the opportunities I've had the chance to pursue and providing just the right feedback throughout the process. Mike Steele has been a tremendous resource since we crossed paths on the north slope of Alaska. Jen Kay has been a mentor and a friend, giving me the opportunity to teach the best possible class. My committee, Mark Tschudi, Jim Maslanik, Lakshmi Kantha, John Cassano, and Julienne Stroeve, have all shared insight and ideas that have made this a better project and me a better scientist. Finally Bob Hawley and Simon Shepherd deserve a belated thanks for their guidance in getting to this PhD program; without your advice, who knows where I would be.

I must acknowledge the Association of Polar Early Career Scientists for so many opportunities to be involved across all levels of scientific management and planning in the US and abroad. Jenny Baseman and the WRCP Climate and Cryosphere Project have also opened doors for me, literally around the world. The APECS and polar science communities have become my people.

Finally, I would particularly like to acknowledge the NASA Earth and Space Science Fellowship (NESSF) for the support necessary to finish this dissertation. The Strauch Family Graduate Fellowship has made the last two years more pleasant in so many ways.

Contents

Chapter

Appendix

Tables

Table

Figures

Figure

Chapter 1

Introduction

Research on the changing Arctic climate has been primarily focused around melt: shrinking ice cover in the summer season catches global attention. Rising temperatures are inextricably linked to melting sea ice, and the old multi-year ice pack is giving way to more transient seasonal ice cover. Often cited as a motivation for studying melt processes - and subsequent warming of the Arctic Ocean - is the feedback mechanism of warmer ocean waters taking longer to cool in the fall, delaying the onset of ice formation and resulting in a thinner icepack at the end of the winter growth season. The processes surrounding the cooling of the ocean surface layer and the subsequent formation of ice have received relatively little attention in the literature. Few studies have directly addressed the impact of growing first year ice later in the season, focusing on modeling exercises.

Ice forecasting will be increasingly important as the summer ice extent continues to shrink. Increasingly, the Northwest Passage and North Sea Route open up the Arctic to shipping and tourism in the summer, but the operable season is limited by the formation of ice in the fall. Existing methods for forecasting are not particularly quantitative (personal communication, NWS Ice Forecast Desk), and any improvements in understanding help make the Arctic a safer place to operate.

The fundamental questions addressed in this dissertation can be summarized by the question “how much of an impact do the feedback effects associated with warming Arctic Ocean temperatures have on winter maximum ice cover volume?”. A fully-coupled, high-resolution sea ice-ocean-atmosphere model could in theory answer all of the questions in this thesis. However, the computer power required to run models at the resolution necessary to resolve the physics is not possible at this time. The importance of small-scale fluid dynamic processes mean that existing scales of models cannot fully capture the system and parameterizations are required to describe the processes not resolved by the grid cells.

Instead, observations are used with the understanding that care must be taken in interpreting results. One of the challenges in observing the Arctic Ocean and sea ice is that all relevant parameters are not necessarily available. This dissertation uses the observations that are available to address and improve a system-level understanding of seasonal processes in heat storage and ice growth throughout the Arctic.

1.1 Motivation for studying ice formation

Climate change has focused attention on increasing sea ice melt in the Arctic. Popular media promotes the image of a sad polar bear sitting on an isolated ice floe. Science, in funding and publication, focuses on the mechanisms, feedback effects, and consequences of increased melting. For good reason: September sea ice extent is declining at a rate of 11% per decade, with some suggestions that the decreases in ice-covered area are accelerating [Kattsov et al., 2010]. Climate models suggest that a summer without a solid central ice pack is coming in the next few decades [Overland and Wang, 2013]. Whatever happens over the summer melt season, each winter sea ice cover forms again and fills the Arctic Basin. This first year ice is coming to dominate the Arctic environment.

Figure 1.1 shows the annual pattern of ice extent in the Arctic. In the mid-summer, ice melt in the Arctic Ocean starts in earnest and continues until roughly the equinox in mid-September at which point radiative forcing shifts toward freezing rather than melting. Over the last decades, the amount of ice that survives the summer melt season has been shrinking at a concerning rate. The low point of this curve is the minimum September extent: this ice is then classified as multi-year (MY) ice. This thesis focuses on the timing

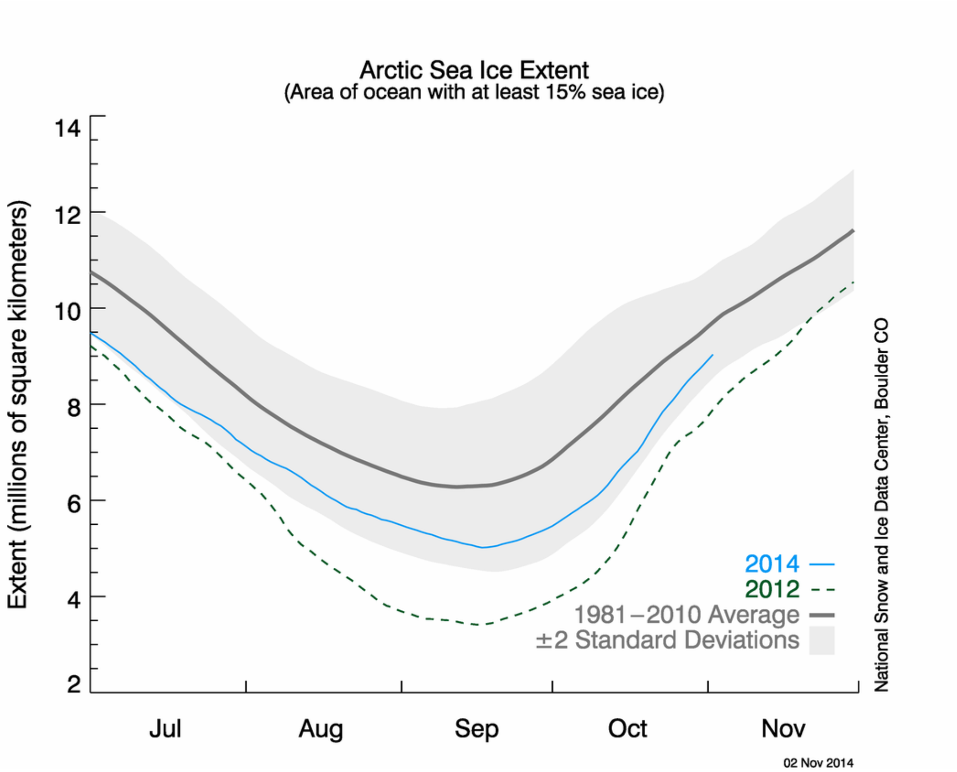

Figure 1.1: Sea ice extent by month for the years 1981-2015. There has been a notable shift towards lower ice extents in all months in the recent years. Image produced by the National Snow and Ice Data Center based on Sea Ice Index data [Fetterer et al., 2002].

of the increase in extent in the fall, though the approach is mainly focused on more regional scales than the basin-wide ice extent estimate presented here. First year ice (FYI) (the ice that forms new out of open water) is known to be thinner and more prone to melting in the summer than multi-year ice [Maslanik et al., 2007, Hutchings and Rigor, 2012]. The portion of the maximum winter extent that is multiyear ice has decreased from 50% to 10% [Maslanik et al., 2011]. The fraction of Arctic ice pack made of FYI has been increasing accordingly. With extremely low extents in the recent summers, the need for understanding the FY ice environment is becoming more important. This leads to the question will FYI thin over time? Delayed ice formation has been suggested to result in thinner ice cover, but to what extent is unknown. Limited studies have suggested a slight thinning trend [Melling et al., 2005], but with little statistical significance and only over small study areas. This is often cited as a reason to study summer melt feedback processes, but never quantified.

With shipping routes opening in the summer through the Northwest Passage and Northern Sea Routes, the late end of the season is important for economic activity: ships in transit and assets that have been deployed need to safely reach harbor or be shut down for winter before the ice grows around them. In the increasingly ice-free summer Arctic shipping lanes, not all vessels will be sufficiently ice-hardened and cannot function once freeze-up initiates. Already, non-ice-rated cruise ships are attempting the Northwest Passage [Schwartz, 2016]. Accurate forecasts of ice conditions allow operators to extend the season as long as possible without risking ships, cargo, or personnel.

1.1.1 Role of ice formation in the climate system

The polar regions play a key role in the heat balance of the planet, as described in Section 2.1.1. Sea ice cover insulates the polar oceans, and its formation is a natural effect of the high radiative losses to the atmosphere from the Arctic Ocean during polar night. During the freeze-up season, atmospheric thermal flux into the polar regions increases dramatically with the increasing global gradient in surface temperatures [Serreze and Barry, 2005].

The role of melt in the feedback processes that are integral to the global changes in climate gets most of the attention from the science community and the public. Loss of high-albedo sea ice increases summer absorption of solar radiation, accelerating the total melt. Declining amounts of thick, multi-year ice result in an overall thinner Arctic ice pack with less volume of ice to melt in the summer before regions are ice-free. Not presented in these descriptions of the feedback processes though is the late end of the season: each year ice grows again, and for these effects to compound from year to year, the summer heat content needs to somehow translate into reduced ice growth over the winter. Otherwise, feedback effects may influence the current season but winter growth resets the system and year to year ice extents would be uncorrelated outside of the global trends in climate and the influence of multi-year climate modes.

1.1.2 Economic interests in the Arctic

Increased open water in the summer Arctic Ocean opens up the region for economic activity. Three primary uses dominate the plans for the emerging open Arctic: resource extraction, shipping routes for linking the Atlantic and Pacific oceans, and tourism.

Ice-free routes through the Northwest Passage and North Sea Route present an alternative to shipping through the Panama Canal or Suez Canal. For example, the North Sea route offers a 40% decrease in travel distance between Shangai and Rotterdam [ABS, 2009]. While demand for ice-hardened vessels is certainly growing, the economic argument for shipping through the Arctic is even more attractive if more conventional vessels can make the trip in the summer.

Extensive rules have been developed with regards to Ice Class vessels meant for polar and winter sub-polar transit [ABS, 2009], but there is significant variability in what can qualify for polar travel. PC7 vessels are meant for transit through open water, and can only navigate through thin ice cover. If ice formed too quickly blocking the route to safe harbor, one of these vessels could be trapped over winter, likely suffering severe damage from the mechanical stresses of ice growth. Accurate forecasts enable operation later into the season, increasing the value of the region, while also protecting the fragile ecosystem from disaster.

Drilling operation requires open water to operate. BOEM [2013] described the limitations experienced during the 2012 drilling season. Despite this being a record year for minimum ice extent, the beginning of the drilling season was delayed by later-than-expected retreat of ice in the Chukchi Sea. Drilling vessels had to halt operation, disconnect, and move off of the first drill site twelve hours after starting because of a large, encroaching ice floe. Forecasting support for operations is provided by Shell's Ice and Weather Advisory Center, a service that provides ice forecasts based (NOAA) on a combination of forecasts from National Weather Service (NWS), National Oceanic and Atmospheric Administration , and the Canadian ice services, as well as satellite imagery. While drilling operations in the

Arctic are currently suspended due to low global oil prices, they are likely to resume at some point [Harsem et al., 2013].

Drilling operations are often required to operate around subsistence hunting timing, pushing the drilling season late into the fall (e.g., after October 3 in BOEM [2013]), stressing the need for accurate freeze-up forecasts. Currently, drilling into hydrocarbon deposits must cease well in advance of a date based on analysis of ice incursion into the area observed from satellite measurements from earlier years. Adjustments to this date may be made by agreement of the Bureau of Environmental Management and NOAA's Ice forecasting services, but it requires everyone agreeing on a forecasting methodology to do so, which is still an emerging area of research. Further understanding of the processes that lead up to freeze-up will improve this system.

As demonstrated in the BOEM [2013] report, there is significant economic interest in being able to extend the season out as long as is safe. Getting assets that are not ice-hardened stuck in the ice would be a major economic hardship, with potentially grave safety and environmental consequences. Many of the regulations surrounding resource extraction in the Arctic are written in order to provide adequate time for spill clean-up before ice growth makes it impossible. Better ability to forecast freeze-up will make these more effective.

1.2 Scientific Questions

This dissertation considers the annual cycle in upper ocean heat storage and sea ice growth. Chapter 3 defines the annual cycle outside the perennial ice edge. Chapter 4 finds empirical relationships to estimate mixed layer depth in order to calculate upper ocean heat content, which is related to delays in freeze-up date. Chapter 5 studies ice formation in polynyas to determine if there is an upper limit to the rate at which ice forms in the ocean, which would mean that the timing of freeze-up would have more of an impact on the end of season thickness than if later-forming ice could grow faster. Finally Chapter 6 looks at end-of-winter first year ice measurements to determine that the freeze-up date has a significant impact on the end of season thickness, but the trapped summer heat in the halocline also slows ice growth over the winter. The following sections outline the discussions and analyses in the following chapters.

1.2.1 How does the upper ocean temperature and salinity evolve throughout the year and particularly prior to the onset of freeze-up in the Arctic seasonal ice zones?

Gary Maykut outlined the process by which the exposed ocean surface mixed layer in the Arctic cools [Maykut, 1985], enabling the surface to freeze. This evolution has not been well described in the Arctic outside of the summer ice edge.

The mixed layer is the top 10-100 meters of the Arctic Ocean, defined by a strong pycnocline separating the relatively fresh mixed layer from the more saline water layers below. Energy fluxes across this boundary are typically relatively small, with a few exceptions in areas of complex topography. In order for sea ice to form on the ocean surface, the surface needs to cool to the freezing point. Unlike in a body of fresh water, the temperature of maximum density is below the freezing point for saline water. This means that water that is close to the freezing point does not float; the entire mixed layer needs to be cooled to freezing before ice can form at the surface.

In the model presented by Maykut, two diagnostic terms describe the heat content of the surface mixed layer of the Arctic Ocean: temperature and depth. Temperature is the integrated effects of heat fluxes, and depth is a function of wind and ice drag (and associated Ekman pumping and internal waves) and freshwater content. The combination – some amount of water measured by the depth at some temperature above freezing – is a total amount of heat contained in the surface layers. In order to freeze, this water must cool to the freezing point through heat loss to the atmosphere at the surface [Maykut, 1985].

This chapter uses salinity and temperature measurements to characterize the seasonal processes in the North American sector of the Arctic. Based on CTD profiles presented in the chapter, mixed layer temperatures at some latitudes have been warming since the early 1990s. Buoy observations suggest that the bulk of fall heat loss (70-80%) is through rapid cooling events associated with storms. Unrelated to the cooling rate are pockets of warm water trapped below the surface mixed layer in the highly stable summer halocline.

Hypothesis Seasonal cycles in temperature and salinity differ in the seasonal ice zone versus the perennial ice pack. Heat is trapped in the summer halocline and persists through freeze-up to slow ice growth later in the winter.

Approach Thermocline and halocline depths in observed temperature and salinity profiles are compared to determine how often significant amounts of heat are found in the summer halocline. These profiles are then classified based on idealized seasonal profiles derived from the literature. The relative fractions of each profile classification show the difference in seasonality between inside the perennial ice edge and outside.

1.2.2 Can mixed layer depth be estimated without a direct measurement in order to calculate heat content?

The heat content of the summer mixed layer is the driving factor in delayed freeze-up dates. The heat content is the integrated heat stored in the water column in the mixed layer, the product of the temperature (relative to the freezing point) and the depth of the mixed layer. The actual processes determining the mixed layer depth are a complicated combination of atmospheric forcing (wind-driven mixing and convective mixing due to cooling at the surface), internal ocean processes, and geographic and seasonal factors. Many of these same processes also determine the mixed layer temperature, often measured as the sea surface temperature. This chapter describes a method for calculating empirical relationships between these factors and direct measurements of mixed layer depth in order to estimate the mixed layer depth in locations without direct observations.

The heat content estimates determined using the empirical relation method correlate better with fall freeze-up dates than does the approach of using a fixed mixed layer depth for the whole basin.

Hypothesis Wind speeds and air temperatures are correlated with mixed layer depths in some locations. These provide a means of estimating mixed layer depth in locations without direct measurements and therefore for estimating upper ocean heat content.

Approach Direct measurements of mixed layer depth are compared to local air temperatures and wind speeds along with geographic parameters and surface temperatures. The factors with the strongest correlations are identified for each region within the Arctic and used to determine an empirical relationship for estimating mixed layer depth from reanalysis or remotely-sensed products. Heat content is then calculated and trends identified.

1.2.3 Is there an upper limit to the rate of ice growth at the beginning of the winter season?

Antarctic coastal polynyas offer an interesting comparison to ice growth processes in the Arctic. On their own, polynyas may offer clues to the increasing ice extent observed in the Antarctic, especially in the Ross and Weddell sea regions. For this project though, polynyas offer an analog to late season ice growth in the Arctic. With warmer ocean temperatures, the onset of freeze-up is delayed to later in the winter. By the time the ocean surface is cool enough to form ice, the atmospheric and radiative forcing will be more wintry and ice growth will proceed faster than if the ocean surface had been able to start to freeze in October as in previous decades. Polynyas are an extreme case of this: open water preconditioned to freezing temperatures forms ice very quickly on exposure to the cold winter atmosphere.

Studying polynya dynamics removes some of the variability of weather conditions in order to capture the heat fluxes associated with ice formation. While the expansion phase (open water area getting larger) polynya dynamics are dominated by the wind effects, during the closing phase (open water area getting smaller) polynyas more closely resemble the conditions under which Arctic sea ice forms. Leads and sensible heat polynyas in the Arctic provide another means for comparison. All show very similar upper limits to ice growth rates, approximately 0.12 cm/day Hirano et al. [2016].

Polynyas also show that ice can form very quickly under the right conditions - if by the time ice is growing in the Arctic the atmosphere is very cold, the growth rates will be faster than if ice is forming under a slightly warmer atmosphere. The comparison between these cases (slow growth at the onset of winter or fast growth delayed by the warmer ocean) can be constrained by the polynya ice growth case.

This chapter considers the case of the Terra Nova Bay polynya using campaign data from 2012 in addition to available observations of ice growth rates from the literature.

Hypothesis In observations of closing phase polynya ice growth, heat fluxes in the polynya setting are similar to the Arctic freeze-up case. Ice growth rates under these forcing conditions may be high enough to compensate for some delay in the onset of ice growth in end of season ice thickness.

Approach Ice growth rates in the Terra Nova Bay polynya are calculated from bulk formulations of surface fluxes, in situ meteorological measurements, and surface temperature retrievals. These estimates are then compared to ice growth rates from polynyas and leads reported in the literature and to observed ice growth rates from drifting Ice Mass Balance buoys in the Arctic.

1.2.4 Is first-year ice thickness changing, and what factors are driving these changes?

Delayed freeze-up is hypothesized to result in thinner ice pack, but ice growth rates are inversely proportional to the amount of ice insulating the warm ocean from the cold atmosphere. If ice is starting to grow later into the winter when the atmosphere is colder, the temperature differential between the ocean and atmosphere will be greater, suggesting that ice will grow faster than it would earlier in the season. Higher rates of energy transfer between the ocean and the atmosphere result in faster growing ice, as can be observed in the extremely high growth rates in Antarctic polynyas.

It is well known that the increasingly first-year ice dominated Arctic has a thinner total ice pack than in the multi-year ice packs of previous decades. Within the areas of first-year ice though, are there significant trends in ice thickness? Is there a correlation between ice thickness at the end of the season and the date of freeze-up? Is the summer heat content, and especially that which may be trapped in the summer halocline, influencing the end-of-season ice thickness?

Hypothesis Small changes in the date of freeze-up do not make a significant difference on the end-of-season undeformed first year ice thickness. Inter-annual variability in atmospheric forcing is a much larger factor than lost growth days due to a late freeze-up date, though a shortened growth season will also make a difference in the end of season thickness. Oceanic heat flux from trapped summer heat further reduces the ice thickness in addition to delaying freeze-up.

Approach End-of-winter first-year ice thickness measurements from IceBridge campaigns will be traced back through time using ice motion products to determine when and where they first froze up. Atmospheric forcing along the path is retrieved from reanalysis products and integrated using a simple one-dimensional sea ice growth model. The relative contributions of atmospheric forcing, length of ice growth season, and summer ocean temperatures are then found through a multiple regression approach.

Chapter 2

Background

This thesis focuses on ice formation in the Arctic, using specific features in the Antarctic to help explain the processes at work in the north. In order to put this in context, this chapter presents a high-level overview of the Arctic climate system including the water masses in the Arctic Ocean, an overview of surface heat fluxes in the context of ocean and ice-covered surfaces, some information on the density and freezing point dependence on temperature and salinity, and a description of the stages of ice growth.

2.1 Arctic climate system

The global climate system is fundamentally a mechanism for maintaining a neutral heat balance on the planet. High solar radiation at the equatorial latitudes is balanced by negative net radiation at the poles [Trenberth and Caron, 2001]. Global climate is driven by the transfer of heat from the regions of positive net radiation to the regions (high latitudes) of negative net radiation. The atmosphere and ocean both contribute to this process – the atmosphere on much shorter time scales than the ocean.

The net horizontal transfer of energy into the polar regions is balanced by the high rates of radiative cooling in the polar regions, especially in the Arctic where the Arctic Ocean acts as a heat sink for the rest of the planet. Inflow from the warmer Atlantic (and to a lesser degree the Pacific) Ocean keeps the deeper waters in the Arctic relatively warm, and the cooling of these waters drives thermohaline circulation in the North Atlantic.

In response to the extreme cooling at the poles, sea ice forms to cover the surface of the ocean. There is some seasonal latitude dependence based on the atmospheric conditions driving the surface freezing: during the winter, the ice pack grows to cover the entire Arctic Ocean, the Bering, Barents, Labrador, and other neighboring seas. Ice extends along the coast into the Gulf of Alaska, along Greenland, and along the eastern coast of Russia. Once the days start getting longer, the radiative balance shifts, the atmosphere warms, and the ice along the edges of the pack begins to melt and break up. Ice retreats throughout the summer until roughly the fall equinox, when the radiative balance once again shifts towards ice formation.

This annual pattern has changed dramatically with global warming. Summer temperatures in the Arctic have increased precipitously, at a rate of nearly twice the global average [Screen and Simmonds, 2010]. The resulting impact on the ice pack has been dramatic: summer ice extents have decreased by more than 30% over the years 1980-2014 [Stroeve et al., 2012]. This decrease is primarily visible in the dwindling amount of multi-year sea ice, which is typically thicker ice and more resistant to melt in the summer.

In the Arctic, winter extents have not decreased comparatively as much as summer ice extent, creating an environment dominated by first year ice. In order to understand this environment, an exploration of the geography of the area – both in terms of the structures in circulation and in atmospheric forcing and the vertical stratigraphy of the Arctic Ocean water masses – is required, as is addressing the processes which drive the increasing summer melt. Both of these depend on the role of the polar regions in the global climate, as driven by the radiative forcing and corresponding global circulation.

2.1.1 Seasonal radiative forcing and global circulation

At the equatorial latitudes, solar radiation incident on the Earth's surface is higher than the outgoing long wave radiation, resulting in net warming. This heat energy is transported poleward by the oceans and atmosphere to even out the radiation budget, as illustrated by

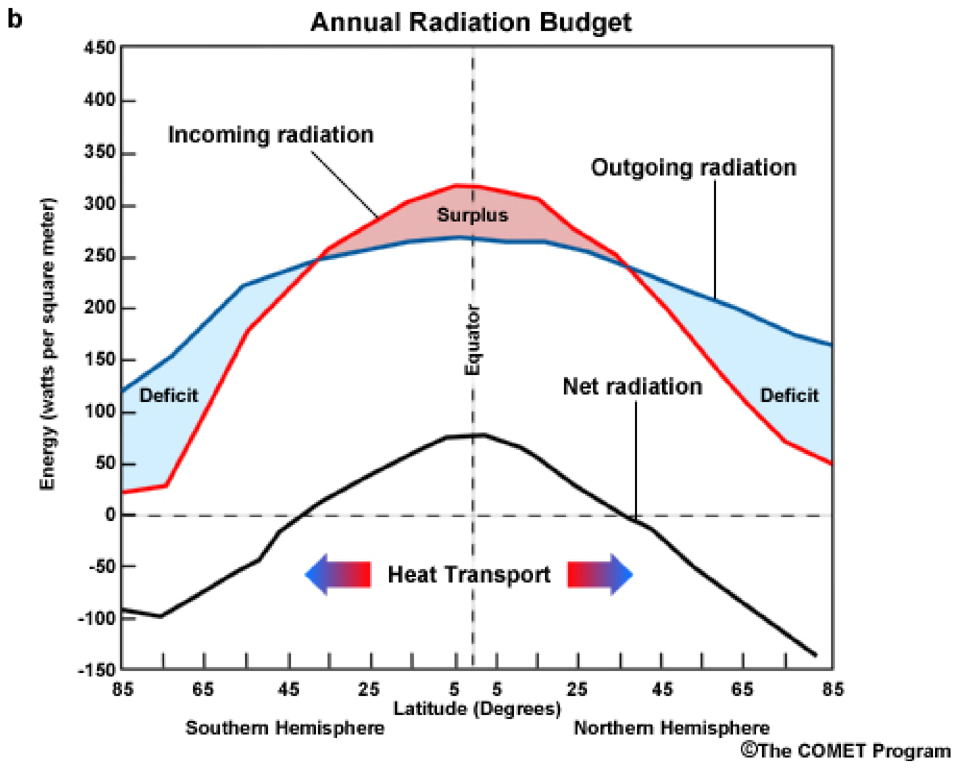

Figure 2.1: Solar radiation heats the tropics. Global heat transport moves this energy towards the poles, where it is emitted as long wave radiation. Figure copied from http://www.ucsusa.org/sites/default/files/legacy/assets/images/ce/conveyor-belt.gif.

Figure 2.1.

The ice cover in the Arctic Ocean minimizes solar radiation input into the Arctic Ocean. Sea ice has a significantly higher albedo in the visible spectrum than open ocean, typically by a factor of 4 to 6 (and higher when the ice has new snow cover). Ice cover also insulates the ocean, moderating the emitted longwave radiation over the winter months.

In the ocean, these processes manifest as the major global currents driven by thermohaline circulation. Currents of warmer waters near the surface are cooled by the atmosphere at the higher latitudes, and the resulting sinking process keeps the conveyor belt moving. The northern North Atlantic and points surrounding the Antarctic continent are the major locations of surface water mass subduction. These areas are where much of the heat absorbed in the equatorial regions is released to the atmosphere.

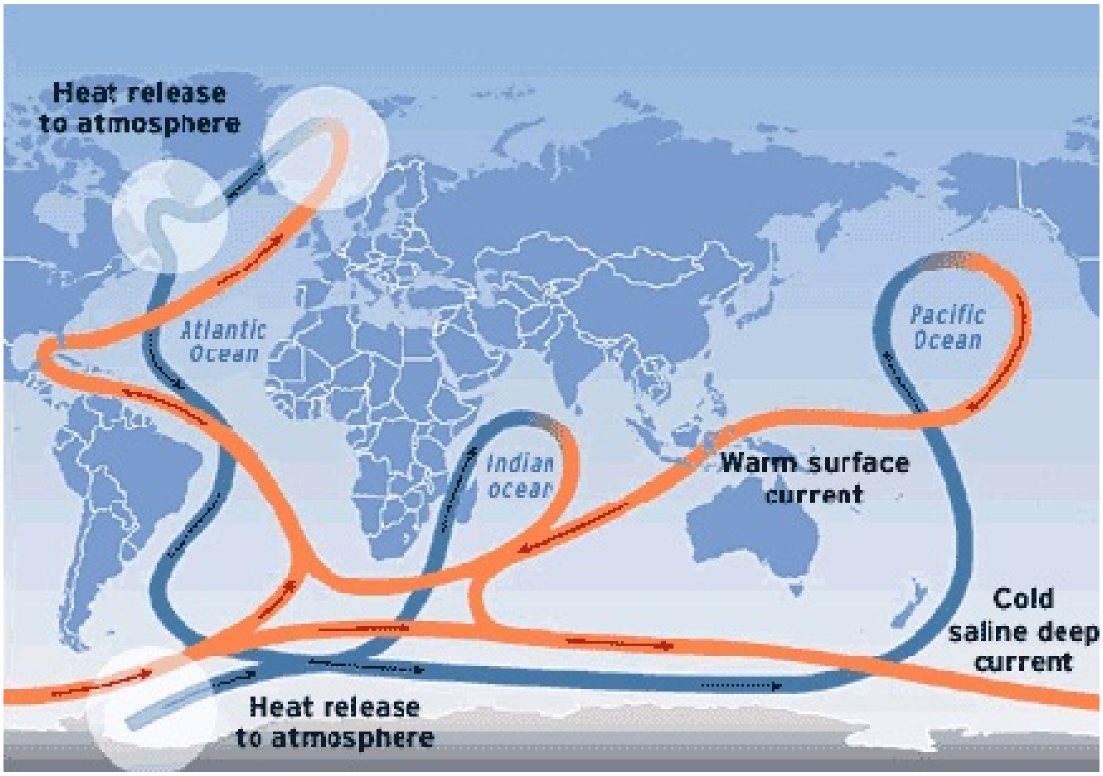

Figure 2.2: Global currents driven by thermohaline circulation. The north Atlantic is the site of much of the water mass modification driving the Atlantic leg of the overturning circulation. Figure copied from http://www.ucsusa.org.

Ocean heat transport moderates global climate. The ocean holds 90% of the heat added to the earth system since the onset of greenhouse-gas driven climate change. Because water moves slowly relative to systems in the atmosphere, the global transport of heat through thermohaline circulation acts to moderate short-term fluctuations in climate.

2.2 Structure of the Arctic Ocean

The global circulation patterns notably miss the Arctic Ocean, as illustrated in Figure 2.2. It is at the northern end of the North Atlantic that warm surface water cools and subsides, eventually forming the deep water that fills the deep Atlantic and keeps the thermohaline conveyor belt moving. There is very limited connection between the Arctic Ocean and the Pacific on the other side. At its narrowest, the Bering Strait is only 50m deep and

85km across.

The transpolar current is driven by the sea surface height differential between the Atlantic Ocean and the Pacific Ocean. Higher salinity (and therefore higher density) in the North Atlantic than the North Pacific results in a 2 meter differential in sea surface height across the Arctic Ocean. This sets up bulk flow across the Arctic Ocean from the Pacific sector to the Atlantic sector, with sea ice and ocean water being exported through the Fram Strait near Greenland. Pacific water flows into the Arctic Basin through the Bering Strait (left side of Figure 2.3), though the amount of total flow is severely limited by the bathymetry. Pacific water is subducted under the surface mixed layer, into an intermediate-depth layer characterized by moderately cool temperatures and moderate salinity [Jones et al., 1998]. On the Atlantic side (right in Figure 2.3), highly saline surface water in the northern North Atlantic cools on contact with the sea ice and the cold polar atmosphere. This increases the density, and some of the Atlantic water is subducted underneath the upper layers of the Arctic. Most cools and forms the North Atlantic Deep Water that moves south through the deep parts of the Atlantic Ocean and drives thermohaline circulation.

In addition to the transpolar drift, there are some regular current systems that have significant impacts on the ice environment. The Beaufort Gyre is an anti-cyclonic system in the Beaufort Sea. It is largely responsible for the clump of multi-year sea ice that is found against the northern coast of Greenland, but also for the advection of this ice out away towards the northern coast of Alaska where summer temperatures melt ice and leave large expanses of open water.

In order to really understand the processes surrounding freeze up in the Arctic, a closer look at the structure of the vertical stratigraphy near the surface is required. This is a little complicated, as the vast majority of studies have looked at the stratigraphy in the ice-covered ocean, but the literature on the open Arctic Ocean is growing with the changing climate. Most of the deeper layers exhibit little change, but the the mixed layer becomes a far more dynamic and interesting place when there is no ice layer above insulating it from

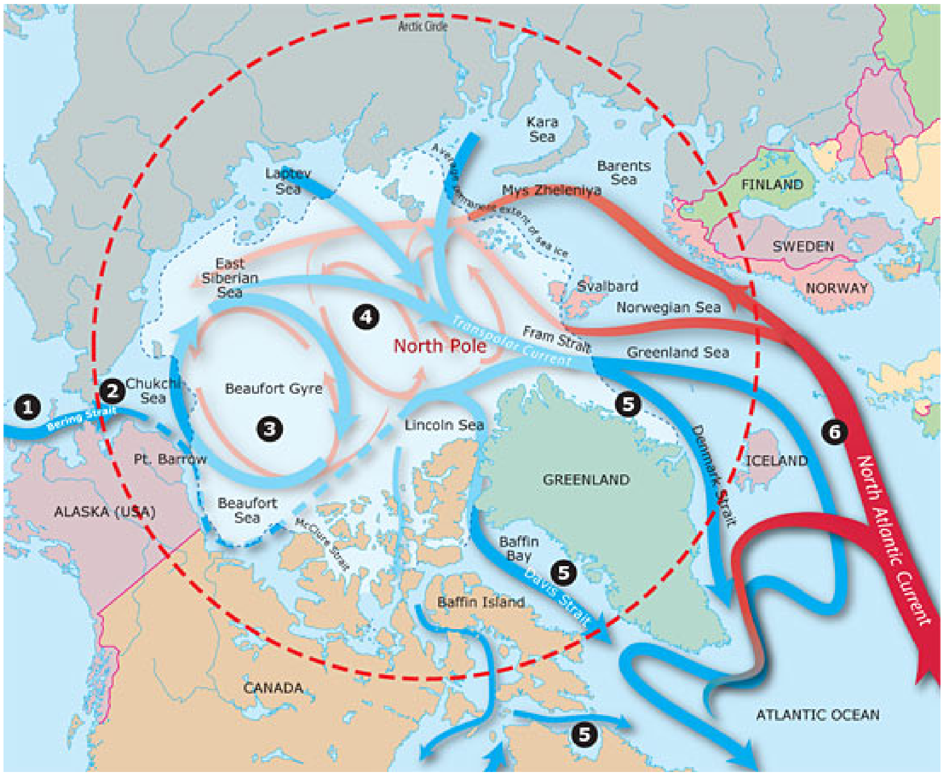

Figure 2.3: Major currents in the Arctic Ocean. Bulk transport is from the pacific sector to the Atlantic sector due to the sea surface slope set up by the differing densities of Pacific water (lower salinity) and Atlantic water (higher salinity). Image reproduced from http://www.divediscover.whoi.edu/arctic/images/ArcticCurrents-labels.jpg.

the atmosphere.

2.2.1 Water masses

This presents a dilemma though: how does sea ice form if there is constantly heat being pumped in with the water masses from lower latitudes? The stratigraphy of the Arctic Ocean water (Figure 2.4) is critically important for the sea ice at the surface. These layers are stable in buoyancy . The surface layer is less dense than the layer below it and the layers below that. This results in very little mixing between layers, limiting the ventilation of the Arctic Ocean but keeping the larger seasonal temperature swings limited to the upper ocean.

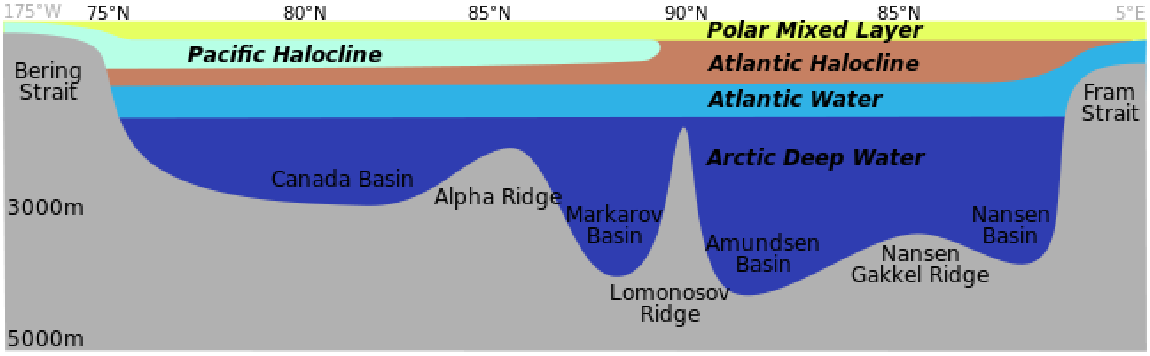

Figure 2.4: Simplified diagram showing the layers in the Arctic Ocean, as observable on a transect from the Bering Strait to the Fram Strait. Figure copied from http://en.wikipedia.org/wiki/Arctic_Ocean.

2.2.1.1 Seasonal layers

At the surface is the polar mixed layer (a longer discussion of the terminology related to the upper ocean is in Section 3.1.1), which will be discussed in great detail throughout this project. It is significantly fresher than any other layer in the Arctic Ocean, and in fact fresher than any other major ocean water mass globally [Morison et al., 2012]. A combination of river discharge, precipitation, and the seasonal cycle of sea ice melt maintain this low salinity. This is the layer that reaches the freezing point and allows ice to exist, but also the layer that responds to atmospheric forcing and is highly dynamic. Included in this “layer” are a number of features and complexities, which are discussed more later. These features include a near surface temperature maximum (NSTM) that has been getting warmer and more consistently present over the last decades, and a strong seasonal signature resulting in a summer mixed layer that forms at the top of the winter mixed layer. These features are discussed at length in Chapter 3.

Figure 2.5 shows profiles of the Brunt-Väisälä frequency (N) in the Beaufort Sea (seasonally open ocean) and the central Arctic (year-round ice cover). The Beaufort Sea is significantly more stable in its stratification as indicated by the large values of N. This is especially true in the top few tens of meters, where the mixed layer sits. As indicated

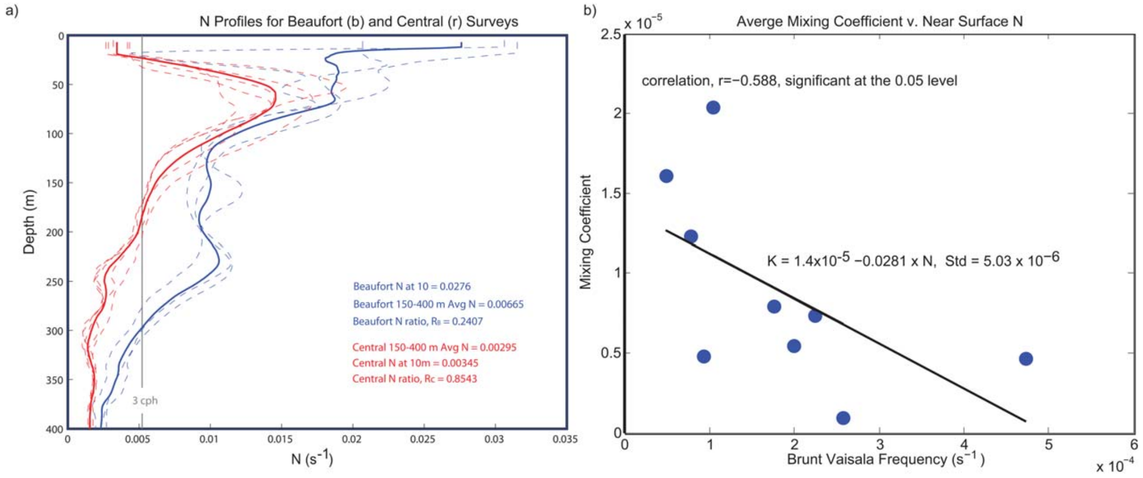

Figure 2.5: Brunt-Väisälä frequency profiles for the central Arctic and the Beaufort Sea. In the Beaufort Sea, highly stable layers at the ocean surface prevent deep mixing. Reproduced from Guthrie et al. [2013].

in the right panel, higher Brunt Vaisala frequencies correspond to lower mixing coefficients and less heat transport across the layers [Guthrie et al., 2013]. In the central Arctic, weak vertical diffusion has been observed on other occasions, and modeling confirms that in order to maintain the cold halocline, vertical mixing across the boundary is necessarily weak [Fer, 2009].

Mixed layer dynamics

Figure 2.6 illustrates the seasonal changes in the central Arctic. In the summer, sea ice melts, releasing fresh water into the upper ocean. This fresh water flux creates the summer halocline, with low-density water sitting at the top of the deeper and more saline winter mixed layer. Solar radiation entering through openings in the ice cover warms the upper ocean at a rate exponentially decreasing with depth, accelerating the melting and fresh water flux at the surface. This warming is primarily above the summer halocline in the central Arctic [Bourgain and Gascard, 2011].

Stratification in the upper Arctic Ocean has changed over the last few decades with increasing ice melt. The most stratified part of the Arctic Ocean is the near surface lay-

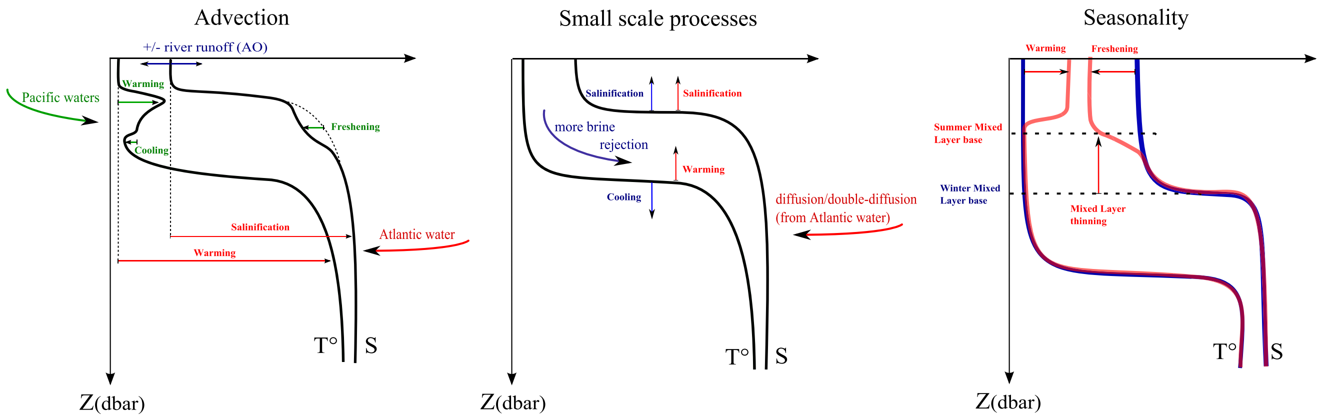

Figure 2.6: Seasonal and process-based evolution of the surface mixed layers as presented in Bourgain and Gascard [2011]. The primary interest for this study is in the seasonal cycle in the right panel.

ers (above 50-100m depth) and includes the summer halocline and mixed layer. The mean annual depths of the summer halocline have shoaled over time [Jackson et al., 2010]. Evidence suggests that the winter mixed layer under year-round ice cover has become shallower over time too, from approximately 50m in the 1980s to approximately 25m in the 2000s [McLaughlin et al., 2011, Toole et al., 2010].

2.2.1.2 Deep ocean water masses

Pacific Water In the Pacific sector, water from the Pacific Ocean forms the next layer down. This is more saline than the surface mixed layer, but the Pacific Ocean water is less saline than Atlantic water, allowing it to persist as a layer between the two. As it gets further from the Bering Strait, the Pacific Ocean water is more likely to have been entrained into either the mixed layer or the Atlantic halocline, and is less likely to be distinguishable as a separate water mass by the time it gets to the Atlantic sector.

Pacific origin waters take two forms based on the season and the pathway across the Chukchi: Pacific Summer Water (PSW, Salinity 33.1 p.s.u., [Coachman et al., 1975, McLaughlin et al., 2011]) and Pacific Winter Water (PWW, salinity > 33.8, [McLaughlin et al., 2011, Weingartner et al., 1998, Pickart et al., 2005, Shimada et al., 2005, Woodgate et al., 2005]). Observations of PSW show it increasing in heat and decreasing in salinity, along with thickening as a layer [Timmermans et al., 2014] since the early 2000s. In the Canadian waters, the PSW, modified over the summer in the Chukchi sea [Steele et al., 2004, Timmermans et al., 2014], is found below the winter halocline.

Atlantic Water The Atlantic halocline is obvious as an increase in both salinity and temperature. Atlantic water is warmer than the mixed layer temperatures (at least in the winter, in the recently open ocean during the summer this is often not the case), but maintains a higher density through the dramatic increase in salinity that occurs in the Atlantic Halocline layer. Below that, Atlantic water is more constant with depth in both salinity and temperature.

As discussed previously, the warm Atlantic layer sits deep in the Arctic Ocean, well insulated from the surface layer. To verify that historical understanding of mixing across this boundary still holds in the modern Arctic – if deep mixing has increased with the increasingly open summer ocean – Guthrie et al. [2013] compared recent and historical mixing observations and found no significant change from the historical records. The Beaufort Sea, which melts out before the central Arctic (still ice covered through the summer) or the eastern Arctic Ocean, exhibits lower deep mixing and internal waves than the central Arctic because of increased stratification [Guthrie et al., 2013]. Freshening of the surface layer due to ice melt and river water input has dramatically increased the stability of the ocean near the surface.

Heat flux upwards from the Atlantic layer in the Barents Sea is similarly modulated by the stratification and stability in the seasonal mixed layer [Lind et al., 2016]. Initial modeling studies suggest that tidal forcing leads to some ventilation of heat from the Atlantic water, but there have not been comprehensive studies of these processes [Holloway and Proshutinsky, 2007].

Arctic deep water Arctic deep water is both highly saline and very cold, making it more dense than the water layers above. It fills the basins in the deep Arctic and inhibits mixing down to the bottom, which is what causes the upper Arctic Ocean to be low in nutrients for primary production [Aagaard et al., 1981].

2.2.1.3 Fresh water input

Figure 2.7 shows the major river systems discharging into the Arctic Ocean. While much of the sub-polar region is fairly dry, there is a tremendous amount of water that eventually gets funneled into the Arctic Ocean from the larger Arctic basin. The remarkably low salinity in the upper Arctic Ocean is due in part to the contributions from these river systems. In the winter, when precipitation in the sub-polar regions is largely in the form of snow, there is very little discharge into the Arctic Ocean. Once this snow starts melting in the spring though, there is a large seasonal pulse of freshwater input. Especially near the major river outlets, freshwater input can have a dramatic effect on the surface ocean.

Studies have used oxygen isotope analysis to attribute sources of freshwater runoff to either meteoric (derived from snow or rain) or sea ice meltwater sources. Rainfall and river runoff cannot be distinguished in this manner, as both river runoff and rainfall come from meteoric water sources ultimately [Yamamoto-Kawai et al., 2009].

Yamamoto-Kawai et al. [2009] shows that in the central Arctic, sea ice meltwater increased by the equivalent of 1.3 $\mathrm{m\,year^{-1}}$ of sea ice. River runoff from the Mackenzie River contributed an anomalously large amount of freshwater in 2007, a record minimum summer ice extent year. In the Eurasian Arctic, river runoff from the six largest rivers increased by 7% over the period from 1936 to 1999. These changes were due to both changes in the North Atlantic Oscillation (patterns of weather systems associated with low pressure systems over Iceland) and the increasing air temperatures [Peterson et al., 2002], which are both factors in the North American Arctic as well. This magnitude of increase in freshwater flux is certainly changing the stratification in the upper ocean. There is limited evidence for increases in precipitation in the Arctic, from observational and modeling studies which show that the largest increase in precipitation may occur near the sea ice edge [Kattsov and Walsh, 2000]. Fresh water in the Beaufort Gyre increased between 2003 and 2010, likely due to increasing sea ice melt, but decreased in 2010-2012, suggesting a shift in the circulation patterns [Krishfield et al., 2014]. When considering previous studies of freshwater sources, Yamamoto-Kawai et al. [2009] concluded that the meltwater component of the surface waters in the southern part of the Canadian Basin has been increasing at $0.27\mathrm{m\,year}^{-1}$ since the late 1980s. A conceptual model of the central Arctic Ocean suggests that the halocline depth should increase with increasing freshwater content [Pemberton and Nilsson, 2016].

The cool summer atmosphere over a cold ocean means that there is significantly less evaporation than there would be in more southern latitudes. Much of the Arctic Ocean is covered in ice year-round, and what is exposed in the summer freezes over in the dry winter, further limiting the potential evaporation. There is some sublimation, but the overall levels are extremely low [Liston et al., 2004]. The net precipitation (high, when the inputs from the broader Arctic basin are included) minus evaporation (low) makes the Arctic Ocean highly stratified, where the surface layer is significantly fresher than the deeper ocean.

As described in Section 3.1.1, the Arctic Ocean is highly stratified with a mixed layer at the surface. This layer is quite fresh relative to the deeper Arctic Ocean and to global mean ocean salinities in general, allowing it to float above the warmer layers at depth. A strong pycnocline determined by this salinity gradient separates the mixed layer (ML) from the deeper ocean.

At the end of the summer, the heat stored in the upper ocean has to be removed in order for the surface to freeze. With saline water, the temperature of maximum density is less than the freezing point. In fresh water, i.e. a lake, the entire body of water could cool to 4°C , at which point any additional cooling at the surface would result in less dense water which floats at the surface and freezes. Ice forms with the bulk of the lake still well above freezing. In the ocean, the cooling water no longer floats. It is because of the mixed layer stratification though that the entire ocean body does not need to cool to freezing: less saline

Figure 2.7: Major river systems that feed into the Arctic Ocean. These contribute to the remarkable freshness of the upper Arctic Ocean and the dramatic salinity gradients that maintain stable stratification. Image reproduced from http://www.arctic.noaa.gov/detect/detection-images/land-arctic-rivers_gro.jpg

but colder water still floats on more saline but warmer water. Only the ML needs to reach freezing – cooling 10-100 meters of water is far more possible than cooling the entire 3000+m of water column in some of the Arctic basins.

2.2.2 Processes governing melt

The primary motivation for studying the freeze-up part of the annual sea ice cycle is to understand the magnitude of feedback effects on the Arctic climate.

When ice melts out in the summer, it exposes the ocean surface to solar radiation. With attenuation values around 0.04 m^{-1}, the upper ocean absorbs some sunlight and this warms the water. Conventional knowledge suggests that water above the freezing point sources heat to ice floes through diffusion, wind-driven mixing, and lateral advection and melts remaining ice until there is no ice left locally. At this point the water in the upper ocean can warm, often getting to several degrees above the freezing temperature [Bradley et al., 2015]. There are several processes that occur during the melt season from late April until the end of the summer which make ice melt proceed quickly.

Solar radiation is largely reflected by fresh snow (albedo of approximately 0.9), but as the snow ages and snow grain metamorphosis progresses, the albedo declines. As the Arctic gets more and more sunlight in the spring, this declining albedo means that more and more sunlight is absorbed by the snow pack until the snow melts. Absorption of solar radiation in the snowpack accelerates grain metamorphosis, with surface melt on snow grains refreezing into larger, rounder crystals.

Once the snow starts to melt, the water needs to go somewhere. Water melting out of the snow pack can pool to form melt ponds, which over first year ice are typically large, shallow, and cover a large fraction of the surface. The undeformed ice has few natural locations for water to pool, so it spreads over the surface into the shallower ponds. Multiyear ice tends to be more deformed, and the snow meltwater pools into deeper but spatially smaller pools [Polashenski et al., 2012].

Meltwater ponds have a lower albedo than the surrounding snow, so incoming solar radiation is absorbed more in these areas, warming the water and accelerating ice and snow melt. Ponds melt through the ice cover down into ocean, opening up pockets of water allowing solar radiation into the ocean where it can warm the surface layer. Thin ice is more transmissive to solar radiation, with thick (2m) ice blocking 99% or more of the photosynthetically active radiation from reaching the ocean [Taskjelle et al., 2015]. First-year ice has a consistently lower surface albedo than multiyear ice due in large part to the difference in melt pond cover, resulting in more solar heat going to first melting the ice cover and then warming the upper ocean [Perovich and Polashenski, 2012].

Warming water underneath the ice then melts the bottom of the sea ice. Bottom melt can account for most of the total ice melt, especially in the Beaufort Sea [Perovich et al., 2008]. Meanwhile, water in the melted-through ponds and former leads is warming and melting ice laterally. Once the snow is all melted off, the ice surface exposed to solar radiation melts as well. These processes are all melting ice, and ice floes decompose into brash ice and then just open water.

Meanwhile, at the edge of the ice pack warmer water from the south interacts with the ice edge, accelerating melt. Weakened ice in this region is especially susceptible to waves, which generate from wind across the open water south of the ice pack. The interactions of waves with the ice pack have not been well characterized in the Arctic due in part to the limited number of years that there has been sufficient fetch for waves to be an significant factor. In general, waves interact with the ice edge, breaking up larger floes. Floe breaking, combined with the melting processes and wind moving ice floes around, creates the Marginal Ice Zone at the edge of the ice pack. This region is defined as being between 15% and 80% ice cover, and has the most extreme albedo feedbacks because of the large amount of open water.

The characteristic that is most important amongst these processes is that they are positive feedbacks: melting begets more melting. The prevalence of positive feedback processes related to sea ice melt is a major contributing factor to Arctic Amplification.

2.2.3 Arctic amplification

Arctic amplification is the phenomenon in climate science in which the Arctic has warmed at rates nearly twice those of the rest of the planet. Though many of the mechanisms involved are still debated, the role of sea ice and the feedback processes associated with its melt seem to play a central role [Screen and Simmonds, 2010]. Models predict a more significant warming over the coming century than has been seen in observations so far, suggesting to some that the concept of Arctic Amplification is overstated in the long-term projections. Analysis of available observational records and short-term modeling efforts suggest that the Arctic is rather in a state of pre-conditioning and will warm at higher rates with the loss of ice cover [Serreze and Francis, 2006].

Atmospheric warming is greatest near the surface and has tracked the loss of sea ice, supporting the role of ice cover-air temperature feedbacks as a primary mechanism for this warming [Screen and Simmonds, 2010]. That said, there is still (by some measure) significant ice present in the summer months limiting the amount of surface air temperature change that can occur over the central Arctic. The increasing length of the melt season and the ongoing retreat of ice is evidence for the pre-conditioning of really accelerated climate change in the Arctic [Serreze and Francis, 2006].

The remarkable loss of summer sea ice extent is also contributing to this feedback: multi-year ice (that which has survived one or more summer melt seasons) is far more resilient than first-year ice. MY ice is thicker (more volume) [Maslanik et al., 2007], accumulates more snow [Webster et al., 2014], and less prone to albedo feedbacks from melt ponds on the surface [Webster et al., 2015]. An ROV study under Arctic sea ice in the summer found that first year ice typically has a transmittance nearly 4 times higher than that of multi-year ice, in part because of higher melt pond fraction on undeformed first-year ice [Nicolaus et al., 2012]. The southern Beaufort has seen notable decreases in multi-year ice cover and corresponding increases in first-year ice cover through the early 2000s-2010s. Moored sonar data from the Beaufort Gyre shows a significant thinning of ice cover, largely due to a loss of multi-year ice between 2003 and 2007 [Krishfield et al., 2014]. During the same period, there was a decrease in FY ice cover in the coastal, Mackenzie delta, and Amundsen Gulf areas, which has been replaced by thin, new ice cover [Galley et al., 2016].

2.3 Surface heat fluxes

In sea ice - ocean - atmosphere interactions, it is often useful to consider the boundary between the ocean (or ice) surface and the atmosphere as a surface across which heat flows. As it is a surface and can therefore have no heat storage, the flux terms must sum to zero.

$$\sum Q = \underbrace{Q_s + Q_l}_{\text{turbulent fluxes}} + \underbrace{\sum R_{lw} + \sum R_{sw}}_{\text{radiative fluxes}} + \underbrace{M}_{\text{Melt}} + \underbrace{C + H_O}_{\text{below surface}} = 0 \tag{2.1}$$

The two turbulent fluxes (related to air moving across the surface) are sensible heat flux and latent heat flux. The next two terms are the radiative balance - long wave includes thermal radiation emitted by the surface and the downwelling long wave radiation emitted by the atmosphere that is then absorbed by the surface. Clouds are particularly important in the latter component, and can often flip the radiative balance of the system. The second radiative component is short wave, or solar, radiation. This is only important in the summer when there is daylight and therefore shortwave radiation in the system. The next in the equation is melt (or freezing), which is heat either released or taken in through a phase change. C represents conductive heat flow through the ice, including snowpack if applicable, if the surface is frozen and H_O is the heat flux from the ocean if the surface is not frozen [Sedlar et al., 2010].

These fluxes vary in both space and time, and can be approached in either the spatial average sense over large areas (as is typically done with remote sensing data products) or in a physics-resolving sense at a point. The bulk treatment, where a large area (on the scale of snow or features in the ice pack, from hundreds of meters for most shortwave imagery to many kilometers for microwave or degrees of latitude in reanalysis and models) may be all covered by a single pixel and therefore a single spatial average estimate of various properties.

2.3.1 Sensible heat loss

Sensible heat flux is related to the temperature difference between the surface (either ice or ocean) and the air and the amount of air moving by the surface (quantified by density and wind speed).

$$Q_s = \rho_a c_{pa} C_{sh} S_w (T_s - T_a) \tag{2.2}$$

where T_s is either the ocean or ice surface temperature, ρ_a is the density of air at the surface, c_{pa} is the specific heat of dry air, C_{sh} is a coupling efficiency coefficient (typically 0.00175 [Weeks, 2010]), and S_w is wind speed, typically measured at 10m above the surface.

Sensible heat is a significant contribution to the energy budget year-round. Heat from the ocean gets conducted up through the ice and snow and then can be lost to the atmosphere. High winds (i.e., during storms) increase the air moving across the surface and therefore the amount of heat that gets lost through sensible heat fluxes.

2.3.2 Latent heat loss

Latent heat flux is related to the evaporation of water molecules off of the surface. As such, when ice covers the surface of the ocean, latent heat flux decreases dramatically.

$$Q_L = \rho_a L_v C_{lh} S_w (q_s - q_a) \tag{2.3}$$

Here, L_v is the latent heat of vaporization, C_{lh} is another coupling efficiency coefficient (also typically 0.00175 [Weeks, 2010]), and q describes the specific humidity at the surface and of the air.

In the winter, once ice covers the Arctic Ocean, latent heat loss decreases significantly. Unlike with sensible heat, there is no moisture flux through the ice cover, so the source for this heat flux is cut off. Similar to sensible heat flux though this term is highly dependent on the wind speed. With no wind, water vapor evaporates on the surface but just sits there, reaching equilibrium water vapor pressure and ending all latent heat flux. In higher winds, the water vapor that evaporates off the surface is immediately moved away from the surface and allows more evaporation to take place.

2.3.3 Radiative fluxes

Radiative heat flux comes in two primary forms: long wave radiation is thermal emission from sources on Earth, including the atmosphere. Solar, or shortwave radiation comes from the sun.

Solar radiation is highly seasonal in the Arctic due to the tilt in Earth's rotation. In the winter, there is no incoming solar radiation and the term goes to zero. At the height of summer (or for many months of summer, depending on how far north the point of interest is), the sun is always up and there is a nearly constant, if moderately low because of the low angle of incidence, incoming solar radiation.

Solar radiation incident at the top of the atmosphere must make it through the atmosphere before reaching the surface. The atmosphere is mostly transparent in the visible wavelengths. Roughly 50% of the solar radiation is absorbed by the atmosphere, mostly in the UV. Clouds however are fairly reflective in these wavelengths (hence appearing white) and in the typically cloudy Arctic (up to 80% cloud cover, [Serreze and Barry, 2005] during certain times of the year), exert a sizable influence on the radiative budget by reflecting much of the incoming solar radiation.

The solar radiation which does make it to the surface then interacts with the surface. Albedo is a more general term for the reflectivity in the visible wavelength and varies dramatically with angle of incidence, wavelength, and most importantly surface type. Fresh snow can have an albedo in the visible wavelengths as high as 0.95, old snow closer to 0.7, bare ice in the range of 0.4 and open water around 0.1 [Curry et al., 1995]. Reflected shortwave radiation is not absorbed by the ice/ocean and does not contribute to warming of the near-surface or ice melt.

The substantial difference in albedos between the surface types is what leads to the albedo feedback effect, where open water absorbs more solar radiation, heats up, and melts more ice. Consistent ice cover, on the other hand, reflects more solar radiation, limiting melt. Even small gaps in ice cover can let solar radiation into the upper ocean, accelerating ice melt [Perovich et al., 2011].

Long wave radiation is primarily emitted by sources on Earth. All matter emits radiation according to Planck's law of blackbody radiation, with the peak in emitted wavelength proportional to the temperature of the object and the total emitted radiation scaling with T^4. All matter has some sort of emissivity function, but water, ice and water vapor behave fairly close to blackbody in the wavelengths emitted at near-freezing temperatures.

The balance of long wave fluxes is composed of the upwelling component emitted by the surface and the downwelling component emitted by the atmosphere. The atmosphere is also emitting radiation in the microwave (long) wavelengths. Blackbody radiation is isotropic, so roughly half of what is emitted by an air parcel in the atmosphere is emitted into the downward direction. The surface receives some fraction of the emitted atmospheric radiation, and of this some is absorbed according to the long wave reflectivity of the surface type.

2.3.4 Melt and freezing

Additional heat exchange at the surface may occur in the form of melting or freezing of ice. This is especially so in the summer, where surface melting is common. Only at the first initiation of freeze-up does ice form at the surface. Given that the source of water to freeze is underneath the ice pack, ice forms at the ice-ocean boundary rather than the ice-atmosphere boundary for most of the season. Solar radiation incident on the surface can contribute to melt, as can warm air temperatures. The heat fluxes that drive sea ice growth occur at the ice/snow-atmosphere interface, and ice growth is slowed by the need to conduct heat through the ice cover.

2.3.5 Below the surface

What happens on the bottom side of the boundary between surface and atmosphere depends on the state of the surface at the time. In open water, the fluxes in and out of the top of the boundary are balanced by heat flux into the ocean, typically manifesting as a change in water temperature. When ice covers the surface, the top fluxes are balanced by heat conduction through the ice that then results in freezing at the ice-ocean interface. These conductive heat fluxes will be discussed in greater detail in Chapter 5.

With heat primarily leaving the ocean at the surface, mixing keeps the surface layer at a constant temperature (and salinity). Three processes account for thermal mixing in the surface layer of the Arctic Ocean:

(1) Wind-induced mixing. Wind drag on the surface induces a current right at the surface. This then exerts a shear force on the infinitesimally thin layer below it, and the net effect is that a gradient in subsurface current is set up, both in terms of magnitude and direction. If this gradient exceeds a certain threshold which is a function of the viscosity of the sea water (salinity, temperature), the sheer will induce vertical mixing through small eddies.

(2) Convective mixing. In a body of water that is at a constant temperature and salinity, if the top is cooled slightly it will become more dense than the water below it. A more dense water parcel will sink though the column until it reaches a vertical position where the density below is greater than the density of the water parcel in question. Cooling at the surface of the mixed layer does exactly that: water parcels are cooled and mix into the rest of the mixed layer, resulting in net heat loss from the surface layer of the ocean.

(3) Thermal diffusion is the process by which a warm water parcel will diffuse heat into a nearby cool water parcel through the transfer of kinetic energy at the molecular level. The rate of heat transfer through thermal diffusion is orders of magnitude slower than through mixing.

2.4 Physical process of freeze-up in sea water

There is a long way to go from summer minimum ice extent to ocean conditions in which ice can form – this is the focus of a substantial part of this thesis. Once the ocean conditions are conducive to ice formation, the ice has to actually form. At the molecular level, this is accomplished by water molecules crystalizing, which requires sufficiently low temperatures and some sort of nucleation. Typically in sea water the latter is not an issue, but supercooled water up to 0.02 °C below the freezing point has been observed in Antarctic polynyas [Drucker, 2003] and during freeze-up.

2.4.1 Temperature dependence on salinity

As mentioned in the discussion of Arctic water masses (Sections 2.2.1 and 3.1.1), the density properties of sea water depend significantly on the salinity and temperature. Likewise, the freezing point also varies with salinity. These two characteristics are well studied, and empirical functions have been established to relate sea water temperature, pressure, and salinity to density and freezing point.

The equation of state for sea water is an empirical relationship, $\rho = \rho(T, S, P)$ presented in Gill [1982] and other sources [Millero and Huang, 2009, Fofonoff, 1985, Sharqawy et al., 2012] to the accuracy with which sea water density, salinity, temperature, and pressure can be measured. The lengthy empirical terms can be looked up in those references and need not be reproduced here.

For sea water, density generally increases slightly with pressure, somewhat with temperature, and significantly with salinity. Given how little ρ varies with pressure and that this thesis focuses on processes at the surface of the ocean, the dependence on pressure is small enough that it can be ignored in this analysis. The temperature dependence is a little more complicated – for any salinity, there is a temperature that corresponds to a maximum density below which the water molecules start to form the bonds that will ultimately hold them in the crystal lattice and the density decreases correspondingly. The temperature of maximum density [°C] is related to salinity by

$$T_{\rho max} = -0.215\,^{\circ}\mathrm{C/p.s.u.} \times S + 3.98\,^{\circ}\mathrm{C} \tag{2.4}$$

The freezing point [°C] is also a function of salinity, decreasing linearly with increasing salinity (in p.s.u., practical salinity units, roughly parts per thousand). Fresh water freezes at 0°C , typical sea water freezes at -1.8°C [Wadhams, 2000]. For water with salinity above 24.7 p.s.u. (considered the transition from brackish water to seawater), the freezing point is higher than the temperature of maximum density, so the maximum density will never occur. The freezing point for sea water is given by

$$T_f = -0.0539\,^{\circ}\mathrm{C/p.s.u.} \times S \tag{2.5}$$

There are a few locations in the Arctic near river outlets where surface salinities can be below this critical value, and there the ice forms very quickly because cooled water can float above a warmer surface layer [Wadhams, 2000]. For the vast majority of the Arctic though, the entire mixed layer must cool because the freezing point is above the temperature of maximum density.

2.4.2 Brunt-Väisälä frequency

The Brunt-Väisälä frequency is a measure of the stability of ocean stratification. In units of s^{-1}, the physical meaning is the maximum frequency of oscillation that would result from displacing a water parcel in the surrounding ocean by a small vertical distance. In more physical terms, it indicates how much forcing would be required to induce mixing. The parameter is defined as

$$N = \sqrt{\frac{g}{\rho}\frac{d\rho(T,S)}{dz}} \tag{2.6}$$

where ρ is the potential density, which is the density a water parcel would have if brought adiabatically to a reference pressure (ocean surface) and is a function of both temperature and salinity as described earlier. g is simply the acceleration due to gravity, and the z direction is defined as positive down (density increases with depth in stable stratification). The derivative of potential density with depth is what describes the stability of the fluid – the quicker the density decreases towards the surface, the more stable it is.

The surface mixed layer in the Arctic Ocean has an extremely high Brunt-Väisälä frequency, up to 0.03 s^{-1} [Guthrie et al., 2013]. For comparison, most of the Pacific has surface mixed layers with Brunt-Väisälä frequencies ranging from 0.008 to 0.015, with N above 0.02 only right near the equator [Emery et al., 1984] where extreme warming and significant precipitation keep the surface layer buoyant.

2.4.3 New ice evolution

2.4.3.1 Frazil to young Ice

Once sea water is cooled to the freezing point, it begins to form ice (illustrated in Figure 2.8). This first starts as frazil, which consists of small discs of ice suspended in water that grow and break and grow some more until the near-surface water column is increasingly high in frazil density. High density frazil slurry is called grease ice for its matte, dark appearance. In calm conditions, this slowly consolidates into thin ice with some thickness to it (around 10 cm thick) that can then grow through congelation freezing.

In windy conditions where the ocean surface has some wave action, the ice formation proceeds slightly differently. Clumps of frazil form into round disks at the surface that bump into each other, forming pancake ice. These rounded rafts of ice form on the order of meter to several-meters across, depending on the wave environment, and the constant bumping causes ridges around the edges. Eventually the surface gets cold enough that the pancakes freeze together, forming a rougher surface than would result from ice forming under calm conditions.

Both of these processes result in brine inclusions (also referred to as pockets, or after some time channels) in the ice. These make the bulk salinity of sea ice non-zero – around 5 p.s.u. is not uncommon, though this is highly variable. Brine pockets change the thermal conductivity of the ice slightly. They also grow and shrink in response to the thermal forcing in the ice, maintaining an equilibrium with the temperature of the ice and the freezing point of the brine concentration in the pockets.

Frazil		Frazil ice crystals are suspended in water at the freezing temperature. Photo copied from http://nsidc.org/cryosphere/glossary-terms/sea-ice?page=2.
Grease ice		Grease ice forms from a high density of frazil. Photo copied from https://photos.travelblog.org/Photos/12073/257194/f/2101807-grease-ice-0.jpg.
Nilas (thin)		Grease ice solidifies into Nilas, which is transparent when thin (around 10cm). Photo copied from http://gallery.usgs.gov/images/12_09_2008/wBRe7IHtt5/medium/IMG_3015.JPG.
Nilas (thick)	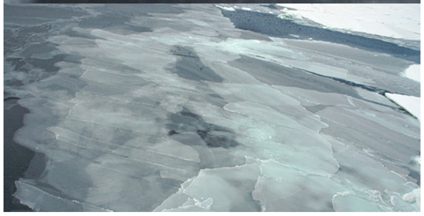	Nilas grows through both increasing ice thickness and rafting until it is no longer transparent. Nilas is still thin enough to bend over waves. Photo copied from http://earthobservatory.nasa.gov/Features/SeaIce/images/01_nilas_ice.jpg.
Young ice		Ice continues to grow though water freezing to the bottom. Photo copied from http://www.npolar.no/npcms/export/sites/np/images/portal-pages/research/havis-NP039674.jpg_1488410821.jpg.
Pancake ice		Frazil forming in wave action can consolidate into pancakes of ice with deformation around the edges from bumping against other pancakes. Photo copied from http://blogs.egu.eu/geolog/files/2013/11/Pancake-ice.jpg.

Figure 2.8: Stages of sea ice formation.

2.4.3.2 Congelation freezing

Once there is a solid ice surface, ice formation transitions to primarily congelation freezing. This consists of cold water below the ice surface freezing to the ice with no nucleation necessary, though frazil suspended in the water column can also bind to the growing ice floe from below. The bottom surface is often very smooth because of this growth process. While the details of the microstructure of sea ice growth are fascinating, these processes fall outside of the scope of this project. The important part is that brine and gas inclusions in the ice effect its optical properties, making sea ice appear more white than is typical of freshwater ice [Eicken, 2003].

Ice growth rates have been studied for some time, starting with in situ observations made by ships frozen into first year ice in the 1870s. In 1872-1874, Weyprecht noted the first relationship between ice thickness and meteorological conditions (freezing degree-days), where ice thickness could be calculated by

$$H = c * \left(\int_0^t (T_f - T_a) dt \right)^n \tag{2.7}$$

where c is a constant, the integrated term is cumulative degree-days, and the power had a value of approximately 1/2 [Weyprecht and GRAZ, 1875, Weeks, 2010]. Degree-day models have been used frequently since, though it has been found that the constant is somewhat variable between observations and the power is a function of the local ice thickness. For thin ice, a linear function of temperature differential was shown to be more a appropriate fit for ice thickness, likely because the assumption that the ice surface temperature is equal to the air temperature is not particularly accurate [Wakatsuchi and Ono, 1983]. Empirical models have been frequently used as well [Weeks, 2010].

Maykut [1986] developed a physical model that captures the main process, conductive heat flux through the ice. Conductive heat flux through the ice must be equal to the heat fluxes leaving the ice at the surface, unless the ice is changing temperature.

$$F_c(z=0) = F_c(z=H) = k_i \left(\frac{T_o - T_f}{H} \right) \tag{2.8}$$

where H is the thickness of the ice, T_o is the ice surface temperature and T_f is the freezing point, based on the assumption that the ice-ocean interface must be at the freezing point. The thickness and surface temperature variables can be solved for by considering the growth (or melt if negative) at the ice-ocean interface, where latent heat release balances the conductive heat through the ice and any additional heat flux from the water below.

$$-\rho_i L \frac{dH}{dt} = F_c(H) + F_w \tag{2.9}$$

Ice growth through most of the winter follows this method of growth. Beyond the thin ice types, which typically last on the timescale of weeks at the most, leads and polynyas are the only other cases of areas of open water in the Arctic Basin through most of the winter. These limited areas grow ice out of open water through the progression of thin ice types similar to freeze-up in the fall. Elsewhere in the Arctic, ice grows by consolidating onto the bottom of the ice pack through congelation freezing.

Chapter 3

Seasonal Cycle of Heat in the upper Arctic Ocean seasonal ice zone

In the seasonal ice zone, the upper ocean undergoes dramatic changes throughout the year. Wintertime sea ice cover melts off in the summer, exposing open water to solar radiation for months at a time. This chapter focuses on the seasonal ice zones in the western Arctic, where some of the most dramatic changes have occurred. This chapter further explains the mechanisms by which summertime processes that extend the melt season and allow for additional absorption of solar radiation have continued impacts into the winter.

3.1 Introduction

As the Arctic Ocean transitions to an environment of primarily first-year ice, there is increasing area of seasonal ice zone (SIZ, defined as the area that is ice-free at some point during the summer melt season). Areas that had not experienced fully open water previously in the satellite record have been ice-free for months at a time in recent summers. The pace of climate change is accelerated in the Arctic [Screen and Simmonds, 2010] and is most obvious in the rapidly decreasing summertime sea ice extent and increasing areas of open water.

Summer melt-out is happening earlier in many locations [Stroeve et al., 2014], leading to a longer season of open water. Solar energy incident on the surface is absorbed by the upper ocean, warming the near-surface waters [Perovich et al., 2007, 2011].

Wintertime sea ice extents have not decreased proportionally as much as the summer ice extents, and increasingly large areas of first year ice are forming out of open water. In order for ice to grow at the surface, water in the uppermost layer of the ocean must be at the freezing point. Heat loss from the summer mixed layer is largely to the atmosphere, through turbulent heat fluxes and radiative cooling. Little or no incoming solar radiation, combined with cold air temperatures and high winds set up by strong surface temperature differentials, leads to strongly negative heat fluxes and rapid cooling of the upper ocean.

The timing of freeze-up has been delayed by several weeks in areas of the western Arctic, in large part due to the high heat content of the summer mixed layer [Stroeve et al., 2014]. There have been suggestions that this delay, by shortening the sea ice growth season, could result in a thinner first-year ice cover [Stroeve et al., 2012].

This chapter describes the transition from warm summertime conditions to the point where freeze-up can proceed and first-year ice starts to grow. Maykut [1985] (also outlined in Serreze and Barry [2005]) described the cooling process prior to freeze-up based on observations from Soviet Union drifting stations located on predominantly multi-year ice floes. Mixed layer temperatures in the Arctic rarely rose significantly above freezing, and the depth of the summer mixed layer was therefore the dominant factor in determining the date of freeze-up [Doronin and Kheisin, 1975]. More attention was given to the initial formation of frazil and grease ice than the process of cooling to the freezing point.

Bourgain and Gascard [2011] described the seasonal cycle in a schematic illustrating the factors influencing the winter halocline. The summer halocline is a transient seasonal phenomenon which comes and goes with the formation of sea ice at the surface. In Bourgain and Gascard [2011], the summer thermocline is drawn as being fully above the summer halocline, where summer halocline water is isothermal and at the freezing point.

Peralta-Ferriz and Woodgate [2015] developed a monthly climatology of mixed layer depths (defined by the pycnocline) around the Arctic based on in situ measurements. They found that mixed layers vary strongly, with consistent differences between summer and winter mixed layers, summers being consistently shallower in all regions of the Arctic. This climatology compared summer mixed layer depths (June-October) to winter mixed layer depths (November-May), neglecting the transition seasons in between. They do include a discussion of the seasonal cycle in mixed layer depth, but only in the context of the salinity profile.

The bulk of study of near-surface heat content comes from ice-anchored buoys (often Ice-Tethered Profilers) rather than free drifting buoys, which means that the studies have been largely limited to areas under multi-year ice. These time series do not see an ice-free summer and therefore do not capture that part of the annual cycle. Nevertheless, these platforms provide valuable insight into the interactions of upper ocean heat and sea ice at the surface.

3.1.1 Stratification in the upper Arctic Ocean

Seasonal processes in the Arctic Ocean occur at the surface in the seasonally-modified Arctic Water, also called the Polar Water Layer, Polar mixed layer, Arctic Ocean Water, surface convective mixed layer, seasonal mixing layers, and others. In this chapter, water in the winter (cold) halocline and above up to the surface will be collectively referred to as seasonally-modified Arctic Water or AW. Calling this layer a“mixed” layer can be misleading, as mixing depth varies with atmospheric forcing and ice cover, and remnants of the “winter mixed layer” can persist even when it is not being mixed. Layers within the AW can be well isolated from surface-driven mixing through much of the year. Water in the AW comes from the Pacific and Atlantic inflow [Jones et al., 1998] and river runoff [Rudels et al., 1996], though it is quickly modified by seasonal processes.

Figure 3.1 shows a vertical profile of the Arctic Ocean as measured by a CTD cast in the western Beaufort (74.33N, 151.70W, July 2005), off the continental shelf about 375 km NNE of Barrow, Alaska. The strong salinity gradient starting at 20 dbar depth is the summer halocline, at a depth that is fairly common for the region [Peralta-Ferriz and Woodgate, 2015]. Relatively fresh sea ice melt-water defines the summer mixed layer, and temperatures in this vary throughout the season. The strong summer pycnocline, set primarily by the

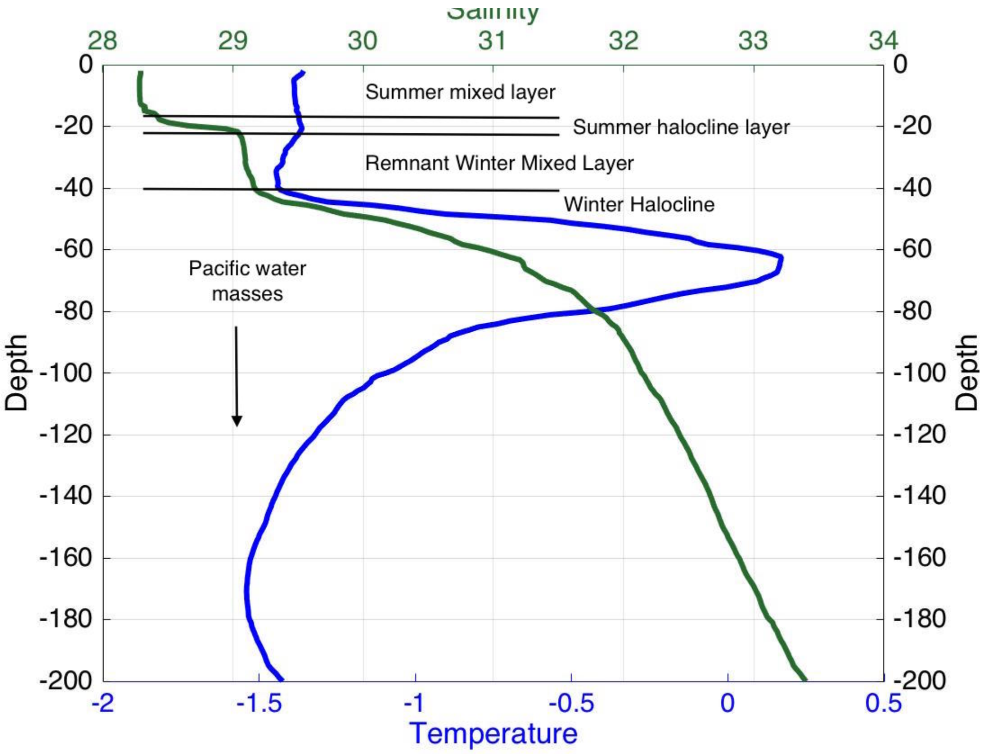

Figure 3.1: Temperature (blue) and salinity (green) profile from a CTD profile in the western Beaufort. This profile was taken at 74.33N, 151.70W, on July 9, 2005.

halocline, inhibits surface-driven mixing below this layer.

The water layer in contact with the surface is most often called the surface mixed layer (SML), and occasionally the summer mixed layer (also, SML. The two terms are interchangeable in the summer and rarely applied in the winter). Lind et al. [2016] calls it the surface layer, making no reference to the mixing that maintains the isothermal and isothermal properties of the layer.

During the summer months, the shallowest halocline is referred to as the summer halocline (SL) or the near-surface halocline [McLaughlin et al., 2011]. This can also be referred to as the upper pycnocline (as salinity drives the density gradient in the upper Arctic) [Shaw et al., 2009]. Rather than defining the summer halocline as a single depth (as in Jackson et al. [2012] and many others), this study considers the summer halocline a layer, defined as the range of depths with a strong gradient in salinity. This means that there can be heat in the halocline layer, which proves useful for explaining trapped heat at the end of the summer season. By limiting the halocline to a single depth level rather than a layer, heat in the water column must therefore be either in the “mixed layer” (which is not fully mixed near a halocline level) or below the halocline. If the halocline can contain heat, then the seasonal cycle in establishing the summer halocline layer has a more direct impact on the seasonal storing of heat in the layer. This is backed up by observations discussed later in the chapter.

The temperature minimum below the summer halocline is the remnant of the winter mixed layer (rWML, Zhao et al. [2014], McLaughlin et al. [2011]). Lind et al. [2016] calls this the Arctic layer in the northern Barents, and by all normal metrics has similar properties to and fills the same roles as the cold halocline layer elsewhere. Often this “layer” is either confused with or included in the halocline layer below.

The significant halocline separating the seasonally modified waters from the deeper Atlantic water (or Pacific Summer Water) is the Arctic Halocline [Zhao et al., 2014], Cold Halocline [Fer, 2009], winter halocline, or sometimes just the halocline [Timmermans et al., 2008]. The seasonally modified Arctic Water is defined by the winter halocline and extends tens [Toole et al., 2010] to about 200 meters down into the water column, depending on location and weather patterns. The cold halocline is characterized by temperatures close to the freezing point and strong salinity gradients with depth, and is typically found above 250m depth in the Canadian basin [Timmermans et al., 2008]. Features like the Beaufort Gyre tend to have a deeper winter halocline due to Ekman pumping, and this depth varies with the strength of the gyre [Watanabe, 2013, Giles et al., 2012, Proshutinsky et al., 2009].

Higher salinity (31-33 p.s.u) Pacific Water entering the Arctic through the Bering Strait is modified while crossing the Chukchi shelf and becomes the Pacific Summer and Pacific Winter Water layers [Steele et al., 2004], defining the halocline below the Upper Arctic Water, in addition to sourcing water into the seasonally modified layers. Advective heat flux in to the Arctic in the form of Pacific Water has been suggested to contribute to ice melt at the surface near the Bering Strait [Woodgate et al., 2010], but further into the basin the Pacific Water is well insulated from the surface by the cold/winter halocline layer [Bourgain and Gascard, 2011].

Elsewhere in the Arctic the halocline is set by the Atlantic Water Layer. There has been significant discussion of the amount of heat flux between the warm Atlantic water layer and the seasonally-modified AW. Estimates range from approximately zero [Fer, 2009] in the Central Arctic (under perennial ice cover) to approximately 1 $\mathrm{W\,m^{-2}}$ (still negligible compared to surface fluxes on the order of 150 $\mathrm{W\,m^{-2}}$) in the Eastern Eurasian basin [Polyakov et al., 2013] where there is both more seasonal ice cover and topographic interactions with Atlantic water flowing into the basin. Changes in Arctic sea ice over the past decades could not be attributed to changing heat flux from the Atlantic water layer in Bourgain and Gascard [2011] but rather to upper ocean interactions with a warming atmosphere.

3.1.2 Near Surface Temperature Maximums

The Near-Surface Temperature Maximum (NSTM) is a feature intermittently observed in profiles (mostly under multi-year ice cover) where temperatures below the summer halocline (defined as the depth of the maximum density gradient) exceed the temperatures at the surface. This feature forms when sufficient solar radiation in the early melt season warms the upper ocean [Jackson et al., 2010]. Summer ice melt forms a seasonal halocline, above which cold, fresh meltwater off of ice floes is separated from lower layers. This halocline traps the warmed water beneath it, inhibiting mixing with the upper layer that exchanges heat with the atmosphere. Typically melt starts before the NSTM forms, forming the halocline that inhibits mixing. Steele et al. [2011] used a high-resolution Arctic Ocean model to determine how and where the NSTM forms. It supported the mechanism suggested in Jackson et al. [2010] and further indicated that the NSTM could be formed in the late season through the cooling of a stratified upper ocean. The survival of the NSTM though the winter was confined to the highly stratified Beaufort Sea region [Steele et al., 2011]. Entrainment of heat from a NSTM into the surface mixed layer occurs when the surface mixed layer mixes down as far as the NSTM. With the NSTM traditionally considered to be below the summer halocline. Both diffusion (slow) and mixing through the summer halocline (fast) result in NSTM heat warming the SML [Jackson et al., 2012].

The NSTM has been observed within or immediately below the summer halocline several times over the last two decades, depending on whether the halocline is a single depth or a layer [Maykut and McPhee, 1995, McPhee et al., 1998, Jackson et al., 2010]. The NSTM has been observed to be between 0.2°C above freezing [McPhee et al., 1998] in the mid 1970s and as high as 0.6°C above freezing in the late 1990s [Shimada et al., 2001], gradually warming over time. In the early to mid 2000s, Ice Tethered Profilers [Toole et al., 2011] observed NSTM features over several years. One ITP observed subsurface temperatures up to 0.7°C above the freezing point only 20m below the surface during the ice growth season [Jackson et al., 2010].

Jackson et al. [2010] described NSTM temperatures up to 1.2 °C above freezing from Ice Tethered Profilers [Toole et al., 2011] in 2009, but noted that there is significant spatial variability in the development of the NSTM over the summer. For comparison, Maykut and McPhee [1995] noted (then unnamed) NSTMs up to 0.4°C above freezing. Timmermans [2015] showed temperatures approximately 1°C above freezing over the 2007-2008 winter. Steele et al. [2011] described the NSTM in a modeling study, accounting for up to 6 °C above freezing in the southern Chukchi. Jackson et al. [2010] also described NSTMs detected in CTD profiles, indicating that NSTMs detected at more southerly locations were significantly warmer (up to 11°C above freezing in 2006, though more typically less than 4°C), with the highest temperatures found at coastal and southerly CTD stations. In Jackson et al. [2010], Steele et al. [2011], the NSTM is found below the summer halocline.

The NSTM is primarily formed by vertical thermodynamics due to the solar heating of water below the ocean surface, but wind-driven processes contribute significantly to the depth of the layer. This heat is absorbed locally by solar radiation that penetrates the ice cover either through leads or melt ponds and areas of thinned ice [Perovich et al., 2008]. Depth of the NSTM over the course of the winter decreased according to average downwelling rates due to Ekman pumping [Jackson et al., 2010]. Some variation around this could be explained by storm-driven ice motion causing drag on the ocean and therefore vertical mixing. Further, the ITPs were not Lagrangian relative to NSTM layer water, so drift into a region where the layer may have formed at a different depth contributed to this variability. There is substantial spatial variability in the NSTM due to ice presence and atmospheric inhomogeneity during formation, as observed in CTD profiles considered in Jackson et al. [2010]. This is a function of ice cover and cloud cover, both of which are highly variable spatially and contribute to the spatial variability in the NSTM observed in the CTD profiles. Sufficient solar radiation entering the water column is attenuated in the region of the water column that becomes the NSTM to raise the temperature to that which is observed in the CTD and ITP profiles described in Jackson et al. [2010].

Jackson et al. [2010] suggest that heat stored below the surface mixed layer (in the NSTM) will increase as the Arctic climate warms and melt initiates sooner. Mixing induced by storms in the winter can entrain heat from the NSTM up into the surface layer, contributing to bottom melting of ice or slowing the growth. This would result in thinner ice cover, which would melt earlier in the spring and feed back into warmer NSTM temperatures. Thinner ice is also more susceptible to motion from the wind, so more stress is transferred from wind on the surface into mixing in the upper ocean, leading to the erosion of the halocline separating the NSTM from the surface layer [Jackson et al., 2010] and contributing the the feedback cycle.

3.1.3 Seasonal cycle

From temperature and salinity profiles and buoy time series, supplemented by discussions of the seasonal cycle and Near-Surface Temperature Maximums in the existing literature, we can describe the process by which the summer upper Arctic Ocean warms and cools when exposed to solar radiation. The profiles shown in Figure 3.2 are idealized, but represent the typical patterns in the profiles. They include the seasonally modified water layers, but not the Pacific- or Atlantic-origin water masses below.

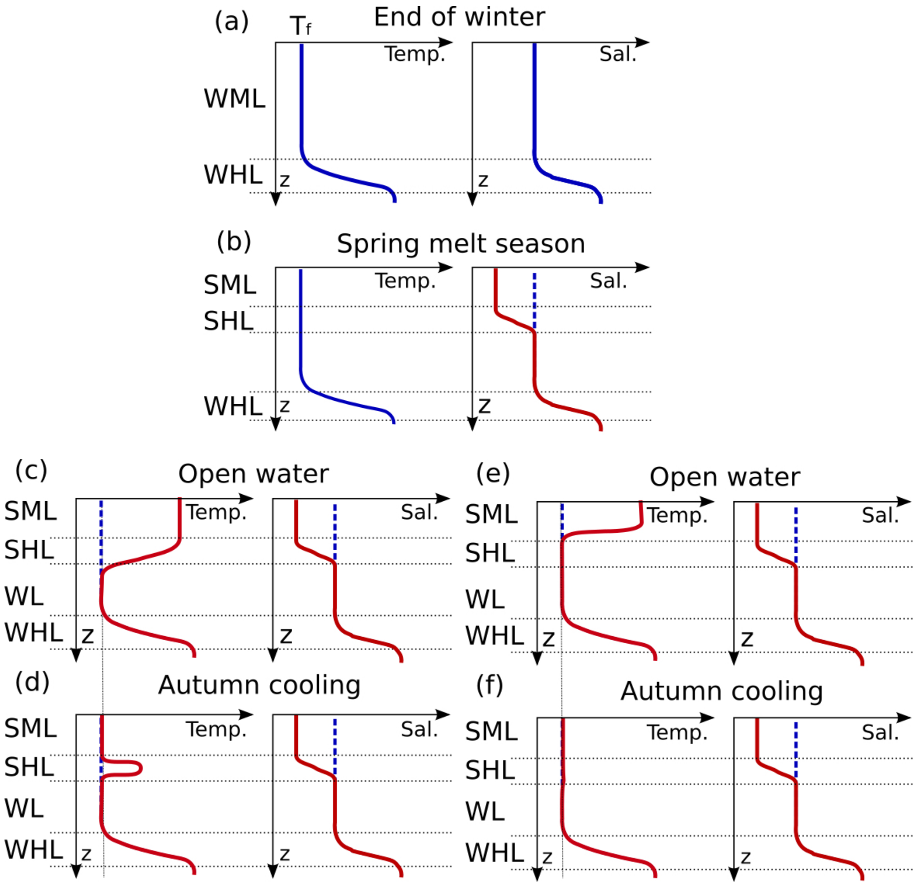

Figure 3.2: Idealized profiles of temperature and salinity in the upper Arctic Ocean for two scenarios of progression through the seasonal cycle starting at (a) the end of winter, then progressing through (b) spring melt season as floes release fresh water, (c) open water that is warmed by solar radiation, (d) cooling prior to freeze-up in the fall, assuming that solar radiation penetrates into the summer halocline layer and forms the summer thermocline in the summer halocline layer. The right track assumes that there is no warming in the halocline layer, with (e) showing a summer thermocline fully above the halocline, and (f) the thermocline fully erased in the cooling process. The freezing temperature is indicated by T_f and salinity varies with location. Blue lines indicate the winter profiles, while red lines show the seasonal deviation from the winter profiles.

Figure 3.2 shows two scenarios for where in the water column summertime heat accumulates in the water column. The two follow the same progression through the end of winter (a) and the beginning of ice melt (b), where fresh water is released from the sea ice into the upper ocean, forming the summer halocline. In the first scenario (left column), solar radiation penetrates into the summer halocline and warms water in that layer. In the second scenario, solar radiation does not penetrate that far into the water column and warms only the surface mixed layer.

3.1.3.1 End of winter

It is useful to think of the profile of temperature and salinity in the upper ocean in terms of seasonal deviations from the baseline profile present at the end of winter, shown in Figure 3.2-a as a solid blue line and in subsequent figures as a dotted blue line. At this point, maximum ice growth has occurred, and when the environment is in steady state, the winter's worth of ice growth and surface-driven mixing will have erased any evidence of the previous summer.

The winter mixed layer extends from the surface down to a strong salinity gradient, the winter halocline. This separates the seasonally-modified water from the deeper (and typically warmer) water masses. Pacific-origin water in the western Arctic, and Atlantic-origin water across the Arctic basins, fills these lower layers.

3.1.3.2 Spring ice melt

Starting in April or May, the radiative balance in the Arctic becomes sufficiently positive that sea ice starts to melt first through surface melting, melt pond formation and growing leads, then due to solar absorption in the leads and bottom melt. During this period, gaps between ice floes and thin ice cover allow solar radiation to warm the upper ocean where it is absorbed. During the SHEBA campaign, the onset of sea ice melt occurred due to increases in downwelling radiation [Persson, 2012]. Analysis of atmospheric conditions in 2012-2013 corroborate this, with longwave radiation being specifically noted as the difference in timing for the onset of snowmelt in the two years [Wang et al., 2016]. One week of earlier snowmelt in June results in 14% additional solar radiation being absorbed over the course of the summer season because of the albedo feedback, according to an idealized model [Wang et al., 2016]. Bottom melt represents a significant fraction of sea ice melt, and adds fresh water to the surface mixed layer [Perovich et al., 2014].

The cumulative effect of the ice melt is a significant reduction in salinity in the water nearest the surface. This forms the salinity gradient which defines the summer mixed layer, where water above the halocline is subject to wind-driven mixing. Water in and below the halocline is protected from atmospheric effects by the strong density gradient. Figure 3.2-b shows this dramatic freshening, where the Summer Mixed Layer is typically 2-3 p.s.u. fresher than the remnant Winter Mixed Layer [Peralta-Ferriz and Woodgate, 2015].

During this season, some solar energy enters the ocean both through leads and thin ice cover. Of this, a small fraction makes it down several meters into the emerging halocline layer before being absorbed. This melt-season heat absorption forms the NSTMs under multi-year ice floes and contributes to the heat content that is eventually stored in the halocline layer in the seasonal ice zone. In areas where sea ice survives the summer melt season to become multi-year ice, the spring melt season lasts until the onset of freeze-up in the fall. Because this season is so long, there is time for heat to accumulate in the halocline layer to form the NSTM.

3.1.3.3 Open water

Once sea ice melts off and the remnants of ice floes melt, open water directly absorbs solar radiation without the shading of ice floes causing spatial irregularity. The energy absorbed goes to warming water rather than melting ice at the surface, and temperatures in the summer mixed layer increase. Wind mixing maintains the mixed layer, though this varies on hourly timescales depending on the wind stress at the moment and the stratification in the water column [Bradley et al., 2015]. Solar energy is absorbed on an exponential profile, with the per-meter absorption coefficient varying with wavelength, organic content of the water, and turbidity. At the surface (top few meters), this exponential profile of absorption, and the corresponding changes in temperature and density, contributes to near-surface temperature gradients that persist until high winds induce mixing [Bradley et al., 2015].

The temperature gradients in the thermocline emerges during this period. In the vast majority of the temperature and salinity (T/S) profiles analyzed for this study, the temperature gradient has a fairly linear slope in °C/m. The linear slope of this feature is not readily explained by a constant solar energy absorption coefficient through the upper ocean and the resulting exponential decay in absorption with depth. It could be explained though as a combination of thermal diffusion (where steep temperature gradients tend to even out over time) and an increased solar absorption coefficient in the halocline layer. This is likely due to organic material or primary producers settling in to the halocline layer, after an early-season ice edge or under-ice bloom [Granskog et al., 2015]. The presence of organic matter and primary producers has been shown to locally increase temperatures 10-20m below the surface [Granskog et al., 2015]. These types of sub-surface layers with high biological and organic content have been observed in the western Arctic [Pegau, 2002].

When they occur over open water, strong storms can significantly deepen the surface mixed layer, with large vertical shear associated with wind-driven currents inducing vertical mixing that is the dominant factor in mixed layer deepening [Rainville and Woodgate, 2009]. Vertical diffusion occurs at an order of magnitude higher rates near the topographic features of the Chukchi shelf edge, with inertial wave activity and vertical shear associated with the change in basin depth accelerating mixing over the background molecular diffusion levels [Shaw and Stanton, 2014]. Increases in open water area both over the shelves and the deeper Arctic Ocean have the potential to increase internal wave activity, leading to more seasonal layer mixing and a less stable halocline [Rainville and Woodgate, 2009].

Figure 3.2-c shows the increase in Summer Mixed Layer temperatures with the isothermal layer extending down to the top of the Summer Halocline and the thermocline overlapping with the halocline. Figure 3.2-e shows the the surface mixed layer without this overlap, in the case where all heat is confined to the summer mixed layer and solar energy does not

penetrate down as far as the summer halocline. Over the course of the summer season, wind-driven mixing slowly deepens the mixed layer, pushing the upper limit of the halocline down towards the rWML.

3.1.3.4 Cooling

At the end of the summer season, the upper ocean must cool before sea ice can form at the surface. If all of the heat absorbed over the course of the summer was confined to the SML, surface heat fluxes, combined with mixing within the layer, could efficiently release all of the heat to the atmosphere. However, if there is heat in the summer halocline layer, the strong density gradient protects the warmth in the halocline and inhibits entrainment into the surface mixed layer or release to the atmosphere.

The Summer Mixed Layer does cool quite efficiently, as processes combine to keep the Summer Mixed Layer well-mixed through this part of the season. Wind-driven vertical current shear induces mixing within the layer from frequent storms (discussed in Section 3.4.4). Buoy records indicate that these storms do occasionally mix into the Summer Halocline causing some loss of heat in that layer, but that the heat in the Summer Halocline layer is generally preserved through until freeze-up. Additional convective mixing results from water cooling at the surface in a salinity regime where the temperature of maximum density is below the freezing point. This form of mixing is buoyancy-driven and does not influence the halocline water at all. Throughout the fall season, the summer halocline continues to deepen through periodic partial entrainment of the SHL into the SML.

Freeze up occurs when the summer mixed layer temperature reaches the freezing point. Frazil ice can grow in the water column and float to the surface, where it congeals into nilas or pancake ice depending on the sea state. Figure 3.2-d shows the end of the cooling season, where the summer mixed layer has reached the freezing point but there is a pocket of trapped heat in a Near-Surface Temperature Maximum feature in the Summer Halocline. The Summer Halocline maintains a strong gradient throughout this season. Figure 3.2-f shows the case where all heat was confined to the SML - the heat from the summer has been fully removed and will not influence winter ice growth. The SH maintains a strong salinity gradient through the fall season, with storm-driven mixing chipping away at upper part of the halocline but not eroding the whole layer.

3.1.3.5 Winter ice growth

As ice grows at the surface, brine is expelled from the seawater as it freezes into ice. A small fraction is trapped in brine pockets within the crystal structure of the ice, but most is expelled into the water column [Weeks et al., 1986]. This rejected brine slowly fills in the salinity deficit that defined the surface layer created during the melt season in early summer. The Summer Halocline is gradually erased over the season, releasing the protected the heat in that halocline layer.

Heat from the Summer Halocline mixing up into contact with the sea ice during this season slows the growth of ice at the surface. Gradual release of relatively warm water to the surface acts more as an oceanic heat flux than sudden pulses of warm water that could induce bottom melting, though the latter has been observed [Jackson et al., 2012]. This slows the rate of sea ice growth rather than actively melting what has already grown. During the SHEBA drift experiment in 1997-1998, there was some heat in the summer halocline in the Canadian Basin, though the strong stratification effectively trapped it through the ice growth season, limiting oceanic heat flux to 0.2 $\mathrm{W\,m^{-2}}$. Over the edge of the Chukchi shelf however, the underlying warm Pacific water increased the heat content and the oceanic heat flux to the sea ice to 3.5$\mathrm{W\,m^{-2}}$, representing a 15% decrease in sea ice growth [Shaw et al., 2009].

It is only after the Summer Halocline is fully erased that mixing in the seasonally-modified layers extends down through the Winter Mixed Layer. Where there is net ice production (the amount of melt in a summer season is less than the amount of ice growth the following winter), this occurs at some point during the winter. The freshwater balance is then maintained by advection of sea ice.

3.2 Data sources

3.2.1 World Ocean Database

The World Ocean Database [Boyer et al., 2013] is an archive of oceanographic measurements made worldwide since the 1970s. For the analysis presented herein, profiles containing both temperature and salinity measurements (salinity being derived from conductivity) from the Alaskan/Canadian sector of the Arctic (180W to 50W, 65N to 90N) since 1990 were retrieved from the database. These profiles come from Conductivity-Temperature-Depth casts (including both standard ship-based CTD and Expendable-CTD (XCTD) data), ocean station observations, drifting buoy data, profiling float data, and a limited amount of data from undulating oceanographic recorders. The following sections describe each data acquisition system and the associated measurement uncertainty.

Appendix B contains two figures that show the breakdown of profiles by type, along with the projects that provided the data sets. Figure 3.3 shows all of the profiles used for this analysis as individual blue dots.

3.2.1.1 CTD profiles

CTD profiles collected over the years in the Arctic Ocean provide a wealth of information about near-surface temperature and salinity profiles, though they do not capture the temporal evolution of water parcels over the seasons. The World Ocean Database [Boyer et al., 2013] hosts submitted CTD profiles with salinity, temperature, and other measurements. 8,297 CTD profiles (including XCTDs) over the last 2.5 decades (1990 to 2015) were available.

CTD profiles were selected for location (Beaufort and outer Chukchi Shelf; too close to the Bering Strait is likely to be influenced by northward flowing Pacific Water that has

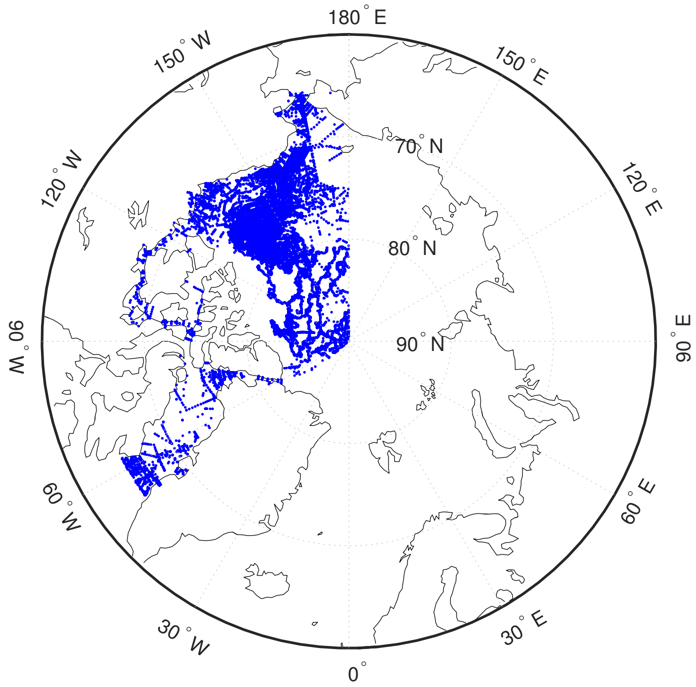

Figure 3.3: Map of the locations where temperature and salinity profiles used for this analysis were collected. Data from the World Ocean Database Boyer et al. [2013].

yet to be modified by seasonal processes) and time of year (early summer: June-July, peak melt season: August-September, and pre-freeze-up: October-November). There are limited CTD profiles from over winter because of the extensive ice cover and limited field activity.

Each profile was analyzed for mixed layer temperature, mixed layer salinity, summer thermocline depth, summer halocline depth, rWML temperature, rWML, and the existence, temperature, and depth of a near-surface temperature maximum between the summer and rWML layers. A full description of the profile processing is in Section 3.3.

The WOD CTD dataset consists of records submitted from operators around the world. CTD accuracy varies with the instrument used, and instruments have improved over time. Dozens of types of CTD instruments, with some unknown, were included in the WOD dataset analyzed for this paper. Modern CTD profilers record temperatures at accuracies of ±0.01°C or better and conductivity at $\pm 0.03 \mathrm{mScm}^{-1}$ or better. Given the diversity of instruments used, a comprehensive error analysis of each profile would not be feasible. The magnitude of temperature and salinity variations that are of interest to this analysis though are on the scale of 1-5°C and 1-2 p.s.u., so the accuracies of the instruments are more than adequate for the task.

CTD instruments vary, and the dataset contains data submitted by many sources. Additionally, prolonged use of CTD instruments used at sea tends to result in slight sensor drift over time. The accuracy of the CTD profiles therefore vary between profiles, with values ranging from 0.010 °C to 0.001 °C for temperature and 0.04 p.s.u. to 0.003 p.s.u.[Boyer et al., 2013]. Further, the quality of a profile is also influenced by the response time of the sensors and the speed at which the sensors are lowered through the water column. Expected rates of change of temperature and salinity in the water column should not exceed the measurement capabilities of these instruments, with the possible exception of fresh meltwater pooling under and around an isolated melting floe. This is unlikely to compromise the quality of the profiles at the surface, and will not influence them below about two meters down [Bradley et al., 2015]. Often additional parameters are available with a CTD profile, but these are not included in this analysis [Boyer et al., 2013].

High-vertical resolution Expendable Conductivity-Temperature-Depth (XCTD) data is included in the analysis with standard CTD profiles. These are free-falling probes wired to the acquisition system at the surface. Depth is estimated from the elapsed time of descent, and can therefore be prone to error at deeper depths. Typical accuracies of XCTD probes are $\pm 0.02°\text{C}$ and as high as $\pm 0.05\,\text{mS}\,\text{cm}^{-1}$ [Boyer et al., 2013, Mizuno and Watanabe, 1998]. XCTD casts make up a sizeable fraction of the profiles north of Alaska in part because of the difficulty getting ship access to the area [Boyer et al., 2013].

3.2.2 Profiling floats

The WOD documentation does not provide measurement error information on the profiling floats that are used in the Arctic. Almost all of the global profiling float data comes from the ARGO systems, which do not usually work under ice cover. Instead there is some information on the various platforms in the metadata for each file, which must be searched individually and then quantified using other sources. There were 366 profiling float profiles in this analysis. These represent a small fraction of the profiles considered in this analysis.

3.2.2.1 Drifting buoys

Drifting buoys account for most of the profiles in the Arctic, with 48986 included in this analysis.

The vast majority of these are the Ice Tethered Profiling buoys [Toole et al., 2011], which by definition only profile underneath existing sea ice. These systems consist of an ice-anchored platform with a cable that is run down a drill hole in the ice. The surface unit holds the batteries and data processing and backhaul systems. The underwater unit is a Sea Bird 41-CP CTD, the same instrument that is used on ARGO floats. This unit slowly ($0.25\ \mathrm{m\,s^{-1}}$) moves up and down the suspended cable to collect profiles [Toole et al., 2011, Krishfield et al., 2008].

The Arctic Ocean Buoy Program has been deploying buoys in the Arctic since the late 1970s. Initially these buoys carried only atmospheric measurements (air temperature, wind speed, pressure) and drift paths of the ice to which they were anchored [Rigor and Ermold, 2008]. In the late 1980s and early 1990s, these buoys were modified to carry CTD sensors and started to measure the near-surface ocean properties. The Polar Ocean Profile buoy was anchored into sea ice with the sensitive electronics embedded into the ice itself. A SBE-16 Seacat CTD sensor is suspended below with sensors at 10, 40, 70, 120, 200, and 300 meters [Rigor and Heiberg, 1997], which captures the larger variability in water masses but not the details of surface mixed layer or the haloclines between. These platforms provided most of the drifting buoy measurements before the ITPs.

Figure 3.4 shows the spatial distribution of profiles collected by drifting buoys, including both the POP and ITP buoys. They have good coverage of the Beaufort north of Alaska and Canada, though the majority of these are limited to times of year with ice cover.

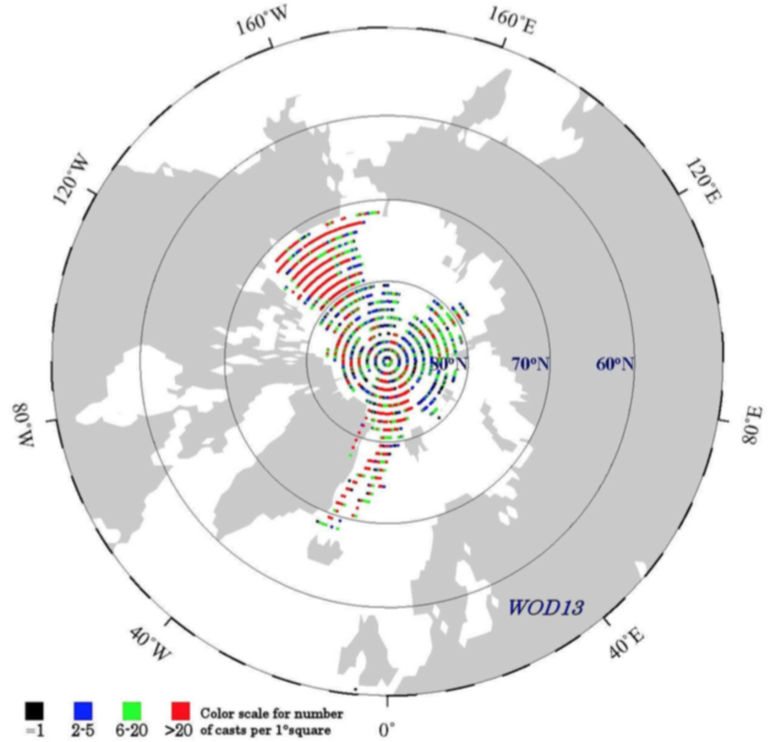

Figure 3.4: Map of the drifting buoy profiles archived as part of the World Ocean Database, reproduced from Boyer et al. [2013].

There is no included ice concentration information in the WOD database. The vast majority of these buoys are suspended by ice floes and can no longer operate once the floe disintegrates. The goal of this analysis is to study areas that are not covered by sea ice year-round, and so these platforms do not offer the most helpful observations, especially in the summer months. They do drift with the ice cover though, and can often drift overwinter into areas that were ice-free the previous season. For that reason these profiles are not excluded from the analysis, but the analysis is considered in the context of latitude in order to capture the differences between the seasonal cycles in the perennial ice pack and the seasonal ice zones.

3.2.2.2 Undulating ocean recorder

Undulating Ocean Recorders are self-contained oceanographic samplers that can be towed behind ships at typical underway speeds. These instruments make it possible to profile large areas in horizontal distance in quick time, as they do not require the ship to stop as do normal CTD profiles. The profiles included in this analysis have both temperature and salinity data and capture profiles up to 500m deep [Boyer et al., 2013]. The instruments are similar to those on more standard CTD profilers, and have comparable measurement accuracies. The response times on the sensors for these instruments is high enough to capture strong temperature and salinity gradients while the ship is moving. The descent rate of the instrument package determines the vertical resolution of the measurements (typically 10s of centimeters), and the depth of profile and ship speed determine the spatial repeat frequency of the profiles [Woods Hole Oceanographic Institution Upper Ocean Processes Group, 2007].

3.2.2.3 Ocean station data

The Ocean Station data refers to low vertical resolution profiles in the water column, including low-resolution CTD and XCTD profiles. These profiles represent 1,979 of the nearly 60,000 profiles included in this analysis. The instruments used to collect these profiles are mostly the same platforms used in the higher resolution CTD profiles, and the uncertainty in the measurements are discussed there. There are also some profiles for which no information on instrument is provided, though these account for a very small fraction of the total number of profiles.

3.2.3 UpTempO buoys

UpTempo buoys are drifting buoys deployed in the Arctic Ocean that have a string of thermistors that extend down into the top 20-60 meters of the upper ocean [Steele et al., 2014]. Most of these buoys do not carry salinity sensors, rather the only measure of mixed layer depth available is the thermocline. These buoys drift freely with surface currents with a small, rounded profile to the wind, and therefore offer a semi-Lagrangian tracking of water parcels. Deeper water experiences slightly different current forcing from wind drag than the surface does, and so the water at the bottom of the thermistor string has a slight effective motion relative to the top of the buoy string. Figure 3.5 shows the UpTempO buoy platform.

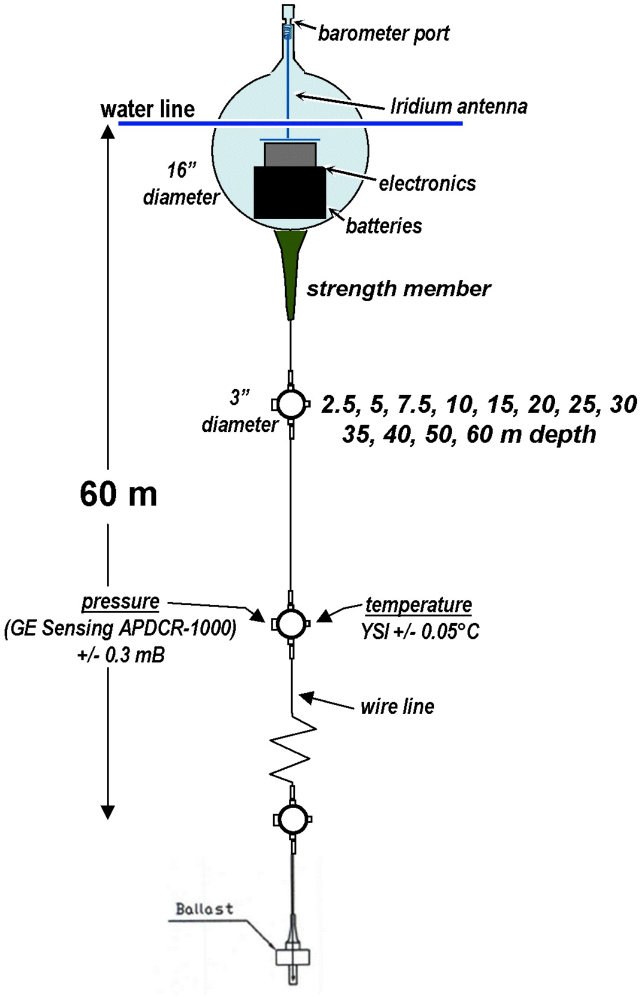

Figure 3.5: Schematic of the UpTempO buoy from http://psc.apl.washington.edu/UpTempO/. Temperature sensors are accurate to 0.05°C and are fixed to the line extending down from the surface.

Several UpTempO buoys were been deployed in 2013-2014, with five capturing relatively long time series of temperature profiles and GPS location with hourly measurements over the weeks and months of drifting freely in open water leading up to freeze-up.

Buoy drift speeds were used as a proxy for wind speeds, as reanalysis wind products in the Arctic suffer from a lack of direct observations. Generally the MERRA reanalysis winds track moderately well with the buoy drift speeds, though there are frequently cases where either the reanalysis winds or the buoy drift speeds up for periods of about 4 to 24 hours when the other dataset does not show the same acceleration. There were also two significant periodic signals in the drift speeds corresponding to 12- and 24-hour periods of the tidal cycle. Subtracting these components of the buoy drift left speeds that captured large wind events observed at the Barrow and Oliktok Point weather stations when the buoys were nearby.

The following analyses assume that the buoys stopped recording at the onset of ice growth. To verify this, we traced each buoy through the passive microwave ice concentration records [Cavalieri et al., 1996a] to determine the date of freeze-up from changes in detectable ice concentrations resulting from ice growth. The mechanical forces that come with ice growth are likely to break the buoy or at least the sensor string, and in several cases there are clearly erroneous measurements (temperatures above 25°C at 30-50m depth) recorded from some of the sensors in the days before the system stopped recording altogether.

UpTempO buoys are not included in the seasonal cycle analysis because they lack the salinity measurements required for that part of the study.

3.3 Analysis

The WOD temperature and salinity profiles are used to study the seasonal cycle in upper ocean temperatures and salinities. South of the perennial ice edge, these are mostly individual profiles that do not follow water parcels through the seasons. The fall season is especially interesting as the surface mixed layer cools to the freezing point, and for that the UpTempO buoys are analyzed separately to investigate the seasonal evolution of those water parcels.

3.3.1 Feature detection

Each of the WOD profiles is analyzed to determine if it fits one of the seasonal profiles shown in Figure 3.2. Figure 3.6 illustrates the process of finding the layer depths, temperatures, and salinities. The algorithm for determining the temperatures, salinities, and depths of particular features is as follows:

(1) Check that the shallowest measurement is within 8m of the ocean surface. This is a cutoff for detecting a shallow mixed layer based on the discussion in Peralta-Ferriz and Woodgate [2015].

(2) Interpolate the profile at 1-meter intervals from the surface (0m) to 100m depth or the lowest measurement on the CTD profile, whichever is shallower. Above the first measurement (if it is below the surface), the temperature and salinity are extrapolated by a nearest neighbor approach, where temperature and salinity are held constant between the surface and the first measurement in the profile. The rest of the profile is linearly interpolated. These profiles are also smoothed with a 10m running average filter to alleviate the measurement noise which could affect the halocline and thermocline detection.

(3) The surface temperature is the temperature at $z = 0$m, which is the uppermost temperature in the profile. The surface salinity is likewise the salinity at $z = 0$m.

(4) The winter layer is found by selecting the minimum temperature in the 100m profile. In some cases the surface temperature is the lowest temperature in the profile, where the summer mixed layer has cooled to a lower temperature than the winter layer below. Because of these cases, the temperature minimum is restricted to depths below 20m. In Figure 3.6 the temperature minimum is found at 40m, indicated by the circle.

(5) The derivative of the temperature and salinity profiles with depth is taken to find the thermocline and the halocline.

(6) Moving down from the surface, the first point where the change in temperature with depth exceeds 1 °C over 10 m (0.1 $°\mathrm{C}\,\mathrm{m}^{-1}$), in either the positive or negative directions is the upper boundary of the summer thermocline. This threshold is informed by the measurement uncertainty of the instruments where a 0.1 °C change in temperature over 1 meter should be detectable by all platforms included in the WOD. Based on a randomly selected sample set of profiles that were analyzed by hand, this threshold does not seem to miss temperature gradients that should be detected.

(7) The summer halocline is found in a similar manner, where the change in salinity with depth must exceed 0.1 p.s.u.m^{-1}. This threshold is also based on the WOD measurement error estimates and also seems to do a reasonably good job at selecting the halocline boundary, selecting depth limits that less than 2 meters off from those manually selected from visual inspection in every one of the random sample set of profiles.

(8) Moving downward further, the last point in the profile that satisfies the above conditions before reaching the winter layer temperature minimum is the bottom of the thermocline (for the temperature profile) or the halocline (salinity profile). The thermocline and halocline are detected independently.

(9) The highest temperature between the winter layer minimum and the surface is saved, and if this temperature exceeds the surface temperature and is located between the upper and lower boundary of the thermocline, it is used for classifying the profile based on the seasonal cycle described above.

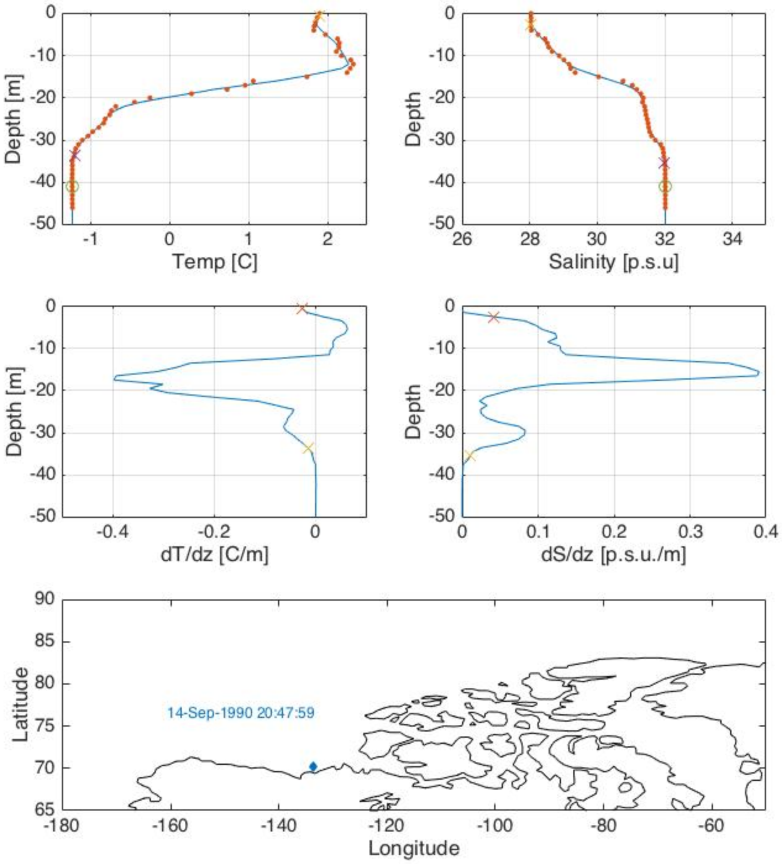

Figure 3.6: An example of the feature selection algorithm. The lines are the interpolated and smoothed profile and the red dots are the actual measurements. The ’x’s indicate the upper and lower limits to the thermocline and halocline as determined by the algorithm, and the circle notes the rWML temperature minimum.

3.3.2 Classification scheme

The classification process is accomplished by setting certain flags during the feature detection processing. Figure 3.7 shows this as a flowchart, where for each profile, there were several steps to classification. Some details are omitted from the flowchart for the sake of clarity.

Profiles that do not pass the strictest levels of WOD quality control [Boyer et al., 2013] are omitted from the classification. Of the acceptable profiles for data quality, there are

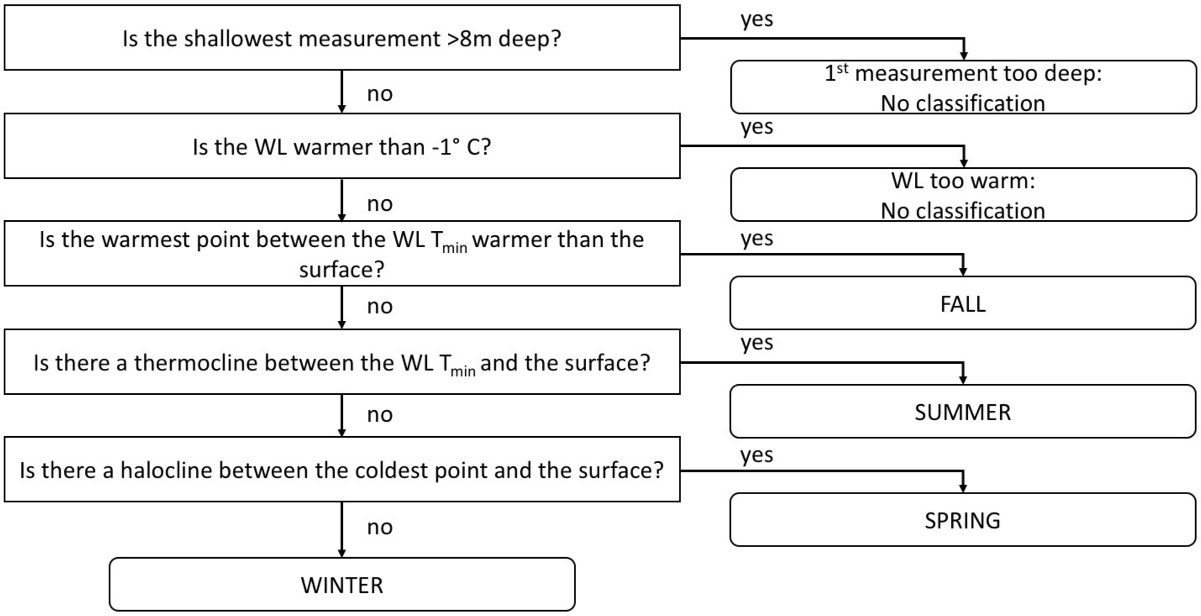

Figure 3.7: Flowchart outlining the classification scheme for the T/S profiles.

two common factors that make a profile “non-classifiable”. The first is that the uppermost measurement is too deep, typically about 50m on moored sensors in the Arctic. These miss the summer mixed layer (if present) and therefore cannot be classified based on the scheme described below. The other disqualifying case is where the winter layer (the minimum temperature below the surface layer) is greater than -1 °C. These are indicative of other processes driving the temperature and salinity structure of the upper ocean, such as water masses entering from the Pacific Ocean. Additionally, some profiles do not match the seasonal classifications adequately well and are therefore not categorized. These represented a small fraction of the profiles, less than 10% with little seasonal variation.

Profiles with a temperature maximum between the surface mixed layer and the winter layer temperature minimum are categorized under the ‘Fall’ category. The seasonal names for these categories are based on the discussion in Section 3.1.3, and will be revisited in the results discussion later in this chapter. If there is a thermocline but no temperature maximum, the profile is categorized as ‘summer’, and if there is a halocline but no thermocline the profile is categorized as ‘spring’. Finally, profiles with no features in either the salinity or the temperature profiles between the winter minimum and the surface are categorized as ‘winter’, so long as that winter minimum is below -1 °C. Because the scenario in panel (e) of Figure 3.2 where fall season cooling fully erases the heat signature from the temperature profile looks identical to panel (b), the spring melt profile, these two cannot be distinguished. Instead this profile is classified as ‘spring’ throughout the year and reflects both processes.

Figure 3.8 breaks down the non-classifiable profiles by type, month of acquisition, and geography. The first row is the fraction of all profiles by location that are not classifiable. These data are binned into grid cells that are 2 degrees in longitude by 1 degree in latitude. The next two rows separate these out into those with warm water where the winter layer would be and those lacking the near-surface measurements necessary to capture the seasonal processes. Profiles not matching the seasonal classification criteria did not show any notable geographic patterns and are not shown in this figure. Warm lower layers are exclusively in the locations were inflow from lower latitude oceans is occurring: north of the Bering Strait where Pacific water enters the Arctic Basin and at the northern end of Baffin Bay (the right corner of the map) where some Atlantic water is present. There was some seasonality to these: there were some profiles with warm mixed layers off the shelf edge in the fall (Sept/Oct/Nov), but not in the other seasons. Profiles that started too deep however were confined to the central Arctic and had no seasonal variation. These accounted for all of the unclassifiable profiles in the winter months, as there were not profiles from the Chukchi shelf in the winter. The rest of the profiles fell into one of the seasonal categories described above.

3.3.3 Buoy analysis

The UpTempO buoy data comes as a time series of temperature measurements at the depths of the temperature sensors [Steele, 2012]. These did not require further analysis, except for extracting the temperatures at various depths over time. Each buoy record was

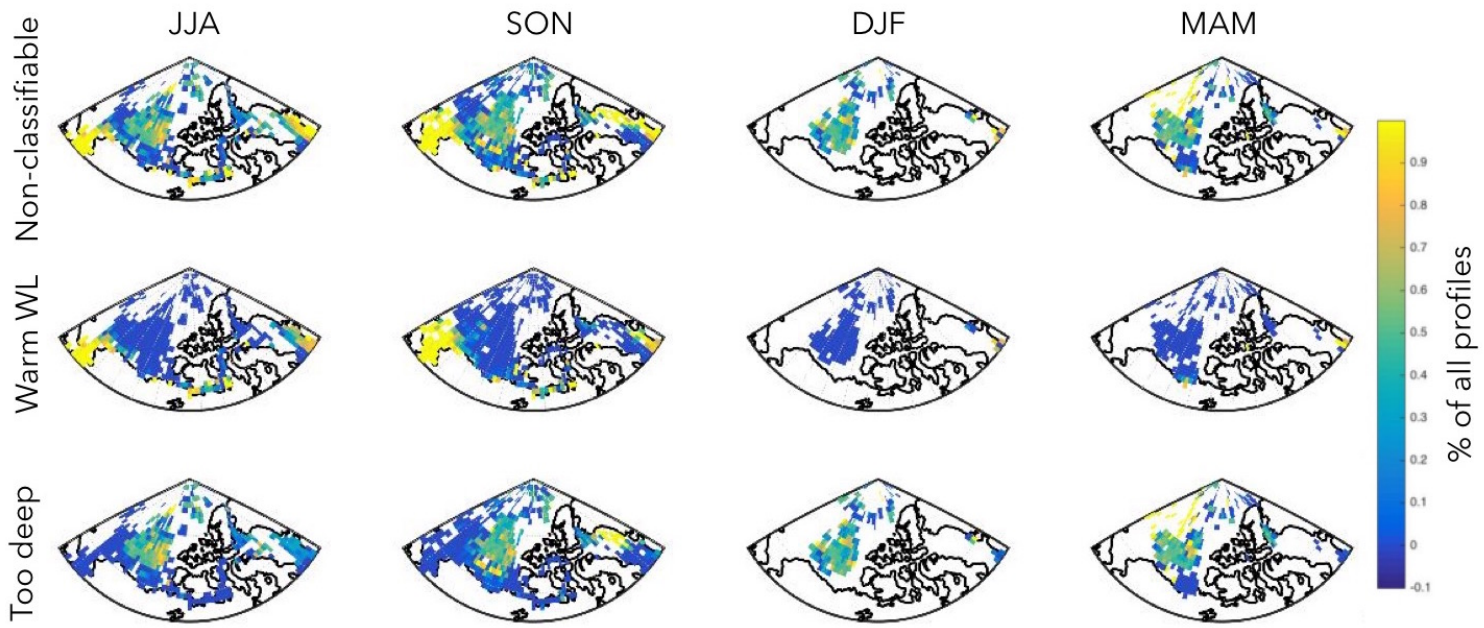

Figure 3.8: Unclassifiable profiles by location. The top row shows the fraction of all profiles in each grid cell that were determined to be unclassifiable, the middle row the fraction with a warm layer in place of a cold rWML, and the bottom row shows those that do not sample close enough to the surface to reliably capture the SML.

checked against local ice concentrations to verify that the end of the data record coincides with freeze-up dates. For the four buoys shown in this analysis, the end of the record occurred within a week of large changes in ice concentration, suggesting that these buoys were killed by the mechanical forces of ice growth.

3.4 Results

The classification analysis shows strong seasonality as expected, though this is only apparent south of about 75N. North of 75N, persistent sea ice cover is still the norm and there is very little evidence of the summer and fall profiles in the annual cycle. Figure 3.9 shows the fraction of years that a particular location was ice covered on September 1: 75N was selected as a threshold because it has experienced open water more often than not since 1990, and because there is a decrease in the number of observations north of 75N.

Based on the CTD profiles and the buoy time series analysis, several notable phenomenae emerged that merit special discussion. Outside the ice edge, summer haloclines and thermoclines are consistently co-located at the base of the summer mixed layer, counter to the figure in Bourgain and Gascard [2011] but shown in Section 3.4.2 and Figure 3.1. Surface temperatures have continued warming over the period 1995-2015, though sparse CTD profiles make this not immediately obvious. This is discussed in Section 3.4.3. Rates of cooling during the fall are highly variable, with the bulk of heat lost in several larger storm/wind events over the course of the season as shown in Section 3.4.4. Finally, these cooling events leave behind warm layers in the halocline that form a NSTM-like feature in regions of seasonally ice-free water in Section 3.4.5.

3.4.1 Seasonal cycles

Figure 3.10 shows the seasonal cycle in classification for the complete set of profiles. Non-classifiable profiles account for 20-45% of the profiles, with lower numbers in the winter when almost all of the non-classifiable profiles are from mooring stations that are active

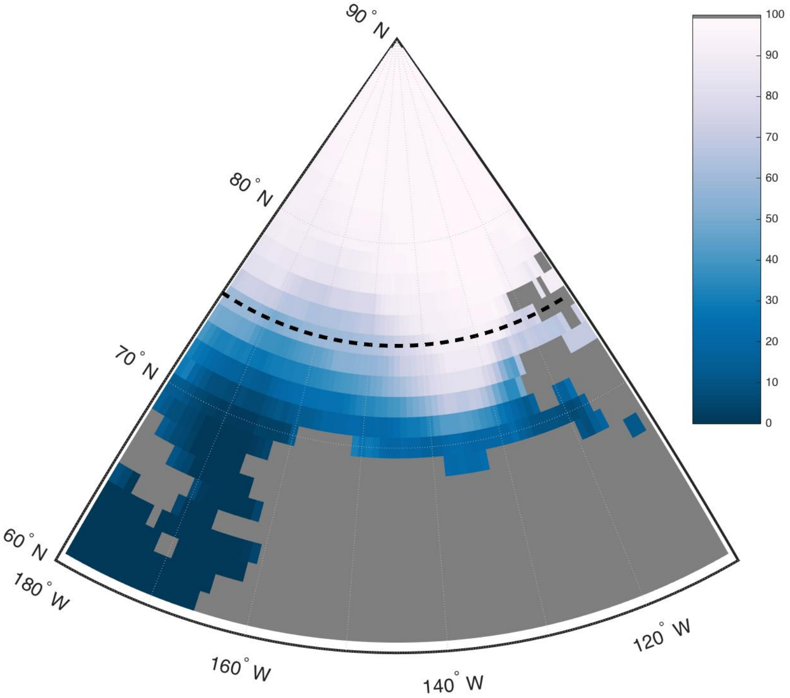

Figure 3.9: Mean ice concentration in each grid cell on September 1 for the period 1995-2015. The dashed line is along the 75N parallel, which is used to distinguish between perennially ice-covered areas and seasonal ice zones in this analysis. The colorbar is ice concentration, with Alaska as the landmass at the bottom of the figure.

year round. There is a notable decline in the fraction of winter profiles during the summer, though they are still the most common except in the month of August when the summer profiles are (very) marginally more prevalent. Summer profiles almost disappear between October and April, to reemerge slightly in May before peaking in July and September. Fall profiles are more prevalent in September, October, November. They likewise disappear from December through June. Spring profiles are present early in the early winter (November and December) and persist through until May. This is because the alternate Fall scenario (all heat removed from the summer layers, shown in Figure 3.2, panels e and f) is also classified in this category, and it takes most of the winter's worth of ice growth to erode the haloclines developed during the melt season.

When the profiles are divided by latitude however, these seasonal patterns become

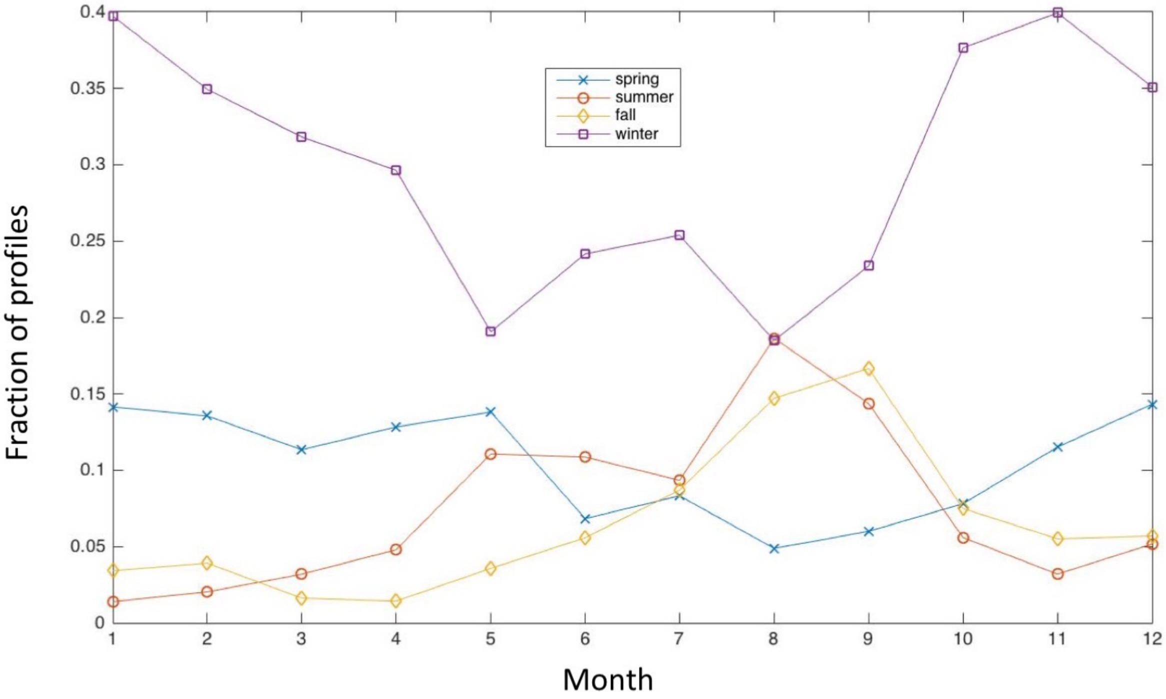

Figure 3.10: Fractions of the total number of profiles by month corresponding to each of the seasonal classifications. This includes all latitudes and the non-classifiable profiles. The seasonal cycle is apparent in each of the classifications, with fewer winter profiles in the summer months and summer and fall profile fractions peaking in the August and September respectively.

much more clear. At lower latitudes below 75N, the winter pattern becomes extremely clear. Figure 3.11 includes all classifiable profiles, divided by latitude into a northern section and a southern section. North of 75N, there is little seasonal variation in the fraction of winter or spring profiles, consistent with the perennial ice cover that far north. There is a very slight increase in summer and fall profiles in June and August/September, respectively, but they still represent less than 20% of the profiles each. In the more southern profiles however, the seasonal cycle is much more apparent, with the spring profiles most prevalent in May, summer profiles peaking in August, and fall profiles most prevalent in September. Summer and Fall profiles show a very similar annual pattern, with a slight delay in the fall profiles. The large number of summer profiles in September and October come primarily from areas near the coast and especially near the Mackenzie River outlet, where there is a continual source of warmer water later into the season. Winter profiles decrease to below 10% in the summer between July and September.

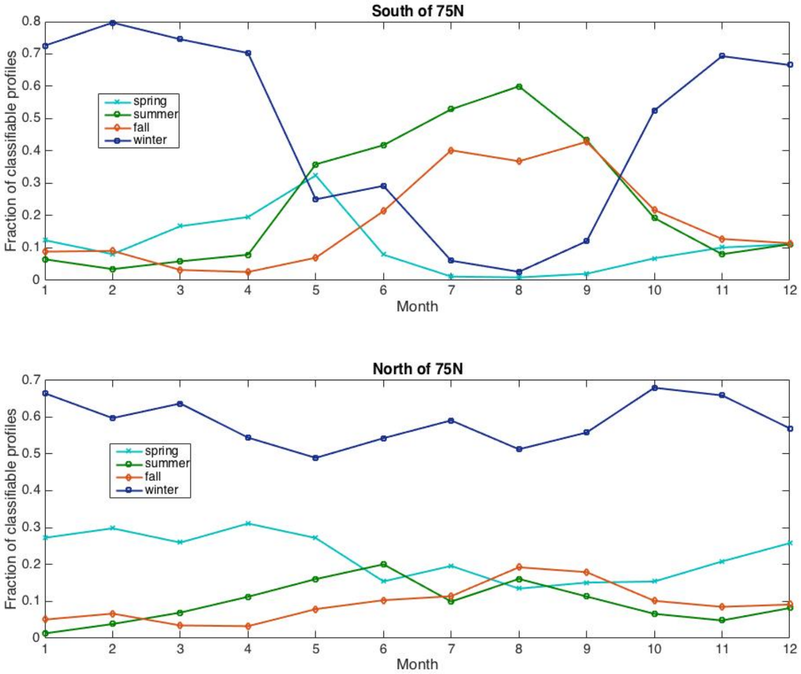
South of 75N

North of 75N

Figure 3.11: Fractions of the classifiable profiles for each season by month, divided into a southern region (south of 75N) which shows signficant seasonal changes, and a northern region with very little seasonal variability.

Figure 3.12 shows these profiles broken out by latitude and month for each seasonal classification. The summer season is longer at lower latitudes. Summer profiles (top) are most prevalent at lower latitudes, while winter profiles (3rd from top) are most prevalent at all latitudes in all but the summer months. Spring profiles trend later in the season with higher latitudes.

Figure 3.12 shows the profiles broken out by year and month. It has only been since about 2008 that there has been year-round coverage available, which corresponds with the increased number of field campaigns and equipment installed during the 2007-2008 International Polar Year. There seems to be a shift up in the fraction of profiles classified as

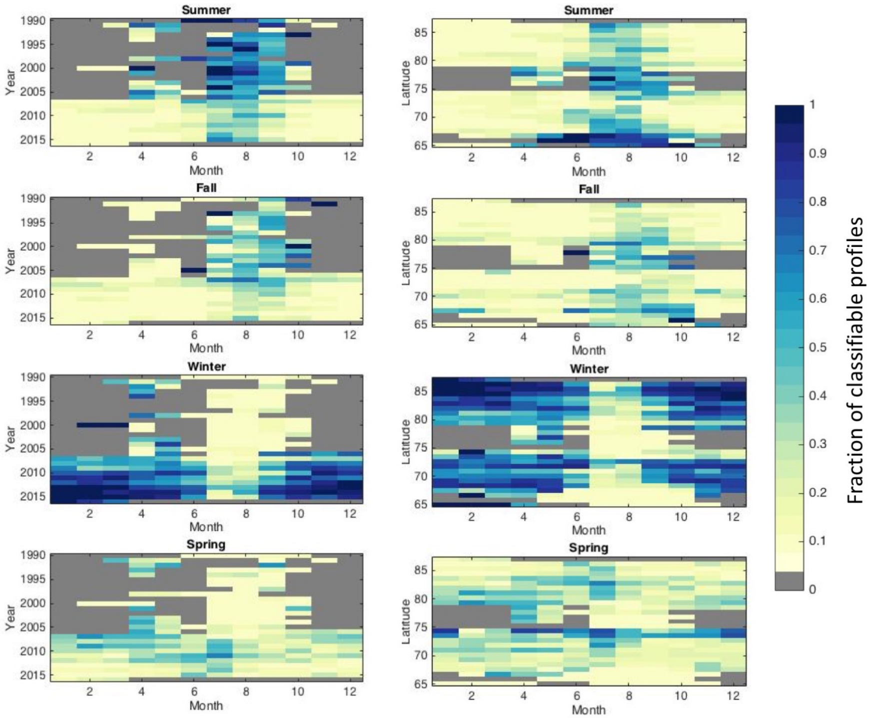

Figure 3.12: Fraction of profiles for each classification by month and year (left column) and latitude (right column). Gray background indicates bins that had no classifiable profiles.

summer and fall around that time, which likely has to do with increased sampling and field campaigns during IPY. Prior to the installation of moored systems and overwinter drifting buoys, year-round measurements were difficult and summertime campaigns only went as far north as the icebreakers could manage. This creates a relative bias towards more southerly latitudes in the first 15-18 years of the dataset (1990-2008).

Finally, Figure 3.13 presents the same profile data as fractions of the classifiable profiles by geography and time of year. The columns represent three-month segments, and each map is the fraction of the the profiles collected in those months, in each bin, that were categorized under each season.

Summer profiles dominate, as expected in the lower latitudes and closer to the coast, as well as through the Canadian Archipelago in June-August. Summer profiles also represent the plurality of profiles through much of the Beaufort sea during this time. In September

-November however, summer profiles are less common except on a very narrow strip near the Canadian coastline. They all but disappear for the winter months, and reemerge slightly starting around the outlet of the Mackenzie river in the spring.

Fall profiles exist in a few small pockets during the summer months, likely because solar radiation that enters the water column between floes can warm the developing halocline layer slightly. In September - November, they account for a large fraction of profiles north of the Chukchi shelf edge, and a moderate (40-50%) fraction throughout most of the rest of the southern Beaufort Sea. Like the summer profiles, fall profiles disappear entirely in the winter and spring months.

Winter profiles are found year-round, with the majority of those in the summer existing at high latitudes where there is perennial sea ice cover. In the central Beaufort, there are some winter profiles during the summer months, but relatively few compared to the other seasonal classes. In the fall, the picture changes somewhat, with winter profiles coming to dominate the central Beaufort and north up to the north pole. In December - February, winter profiles account for almost all of the classifiable profiles, but with somewhat limited geographic area of measurement coverage. Spring is similar, though the fractions of winter profiles is slightly reduced in favor of spring profiles.

The spring profiles represent the least common class, as the temperature profile that defines the class is very much a transitional phase. Nevertheless, spring profiles are relatively common in the central Beaufort in June-August, where ice breakup occurs slightly later in the summer. Interestingly, spring profiles can be found near the north pole year-round. This can be explained if the annual ice melt in these water columns in a year is greater than the annual ice growth: the summer halocline is never fully eroded over the winter, leaving the ‘spring’ type profile year-round.

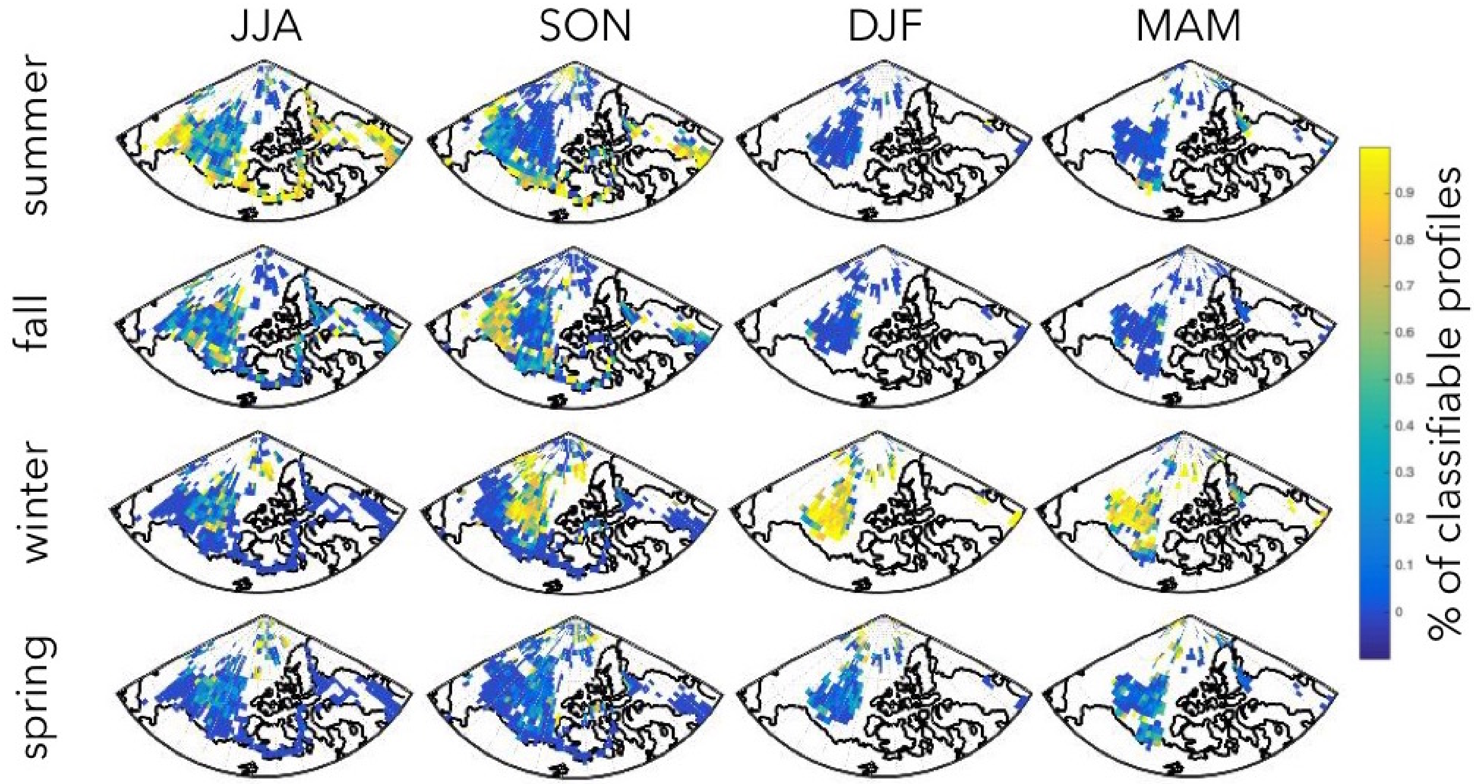

Figure 3.13: Fractions of classifiable profiles by geographic location (2 degree longitude by 1 degree latitude grid), by month of profile acquisition and profile class. White space indicates no classifiable profiles existed in those locations in those months.

3.4.2 Summertime heat in the halocline

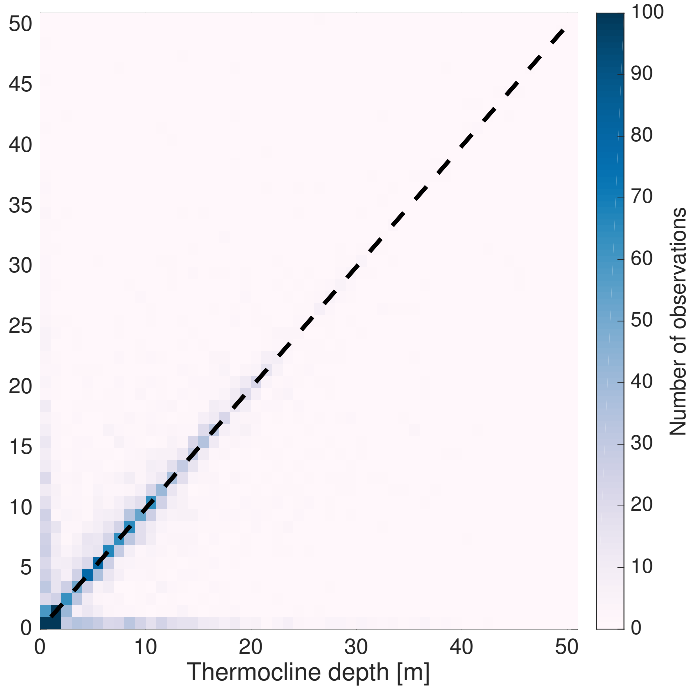

Figure 3.14: 2-D histogram of mixed layer depths calculated from temperature and salinity profiles from the Western Arctic. The majority of the roughly 25,000 profiles have precisely co-located halocline and thermocline tops, with some cases having a shallower halocline. The color indicates the frequency of occurrence of profiles with thermocline and halocline depths in the corresponding depth bins.

The first question that was considered in this study is a simple, but important one: where does the summer thermocline (created by absorption of solar energy into the upper ocean, combined with wind-driven mixing at the surface) form relative to the summer halocline? In Figure 1 of Bourgain and Gascard [2011], the thermocline is drawn such that the halocline and thermocline do not overlap, with the thermocline fully above the halocline. This is an idealized figure illustrating that seasonal processes occur and not not necessarily intended as an accurate portrayal of the seasonal layer dynamics in the Arctic.

In Figure 3.1, a CTD profile randomly selected from the WOD records in the Beaufort Sea, the thermocline and the halocline are located at the same depth, starting at approximately 20 meters. This profile proved fairly representative after analysis of approximately 25,000 T/S profiles from the World Ocean Database, collected in the western Arctic (Chukchi and Beaufort regions) south of 75N in July-October (before significant cooling initiates at the surface) of 1995-2015.

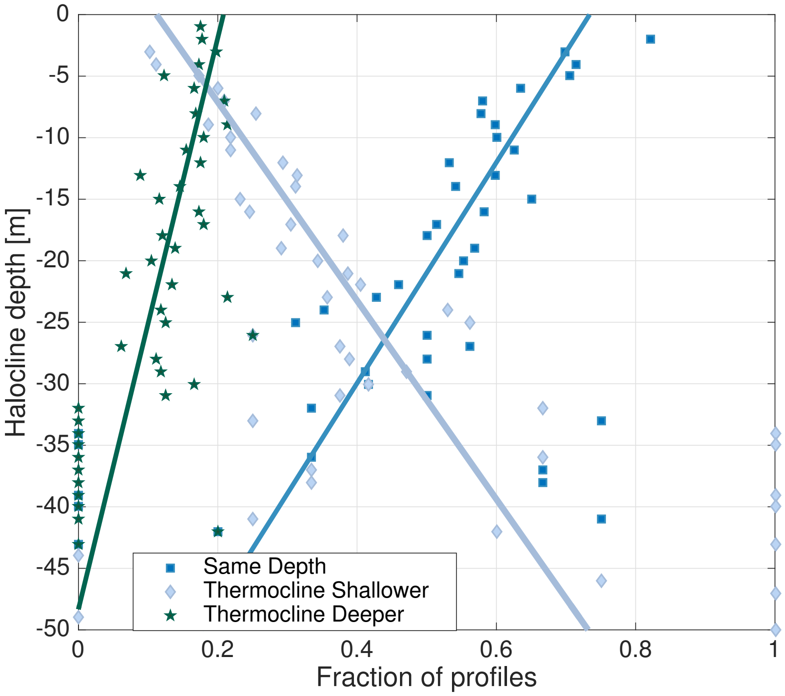

Figure 3.15: Fraction of profiles for a given halocline depth (y-axis) with thermoclines starting above (light blue), at the same depth (dark blue) or below (green) the upper limit of the halocline. The solid lines are linear fits to the depth-bin fractions, meant to provide a general sense of the trend.

In most of the CTD profiles, the thermocline and the halocline set by the summer mixed layer start within 1m of each other. Figure 3.14 illustrates this, showing a 2-D histogram of the depths of the top of the gradients in temperature and salinity. The dashed line shows a 1:1 correspondence. In most profiles, the halocline starts at depths less than 15m. Figure 3.15 shows the fraction of profiles with a halocline at a given depth for which the thermocline starts above, at, or below the depth of the beginning of the halocline. There is a clear change with depth in the relative fraction of co-located profiles, defined as upper limits of both the halocline and the thermocline being within 1 meter of eachother. At very shallow halocline depths, the thermocline is more often than not located at the same depth as the halocline. As halocline depths increase, the thermocline is more likely to fall into the scenario where it is above the halocline. At deep haloclines (below 40m), almost all profiles have a shallower thermocline. There are some cases where the thermocline is deeper than the halocline, and these are usually a ‘spring’ type profile where the summer halocline has developed but there has been little or no warming in the upper ocean. These are most prevalent where the halocline is very shallow and decrease in likelihood with depth.

3.4.3 Arctic surface warming

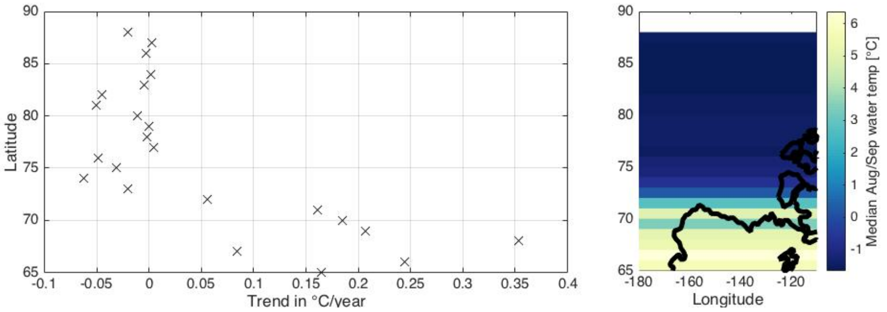

Figure 3.16: Median mixed layer temperatures measured by CTD profiles collected in the Western Arctic (between 180W and 110W) in August or September between 1995 and 2015. The right panel shows the mean surface temperature by latitude. There has been a warming trend over the last 20 years at lower latitudes and little change at higher latitudes.

Figure 3.16 shows the pronounced trend in warming ocean surface temperatures at the lower latitudes in the Arctic as measured by CTD profiles in August and September of each year. This analysis included the 1,025 CTD profiles from the Pacific side of the Arctic in the months of August or September from the period 1995 to 2015 that are distributed through the WOD [Boyer et al., 2013]. Trends corresponding to latitudes at and below 74N are statistically significant at the 5% level, while trends above 75N are not due largely to sparsity of observations at the higher latitudes.

Mixed layer temperatures in 2004 and the period 2010-2011 were especially high, with most observed mixed layer temperatures between 70° and 71° N at or above 8°C (roughly 10°C above freezing). Similar or warmer temperatures to those years further north in 2008 and 2015 suggest that these may just happen to be the years that there were sufficient observations at those latitudes and not that they were exceptionally warm years. The warming trends are slightly less pronounced further north, but persist up to about 75°N where there stop being enough recent observations in the database to make any conclusive statements.

Steele et al. [2008] identified the most pronounced warming in Arctic (and peripheral Arctic seas) between 2000 and 2007. CTD profiles in the western Arctic, shown above, indicate record warm temperatures since 2010, suggesting that the warming trend observed in 1965-1995 has continued unabated, if not accelerated [Steele et al., 2008].

3.4.4 Fall season cooling events

The temperature evolution measured by drifting UpTempO buoys shows how upper ocean temperature profiles change over the cooling season. The buoys are not perfectly Lagrangian, but offer the closest approximation available to tracking water parcels through the season. Figure 3.17 shows the time series of mixed layer temperature over the fall season as observed by four buoys deployed in 2013. The black dashed line indicates the equivalent constant cooling rate. The effective seasonal cooling rate was $0.1 \pm 0.02°\mathrm{C day}^{-1}$ for each of the UpTempO buoys, based on the assumption that the mid-September deployment for the later buoys coincided with the peak of the summer heat, which is backed up by the first profile shown in Figure 3.17.

Rapid cooling events dominate the total amount of cooling observed over the fall seasons for these four temperature records. Cyan lines indicate cooling rates greater than five times the seasonal average (indicated with the dashed black lines), approximately $150\ \mathrm{W\,m^{-2}}$ heat flux equivalent assuming a 10m mixed layer. These events occur when air temperatures cooler than the water temperature while there are moderate to high winds. Especially high winds (estimated from buoy drift speeds) tended to be more associated with the warming

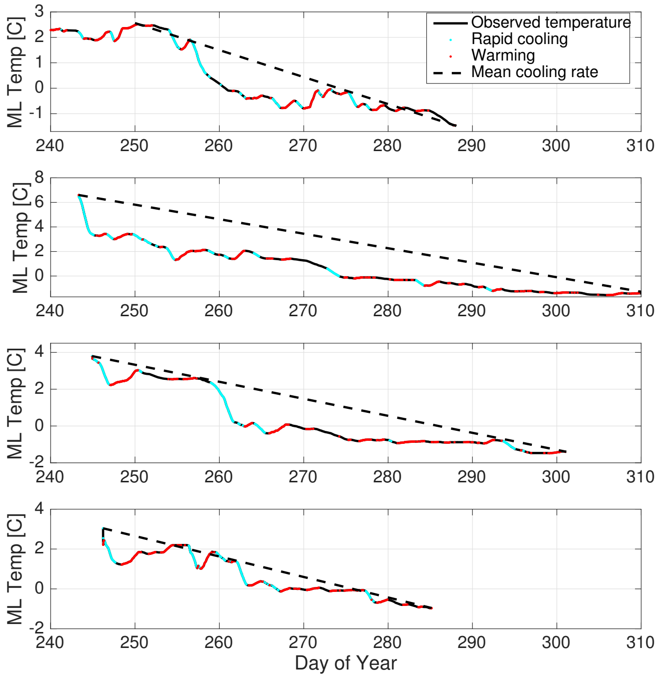

Figure 3.17: Four UpTempO buoy records from 2013. Cooling rates exceeding five times the effective seasonal cooling rate (approximately 0.1 °Cday^{-1}) are indicated in cyan and warming periods are indicated in red. Buoys 2-4 were deployed in early September, right as significant cooling began for the fall season. Measurement accuracy is within 0.05 °C and is narrower than the lines on the figure.

events indicated in red, where high winds driving mixing in the upper ocean entrain heat from the halocline layer into the SML.

Rapid cooling events accounted for 70 to 80% of the total cooling in these profiles. For each buoy profile, there was 4 to 8°C of net cooling between the September maximum temperature and reaching the freezing point in October or November. On top of this heat loss, the frequent warming events added an additional 2.1 to 4.0 °C of heat that needed to be removed again before freeze-up could commence.

3.4.5 Trapped heat before freeze-up

A near surface temperature maximum feature reliably emerges in the buoy records as the summer mixed layer cools - either through storms or through gradual heat loss. In all of the buoy profiles, and in more than 80% of the CTD profiles, the summer mixed layer cools to a freezing point below the temperature of the winter mixed layer. Temperatures in the winter mixed layer averaged -1.52 °C, approximately 0.3 °C above the typical WML freezing point (-1.8°C). This is apparent in Figure 3.1, where the coolest point in that winter mixed layer is -1.5°C despite a local freezing temperature of -1.78°C. This heat is absorbed locally from incoming solar radiation [Perovich et al., 2007], and the increasingly long ice-free season [Stroeve et al., 2014] allows for more time for the small amounts of solar radiation to contribute notable amounts of heat deeper in the water column.

In almost all CTD profiles from the late summer and fall seasons, there is also a layer of warm water trapped in the summer halocline that is significantly ($>$ 1 °C) above the freezing point. In the late summer, water in the summer halocline layer is typically at a temperature equal to or cooler than the summer mixed layer temperature, but as the summer mixed layer cools the halocline layer emerges as a NSTM-like feature with warmer water temperatures than the layers below or above. The strong density gradient at the halocline prevents the heat from mixing into contact with the surface during the cooling season. This heat is particularly vulnerable as ice grows at the surface and rejected brine erodes the summer halocline. With the onset of the sea ice growth, heat is gradually released to the surface where it can slow ice growth and result in a thinner first year ice cover. These features include near-surface temperature maximums, but when observed outside of multi-year ice cover are notably warmer than those in the perennial ice zone, typically 4-6 °C but as high as 8 ° above freezing in CTD profiles outside of the ice edge in October and November (when the seasonal NSTM-like feature is most prevalent). In the buoy profiles, NSTMs were typically 2-5 ° above freezing, but cooled slightly between mid-September and freeze-up.

Heat below the summer mixed layer averaged between 2×10^5 kJm^{-2} and 3×10^5 kJm^{-2}in the buoy profiles in September-October and 3.5×10^5 kJm^{-2} in the CTD profiles conducted in August-September. Heat content values for both types of measurements were calculated by subtracting the total heat content in the summer mixed layer from the integrated heat content above the minimum temperature in the remnant winter mixed layer. Heat content is defined as the integral of temperature relative to a nominal freezing point ($T_f = -1.8 \pm 0.05$°C for surface salinities observed in the region) over depth times the heat capacity of the water column, as in Equation 3 of Jackson et al. [2010]:

$$HC_{UAW} = \rho_0 C_p \int_{WML}^{surface} (T(z) - T_f) dz \tag{3.1}$$

Heat content below the summer mixed layer (mostly in the summer halocline, abbreviated SH) is this integral over the seasonally-modified water layers minus the heat content of the summer mixed layer:

$$HC_{SH} = HC_{AW} - \rho_0 C_p Z_{SML}(T_{SML} - T_f) \tag{3.2}$$

In Equations 3.1-3.2, ρ_0 is the nominal water density (1025 kgm^{-3}), C_p is the specific heat (4.00 kJ kg^{-1} K^{-1}), and Z_{SML} is the depth of the Summer Mixed Layer. Equation 2 works on the assumption that the Summer Mixed Layer is well mixed, and that the temperature is constant through the layer. In a time- or spatially- averaged sense, this is a fair assumption as any deviations from an isothermal mixed layer tend to be sparse spatially or short-lived in nature [Bradley et al., 2015]. Error due to uncertainty in the exact freezing point is small relative to the amount of heat in the layer because the uncertainty in the freezing point is small (±0.05 °C) relative to the temperatures observed in this layer.

There is certainly some heat loss from the summer halocline layer over the course of the cooling season, as evidenced by the buoy profiles. In the week prior to freeze-up, buoy profiles showed an average of 1.8×10^5 kJm^{-2}. Ice equivalent is calculated following Equation 3 of Timmermans [2015],

$$\delta h_i = \frac{\rho_0 C_p Z_{SML}(T_{SML} - T_f)}{\rho_i L} \tag{3.3}$$

where ρ_i is the density of sea ice (900 kgm^{-3}) and L is the latent heat of freezing (2.67×10^5 Jkg^{-1}). This amount of halocline-trapped heat could decrease first-year ice growth (δh_i) by 70 cm if fully released to the sea ice over the course of the winter. Timmermans [2015] found that stored heat in Near Surface Temperature Maximums below multi-year ice could reduce the growth of sea ice by up to 25%, or about 50 cm in a 2m thick ice pack.

3.5 Conclusions

Warming temperatures in the Arctic are extending the melt season, leading to areas of seasonally open water that have historically been ice-covered year round. Seasonal cycles in near-surface temperature and salinity profiles are different outside of the perennial ice cover. With summer thermoclines and haloclines colocated in the top few tens of meters in the western Arctic, long open water seasons lead to increasing summer temperatures in both the mixed layer and the halocline layer. This results in increasingly large amounts of heat trapped in the halocline layer as the mixed layer above cools in the fall. Storm and high wind events account for the majority of cooling in the mixed layer, which suggests that if the Arctic becomes stormier with climate change, the timing of freeze-up may not shift as late as it might otherwise. Regardless of the timing of freeze-up, the warm halocline layer gets trapped under the new ice. As first-year ice grows through the winter, the summer halocline erodes and releases stored heat up into contact with sea ice where it slows ice growth and results in thinner first-year ice cover.

Factors contributing to accelerated ice melt in the summer (e.g., ice-albedo feedback) have little year-to-year effect if they do not result in thinner ice cover the following winter. Warm summertime temperatures have been linked to delays in the timing of freeze-up, but because the rate of ice growth is related to the thickness of the ice, delays in freeze-up are compensated for by increased rates of ice growth later in the season, resulting in minimal differences in end of season ice thickness. Trapped heat in the halocline at freeze-up is a mechanism by which warm summer mixed layer temperatures reliably thin ice growth the following winter, resulting in thinner first-year ice cover and a higher propensity to melt out earlier in the summer.

The seasonal cycle of heat and salinity in the upper Arctic Ocean is well suited for further study using high-vertical resolution ocean models. In particular, the use of a turbulence-resolving upper ocean model could provide insight into the stability of the summer halocline layer and the response in the stratification in the seasonal layers to strong storms. These were not pursued in this dissertation as the focus is primarily on the observational evidence, and a modeling study of these processes would require considerable model development.

Chapter 4

Estimation of Arctic Ocean summertime heat content

4.1 Introduction

As described in the previous chapter, during the summer months ice-free areas of the Arctic Ocean warm with the absorption of solar radiation. This heat is found near the surface, as the solar radiation cannot penetrate very far into the water column. Before ice can form at the surface, the excess heat energy has to be removed from the surface mixed layer so that the water can reach the freezing point. Summer mixed layer heat content is therefore the determining factor in the timing of freeze-up. With the decrease in summer sea ice extent, the summer mixed layer is warming across the Arctic. This is leading to an overall increase in heat content in the summer mixed layer. There has been some interest in relating heat content to timing of melt out and freeze-up [Stroeve et al., 2014]. In Chapter 6 the topic of summertime heat and its relation to end-of-season ice thickness is considered.

SML heat content is the heat energy in the water integrated over the depth of the mixed layer. The ML depth can only be measured directly though, making summer heat content hard to estimate on a basin-wide scale. There is substantial spatial and temporal variability in MLD [Peralta-Ferriz and Woodgate, 2015]. Mixed layer depth cannot be estimated from the surface or through remote sensing methods. In situ measurements are necessary, and in the Arctic these measurements are very costly. Drifting buoys with strings of sensors can sense the mixed layer depth, but are sparse in the Arctic. This chapter examines empirical relationships with meteorological and geographic parameters in an effort to find a means of estimating mixed layer depth (MLD) in order to evaluate summer heat content.

Being able to estimate mixed layer depth also has an operational use: acoustic sensing in the Arctic is sensitive to the mixed layer depth, where strong salinity and temperature gradients create channeling effects and can alter the propagation of sound through the ocean. The mixed layer depth has operational impacts, especially for acoustic detection of vessels and submarines in the Arctic. At cold temperatures, salinity gradients in sea water have strong channeling effects on sound propagation and can allow for sound waves to travel extremely long distances with remarkable coherence [Mikhalevsky et al., 1999].

The annual cycle in heat peaks in the summer and fall seasons when there is open water at the lower latitudes in the Arctic Ocean. It is for this reason that the analyses presented here will consider only the summer and fall seasons only in this analysis.

4.1.1 Summer mixed layer

The summer mixed layer was described extensively in Chapter 3. This layer is defined by the summer halocline, typically between 8 and 15 m deep in the western Arctic. This surface layer stays well mixed because of wind drag on the surface - vertical sheer in induced currents keeps the water mixed, isothermal, and isohaline generally. At any given time there may be surface layers that deviate from this, either through sea ice melt water pooling at the surface or solar absorption in the top meters (significantly fresher or warmer, respectively, than the mixed layer) that persist in periods of low winds [Bradley et al., 2015], but moderate wind drag is enough to keep the layer well-mixed.

While the summer halocline layer (see Figure 3.1) does sometimes hold significant amounts of heat from the summer, it is small compared to the mixed layer heat content and does not need to be released before freeze-up can commence.

4.1.1.1 Prior MLD estimates

In prior analyses, it has been assumed that the mixed layer is 20m deep across the Arctic throughout the summer. [Stroeve et al., 2014]. While this is a round number for a pan-Arctic estimate, there is substantial regional variability. Peralta-Ferriz and Woodgate [2015] and others have shown that the mixed layer depth varies both seasonally and regionally around the Arctic due to factors including local variability in wind drag on the surface, regional Ekman pumping, or interactions with local bathymetric features and coastlines. For example, in the southern Beaufort during the summer, mixed layer depths are often 10m deep or less, while in the central Arctic they can exceed 30m [Peralta-Ferriz and Woodgate, 2015]. MLDs vary seasonally, shoaling in the early summer and gradually deepening over the ice-free season.

4.1.2 Mechanisms for setting the depth of the SML

The mixed layer depth in the fall and spring is defined by the summer halocline. When sea ice melts in the spring, it releases fresh water into the upper ocean. This amount of fresh water limits the salinity and the depth of the mixed layer - a deeper mixed layer will be more saline than a shallower one, just by the limits of the freshwater budget. The strength of the summer halocline has to do then with the mixing that determines the depth of the halocline.

Without wind-induced mixing, the fresh SML would be no thicker than the ice cover from which it melted. Vertical mixing during the melt season determines the MLD and the salinity of the layer. Stratification (in density, driven by salinity) in the water column has been shown to be the primary driver of MLD variability throughout the season, with wind-driven mixing accounting for only about 10% of the variability in depth [Peralta-Ferriz and Woodgate, 2015].

4.1.2.1 Wind-driven mixing

Wind drag at the surface during the open water season maintains the mixing through the summer and keeps water in the mixed layer consistent in temperature. Solar energy is absorbed on an exponential profile, and a significant fraction of solar energy is absorbed in the top few meters of the ocean, though this varies signfiicantly with turbidity. Without wind mixing, this absorption causes strong temperature gradients in the top two meters of the ocean, where positively buoyant warmer water floats on top of cooler mixed layer water [Bradley et al., 2015]. Wind mixes this heat into the SML, so that it is evenly distributed with depth down to the summer halocline layer, where strong density gradients caused by the halocline resist mixing under most conditions.

4.1.2.2 Convective mixing (fall)

The fall season brings additional mixing to the SML, contributing to an overall deepening of the mixed layer. Convective mixing, driven by cooling at the surface and increasing water density, accelerates mixing in the fall. This contributes to the rapid heat loss prior to the onset of freeze-up (see Section 3.4.4). Within the isopycnal mixed layer at the surface, a change in temperature of a water parcel is enough to increase the density relative to the water below it. The sinking, recently cooled water is replaced at the surface by warmer water from below, which can then be cooled and continue the process.

4.1.2.3 Fresh water in the SML

The annual budget of fresh water in the upper ocean is dominated by the seasonal cycle of sea ice growth and melt. Figure 4.1 shows the fluxes as relative (not to scale) quantities - in any given region of the Arctic, ice growth and the subsequent melt season take up and release a huge amount of fresh water, and other sources account for only a small amount of the freshwater budget [Yamamoto-Kawai et al., 2009]. For a 1-meter square area, 1.5

meters of sea ice growth over the course of the winter (assuming thermodynamic growth) is the equivalent of 1.1 meters of freshwater (0 p.s.u.) being removed from the upper ocean, following equation 1 of Peralta-Ferriz and Woodgate [2015].

$$FW(t) = FW(t - 1year) - S_{ice} \times \int_{1year} dH_{ice} + \sum_{1year} (FW_{precip} + FW_{river} - FW_{evap}) \quad (4.1)$$

The freshwater budget should be considered on an annual basis because of the seasonal cycle in sea ice growth and melt. To consider the change from the fresh water content a year ago, consider the net ice melt from the previous year, add the contribution due to net sea ice melt, and then add the total input of fresh water from rain, snow, and river runoff minus a small amount of evaporation.

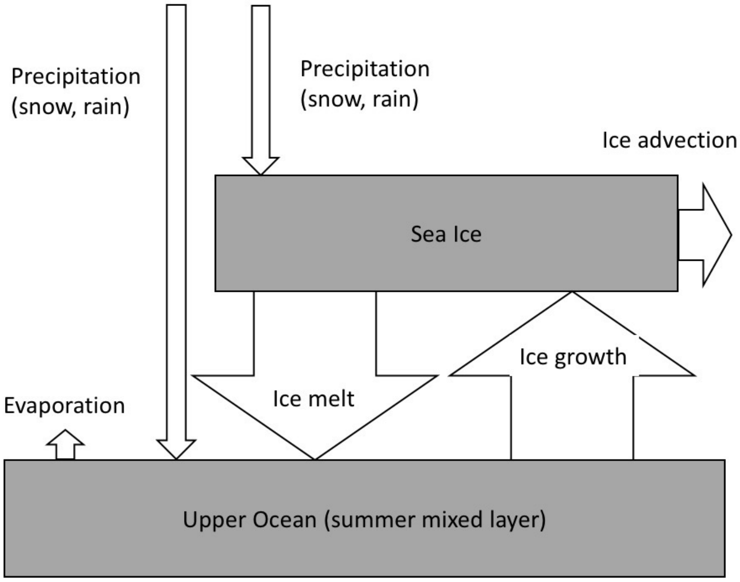

Figure 4.1: A schematic of the freshwater budget in the Arctic Ocean. Not included are the advection of fresh water from the Pacific or river sources which are limited to certain locations in the Arctic Ocean.

4.1.2.4 Regional differences in mean summer mixed layer depth

Mixed layer depths vary on both ice floe scales (10s of meters to 10s of km) and on regional scales. Peralta-Ferriz and Woodgate [2015] is a lengthy paper describing the climatology of mixed layer depths throughout the seasons, basins, and in response to changes in ice concentration, wind forcing, and stratification in the water column. In general, the deepest MLs are found in the Barents Sea (168m), Eurasian Basin (72m), and Makarov Basin (56m) in the winter, with slightly shallower (29-35m) MLDs in the western Arctic during the same season. In the summer, MLDs shoal across the Arctic, with depths as shallow as 8-9 m in the Southern Beaufort and Canadian Basin regions common in July and August. See tables 3 and 5 in Peralta-Ferriz and Woodgate [2015] for significantly more detail on the regional variability of the mean state MLDs.

4.1.3 Impact of stored heat on freeze-up timing

A key part of the interest in the ML heat content around the Arctic is the relationship with the timing of freeze-up. Heat content in the upper ocean can be defined as

$$HC = \rho_o C_p \int (T - T_f)(S,P)dz \tag{4.2}$$

where the temperature above freezing $(T - T_f)$ depends on the freezing point which is a function of the salinity and pressure of the water and integrated over the upper ocean. Using the average heat content per meter rather than the total heat content accounts for variability in the water layer depth [Jackson et al., 2010]. There has not been a systematic study of late-summer upper ocean heat content in recent years. Given the dramatic changes in the Arctic over the last decades, anything older than several years would no longer be especially representative of the current Arctic Ocean.

Climate models do capture the increasing delay in ice formation in the fall with increasing summer mixed layer heat content [Holland et al., 2006]. CMIP5 models do not capture the extent of the increases in ocean temperature however, suggesting a disconnect in the process driving the change [Ding et al., 2016]. Analysis of CMIP5 models attributes decreasing snow on sea ice over the 21st century to delayed onset of freeze-up [Hezel et al., 2012]. Not all models capture the complexity of the stratigraphy of the Arctic Ocean (see Lique and Steele [2013], especially figure 2d) and therefore are likely not capturing the full extent of the effects of climate change in the region.

Stroeve et al. [2014] considered the changes in length of the Arctic summer melt season (from initiation of melt in the spring to the end of any sign of melt occurring in the fall) over the last several decades. Using satellite estimates of ice concentration, dates of melt onset, continuous melt, freeze onset, and continuous freezing were determined. That analysis works with an equation from Steele et al. [2008] that relates the increased summer sea surface temperature to the delay in autumn freeze up:

$$\Delta t = \frac{OHC}{\rho_{air} C_p(air) C_h(air) \Delta T_{aw} W_{10m}} \tag{4.3}$$

where OHC is upper ocean heat content in units of J/m^2, and the denominator is in order, air density (1.3 kg m^{-3}), air heat capacity (10^3 $JKg^{-1}.^{\circ}C^{-1}$), air-water heat exchange coefficient (approximately 10^{-3}), the temperature difference between air and water ($\leq 10^{\circ}C$), and the wind speed at 10 meters above the surface (variable, but often on the order of 5-10 m s^{-1}).

This equation takes the heat content above some baseline (equivalent to selecting a baseline temperature, i.e. freezing) in units of Joules per area (J m^{-2}) and divides out the cooling rate in order to get the delay from that baseline until the surface is cool enough to freeze. The issue with this calculation is the method used for ocean heat content. In Stroeve et al. [2014], ocean heat content is the sea surface temperature in degrees above some nominal freezing point, scaled by the conversion between water temperature and heat content, and integrated over a constant 20 m deep mixed layer. The mixed layer depth is highly variable, and this approach overestimates heat in the western Arctic and underestimates heat in the eastern (Atlantic) Arctic.

4.2 Observations

In order to develop an empirically-based means of estimating the mixed layer depth and therefore the heat content, we first need observations of the mixed layer depth. For this, CTD and XCTD (Conductivity-Temperature-Depth and Expendable Conductivity-Temperature-Depth) profiles from the World Ocean Database [Boyer et al., 2013] are considered, as described in Section 3.2.1.1. These profiles are then processed to determine the MLD (based on the thermocline), as this is where the heat is stored.

4.2.1 CTD profiles

The World Ocean Database dataset is described in detail in Section 3.2.1.1. For this analysis, only profiles with high resolution CTDs and XCTDs are included. Figure 4.2 shows the locations of each of the CTD profiles considered in this analysis, with the regions labeled. Figure 4.3 shows these by month and year: the vast majority of overwinter profiles come from the Barents and northern North Atlantic in areas that are ice-free year round.

4.2.2 Determining MLD

With each CTD profile, the mixed layer depth is determined using an automated process. If the shallowest measurement is greater than 10 meters deep, the CTD profile is discarded from this analysis in order to capture the MLDs described in Peralta-Ferriz and Woodgate [2015]. The mixed layer temperature is defined as the the average of the top two recorded temperatures on the profile. If they are more than 0.1 $^{\circ}\mathrm{C\,m^{-1}}$ apart, only the first measurement is considered in the mixed layer and it is assumed that the thermocline begins somewhere between the first and second recorded measurement. This threshold was selected based on an analysis of 25 randomly selected profiles to distinguish between measurement noise and actual thermoclines.

Each CTD profile is then linearly interpolated along the depth axis at 1 meter intervals

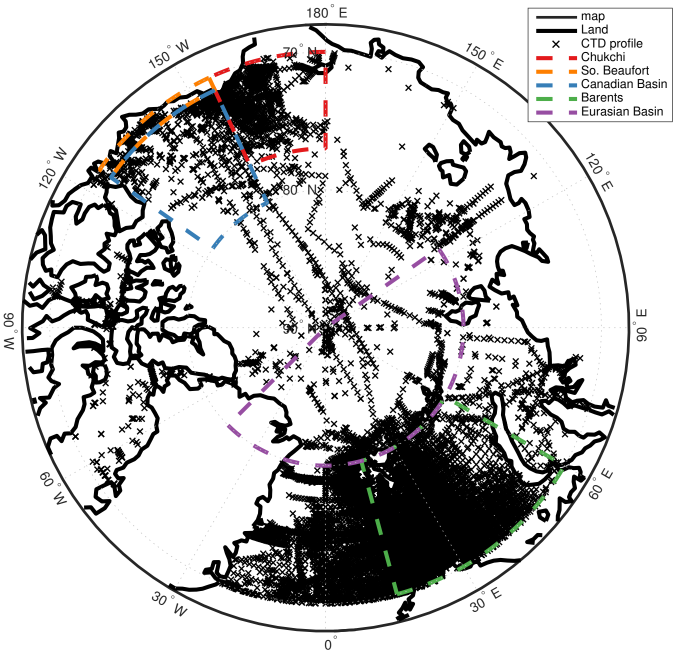

Figure 4.2: Regions as defined in Peralta-Ferriz and Woodgate [2015] and used for fitting empirical relationships between mixed layer depth and meterological and geographical parameters. Each CTD profile in this analysis is marked with an ‘x’.

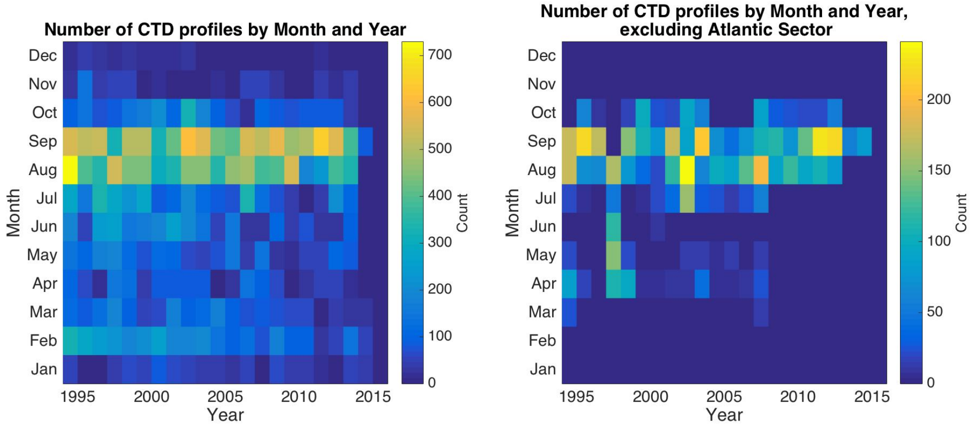

Figure 4.3: CTD profiles by month and year. Left panel includes all profiles, and the right panel excludes the profiles in the Barents Sea and the northern North Atlantic.

down to 100m or the depth of the last recording on the CTD profile, whichever is shallower. Above the first measurement, the profile is filled in with the mixed layer temperature as determined above. Then the first derivative of temperature with depth is taken. The first point (closest to the surface) where the slope in temperature exceeds 0.1°C per meter in either the positive (warmer with depth) or negative (cooler with depth) direction the top of the summer thermocline. This threshold was selected from analysis of a set of 25 randomly selected summer and fall profiles from around the Arctic Ocean in order positively identify thermoclines but exclude temperature variations due to either small, local effects or measurement noise from some of the older, less accurate instruments included in the dataset.

The few profiles where no thermocline was detected above 50m depth were discarded. These either contained a very minimal summer thermocline at shallower depths that was not strong enough to be detected by the algorithm, or there was no thermocline at the summer mixed layer depth. In some instances, CTD data was too noisy to detect any clear layers.

The same process for temperature is also done with the salinity profile to find the summer halocline depth. For this analysis only the summer thermocline was used, as it is the heat content that is of interest.

4.2.3 Reanalysis observations

For both the basin-wide estimates and the CTD fit analyses, reanalysis meteorological products are used. There are only very sparse observations of near-surface weather in the Arctic, and while the ships that conduct the CTD profiles are usually carrying meteorological instruments, that data is not logged with the profiles themselves.

Initially the analysis was done using MERRA reanalysis data [Rienecker et al., 2011] for the surface level wind speeds and air temperatures because of the reviews in Lindsay et al. [2014]. Their analysis indicated that the MERRA reanalysis product wind speeds were among those with the lowest bias, and that the parameters, when applied to the PIOMAS ice model, were a better match to the observations than other reanalysis products. The analysis was re-rerun using MERRA2 because the MERRA product was discontinued, with the data set ending in February 2016. While the CTD profiles used to develop the empirical relationships were only available through 2015, it will be possible to extend the MLD and heat content estimation forward in 2016 using meteorological observations and reanalysis products as they become available for later comparison with in situ observations. Limited changes to the sea ice and land ice processes in the MERRA2 reanalysis code suggest that performance over Arctic sea ice will improve marginally if it changes at all - this improvement would more likely be due to global upgrades in model physics rather than ice-related processes [Bosilovich et al., 2015]. It is therefore expected that the MERRA2 reanalysis products will not be worse than the MERRA products and may show slight improvements in estimating the meteorological conditions in locations with few, if any, observations.

Figures 4.4 and 4.5 show examples of the wind and temperature reanalysis products used for this analysis. The 2-meter surface products are used for both wind speeds and temperatures so that there is consistent coverage in the Arctic.

4.2.4 SST NOAA product

The NOAA sea surface temperature product [Boyer et al., 2013] is an optimal interpolation of the available measurements of sea surface temperatures around the world oceans. It is gridded to 1 degree grid cells and comes with an ice concentration product. Examples of these products are shown in Figures 4.6 and 4.7. This product combines in situ SST obserations with satellite-based products and ice concentration information to create a gridded weekly average SST estimate for the world's oceans. The data quality in the Arctic is limited by low numbers of in situ observations, difficulty with satellite retrievals around sea ice, and high spatial variability. Comparison with other SST products shows an RMS error up to 0.5C in the Arctic [Reynolds et al., 2002].

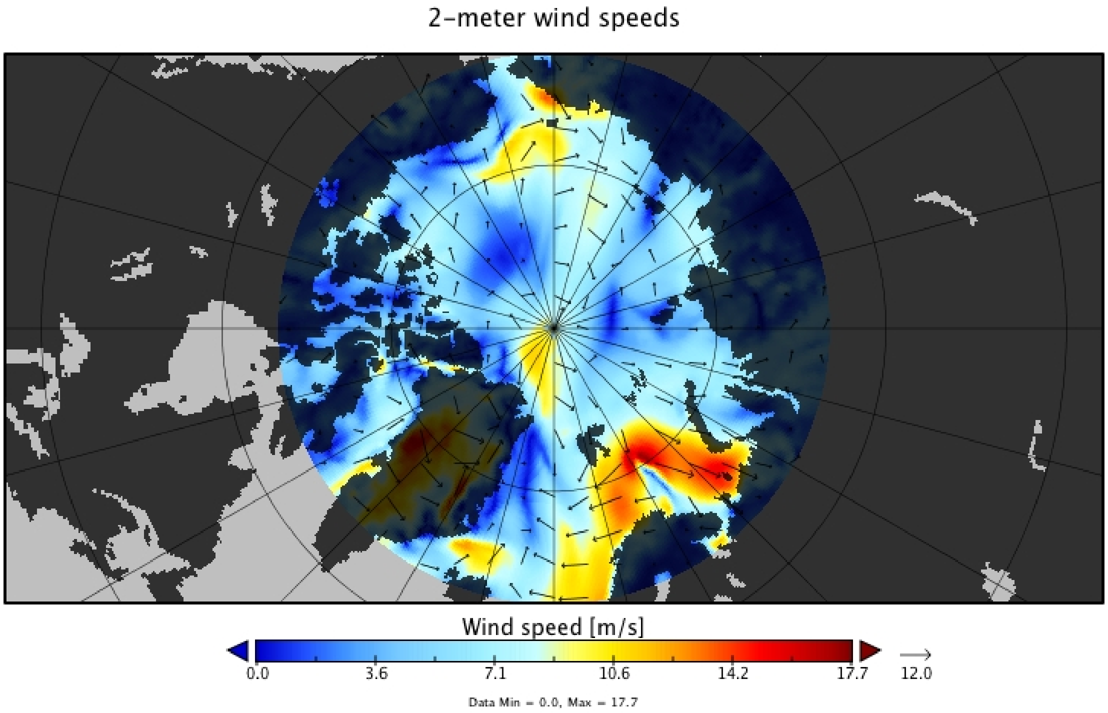

Figure 4.4: Example of MERRA 2 reanalysis wind speeds for one day in September 2007.

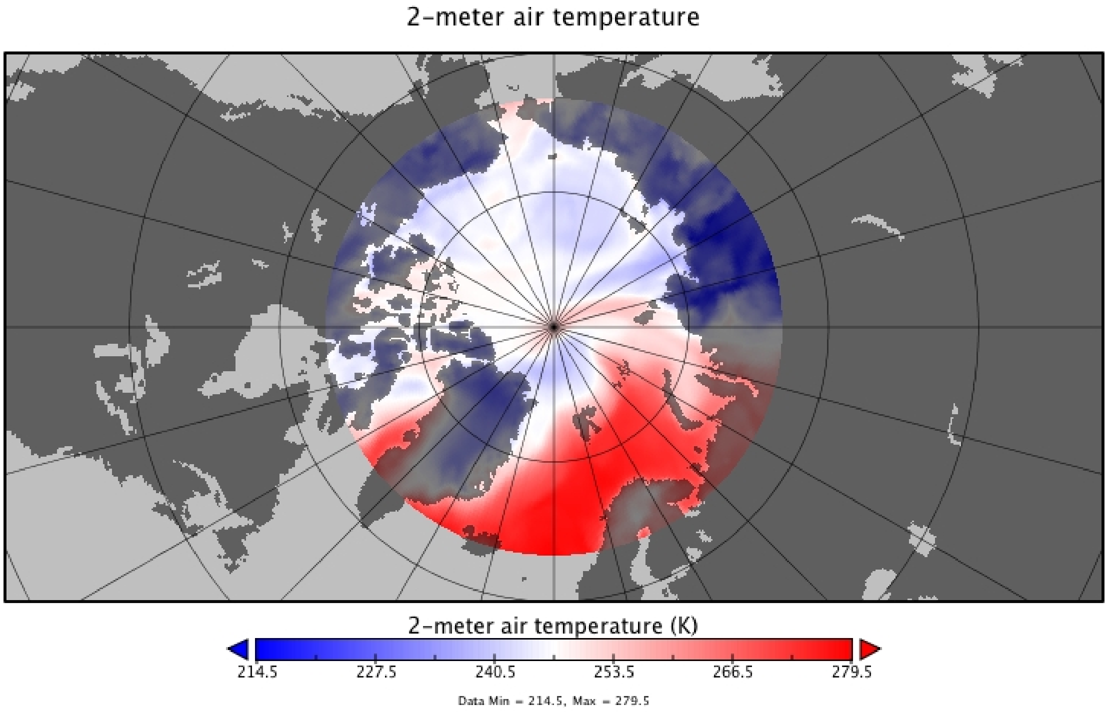

Figure 4.5: Example of MERRA 2 reanalysis surface air temperatures for September 2007.

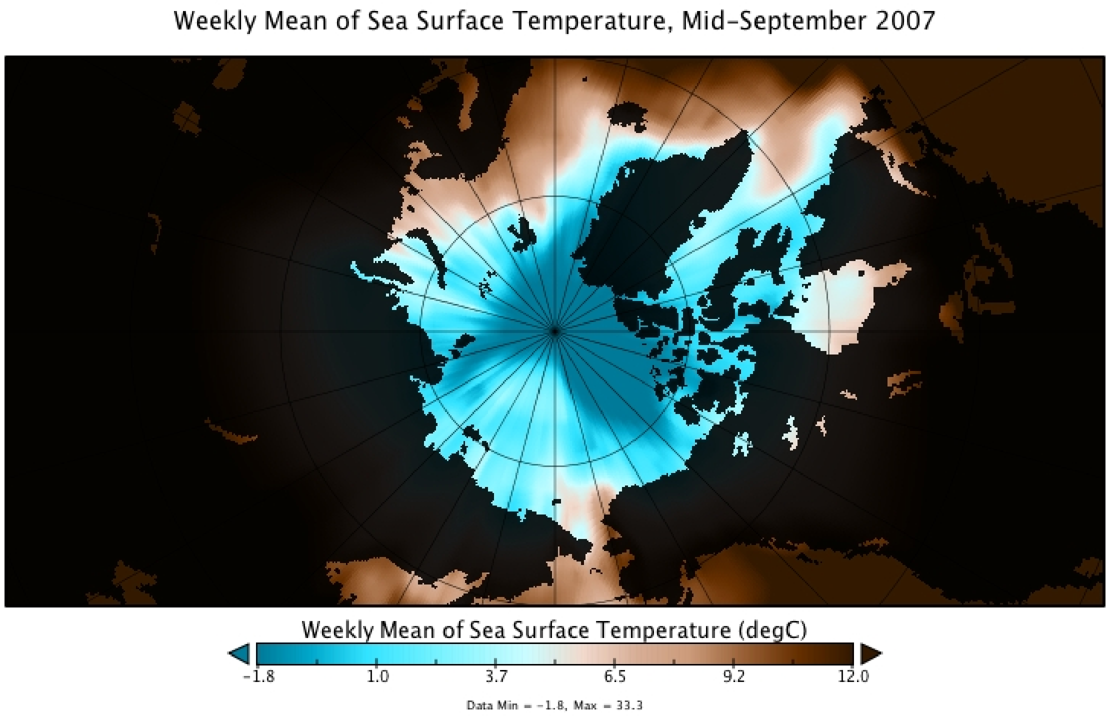

Figure 4.6: Example of the weekly mean of sea surface temperatures from the NOAA optimal interpolation product for the week of September 23, 2007.

4.3 Determining Empirical relationship

4.3.1 Regional definitions for the analysis

Different processes dominate in different regions of the Arctic: in the Beaufort, high winds drive regional variability in sea surface height, drawing low-salinity mixed layer water into the gyre [Giles et al., 2012]. In the Barents, interactions with higher salinity Atlantic water dominate [Peralta-Ferriz and Woodgate, 2015].

In order to account for regional variability in the drivers of mixed layer depth, this analysis looks at five regions in the Arctic, plus the whole Arctic Ocean excluding the Barents and North Atlantic sectors. Figure 4.2 outlines these regions, with latitude and longitude limits listed in Table 4.1. Each CTD profile in the World Ocean Database record [Boyer et al., 2013] is indicated by an ‘x’ on the map.

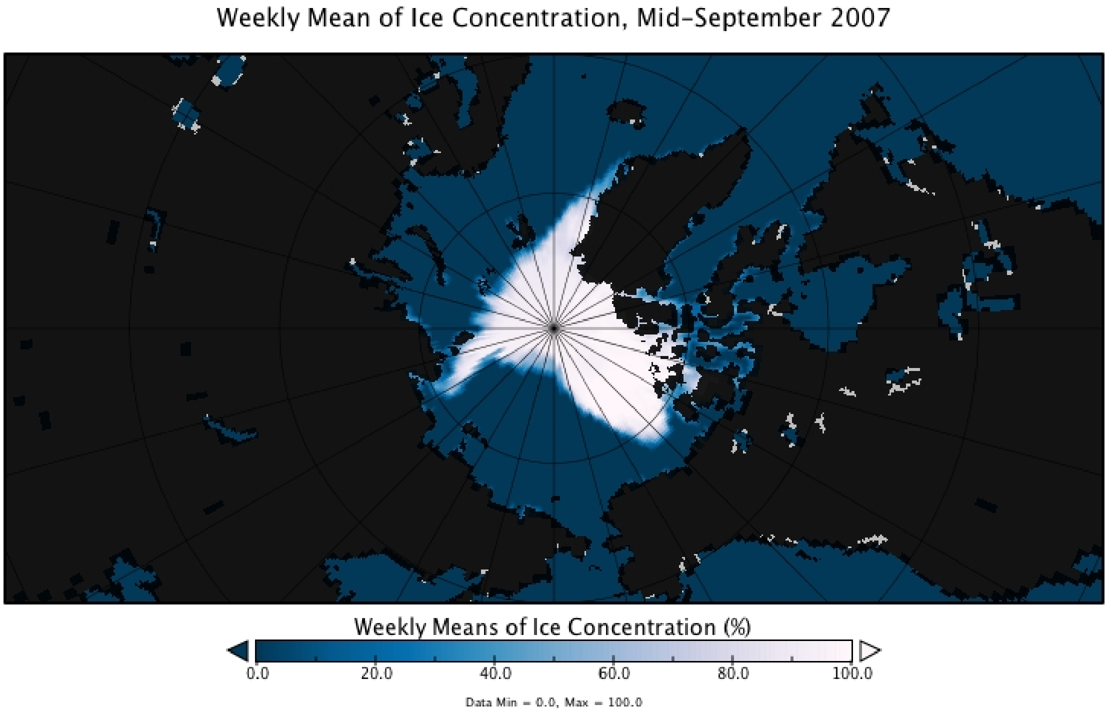

Figure 4.7: Example of the weekly mean of ice concentrations from the NOAA optimal interpolation product for the week of September 23, 2007.

These regions consist of:

Table 4.1: Latitude and longitude limits for the regions used in this analysis.

Basin		Latitude		Longitude	
1	Chukchi	70N	77N	180 W	155W
2	Southern Beaufort	70N	72N	155W	125W
3	Canadian Basin	70N	72N	155W	125W
4	Makarov Basin	78N	90N	150E	45W
5	Barents Sea	70N	80N	15E	60E
6	Eurasian Basin	80N	90N	45W	125E

The final “region” of the Arctic is the whole basin minus the Atlantic and Barents sectors. This is everything west of 30W and east of 90E, all the way north to 90N. This was included in the analysis to see if the regional approach resulted in lower error than a larger area.

4.3.2 Evaluating Parameters

Empirical relationships were determined in two steps: various meteorological, geographic, and oceanic factors were compared to the mixed layer depths determined from the CTD profiles. The parameters with the highest correlations with MLD in each region are then used to fit an empirical relationship to the direct observations.

The parameters that were considered are listed here with the source of the data. The final three on the list are approximations of heat fluxes based on their constituent factors.

- Latitude (WOD) - related to geographic effects and the presence of sea ice throughout the year.
- Longitude (WOD) - related to geographic effects especially the influence of Atlantic water.
- Day of year (WOD) - captures seasonal deepening.
- Year (WOD) - captures interannual trends in MLD.
- Date (WOD) - captures interannual trends in MLD.
- Air Temperature (MERRA2) - related to convective mixing in the surface layer.
- U Winds (MERRA2) - related to wind-driven mixing in the surface layer.
- V Winds (MERRA2) - related to wind-driven mixing in the surface layer.
- Windspeed (calculated from U wind and V wind vectors) - related to wind-driven mixing in the surface layer.
- Surface temperature (WOD) - related to convective mixing in the surface layer and captures seasonality related to ice melt.
- Temperature differential (Air temperature - Surface temperature) - related to convective mixing in the surface layer.

- Sensible heat flux (Windspeed × Temperature differential) - related to wind driven mixing and convective mixing in the surface layer.
- Radiative heat flux (Air temperature^4 - Surface temperature ^{4}) - related to wind driven mixing and convective mixing in the surface layer.

Because this analysis is looking at linear correlations between parameters, the constants that go into calculating the radiative heat flux and the sensible heat flux are omitted from the analysis.

Figures 4.8 and 4.9 show the correlation coefficients between the mixed layer depth and each of the parameters. Correlation coefficients indicated by black x's are statistically significant, while those indicated by red o's are not at the 5% level ($p < 0.05$).

4.3.2.1 Summer season

Figures 4.8 shows the correlation coefficients by basin for the summer season. The number in the title of each plot is the number of CTD profiles and corresponding meteorological parameters that went in to calculating these coefficients for each basin. These indicate only correlation, though the motivation for selecting these particular parameters was based on probable causes of mixed layer depth variability. Mixing depth is determined by a number of factors, but the amount of vertical mixing is primary among them. Physical conditions that would then encourage mixing (like high surface-level winds) would likely lead to deeper mixed layers.

Chukchi For the Chukchi in the summer, the three strongest correlations are latitude, sea surface temperatures, and air temperatures. These are all correlated with each other - surface air temperatures tend to follow sea surface temperatures, and temperatures generally tend to get cooler with increasing latitude. Higher wind speeds are correlated with thicker mixed layers, which makes sense because of wind-driven mixing. Warmer air and surface temperatures are correlated with thinner mixed

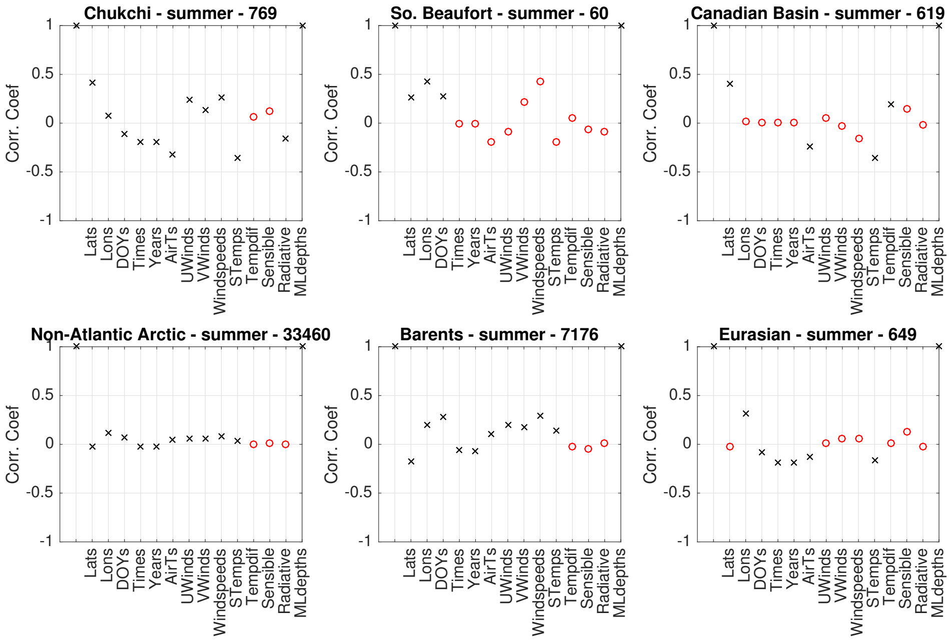

Figure 4.8: Tables of correlation coefficients for relevant parameters for the summer season in each basin. The black x's indicate correlations that are statistically significant at the 5% level, while the red circles indicate correlations that are not.

layers though, which is not as obvious: cooling of surface water leads to convective mixing and deepening of the mixed layer, but this process would not be prevalent in the warmer summer months. Instead, it is likely that there are a few CTD profiles in this analysis where the summer mixed layer has not yet developed, and this may be a source of error in the analysis.

Southern Beaufort The mixed layer depth in Southern Beaufort is most strongly correlated to the wind speeds and sensible heat flux. Interestingly, there is little correlation to either direction of wind, suggesting that it is irrelevant where the wind is coming from. In the Southern Beaufort, the air temperatures are strongly inversely correlated with wind speeds. Wind speeds are also highly correlated with the day of the year, where the strong temperature gradient between relatively warm snow-free land earlier in the summer sets up strong pressure gradients and therefore strong winds earlier in the season.

Canadian Basin The mixed layer depth in the Canadian Basin is most closely correlated with surface temperatures and latitudes. The negative correlation with surface temperatures suggest that as temperatures warm, the mixed layer shoals. This may indicate that some profiles represented the remaining winter mixed layer rather than a summer mixed layer, as high latitudes and cold surface temperatures may be areas that are mostly ice covered.

Barents Sea The mixed layer depth in the Barents sea has very little correlation to any parameter: there is a slight correlation with latitude, where more northerly locations have a fully developed Arctic-style summer mixed layer and more southerly latitudes are dominated by inflow from the Atlantic Ocean.

Eurasian Basin In the Eurasian basin, the longitude is the most prominent correlation with mixed layer depth. In this region, longitude would be indicative of the influence of surface waters from the Northern North Atlantic. Sensible heat flux is also a very minor correlation, and is included as the second term.

The non-Atlantic Arctic is shown in the bottom left panel on these figures. Across the arctic in the summer, MLDs are very slightly positively correlated with wind speeds, agreeing with the regional analysis in Peralta-Ferriz and Woodgate [2015]. There are also slight correlations with Longitude and wind speeds.

4.3.2.2 Fall season

In the fall season, the mixed layer cools to the point where sea ice can grow on the surface. Convective cooling - where convective mixing brings warmer water in the mixed layer to the surface where heat can be released to the atmosphere - accelerates cooling but also adds a process to the list of things that determine the mixed layer depth.

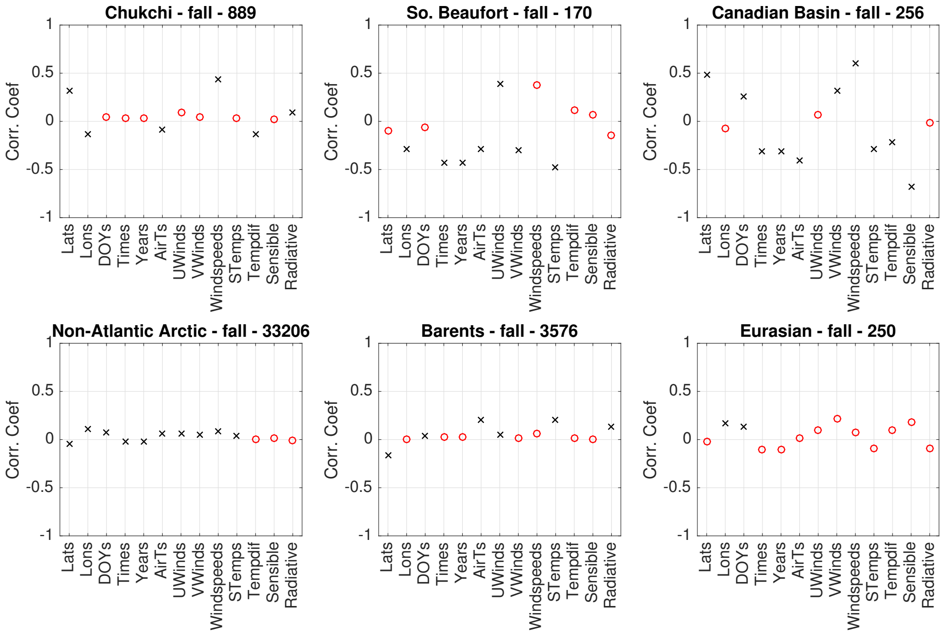

Figure 4.9: Tables of correlation coefficients for relevant parameters for the fall season in each basin. The black x's indicate correlations that are statistically significant at the 5% level, while the red circles indicate correlations that are not.

Like in Figure 4.8, Figure 4.9 shows the correlation coefficients for each pair of parameters for each basin. Again, the black x's indicate statistical significance at the 5% level.

Chukchi For the fall season in the Chukchi, wind speeds are the most significant correlation with mixed layer depth followed by latitude; higher latitudes correlate with deeper mixed layer depths, as do higher wind speeds. Interestingly, there is a slight inverse correlation (still statistically significant) with the temperature differential, which is related to the seasonal deepening of the mixed layer as described in Chapter 3 and Peralta-Ferriz and Woodgate [2015].

Southern Beaufort In the southern Beaufort, sea surface temperatures correlate well with mixed layer depth, where warmer SSTs are found with shallower mixed layers. Wind speeds in this region have an interesting effect: higher easterly winds correlate with deeper mixed layers, while higher northerly winds correlate with shallower mixed layers. This likely has to do with Ekman pumping effects along the coast, where northerly winds induce north-easterly flows along the coast and draw water up and away from the shore.

Canadian Basin The dominant term in the correlation matrix for the Canadian Basin is the sensible heat flux. Note that this is an approximation of the sensible heat flux bulk formulation, where the temperature differential between the sea surface and the near-surface air is scaled by the wind speed at the time. Latitude is the second most significant correlation for the MLD in the Canadian Basin, increasing in depth with latitude. This is one area where a small amount of error may come from a winter mixed layer depth detected by the algorithm rather than a summer mixed layer.

Barents Sea In the Barents Sea in the fall season, there are no especially strong correlations between the meteorological or geographic parameters and the mixed layer depth. There is a slight positive correlation with surface temperatures, air temperatures, and the approximate net radiative flux, and then a slight negative correlation with latitude. For the empirical relationship, the sea surface temperature and latitude terms were selected.

Eurasian Basin The Eurasian basin in the fall is mostly covered in sea ice, resulting in a slight correlation with surface temperatures where areas that are ice covered have slightly deeper MLDs than areas that are not (and have correspondingly warmer SSTs). There is also some relation with the northward wind component, which would correspond with Ekman pumping along the ice edge.

Across the whole (non-Atlantic) Arctic, no parameters correlated particularly well in the fall. Many parameters were statistically significant, but all correlations were weak.

4.3.3 Empirical Relationship

For each basin and season, the top two strongest correlations were selected and used to compute the empirical relationship between the meteorological parameters, geographic parameters, and mixed layer depth. The coefficients are found using a least-squares multiple linear regression for the two dominant factors and the product of the two. The resulting equation is of the form:

$$H_{MLD} = c_1 X_1 + c_2 X_2 + C_3 X_1 X_2 + C_4 \tag{4.4}$$

where X_1 and X_2 are the two parameters selected from the correlation analysis. Tables 4.2 and 4.3 list the resulting equations with the parameters and coefficients for each region by season.

Table 4.2: Summer equations

Basin	c_1	X_1	c_2	X_2	c_3	X_1X_2	c_4
Chukchi	67.7	$\times T_{SST}$	+2.09	$\times \Phi$	- 0.96	$\times T_{SST}\Phi$	-135.9
Southern Beaufort	1.12	$\times V_{wind}$	+ -0.24	$\times F_{sens}$	+ 0.016	$\times V_{wind}F_{sens}$	+ 3.02
Canadian Basin	-0.90	$\times T_{SST}$	+0.96	$\times \Phi$	-0.0048	$\times T_{SST}\Phi$	-53.3
Barents	2.02	$\times \Phi$	+15.6	$\times T_{SST}$	-0.19	ΦT_{SST}	-143.4
Eurasian Basin	0.015	$\times \Theta$	$+ - 0.0017$	$\times F_{sens}$	+ 0.00029	ΘF_{sens}	+12.59
Non-Atlantic Arctic	0.0042	$\times V_{wind}$	$+ - 0.25$	$\times \Delta_T$	0.017	$V_{wind}\Delta_T$	17.65

Table 4.3: Fall equations

Basin	c_1	X_1	c_2	X_2	c_3	X_1X_2	c_4
Chukchi	3.92	$\times V_{wind}$	+1.92	$\times \Phi$	- 0.051	$\times V_{wind}\Phi$	-128.6
Southern Beaufort	0.79	$\times T_{SST}$	+ 0.36	$\times V_{wind}$	+ -0.13	$\times T_{SST}V_{wind}$	+ 2.94
Canadian Basin	-0.086	$\times F_{sens}$	+0.15	$\times V_{wind}$	-0.00044	$\times F_{sens}V_{wind}$	+11.7
Barents	-19.1	$\times T_{SST}$	+0.96	$\times \Phi$	-0.28	$T_{SST}\Phi$	-53.6
Eurasian Basin	0.612	$\times \overrightarrow{V_{wind}}$	$+ - 0.655$	$\times T_{SST}$	+ 0.19	$\overrightarrow{V_{wind}}T_{SST}$	+22.7
Non-Atlantic Arctic	0.0060	$\times \Theta$	+0.13	$\times T_{SST}$	0.0056	$T_{SST}\Theta$	16.39

These equations are by no means indicating causation. They are empirical relationships that are statistically derived from parameters selected for their physical relevance.

4.3.4 Calculating the MLD

Once the regional empirical relationships were established, mixed layer depths across the region could be calculated from the reanalysis atmospheric parameters [Global Modeling and Assimilation Office (GMAO), 2015] and the NOAA optimal interpolation SST product [Reynolds et al., 2002]. These two products, along with the geographic parameters (latitude, longitude), were sampled at 1 degree resolution across the regions defined in Section 4.3.1 on the dates of the analyses. In order to capture the ice-free season evolution, the first of the month for July through November for each year of the NOAA data, 1995-2015, was considered. This resulted in 21 years for each month, for a total of 105 MLD estimates across the Arctic.

The NOAA SST data is a weekly data product, so the week containing the 1st of the month is sampled. There could be some error introduced from the difference in the SST averaging over the week, but given that the difference between consecutive weeks is generally small, it is unlikely to be causing substantial error relative to that which is inherent in taking a spatially variable complicated physical system and representing it with a few estimated variables.

In areas outside the regions of the empirical fits, the mixed layer depth is set to zero so that it does not impact heat content estimates in later analyses.

Figure 4.10 shows the resulting MLD estimate for one day in September, 2007. The different empirical relationships are clear at the edges of the defined regions. The discontinuities at the edges of the regions are the result of the different empirical fits applied to each region.

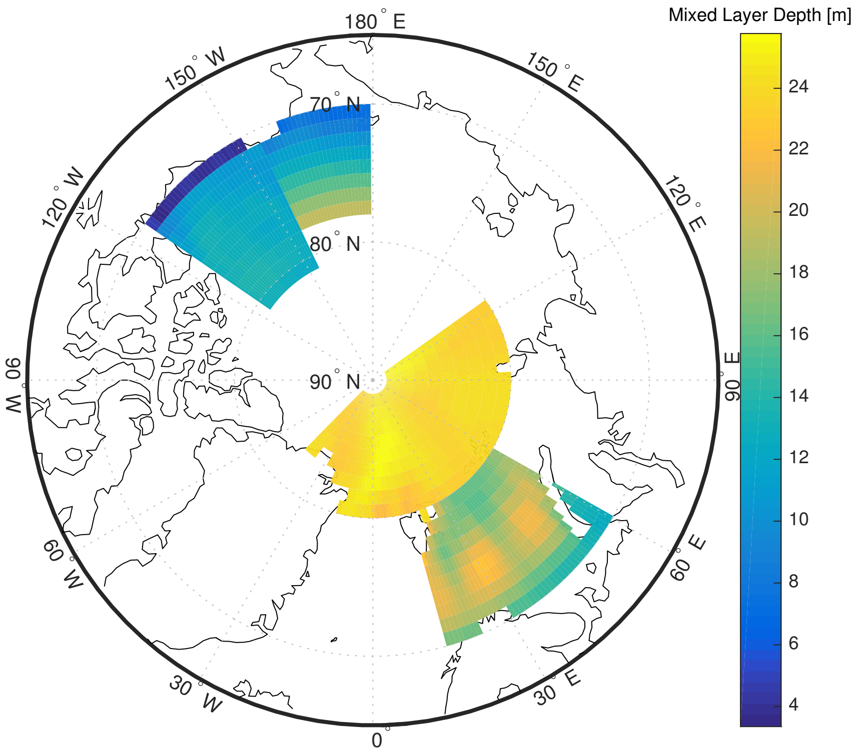

Figure 4.10: Example of the mixed layer depth estimates for the five basins of analysis for one day in September 2007.

4.3.5 MLD Error Estimates

For each region, the mixed layer error estimate is calculated by sampling the mixed layer depth estimates at the locations of the CTD profiles. Because the mixed layer depths were only calculated on the 1st week of the month, CTD profiles collected within three days of either side of the first of the month are considered. For example, CTD profiles conducted between the 28th of July of 1998 and the 3rd of August of 1998 are compared directly to the mixed layer depth estimate for August (1), 1998.

In each region, all CTD profiles within a 3-day window of the MLD estimate dates are considered in the error analysis. It is possible that some of the profiles, especially for the July case, are the remnants of the winter mixed layer rather than the summer mixed layer.

For these cases, an empirical fit mostly tuned to the shallow summer mixed layer is likely going to underestimate the deep winter mixed layers. Error is defined as

$$\epsilon = MLD_{observed} - MLD_{estimated} \tag{4.5}$$

so a positive error estimate indicates that the empirical relationship overestimated the depth of the mixed layer while a negative error suggests that it overestimated the depth.

Figure 4.11 shows these error measurements for each basin and season for three methods of estimating the mixed layer depth. Most, like the Chukchi, Southern Beaufort, and Canadian Basin, result in error distributions for the empirical approach akin to normal distributions with the bulk of the observations within ±10m of the estimated mixed layer depths. These distributions are also reasonably symmetric around 0, so that positive error in one profile is balanced out my negative error in another. The major exception to this is the Barents Sea profiles, especially in the fall. The distribution is highly non-symmetric, with the highest counts in cases where the error is 10m or more off in the negative direction (empirical approach overestimated depth). In the fall the error is similarly bad, though slightly less asymmetric. The other two approaches were more likely than not to result in error distributions that are biased either high or low.

The mixed layer depth climatology used for the error histograms was the average mixed layer depth for each season as shown in Figure 6 of Peralta-Ferriz and Woodgate [2015]. A highly nuanced approach (i.e., weighting that average by timing of observations) applying the climatology could approach a mean-zero error. The climatology was based on regional averages from the same WOD dataset, so by capturing some of the variability in addition to the regional means, the empirical approach performs slightly better at estimating the mixed layer depth.

These errors are presented as absolute error rather than percent error because the absolute error is more applicable to calculating heat content. If the empirical approach estimates a 10 meter mixed layer depth somewhere where the actual depth is 5 meters, the

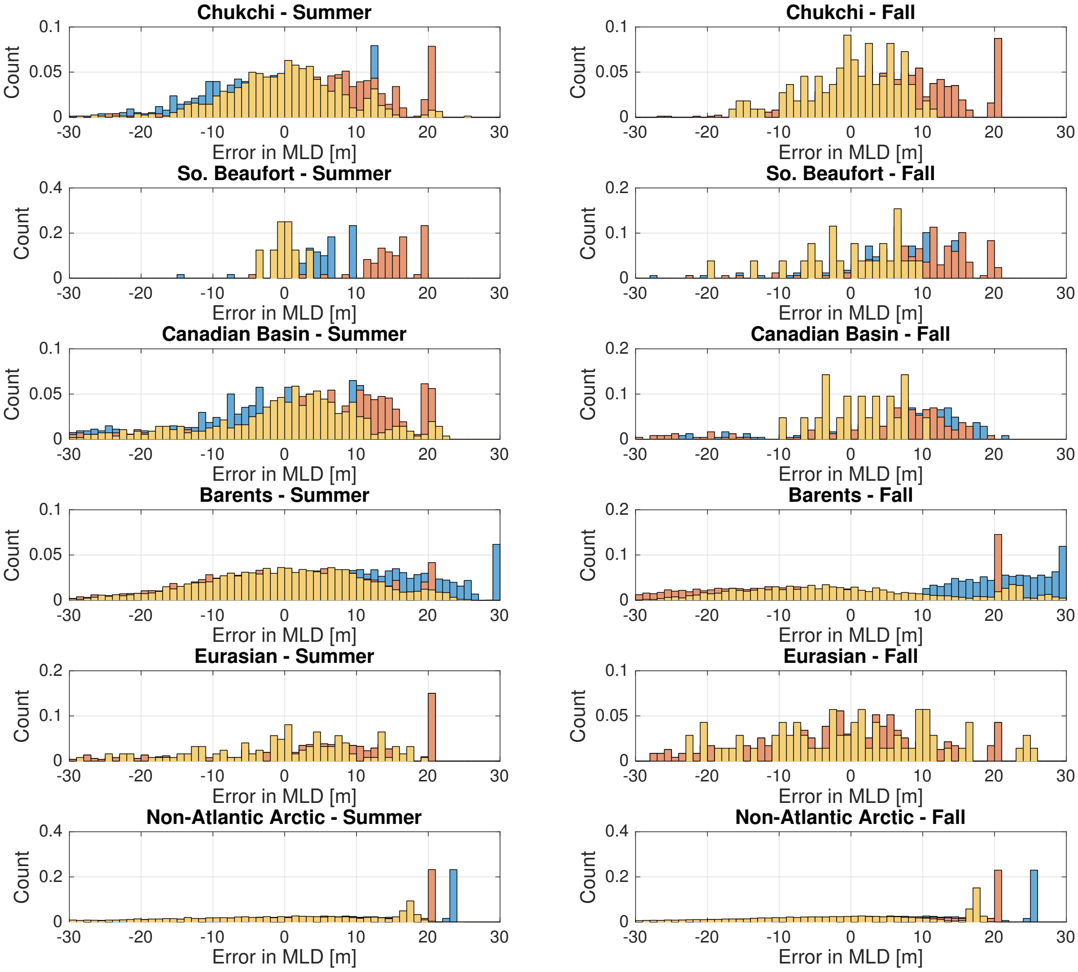

Figure 4.11: Histograms of error in the fit for each CTD profile by region and season. Positive error indicates that the estimation method overestimated the mixed layer depth. The blue histogram is using fixed mixed layer depths from the Peralta-Ferriz and Woodgate [2015] climatology, the red histogram is a fixed 20-meter mixed layer depth, and the yellow histogram is the mixed layer depths derived from the empirical fit approach presented here.

error is 100%. If a 100% error happened somewhere where the mixed layer depth was 35 meters, the absolute error would be far higher. Given that sort of variability in the depths, the absolute error conserves the total amount of extra water column that is either over- or under-estimated by an approach to finding the mixed layer depth. When calculating heat content for a region, overestimating the mixed layer depth in one location could be balanced out by underestimating the mixed layer depth in another location with the same mixed layer temperature. That spatial averaging breaks down slightly when an overestimate occurs in somewhere with notably non-average temperatures for the region, but it is still a better estimate than using a fixed depth that is known to be biased.

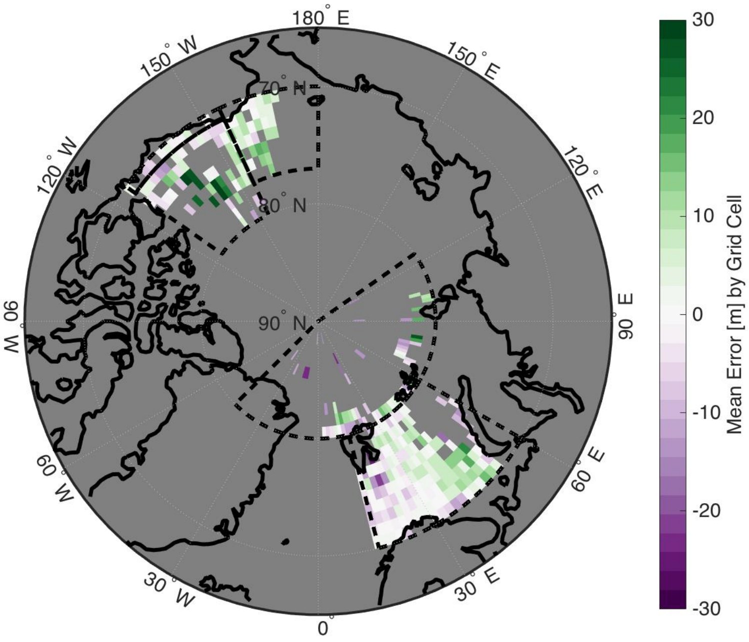

Figure 4.12: Map of mean error estimates by grid cell for each CTD profile and corresponding MLD estimates.

Figure 4.12 shows this information spatially: where there are CTD profiles to compare the estimated mixed layer depth to, the color shows the mean error for that grid cell. Some grid cells have one or few comparisons, and these represent the locations with the most egregious errors, especially the significant underestimation of the mixed layer depth in the central Canadian Basin. This location suggests that this particular set of CTD profiles captured the winter mixed layer rather than the summer mixed layer depth.

There is some spatial pattern to the error in the Barents sea, with slight overestimates of the mixed layer depth in the western half of the region and underestimates in the eastern edge. The eastern edge of this region is often more influenced by Atlantic water, which could explain the error: the mixed layer depth is determined by the inflow from the Atlantic rather than by seasonally modified water in the Arctic.

4.4 Heat content in Arctic Ocean basins

With the estimated mixed layer depth, it becomes possible to calculate the total amount of heat stored in the surface mixed layer. With the assumption that the water is isothermal through the mixed layer (per the definition of mixed layer), the heat content is

$$H_{ML} = c_p \rho_{sw} \times MLD \times T_{SST} \tag{4.6}$$

The sea surface temperature is the NOAA SST product, and the mixed layer depth is the estimated depth from the empirical fit. c_p is the specific heat of sea water and ρ_{sw} is the approximate density of sea water (1025 $\mathrm{kg\,m^{-3}}$).

4.4.1 How heat content relates to MLD and SST

Figure 4.13 shows how the heat content, and the interannual trends in heat content, compare between methods of estimating the mixed layer depth. These figures integrate the heat per unit area ($\mathrm{m^2}$) in each grid cell over the region from 180W to 120W and 65N to 90N. For the 20m and pan-Arctic fit methods, all ocean grid cells have a calculated heat content and contribute to the total heat content for the area. For the Regional MLD fit, the mixed layers are only defined in the regions discussed in Section 4.3.1. Everywhere else in the Arctic the mixed layer depth is set to 0. The total heat content is comparable between the estimation methods because it is in units of per area.

All methods and all months show a warming trend since 1995. The magnitude of these trends varies however, even between the two directly comparable methods. At the early and late ends of the season, the 20-meter method shows a trend approximately 4 times larger than the pan-Arctic fit trend. The seasonal process becomes more apparent in Figure 4.14: in the empirically-based mixed layer depth estimation methods, the largest trend in heat content is in September, when there is both a large trend in decreasing ice extent and a trend in increasing sea surface temperatures. In the 20m method, the trends earlier in the season are magnified by the over-estimation of the mixed layer depth, and the July trend is anomalously high. The 20m method also estimates trends at 4-10 times the rate of the regional fit method does.

Much of this trend in heat content can be ascribed to the Chukchi Sea. In Figure 4.15, trends toward increasing heat content are first present in the Chukchi Sea and near southern part of the Canadian Archipelago. Trends are more widespread in August and September and disappear from all but the Chukchi in November.

4.5 Relating summer heat content to sea ice cover

Summer heat content is interesting in its own right as a measure of climate change in the Arctic, but it is especially relevant in how it feeds back into the annual cycle of sea ice growth and melt in the seasonal ice zones.

4.5.1 Fall ice concentrations

In Figure 4.17, summer mixed layer heat content is correlated with early season ice concentration for each month of the summer heat analysis and ice concentrations in mid-October, mid-November, and mid-December. These ice concentrations were selected to account for early- mid- and late-season freeze-up dates. Each column in these figures contains

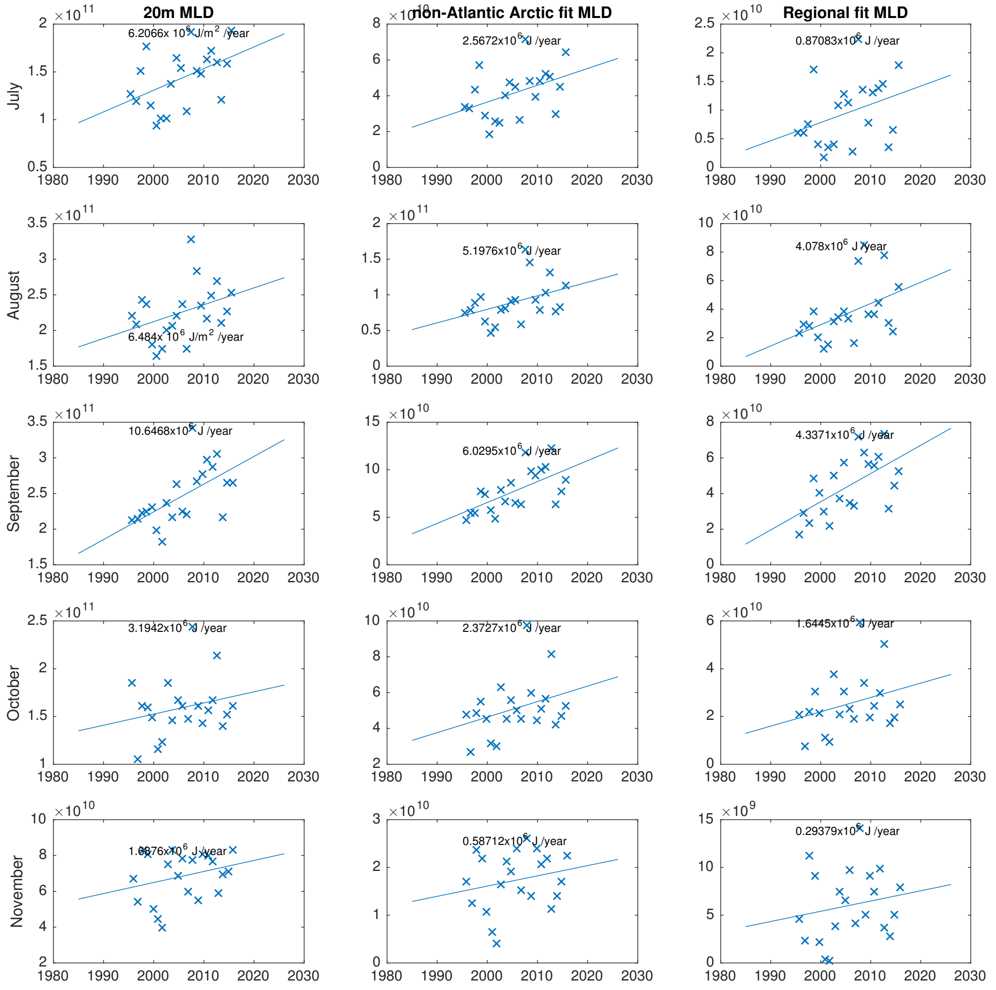

Figure 4.13: Heat content per unit area for the western Arctic (latitudes 65N to 90N, longitude 180W to 120W) for three methods: a fixed, 20m deep mixed layer, a variable mixed layer based on a fit derived from the non-Atlantic sectors of the Arctic Ocean (90E to 50W), and the regional fit method described earlier. Note that the total amount of heat varies between methods, as does the magnitude of the trend.

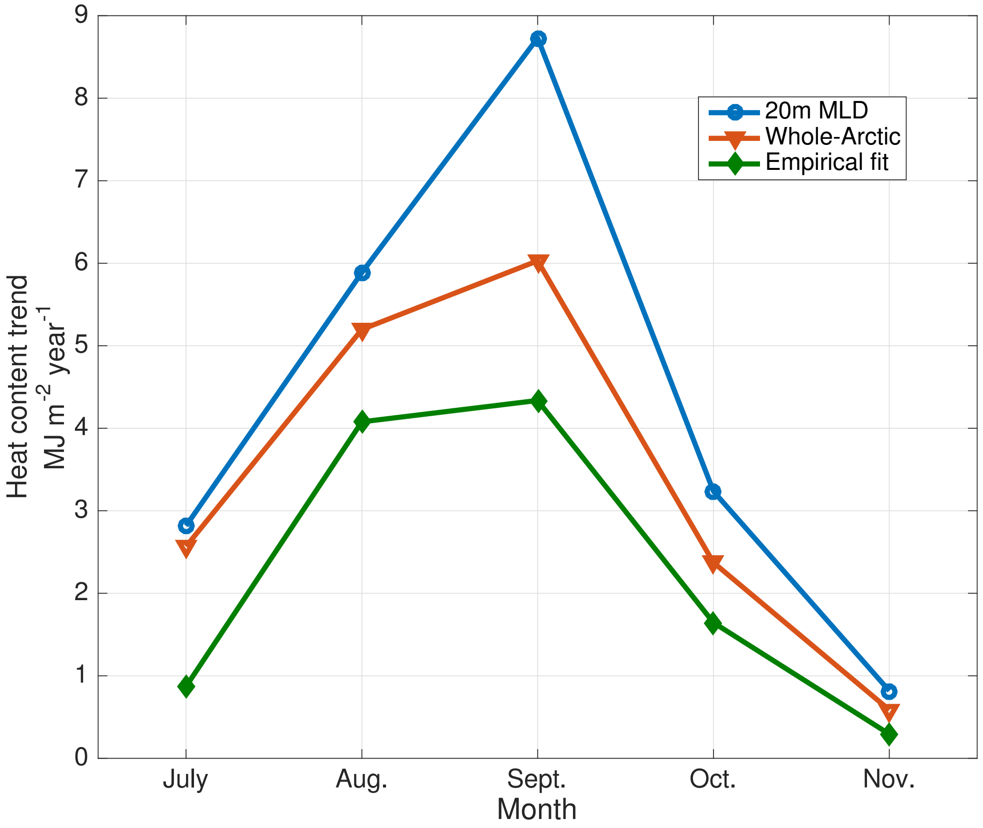

Figure 4.14: Trends in heat content per unit area for each month using a 20-m constant MLD, the pan-Arctic fit, and the regional fit estimated MLDs. These trends only include the western Arctic

a month's ice concentration, and each row is the summer heat content for one month. Each figure then shows the correlation between the heat content for the summer month and the ice concentration for the fall month. Note that the ice concentrations are selected from the middle of each month and the heat content estimates are for the first of the month. This offset makes it possible to compare heat and ice concentrations in November and October. Each correlation coefficient is calculated on a pixel-by-pixel basis. The background shows the contour of the bathymetry in the Chukchi and Beaufort for comparison. For reference, Figure 4.16 shows the trends in ice concentration for each of the fall months.

Generally, we expect to see a negative correlation between these: the more heat in the

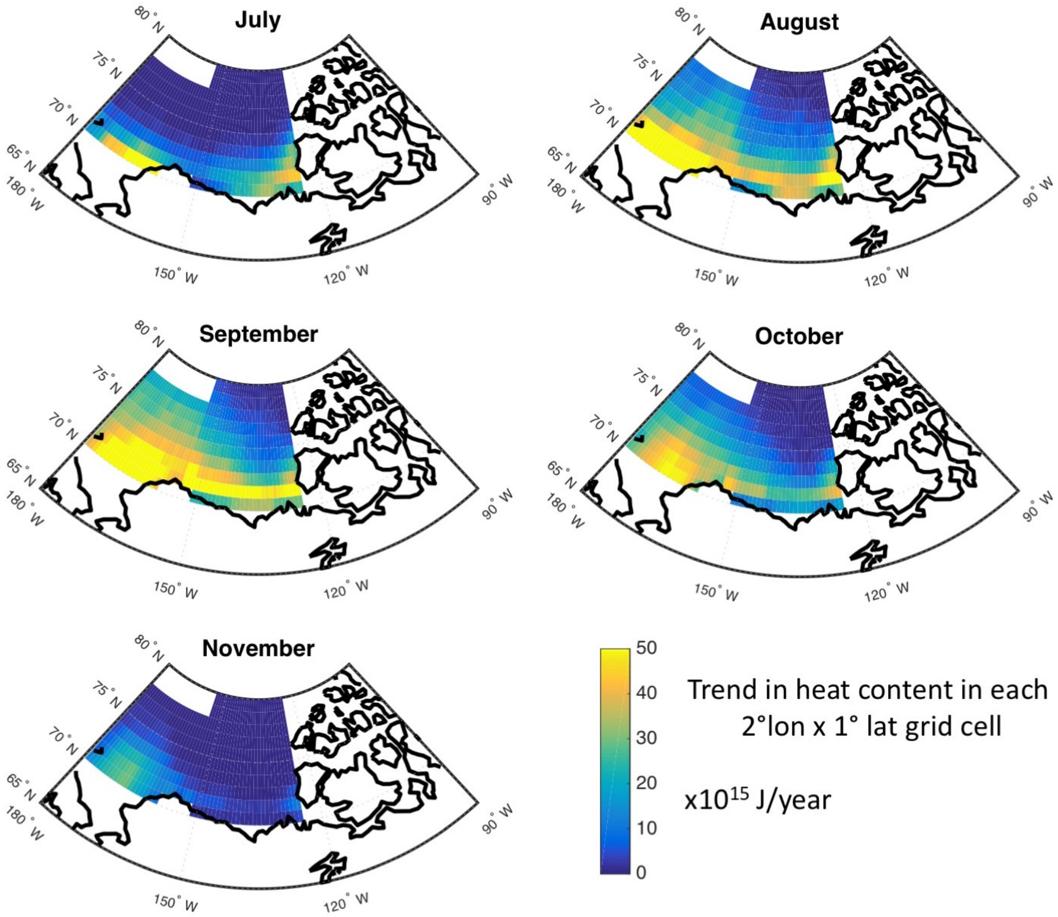

Figure 4.15: Trends in heat content per grid cell (not normalized to area) by month for the western Arctic.

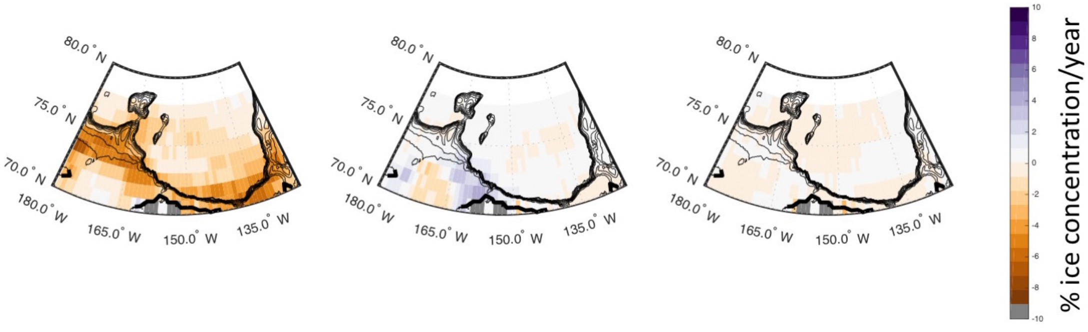

Figure 4.16: Trends in ice concentration (in percent cover per year) for mid- October, November, and December. The contours indicate bathymetry to show the Chukchi shelf edge in each panel.

summer ocean, the later ice forms. A positive correlation would mean that years that have warmer summer temperatures are more likely to have higher ice concentrations at the time of the comparison.

Figure 4.17 compares these parameters directly. In the left column, comparisons with October ice concentration, there is an increasing area of statistically significant negative correlations as the summer progresses. In November, there is very little statistically significant correlation until November, when the areas that are still above the freezing point correlate with the areas that are ice free. In December there are few areas with significant correlations with heat content at any point in the summer or fall.

4.5.2 Freeze-up Dates

Figure 4.18 shows the correlation coefficients between the heat content and the freeze-up dates (in day of year) in the top panel and de-trended anomalies in the bottom panel. These correlation coefficients, with a very small number of exceptions, are not statistically significant because of the short number of years with ice-free summer seasons at most locations and the limited number of years of the heat content estimates. Combined with relatively large interannual variability, almost all of the correlation coefficients (more than 95% of grid cells on the map) are not statistically significant at the 5% level. The map of correlation coefficients are generally positive as we would expect, though there are some locations with persistently negative correlations through both approaches to estimating heat content. For comparison, the second row uses the heat content assuming a constant, 20m deep mixed layer. This effectively conveys only the contribution of the sea surface temperatures to the freeze up dates. The patterns generally are very similar to the regional fit approach, but usually have slightly lower correlation coefficients. The third row in each set is the difference between the two, magnified by a factor of two on the color scale. Generally the regional fit does marginally better across the domain, with the exception of the mid-Chukchi shelf in August. Here the surface temperature approach outperforms the MLD approach, suggesting

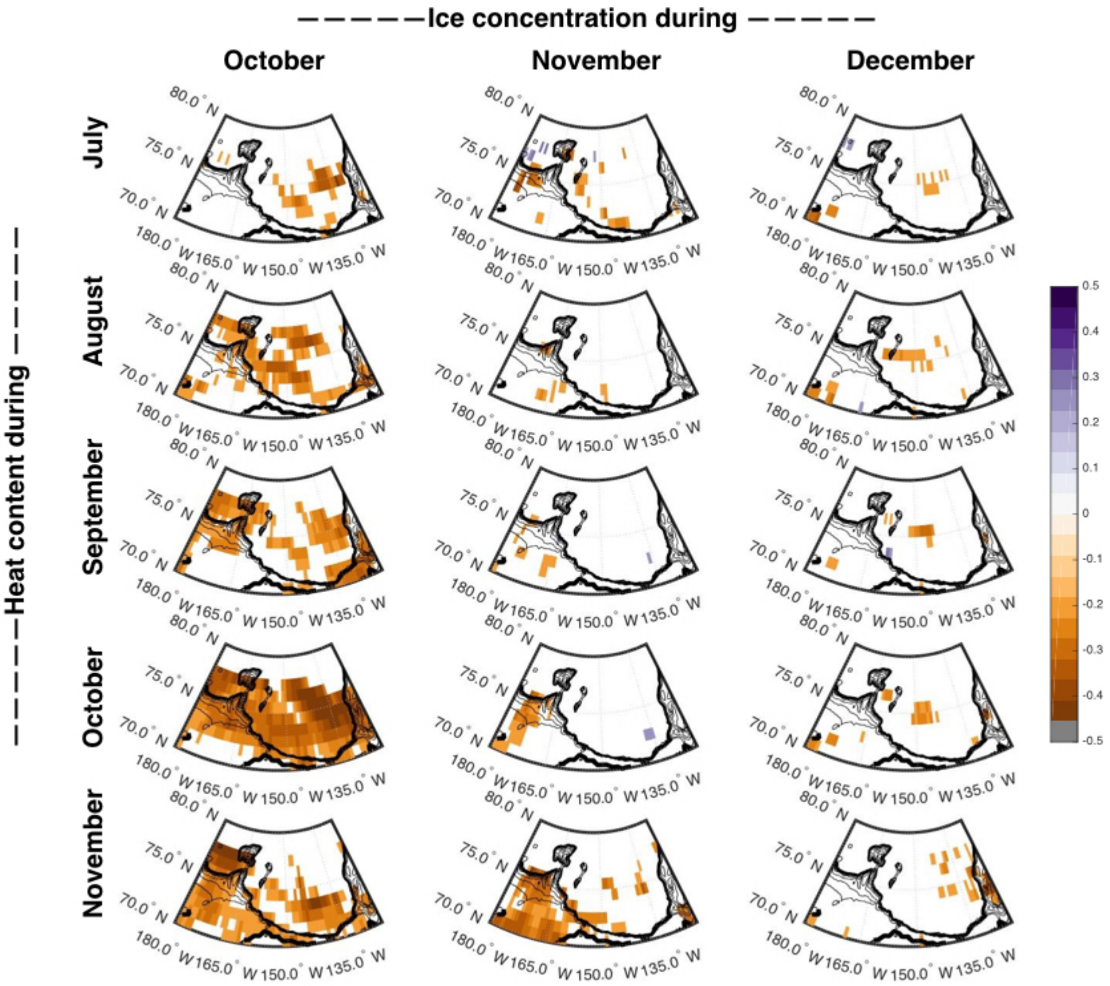

Figure 4.17: Correlation coefficients between the summer heat content (rows) and the fall ice concentrations (columns) in the western Arctic. Heat content estimates correspond to the first of the month, ice concentrations to the 15th. This figure only shows statistically significant correlations.

that either the MLD fit does not accurately capture the mixed layer depth, or more likely that the mixed layer depth in August is not a driving factor in the timing of freeze-up in November in this area because of advection of heat with the currents in the Chukchi shelf break region. That said, neither the regional empirical approach nor the 20m approach to estimating mixed layer depth results in statistically significant correlations.

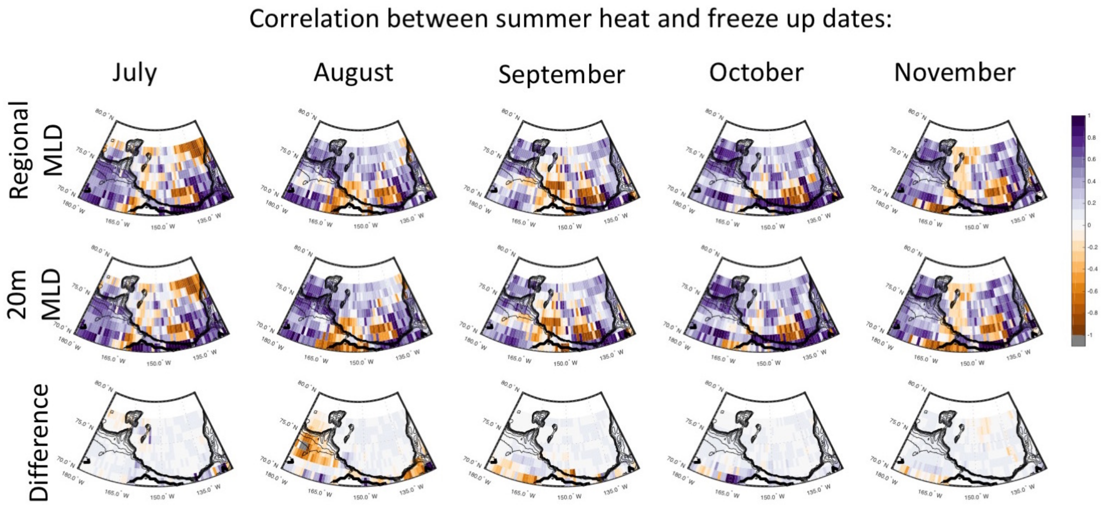

Figure 4.18: Map of correlation coefficients between heat content for each month and the fall freeze-up date. Few of these are statistically significant at the 5% level due to a small number of years with ice-free conditions and relatively large interannual variability.

4.6 Conclusions

Different regions within the Arctic seem to have different factors driving variability of the depth of the summer mixed layer. Wind is more likely to be a dominant factor in the fall across the Arctic, while surface temperatures and geographic parameters are typically more important in the summer. This indicates that summer mixed layer depth is best estimated by considering the presence of ice cover and the time since melt out (using the SST as a proxy). Fall mixed layer depth is then related to the amount of wind-driven mixing. This analysis only considered the local and time-of-observation wind speeds, because there is currently no to track where water parcels came from, and following the time evolution of the mixed layer depth would require Lagrangian tracking of some sort. Factoring in a parameter that captures the cumulative wind drag on the surface over the past month of the melt season could perhaps improve the estimation approach.

Empirically fit methods for estimating MLD do an adequate job outside of the Barents Sea, given coarse forcing data and complicated, spatially heterogeneous processes that determine the MLD. Using the 20-meter estimate for MLD overestimates regional heat content trends by a factor of 2-5 throughout the season when compared to the regional fit method. Increasing heat content (estimated using the regional empirical approach) correlates well with decreasing October sea ice concentration. The regional fit method also correlates with freeze-up dates marginally better than the 20-m method, which is effectively just considering the mixed layer temperature and not the depth, though this result is not statistically significant.

Summer mixed layer depths and the corresponding heat content are changing over time. As heat in the summer mixed layer must be removed prior to ice growth in the fall, increasing summer heat content leads to delayed freeze-up. The following chapters address how this in turn leads to thinner first year ice cover and a positive feedback loop that will maintain high rates of sea ice loss into the future.

Chapter 5

Antarctic Coastal Polynyas

Polynyas are areas of consistently open water in the sea ice pack. The polynya in the Terra Nova Bay (TNB) of the Ross Sea in Antarctica forms as the result of strong winds flowing down off the continental slopes and pushing sea ice in the bay away from the ice sheet edge. As the ice is blown out into the ice pack, it exposes water to the cold atmosphere freezing the surface and expelling brine into the remaining water column Buffoni et al. [2002]. The new ice is then pushed out by the persistent winds: this process continuously forms new sea ice in a manner often described as an ice conveyor belt.

The purpose for studying polynyas in this dissertation is to investigate whether there is an upper limit to ice growth rates. If even in the most extreme environments (like Antarctic coastal polynyas), ice growth rates never exceed some threshold, it is more likely that a delay in freeze-up date in the Arctic will have a substantial impact on the end-of-season ice thickness for first-year ice. Because ice growth rates are inversely proportional to the thickness of ice cover, ice that started to grow later would grow faster under the same atmospheric forcing. How much faster would then determine how much of a difference a delay in the freeze-up date makes in the first-year ice thickness.

The dynamics of polynyas are important for the study of polar climate systems because heat flux between the ocean and the atmosphere is many orders of magnitude higher in a polynya than it is through the ice pack. The TNB polynya in particular is valuable for the role it plays in the global climate system: high salinity shelf water (HSSW) formed from the "sea ice factory" effect is one of the major sources of the Antarctic Bottom Water (AABW), which drives thermohaline circulation in the Southern Ocean and feeds bottom waters into the major world oceans [Buffoni et al., 2002]. High salinity water left behind sinks down to join with dense water from under the Ross Ice Shelf to form the High Salinity Shelf Water (HSSW)[Orsi and Wiederwohl, 2009], a major component of AABW. Figure 5.1 and 5.2 show the persistence of the polynyas around the Antarctic continent [Arrigo, 2003]. The most frequently active polynyas only have ice cover approximately 30% of the time.

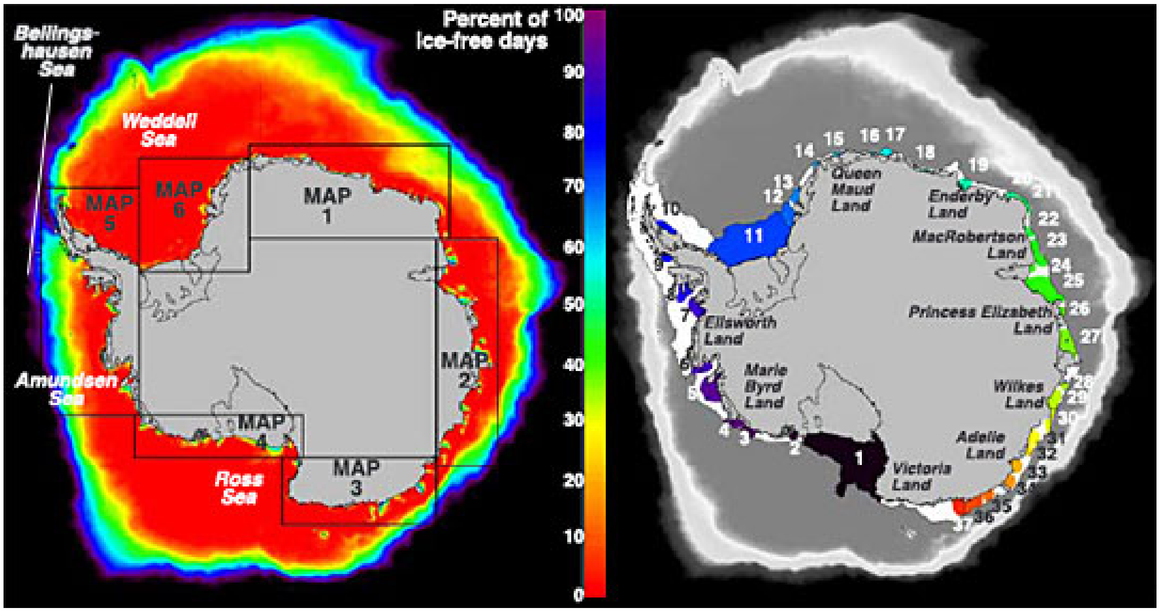

Figure 5.1: Map of polynyas around the Antarctic continent, with polynyas shown as areas with high percent of ice-free days close to the edge of the continent or along ice shelves. The right figure highlights each polynya in color, with the corresponding inset map number for the next figure. Reproduced from Arrigo [2003].

The dynamics of a polynya can be thought of in terms of two phases: an expansion phase where the wind drag on sea ice is dominating and ice that forms is getting pushed out away from the coast, and a closing phase where the wind forcing lets up and ice growth dominates. During the expansion phase, the area of open water grows; during the closing phase, the ice extent increases. The expansion phase is a dynamic unique to polynyas and interesting in its own right, but the closing phase makes a good comparison to ice formation

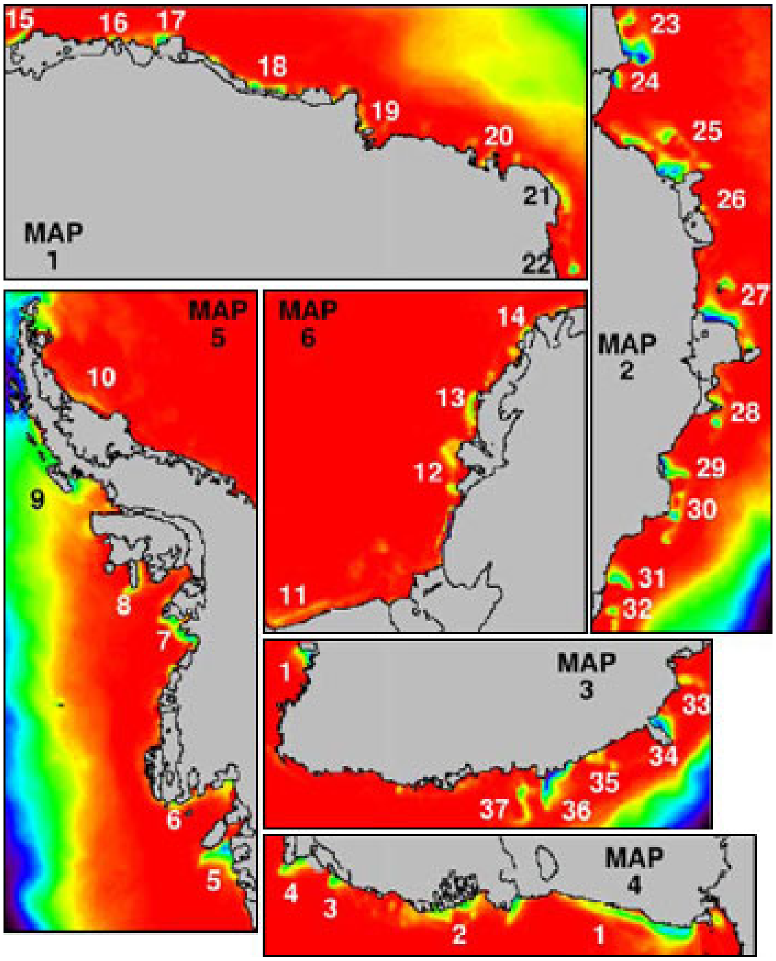

Figure 5.2: Detail on the map of polynyas around Antarctica, with the inset maps from Figure 5.1. Reproduced from Arrigo [2003].

in the late-season Arctic when extreme radiative cooling and moderate turbulent fluxes make for rapid growth of ice cover. When the expansion phases and the closing phases alternate in quick succession, the polynya maintains a roughly consistent size with small fluctuations.

5.1 Terra Nova Bay Polynya

Heat fluxes (and corresponding sea ice production) from polynyas have been estimated using ice extent remote sensing products [Fusco et al., 2009, Ciappa and Budillon, 2012]. Ciappa and Budillon [2012] studied the region in May and June 2009, finding opening and closing phases often alternated on timescales of less than 24 hours. The warmest surfaces on the imagery correspond to areas of open water and grease ice, which is often shaped by the wind into stripes called Langmuir wind rows [Ciappa and Budillon, 2012]. During the expansion phase, ice is forced out of the open water area and the ice edge is a sharp line, while during closing phases the thermal differences between the open water and the ice pack was more smooth [Ciappa and Budillon, 2012], much like the edge of the Arctic ice pack in the freeze-up season.

Surface temperatures used for estimating ice extent are somewhat variable. In using ice surface temperature estimates from the MODIS sensors, Ciappa and Budillon [2012] used 264K for the threshold temperature in the polynya expansion phase and 266K during the closing phase. These temperatures are lower than the sea water temperature because mixed pixels are measured as an area-weighted mean of the sea surface temperature (the freezing point of sea water) and the ice surface temperature. The two phases are marked by different temperatures because in the expansion phase, ice that has formed is getting pushed out to sea, and it tends to be slightly older and therefore thicker and cooler at the surface. In the closing phase, ice is growing back into the polynya area, resulting in thinner and warmer ice surfaces in the mixed pixels [Ciappa and Budillon, 2012].

5.1.1 Climatology

The Terra Nova Bay polynya is a particularly important part of the Ross Sea production of deep water. The katabatic winds off of the continent are the primary driver of maintaining the open polynya in the winter [Bromwich, 1990]. Annual variability in yearly-average heat flux is one to two orders of magnitude smaller than the seasonal variation in the heat fluxes associated with the polynya [Budillon and Spezie, 2000]. Figure 5.4 shows the annual climatology for winds, ice cover, and column oceanographic measurements from a mooring in the bay maintained by the nearby Italian station [Budillon et al., 2009].

A (relatively) warm surface layer exists in the summer, but with the onset of winter conditions in March an increase in turbulent mixing due to the high katabatic winds

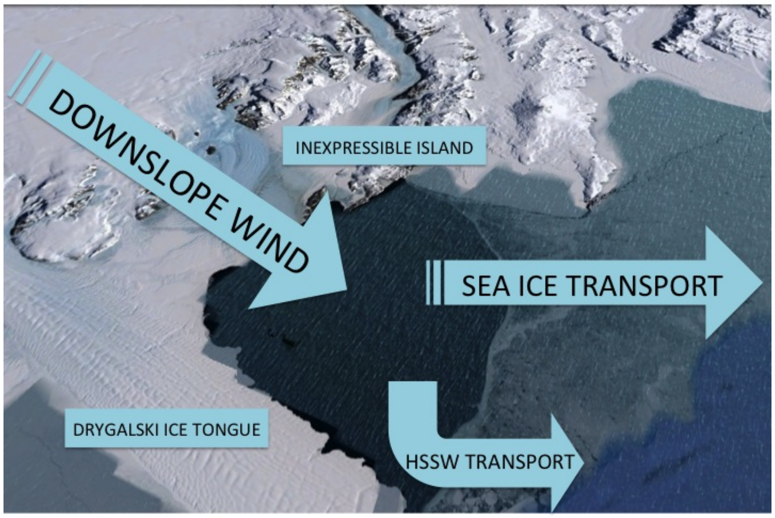

Figure 5.3: Satellite image composite of the Terra Nova Bay polynya (from Google Earth) with the dominant winds, local geography, and direction of ice transport labeled. For reference, the polynya is approximately 60km wide and 50km long in the along-wind direction, though both of these dimensions are highly variable.

erases this signature very quickly [Budillon et al., 2009]. The summer season is marked by substantial heating from the atmosphere into a largely ice-free ocean [Budillon and Spezie, 2000].

TNB has been observed by satellite imagery, with [Ciappa and Budillon, 2012] comparing ice surface temperatures retrieved by the MODIS instrument to SAR images. Timescales of opening and closing can be on the order of as little as 24 hours [Ciappa and Budillon, 2012], as an abrupt stop in wind forcing will be immediately met with ice growth under the cold atmosphere. The polynya is primarily forced by katabatic winds off of the Reeves and Priestly glaciers, wind patterns that cannot necessarily be discerned from the AWS maintained by the Italian program in the TNB region.

The blocking effect of the Drygalski Ice Tongue to the south of the TNB is an important part of the formation of the polynya [Ciappa and Budillon, 2012]. Ross sea ice in the western part of the region would likely drift into the polynya area if not for the ice tongue blocking

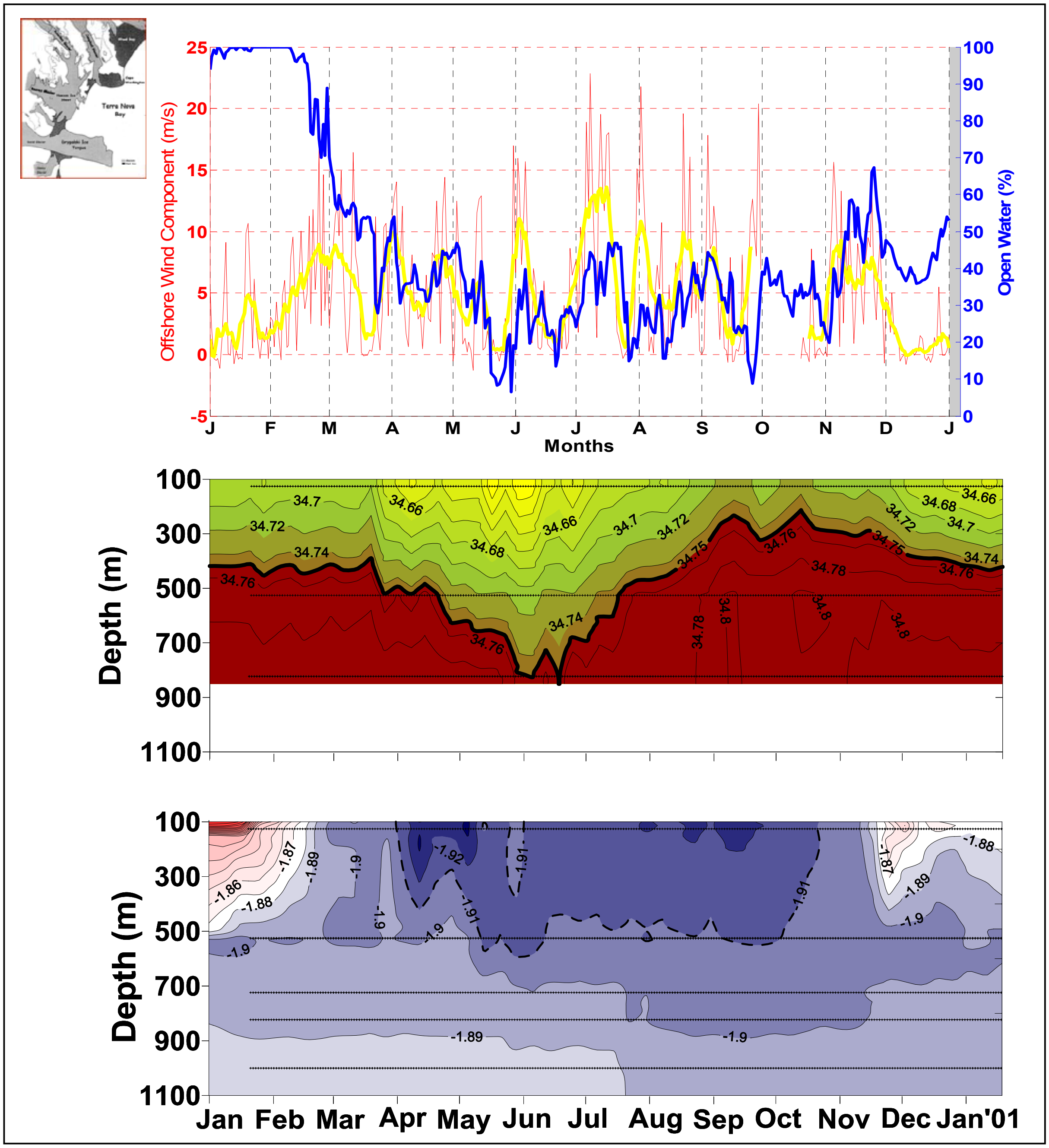

Figure 5.4: Climatology of the Terra Nova Bay polynya area, as measured from the nearby Italian research station and their mooring. Winter brings intermittent high winds off of the continent, and open water area responds accordingly. The second panel shows salinity (p.s.u.) and the third panel shows the water temperature (°C) throughout the year. Reproduced from Budillon et al. [2009].

the area, effectively protecting the bay and allowing the polynya and wind forcing processes to operate independently from the regional ice drift [Kurtz and Bromwich, 1983].

5.1.1.1 Ice growth rates and bottom water formation

Estimated production of HSSW ranges from 0.3 to 1.2 Sv, with the uncertainty attributed to rates of ice production Buffoni et al. [2002]. Residence time for deep water formed in the Ross Sea is typically short, on the order of 2-4 years [Budillon et al., 2009], so the atmospheric forcing of the Ross Sea ice production is quickly encoded in the deep water. An increase in offshore wind is correlated with an increase in the salinity of the surface layer [Budillon et al., 2009], which makes sense in the context of ice formation extruding brine which forms the water mass. Circumpolar deep water from the Antarctic Circumpolar Current is the major source of warm water entering the Ross Sea area [Locarnini, 1994].

Ice production rate is a function of the net surface heat flux, and can be expressed as

$$P_i = \frac{Q_T}{L_i \rho_i} \tag{5.1}$$

where Q_T is the net heat flux (W/m^2), L_i is the latent heat of freezing (J/kg), rho_i is the density of ice, and P_i is the ice growth rate in units of [m/s]. Salt release is directly related to this,

$$P_s = \rho_i \bar{P}_i A_p (S_w - S_i) \tag{5.2}$$

This form takes the mean ice growth rate across the polynya times the area (A_p), multiplied by the volume of ice growth (P_i) and the density of the ice. This could also be accomplished in a spatial integral form for higher accuracy. The last term is the difference in salinity between the ocean water and the formed ice, typically $S_i = 0.31 S_W$ for frazil ice [Martin, 1981]. HSSW formation is directly proportional to the salt release from the freezing ice,

$$P_{HSSW} = \frac{P_s}{\rho_{HSSW}(S_{HSSW} - S_{SW}) \times 10^{-3}} \tag{5.3}$$

The values for the density and salinities of the HSSW and Warm Core water are listed in Fusco et al. [2009]. This relationship allows the heat fluxes across the surface to be directly converted to the rate of formation of high salinity shelf water.

Because the HSSW and ABW move slowly, these formation rates are typically considered as annual averages. High winter rates of ice formation are offset by near-zero rates of ice formation in the summer. Changing winter conditions (i.e. if there are substantial changes to the wind regime off the continent) could then tip the balance towards very little ice formation and therefore slowing the HSSW formation.

Water transport within the polynya is certainly effected by the high winds at the surface. The prevailing currents are north-eastward, consistent with Ekman transport – wind drag on the surface produced subsurface currents of exponentially decreasing strength and increasing turning angle to the left of the wind forcing in the southern hemisphere [Buffoni et al., 2002].

5.1.1.2 Wind profiles

The wind regime at Terra Nova Bay is remarkable: during winter conditions, wind direction is consistently offshore and the speeds variable but reliably high. There is very little directional variance in winds channeled though the local topography into the bay [Bromwich, 1989, 1990]. The distribution of wind within the polynya is characterized by a central jet down the middle, with decreasing wind speeds closer to the edge of the polynya area. Off-shore wind speeds measured during the 2012 campaign [Cassano et al., 2016] during one expansion-phase flight are shown in Figure 5.5. In the middle of the polynya, winds as high as 32 m/s were measured at 100m above the water surface.

5.2 Field campaign

Figure 5.6 shows the daily passive microwave-derived ice concentration for the study area (NASA Team algorithm, Cavalieri et al. [1996b]). The Terra Nova Bay Polynya is the

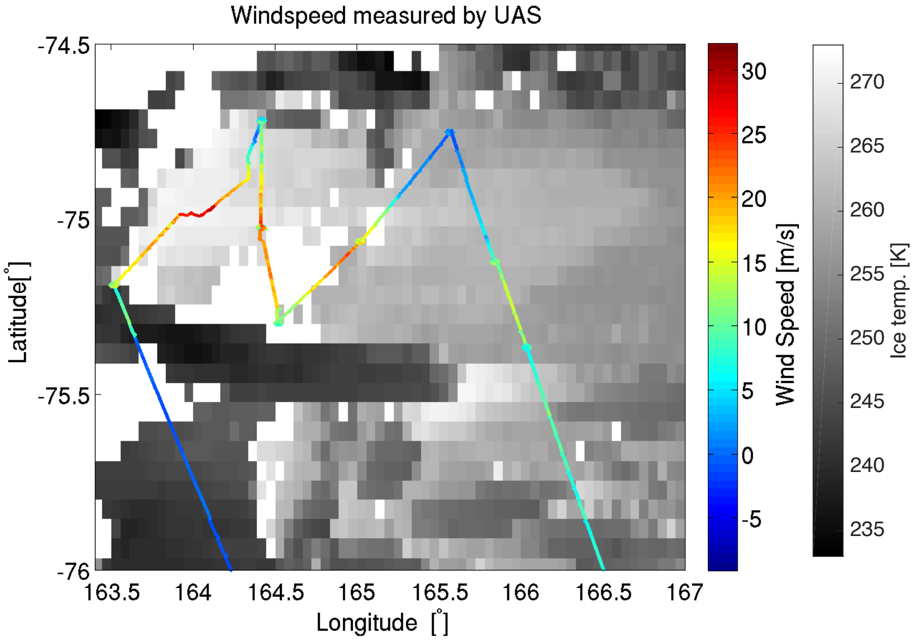

Figure 5.5: Off-shore wind speeds measured by the Aerosonde aircraft during the 2012 campaign. Winds exceeding 30 ms^{-1} were observed during the campaign during expansion-phase wind events. The background image is the MODIS ice surface temperature product for context in the region.

area midway up the coast on the west edge of the Ross Sea. It undergoes several periods of expansion (ice being blown out to sea) and closing (ice growth closing back in). One period of closing that corresponded to a fight in the TNB region was on 9/22-9/24.

There have been two field campaigns using Aerosonde unmanned aircraft in the Terra Nova Bay polynya region, one in 2009 [Cassano et al., 2010, Knuth et al., 2013] and one in 2012 [Cassano et al., 2016]. The 2009 campaign was during an anomalously stormy year and did not witness particularly representative conditions [Knuth and Cassano, 2011]. This analysis focuses on data from the 2012 campaign. The campaign consisted of six flight days over two weeks of operation in late winter (September). Science flight activity was concentrated in the polynya region shown in Figure , with one extra day flying over the Ross Sea Polynya. The airborne instruments included:

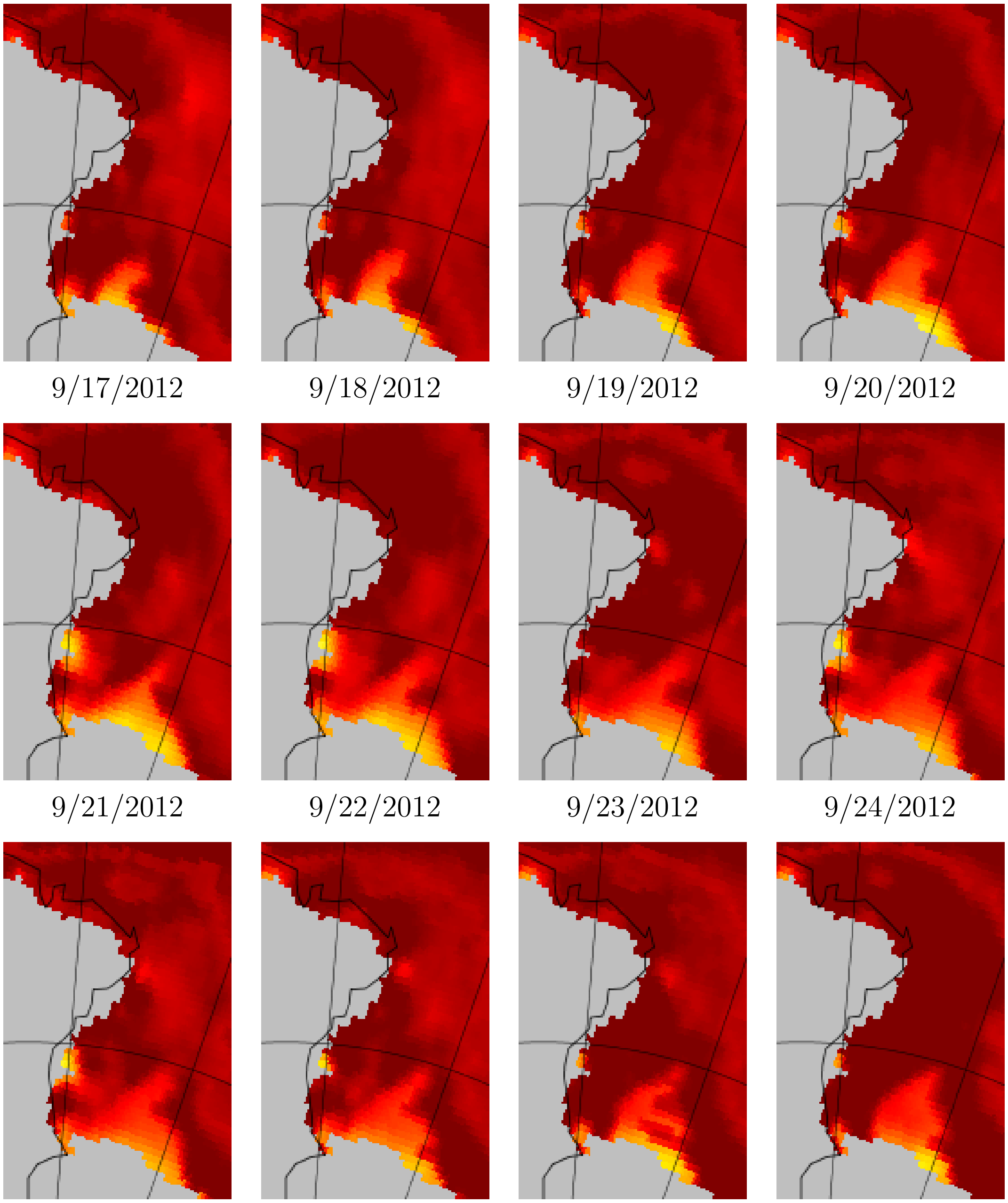

9/17/2012 9/18/2012 9/19/2012 9/20/2012

9/21/2012 9/22/2012 9/23/2012 9/24/2012

9/25/2012 9/26/2012 9/27/2012 9/28/2012

Figure 5.6: Daily ice concentration maps for the western Ross Sea region, with the Terra Nova Bay polynya being just north of the small ice tongue sticking out form the coast, highlighted in the first frame. The polynya goes through both expansion and closing phases during the campaign. Yellow indicates low ice concentration (approximately 40% at the lowest, due to mixed pixels). Terra Nova Bay is immediately south of the left of the location where the lat/lon grid lines intersect by the coast.

- In situ meteorological sensors. The aircraft carried instrumentation to measure local temperature, relative humidity, and air pressure.

- Wind vectors in the north and east directions were calculated by the aircraft autopilot system.

- Surface temperature. The Everest surface temperature instruments is an IR thermal sensor to measure skin temperatures of the ice and ocean surface below the aircraft. Two different models were flown on different aircraft during the campaign: each had a different minimum temperature.

- Camera. The aircraft carried a camera for capturing visible imagery, but it did not get much use because most of the flights were conducted overnight in order to schedule landing and take-off during daylight.

- CULPIS. The CULPIS instrument is a laser altimeter for detecting surface elevation. GPS and IMU noise on the instrument made it impossible to retrieve sea ice thickness from the CULPIS data.

5.3 Thickness from ice surface temperature

For thin ice, ice surface temperature is linearly related to the ice thickness. This relationship is typically considered valid for ice thicknesses of up to 1 meter [Drucker, 2003]. This method is described in Section 5.3.

The Aerosonde aircraft flown during the 2012 Terra Nova Bay campaign carried a downward-looking IR thermal sensor. This, as it turned out, was the more useful instrument for estimating ice thickness. Figure 5.7 shows the surface temperature measurements from the campaign plotted with interpolated geographic points in the MODIS Ice Surface Temperature product image captured during the flight. The two correspond well over open water and at the time when the image was taken, but there is some time lag between the image and the UAS measurements that is significant later in the flight as a difference between the two surface temperature measurements.

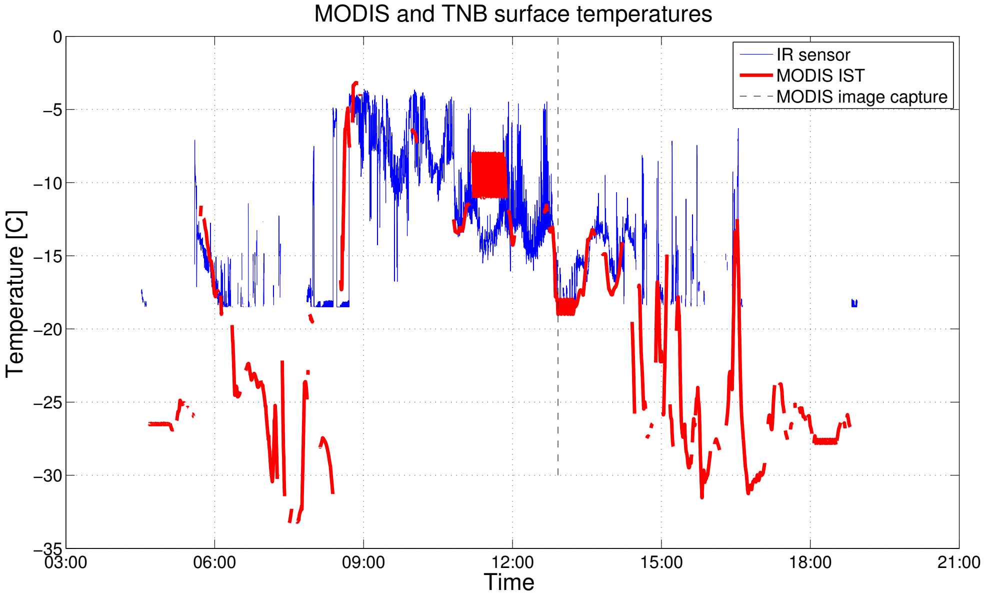

Figure 5.7: Surface temperature measurements for one flight in Terra Nova Bay (blue) and the interpolated MODIS surface temperature remote sensing product along the flight track (red). Right around the time of MODIS image capture, designated by the vertical dashed line, the two temperature measurements agree very well.

With knowledge of the boundary layer meteorological state, the surface conditions can be used to estimate the ice depth and the fluxes across the ice-atmosphere/ocean-atmosphere boundary. Similar methods have been used in a number of locations, but local meteorological parameters are often the largest sources of uncertainty [Mäkynen et al., 2013].

5.3.1 Measured data

The Aerosonde system measured the necessary meteorological conditions at 100m. The equations were formulated for a 10 meter height, so the coupling coefficients may need to be adjusted slightly based on theoretical ABL wind and temperature profiles.

The parameters measured by the aircraft that were used here were: (1) air temperature, (2) relative humidity, (3) pressure, (4) surface temperature, and (5) wind speed. Additionally, latitude, longitude, and aircraft altitude were recorded from the onboard GPS.

The surface temperatures needed some correction to make sense - the highest surface temperature recorded on the 9/25 flight was -3.9°C , over an area that was almost certainly open water. These observations came from an IR temperature instrument with post-processing that did not account for surface emissivity or atmospheric emission. The substantial wave action and wind likely generated a lot of sea spray and suspended moisture, which would likely be supercooled and could influence the IR thermal temperature measured from 100m altitude. This idea is supported by the surface temperature measurements getting cooler the higher up the aircraft flew, even when it was circling over the same location. Surface temperatures were corrected by a uniform addition of 1.9°C in order to get the open ocean temperatures to the correct value (freezing point, determined using TNB climatology [Budillon et al., 2009] to be -1.9°C), and surface temperature measurements made from higher altitudes are omitted from the analysis. This factor was applied across the board to all measurements, on the theory that the 100m of boundary layer between the surface and the aircraft was cooling the IR signal. For the surface flux analysis, only the measurements from the aircraft flying level at 100m were used. Anything from higher altitudes was discarded because of the inconsistent surface temperature measurements.

Additionally, the thermal IR measurement system on one aircraft only worked as low as -18°C (before the temperature correction). Any data points measuring a surface temperature below -17.5°C were discarded because the instrument response seemed to be non-linear with temperature close to the low end saturation.

5.3.2 Boundary layer wind estimation

Bulk formulations for sensible and latent heat fluxes assume that the wind speeds are measured at 10m above the ocean/ice surface. The UAS in the TNB campaign only flew as low as 100m above the surface, so the wind measurements and temperature measurements need to be adjusted to work with the existing coefficients.

Unfortunately there is little information available about wind fields between 100m and the surface over polynyas. The few studies that have used bulk formulations for estimating surface fluxes in polynyas have used reanalysis products for the meteorological parameters (e.g., Preußer et al. [2015]), which have surface-level wind estimates available. Reanalysis products are relatively coarsely gridded relative to a polynya's size however, and do not capture the small scale processes that result in the coastal polynyas.

For lack of other information, I extrapolated the wind field down to the surface using a logarithmic curve (based on Tennekes [1972]). Figure 5.8 shows this in panel two, with two vertical profiles of wind speeds from almost the same location extrapolated down to the surface. The curve is tuned so that the derivative with height matches that of the measurements (smoothed) for the profile between 100m and 150m AGL. The other panels show the air temperature, density, and pressure, linearly extrapolated to the surface with the slope tuned to match the gradient above where possible. The difference between the two profiles is shown in the black lines and the top x-axis on each panel.

While it is possible that low-level wind jets exist in this region, there is not sufficient information to establish when and where they might be. This approach offers a conservative estimate of the heat fluxes at the surface. Temperature at the surface is linearly extrapolated matching the slope (lapse rate) at the lower part of the nearby profiles. Typically the difference between the observed 100-meter and the estimated 10-meter air temperature with this approach is approximately 1 degree C. There may be surface effects or features in the wind patterns (like low-level jets) that change the temperature profile near the water/ice surface, but without additional observations there is no basis to assume additional features.

5.3.3 Upward fluxes

The method of using surface temperatures to estimate ice depth depends on the balance of heat flux through the boundary as described in Section 2.3.

Sensible heat flux was relatively easy to calculate, with all parameters measured di-

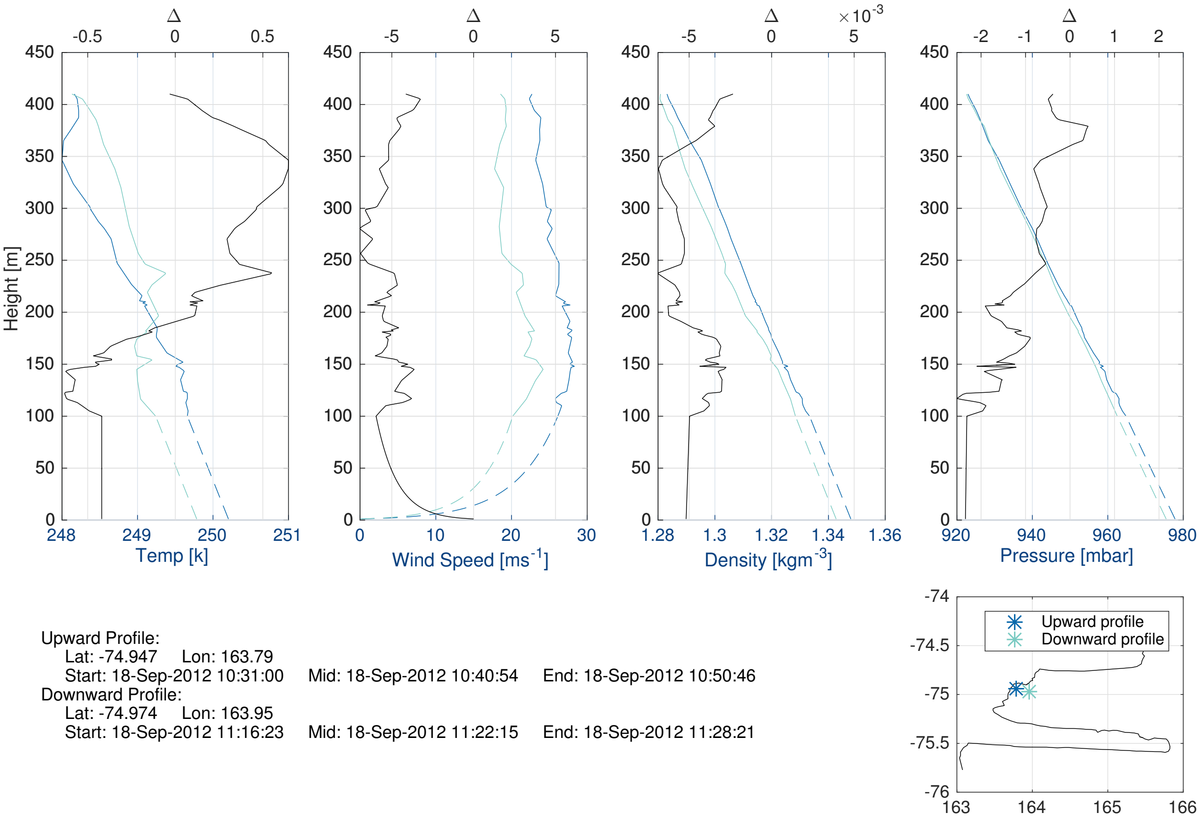

Upward Profile:
Lat: -74.947 Lon: 163.79
Start: 18-Sep-2012 10:31:00 Mid: 18-Sep-2012 10:40:54 End: 18-Sep-2012 10:50:46
Downward Profile:
Lat: -74.974 Lon: 163.95
Start: 18-Sep-2012 11:16:23 Mid: 18-Sep-2012 11:22:15 End: 18-Sep-2012 11:28:21

Figure 5.8: Air temperature, wind speed, density, and pressure profiles for a pair of nearby profile flights. The dotted lines below 100m are the extrapolated profiles. The lower right panel shows where in the TNB polynya these flight profiles were conducted. The black lines (and the top x-axis) show the difference between the two profiles conducted at each site.

rectly:

$$F_s = \rho_{air} c_{pair} C_{bulk} S_w (T_{air} - T_{surf}) \tag{5.4}$$

The density of air at the surface is a function of pressure and temperature and was taken to be 1.435 kgm^{-3}. Heat capacity of air (c_{pair}) is a standard value, also a function of temperature, and for this analysis 1006.1 was used. The C_{bulk} constant is a measure of the efficiency of heat transfer between ocean or ice and the air, and was given as 0.00175 in Weeks [2010]. This efficiency coefficient is the part of the calculation where the 100 meter versus 10 meter measurement height likely makes the most difference. This value will be checked against more sources before this effort goes to publication.The remaining parameters are measured, wind speed, air temperature, and surface temperature.

Latent heat was a little more involved to calculate, as it is a function of the specific humidity which was not directly measured. In order to relate the relative humidity to specific humidity, a function of temperature was required to calculate the saturation vapor pressure of water, which is then converted to the actual vapor pressure of water and then the specific humidity, as described in the following equations:

$$VP_{h2o} = \underbrace{RH/100}_{\text{RH in decimal}} \times 6.11 \times 10^{\left(\frac{7.5T_a}{T_a+273.15}\right)} \tag{5.5}$$

where T_a is the air temperature in °C and RH is a percentage (0-100).

$$q_a = \frac{6.22 * VP_{h2o}}{P_{air}} \tag{5.6}$$

This equation for specific humidity (q_a) is a slightly simplified form described as appropriate for polar regions [Weeks, 2010], but this will also be revisited before publication. At the surface (0m altitude) these same equations apply except that the relative humidity is assumed to be 100% and the pressure is the atmospheric air pressure at that point, 1013 mbar. The specific humidity is then just a function of the surface temperature. Over ice, there is a slightly different form for the function to find the vapor pressure (from the WHOI website at http://www.whoi.edu/page.do?pid=30578, a published form of this has not yet been found.)

$$VP_{h2o,ice} = 1 \times 10^{\frac{0.7859+0.03477.*T_i^K}{1.0+0.00412.*T_i^K}+0.00422*T_i^K}; \tag{5.7}$$

where T_i^K is the ice surface temperature in Kelvin.

Once the relative humidity measurements (both air, q_a and surface, q_s) are converted to specific humidity, the latent heat can be calculated.

$$F_L = \rho_{air} L(T_a) C_{bulk} S_w (q_a - q_s) \tag{5.8}$$

The latent heat associated with the evaporation of water is a function of temperature, and is given in Weeks [2010] to be

$$L(T_a) = 2.5 \times 10^6 - 2.274 \times 10^3 T_a \tag{5.9}$$

where T_a is in °C .

The next component of the heat budget for the surface is the net long wave radiation. The surface emits approximately according to blackbody radiation, where the integrated long wave emission is

$$F_{LW\uparrow} = \varepsilon_i \sigma (T_s^k)^4 \tag{5.10}$$

where ε_i is the emissivity of the surface (approximately 0.9 in the long wave for ice and slightly lower for water [Comiso et al., 1997]), and σ is the Stefan-Boltzmann constant. This is moderated slightly by downwelling long wave radiation from the atmosphere, which is approximated by

$$F_{LW\downarrow} = \sigma * (T_a^K)^4 \times (0.746 + 0.0066 * VP_{h2o}) * (1 + 0.26 * CF) \tag{5.11}$$

where CF is cloud fraction [Weeks, 2010]. Cloudiness could be estimated from satellite instruments (optical for flights in daylight or thermal IR for night flights). For the analysis as presented, the cloud fraction is assumed to be a constant 0.1 as flight days were selected to coincide with minimal cloud cover whenever possible. The total long wave radiation is then

$$F_{LW} = F_{LW\downarrow} + F_{LW\uparrow} \tag{5.12}$$

The last component of the air-surface fluxes is shortwave radiation. There is no good measure of shortwave radiation during this study, but the flights were all conducted at night when there was no incoming solar. The aircraft needed daylight for takeoff and landing, and in order to do both of these actions during the day on an 18 hour flight, the time over TNB needed to be at night. During the early part of the campaign, there were roughly 8 hours of daylight per day, and by the end of the campaign days were approximately 13 hours. Data collection in Terra Nova Bay was in the dark through the whole period.

Combining these terms, the net upward flux out of the surface is measured. This is balanced by heat conduction through the ice:

$$F_{up} = F_S + F_L + F_{LW} = F_{ice} \tag{5.13}$$

By assuming that the ocean-ice interface is at the freezing temperature, $T_o = -1.9°\text{C}$, and that the ice thermal conductivity is 2.03 $\text{Wm}^{-2}°\text{C}$, the thickness of the ice can be calculated from the heat flux through the ice. This assumes no snow cover, which given the extremely recent formation of the ice and the high winds, is a safe assumption for this particular analysis.

$$H_{ice} = k_{ice} \frac{T_s - T_o}{F_{ice}} \tag{5.14}$$

Given the climatology presented in figure 5.4, it is safe to assume that all ocean water in contact with the surface in the polynya during the winter is at the freezing point. At the ice-ocean interface, the conductive heat flux going up though the ice is balanced by ice formation, which relates growth rate to the heat flux by the density of ice and the latent heat of freezing through equation 5.1.

5.3.4 Results

Figure 5.9 shows some results from the surface-temperature based ice thickness calculation, plotted in color over the black and white image of MODIS Ice Surface Temperature data [Hall et al., 2004]. The thick black line indicates the approximate coastline. For reference, the dark tongue immediately south of the area of concentrated flight activity is the Drygalski Ice Tongue. Missing pixels (white) in the MODIS data are generally those filtered out due to cloud cover, though there are some issues with the cloud detection algorithm and some of those may be due to high amounts of suspended moisture in the air [Ovadnevaite et al., 2014, Norris et al., 2013]. White flight paths do not have sufficient data for calculating surface fluxes: either they were too high (500m rather than 100 m flight level) or the thermal surface temperature sensor did not work.

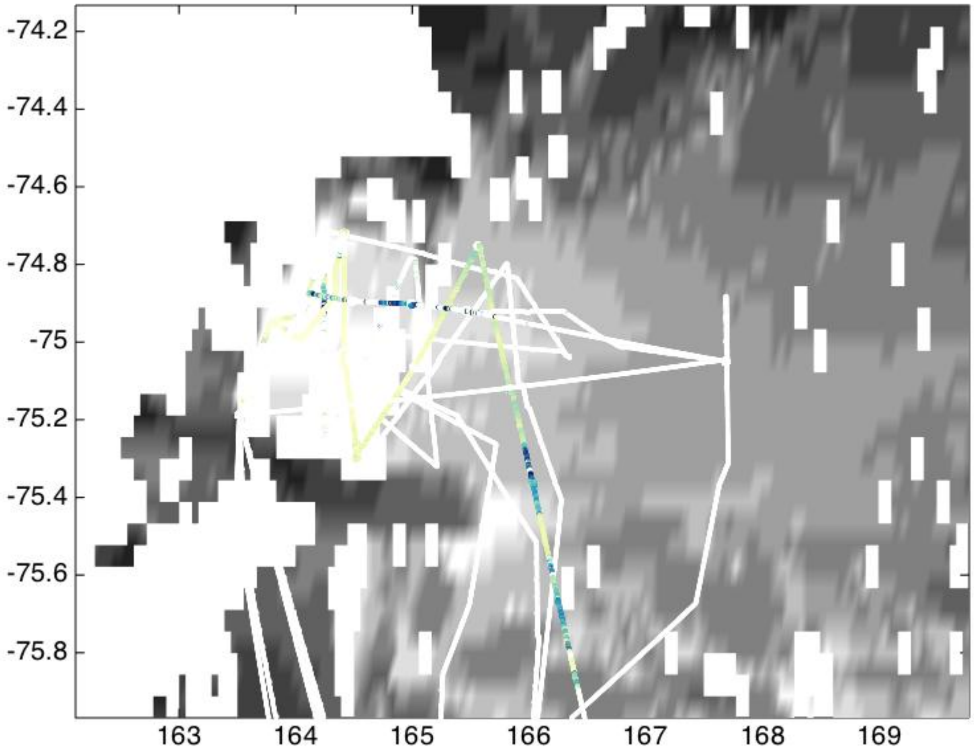

Figure 5.9: Ice thicknesses calculated using the surface temperature method are shown in the color with <10cm ice thickness in yellow and 1 meter thick ice in blue. The white flight paths did not have surface temperature measurements to sufficient accuracy for this method, typically because they were too high (≈ 500 m), or had instrument failure preventing surface temperature collection.

5.3.4.1 Calculated ice formation rates

Ice formation rates calculated from the flux analysis range from 15-18 cm/day in the center of the polynya to 0.5 cm/day along the north edge of the polynya. The highest rates of ice formation are in areas of open water and very thin ice, with lower ice growth rates further out where the ice gets thicker.

Figure 5.9 shows the ice thicknesses calculated along several tracks over the campaign. Crossed paths do not represent the same day or necessarily phase in polynya activity. Areas that had zero ice cover one day may have significantly more ice cover another day. The long, zig-zagged track is from the 22nd (closing phase) and shows gradual increases in ice thickness as the aircraft moves downstream over the polynya.

Figure 5.10 shows the track of the aircraft in the polynya in the top panel. The lower panels have the same longitudes on the x-axis.The flight path moved downstream across over the ice and then back, resulting in the multiple passes and the small amount of variability in the ice growth rate estimate. High growth rates at the upstream end of the polynya correspond to the highest winds, where the turbulent fluxes are highest as well. Out beyond the end of the polynya the calculated ice growth rates turn negative, because the ice thickness is thicker than the thermal equilibrium given the atmospheric forcing. It does not mean that the ice is melting, rather that it is just not growing. This is likely because of highly deformed thick ice that got cold during the previous days when air temperatures were cooler and has yet to warm up to a slightly warmer surface temperature.

5.3.4.2 Dependence on wind speed

Figure 5.11 plots the relationship between the ice thickness calculated by the surface temperature method and the corresponding 100m wind speed. Ice corresponding to lower wind speeds is likely to be older and therefore thicker. There is a similar prevalence of deformed, thick ice (0.6 to 1.2 m) over a wide band of wind speeds (5 to 15 m/s) which may correspond to areas that get sufficient wind forcing to deform ice, but not so much as to clear the ice out of the area. The relationship is also a function of the areas in which data was collected. The flight path zig-zagged across the polynya area. Once the aircraft was far enough out to be finding deformed ice, winds have diffused slightly and the maximum windspeed along this transect was 15 m/s.

5.4 Other observations of ice growth rates

Hirano et al. [2016] estimated the ice production in the coastal polynya near Barrow, Alaska, which is a hybrid latent and sensible heat polynya just southwest of the the end of

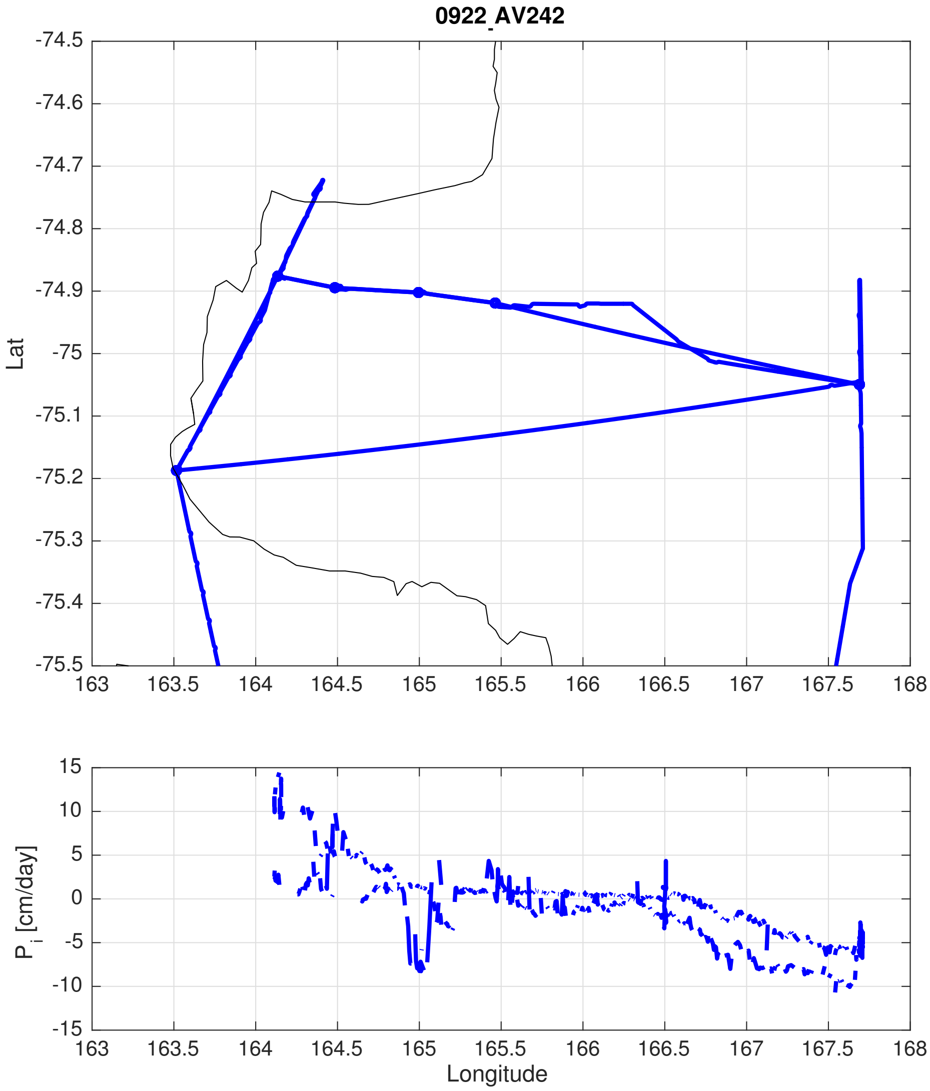

Figure 5.10: Ice growth rates calculated using the surface temperature method and corresponding ice formation rates. The top panel shows the flight path for the day: negative growth rates are locations where the ice is thicker (likely because of deformation) than the thermodynamic equilibrium for the amount of heat flux from the surface.

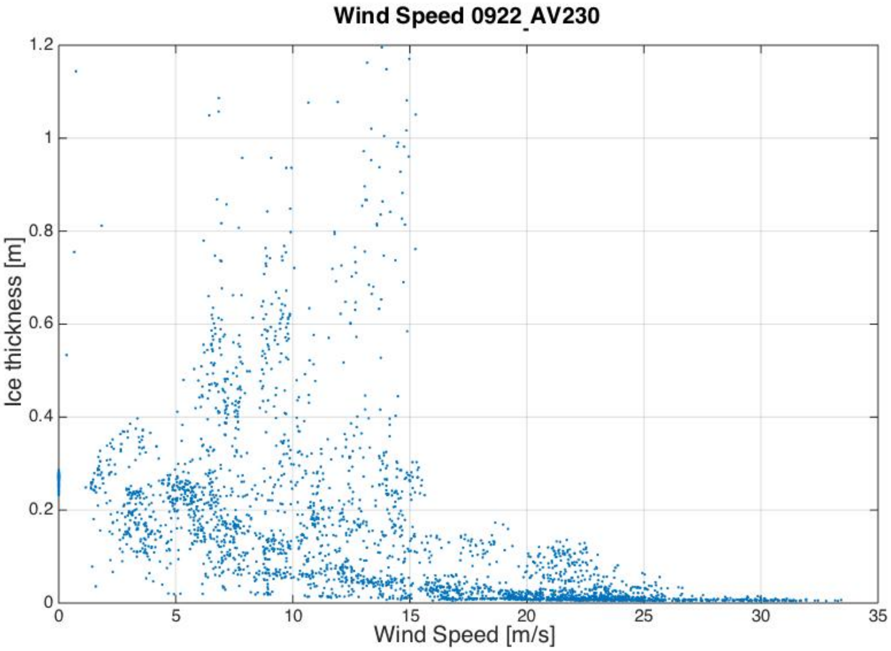

Figure 5.11: Ice thicknesses compared to the local wind speed measurement. Thicker ice only exists in areas that experience lower wind speeds.

Barrow canyon. It is triggered by wind events, at which point upwelling Atlantic water from below maintains the open polynya. When the polynya is in an ice growth phase though, ice growth rates were estimated as high as as 0.16 but more typically 0.05 -0.10 $\mathrm{m\,d^{-1}}$.

Growth rates in the Arctic under existing sea ice have been measured as high as 1.3 cm/day [Perovich et al., 2003] for a full day of growth under moderately thin (50cm) first-year ice during December. Figure 5.12 shows the distribution of ice growth rates from 14 ice mass balance buoy records [Perovich et al., 2014]. These are the instantaneous growth rates (difference in ice thickness between measurements 4 hours apart) and prone to some measurement noise. Few measured growth rates above 13 cm/day exist, and these are rare. Most ice growth occurs at rates below 5 cm/day.

Satellite-derived estimates of ice growth rates in six Antarctic coastal polynyas during winter 2011 and 2012 showed maximum ice growth rates only exceeded about 0.1 $\mathrm{m\,d^{-1}}$ on occasion [Tamura et al., 2016]. A different means of observation, using in situ measurements

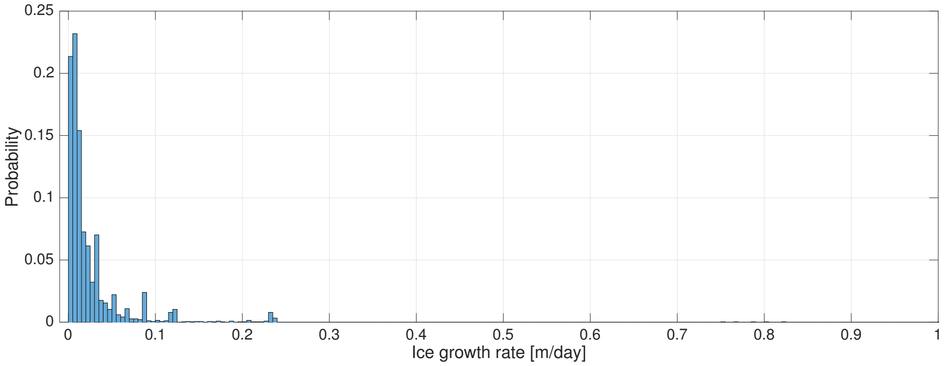

Figure 5.12: Distribution of ice growth rates measured by ice mass balance buoys. The small spike near 0.23 m/day comes from measurements within the first day of installation for a couple different buoys, and is probably more related to the instrument installation than natural ice growth.

from instruments mounted on Elephant seals, occasionally found growth rates as high as $0.16\ \mathrm{m\,d^{-1}}$ [Tamura et al., 2016].

5.5 Implications for Arctic ice formation

The fluxes dominating during late-season ice growth in the Arctic are the same processes at work during the closing phase for a coastal polynya. During the 2012 Terra Novay Bay campaign, there were two periods of the closing phase long enough in duration to show up on the daily satellite record during the weeks of the campaign: 9/22-9/24 and 9/26-9/28. The latter was after the last flights in Terra Nova Bay, but the first phase coincides with two flights on the 22nd. During these flights, sea ice growth rates were calculated to be as high as 15 cm/day, which is approximately the same as the highest growth rates reported by several other studies.

Given that heat fluxes decrease considerably with increasing ice thickness, for newly forming thin ice cover it is reasonable to expect similar growth rates as those observed in the polynya closing phase in the Arctic if freeze-up is delayed slightly later into the season. Further, if sea ice has a practical upper limit to growth rates early in the season, a delay in freeze-up is more likely to result in thinner sea ice at the end of the winter season. There is in nature some upper limit to how fast sea ice can grow at the beginning of the season, where weather and the surface fluxes limit ice growth rates even in the cases of very thin ice. Ice that forms later cannot just ‘catch up’ in thickness to ice that formed slightly earlier, leaving late-forming ice with a thickness deficit that it will never fully recover from.

Chapter 6

Impact of delayed freeze-up

The reason for interest in the evolution of the upper ocean prior to the onset of freeze up is in large part to determine how late in the season freeze-up will initiate. This is useful on its own from an operational perspective, but may also play a significant role in determining the health of the ice pack in the future. The dramatic loss of multiyear ice is leading to an overall thinner ice pack [Maslanik et al., 2007], but will that trend continue as the first-year ice dominates the environment?

Delayed freeze-up is hypothesized to result in thinner ice pack, but ice growth rates are largely determined by the amount of ice present to insulate the warm ocean from the cold atmosphere. If ice is starting to grow later into the winter when the atmosphere is colder, the temperature differential between the ocean and atmosphere will be greater, suggesting that ice will grow faster than it would earlier in the season. Fast enough ice growth at the beginning of the season reduces the difference caused by the delay in onset of freeze-up. Higher rates of energy transfer between the ocean and the atmosphere result in faster growing ice, approaching the extremely high growth rates observed in Antarctic polynyas.

Thinner first-year ice is more prone to melt, and the overwinter motion of ice floes can precondition certain regions for anomalous melt the following summer [Hutchings and Rigor, 2012]. An upward looking SONAR site in the southern Beaufort Sea has identified a slight (not statistically significant) trend towards thinner first-year ice cover, of 0.07 m decade^{-1} [Melling et al., 2005]. Laxon et al. [2013] found that first year ice has thinned slightly in the autumn between the ICESat record (2003-2008) and the CryoSat-2 period (2010-2012), possibly due to freeze-up dates moving later in the season. Winter thicknesses did not change notably between these periods [Laxon et al., 2013]. This distinction suggests that first-year ice growth over the winter may not be as sensitive to freeze-up dates as suspected.

Ice drift speed in the Arctic is increasing at rates of approximately 10% per decade, with substantial spatial variability and some periods exceeding 40% per decade. These trends cannot be fully attributed to changes in wind forcing, and in many areas sea ice thinning is likely to be the cause of this increase in drift velocities [Spreen et al., 2011]. Ice motion can influence ice thickness as well: significant on-shore drift of ice west of the Canadian Archipelago is credited with a large amount of the increase in sea ice volume between 2013 and 2014 in Kwok and Cunningham [2015]. Thinner ice cover is weaker and more prone to deformation, which results in increased ice volume, while thicker sea ice is stronger and therefore less prone to advection out of the Arctic basin [Spreen et al., 2016].

This section uses airborne ice thickness measurements to evaluate the role of delayed freeze-up on the end-of-season first-year ice thickness. This involves both inter-annual comparisons relating ice thicknesses to mean formation dates for a region, and intra-annual comparisons accounting for both the date of freeze-up and the atmospheric forcing over the course of the winter.

6.1 Theory

Heat fluxes at the atmosphere-ice interface drive the growth of sea ice. These are balanced by conductive fluxes through the ice pack. At the ice-ocean interface, oceanic heat fluxes source some of this heat, but mostly it comes from latent heat release of freezing ice at the boundary. Ice growth without snow cover is explained in Section 2.4.3.2.

Snow on sea ice is a controlling factor in how fast ice can grow by the effect is has on the overall thermal conductivity. The thermal conductivity of snow is much lower than that of ice, so even a relatively thin layer significantly slows the growth rate. As described in section 5.1.1.1, the growth rate of ice is proportional to the conductive flux through the ice and snow, which is limited by the thermal conductivity of the combined system.

6.1.1 Thermal conductivity of sea ice and snow

Measurements of snow conductivity during the SHEBA campaign showed that thermal conductivity of snow is highly variable based on the metamorphic state of the snow and the density, but that k_s values averaged 0.14 $Wm^{-1}K^{-1}$ for the bulk snowpack with typical snow stratigraphy. This consisted of buried depth hoar with extremely low thermal conductivity $k_s = 0.04$ to 0.16, buried underneath hard wind slab with $k_s = 0.50$. This is in turn underneath a layer of more recent snow that has not been subjected to either the extreme thermal gradients of the early season (forming the ubiquitous depth hoar) or exposure to significant wind (forming wind slab from highly deformed snow crystals); this layer had a lower thermal conductivity at $k_s = 0.078$. The snow pack was occasionally capped with another smaller layer of wind slab, which exhibited properties similar to the lower layer of slab [Sturm, 2002].

For comparison, thermal conductivity of sea ice is approximately 2.24 $Wm^{-1}K{-1}$ [Drucker, 2003]. The result is that it takes very little snow to effectively insulate the ice, especially when thin snow packs are typically dominated by a layer of highly-metamorphized depth hoar capped with dense wind slab. Over young ice, even a thin snow layer makes a dramatic difference in the combined thermal conductivity and therefore the growth rate [Maykut, 1978].

6.1.2 Ice growth under snow

Ice growth under the snow is slowed by the insulative effects of the snow cover. Rather than being just the thermal conductivity of the ice that limits the growth rate, the thermal conductivity of the snow layer on top also contributes. The basic form of the growth rate equation does not change – it is still the heat flux leaving the ocean that forms ice through

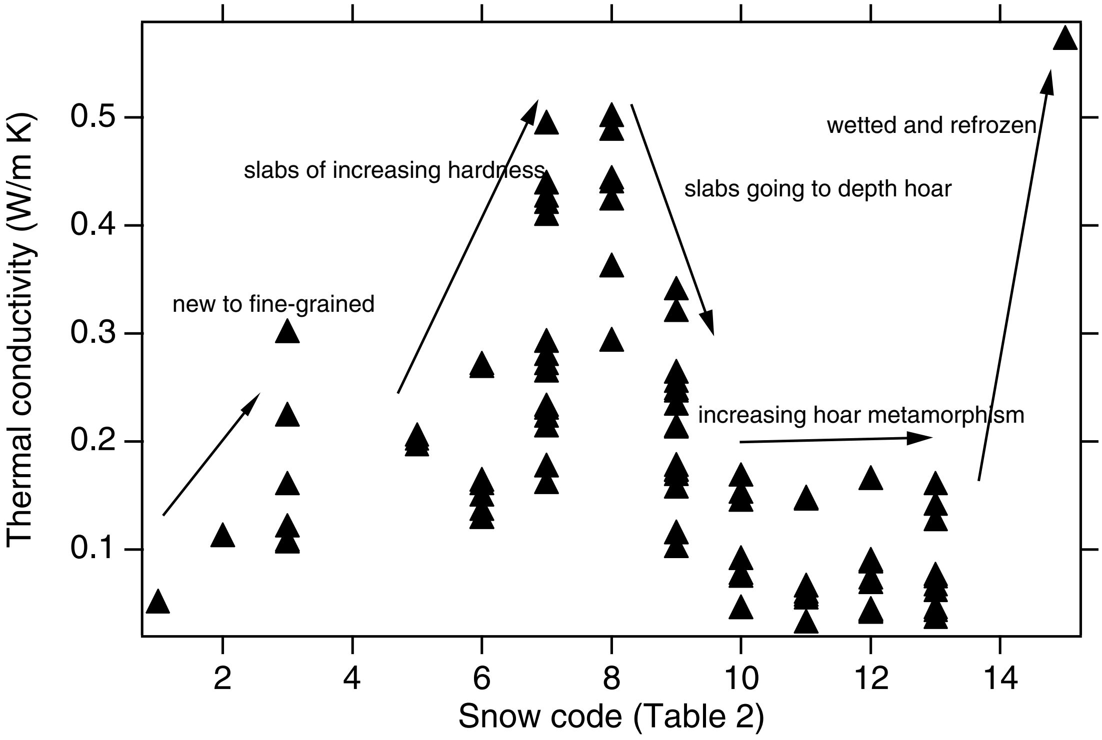

Figure 6.1: Thermal conductivity of snow, reproduced from Sturm [2002]. New, unconsolidated snow has low thermal conductivity. As wind slab hardness increases, the thermal conductivity increases with the higher density and consolidation of the snow grains. Increasing degrees of hoar metamorphism have little effect on the thermal conductivity, as it is consistently low for this snow type. Wet and refrozen snow found near the ice interface often had a much higher thermal conductivity, though still much lower than that of pure ice (2.24 $Wm^{-1}K{-}1$).

the latent heat of freezing.

$$P_i(snow \neq 0) = \frac{Q_\uparrow}{L_i \rho_i} \tag{6.1}$$

The difference between this and equation 5.1 is that the heat flux from the ocean to the atmosphere is severely limited by the insulating snow cover.

$$Q_\uparrow = \frac{k_i k_s}{k_i H_s + k_s H_i}(T_f - T_o) \tag{6.2}$$

It is this limited surface heat flux that makes snow cover on sea ice so important. If ice forming later in the season receives less snow fall (the bulk of solid precipitation in the Arctic presently comes in fall and early winter), there will be less snow cover insulating the ice and it will grow faster. The question then is whether the seasonal snow fall timing will shift with the later freeze-up of the ice.

6.1.3 Change in snow on sea ice

Climatology says that snow primarily falls early in the fall and winter season, with the bulk of solid precipitation occurring in August through October [Cullather et al., 2000]. This is illustrated in Figure 6.2, where different sources of precipitation data all show significantly higher rates in late-summer and fall and lower in the winter. Whether this is shifting significantly with the delay in ice formation is still being debated. Models [Hezel et al., 2012] suggest that there will be a substantial delay by the end of the century. From the system perspective, the outcome is uncertain: with later freeze-up in the Arctic there will be a longer period with moisture available for the atmosphere to draw from, but there is less energy in the atmosphere with which to evaporate water.

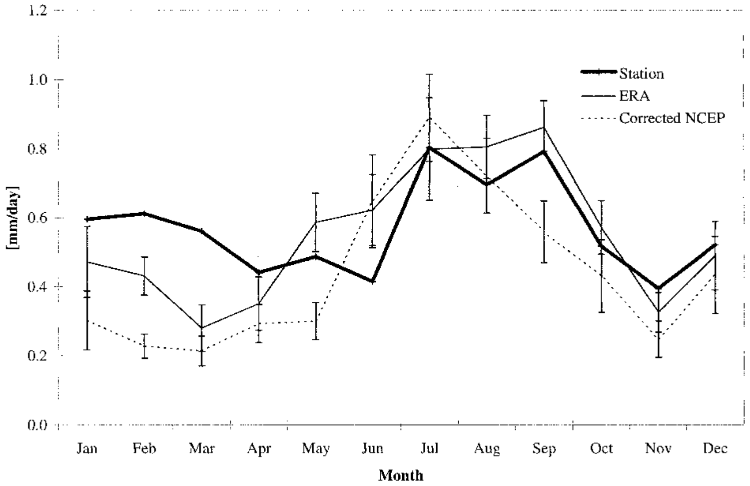

Figure 6.2: Annual mean precipitation from station measurements, ERA and NCEP reanlysis data. Peak precipitation occurs in the months when there is open water in the Arctic from which to draw moisture. Figure reprinted from Cullather et al. [2000].

The mechanism for this phenomenon is linked to ice growth - snow later in the winter season is limited by the small amount of moisture in the cold atmosphere, as there are few sources of moisture in the frozen Arctic. In order for precipitation to fall, the atmosphere must be holding the moisture in the first place. The cold winter atmosphere has relatively little holding capacity, so it is difficult to bring in significant quantities of water vapor from lower latitudes where there is still exposed ocean. The result is a very dry climate though the winter months, with precipitation in the Arctic only really picking up mid-summer when melt ponds and eventually open ocean water come to dominate the surface.

Modeling studies through CMIP 5 have shown that snow depths on late-season (April) sea ice will decrease throughout the 21st century [Hezel et al., 2012] due to delayed start to snow accumulation. There is some seasonality to the signal, with increasing snow fall in the winter (likely due to the increasingly available moisture sources late into the freeze-up season) and decreasing snow fall in summer and fall (warmer temperatures make solid precipitation less likely). Models predicted significantly less snow on first year ice, which dominates the future Arctic. The models predict increasing precipitation, especially in the latter half of the 21st century, but that this predominantly falls in the form of rain earlier in the season rather than increased snowfall in the winter [Hezel et al., 2012].

Measurements of snow accumulation on first year sea ice in the most recent decade are similar to what they have been in the past [Warren and Rigor, 1999, Kwok and Cunningham, 2008]. This represents a change in the timing of both ice formation and snow fall (typically early fall, as precipitation is much more likely in proximity to the open ocean from which to draw moisture). Similar snowfall totals mean that the end-of-season ice thickness will be limited to a similar depth as in the past because it is the total insulative properties of the ice/snow column over the ocean that primarily governs ice growth. This has been shown by modeling, airborne observations including operation IceBridge, and IceSAT observations [Kwok and Rothrock, 2009]. These all have significant uncertainty however, and the theory requires the assumption though that summer heat is all removed prior to the onset of freeze-up. The fact that summer ice extents have slightly recovered after the all-time-low in 2012 suggest that the annual cycle to some extent resets with freeze up in the fall [Thomson et al., 2013]. Externally driven climate change is the main mechanism for the continued downward trend in ice extent and exceptional melt (2012) or exceptional ice transport (2007) events are noise around signal.

If not all of the heat from the summer mixed layer is released on the transition to freeze-up (i.e. stored in the NSTM), it may be released through the water column towards the ice and atmosphere slowly over the course of the winter. Rather than having zero heat flux across the ice-ocean boundary (in the cooled-ML model, water is at the freezing temperature and the only heat exchange is though the freezing of ice), the heat flux at this boundary could be on the order of 5-7 Wm^{-2} [Lytle and Ackley, 1996, Lewis et al., 2011], and thermodynamic ice growth would be accordingly smaller (on the order of 1.1 to 1.4m, down from 1.5 to 1.8 [Thomson et al., 2013]). This case, where the ice pack is ultimately thinner, would have lasting implications. First-year ice tends to have larger melt pond coverage fraction [Polashenski et al., 2012], which in turn is linked to higher albedo effects [Perovich and Polashenski, 2012], earlier ice retreat and a longer summer during which the ocean can absorb solar heating. If the process continues – warmer ocean storing some heat into the winter season, resulting in a thinner ice pack and feedback effects continuing into the following season – ice cover in the summer Arctic will disappear more quickly than it would otherwise.

6.2 Ice thickness observations

NASA's IceBridge campaign measures ice thickness at the end of the growth season over the past several years. If delayed onset of freeze-up is limiting the total ice growth over the summer, there should be two apparent features in the Ice Bridge data:

Ice thickness would vary substantially with latitude. Atmospheric forcing being equal, sea ice that formed later in the season would be on average thinner than ice that forms earlier in the season. IceBridge flight tracks over the sea ice measure freeboard (and therefore ice thickness) over distances of thousands of kilometers, capturing both multi- and first-year ice in the path. First-year ice growing at more southern latitudes typically starts to grow later in the fall, with ice edge generally advancing out from the central Arctic over the freeze-up season. Ice moves over the course of a winter season. Wind and ocean currents both move ice around, and two floes that first froze at very similar times in the fall could be different thicknesses based on snow accumulation and drift track through weather systems in the Arctic. Analysis will need to correct for ice motion and atmospheric forcing, but the date of freeze up for an ice parcel should then be to some degree correlated with the ice thickness.

Ice thickness would vary year-to-year depending on the length of the ice-free season. Winter seasons following particularly warm summers with lots of melt and long ice-free seasons should have thinner ice packs than in years with cooler summers and earlier freeze-up. Years with longer summers should then have generally thinner first-year ice cover than years with shorter ice-free seasons.

6.2.1 Approach

6.2.1.1 Ice thickness

The IceBridge thickness product [Kurtz et al., 2015] is calculated from the Airborne Topographic Mapper (ATM), which is a laser altimetry system used to measure the ice surface elevation. With highly accurate GPS and inertial measurement unit data, the range from the aircraft (typically flying at 1-2km) to the ice surface can be accurately converted to a surface elevation measurement. IceBridge data is available from the National Snow and Ice Data Center (shown in Figure 6.4).

As with any optical system, the surface height measured is that of snow cover on top of the sea ice. Uncertainty in snow cover is the dominant factor in uncertainty in ice thickness products, accounting for as much as 70% of the total uncertainty [Zygmuntowska et al., 2014]. To capture the total thickness of ice that is covered by snow, there are several parameters that must be either known or assumed in order to solve the buoyancy equation for ice thickness.

$$H_i = \underbrace{\frac{\rho_w}{(\rho_w - \rho_i)} F_i}_{\text{water displaced by ice weight}} + \underbrace{\frac{\bar{\rho_s}}{(\rho_w - \rho_i)} H_s}_{\text{water displaced by snow weight}} \tag{6.3}$$

Ice thickness (H_i) is the ice thickness, of which a small fraction sticks out above the water and is called the freeboard (F_i). If a laser is used to measured this height, it also measures the snow depth above the ice surface ($F_L = F_i + H_s$). Snow depth is typically assumed from climatology (specifically Warren and Rigor [1999]), but given the rapidly changing Arctic climate this may not be a successful approach for very long. The IceBridge mission carries a snow radar system [Farrell et al., 2012], with accuracy of approximately 5cm. The ice and water densities (ρ_i and ρ_w) can be well approximated without in situ measurements. Snow density in the Arctic is highly variable, with wind slabs reaching densities of nearly 0.35 g/cm^3 and depth hoar with density around 0.05 g/cm^3 [Sturm, 2002]. For the IceBridge thickness retrievals, a constant, intermediate snow density of 0.264 g/cm^3 is used [Farrell et al., 2012].

This method of freeboard retrieval requires a perfect knowledge of ocean surface height at the location of the measurement. An area of open water (i.e. lead) is used as a tie point, where the elevation is known to be at sea level. An open lead makes ice thickness measurements in the area more accurate, but in lieu of manually finding leads for correcting the ice thicknesses, an empirical offset is applied [Farrell et al., 2012]. Uncertainty in the thickness estimate grows with distance from leads.

6.2.1.2 Ice thickness distributions

The ice thickness distributions are calculated by selecting clusters of 100 ice thickness observations along the flight track of the IceBridge campaigns. For each set of 100 measurements, requiring standard deviations in latitude and longitude of less than 0.1 ensures that the measurements are actually from from the same area and do not include any gaps

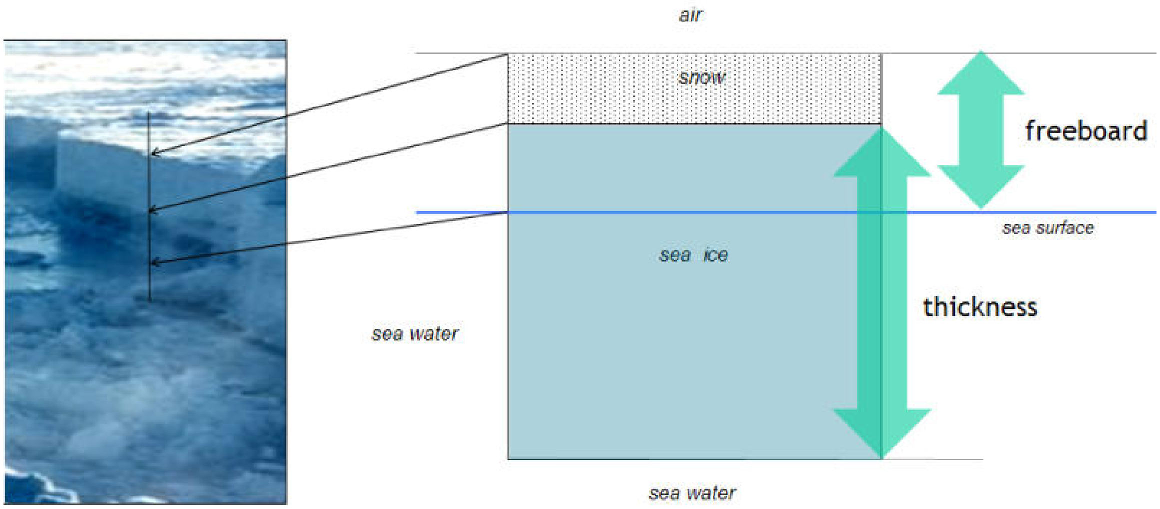

Figure 6.3: Illustration of snow on sea ice and the freeboard calculation. Snow cover is much less dense than the ice, so snow and some amount of ice floats above the water level while the bulk of the ice is below. Image copied from http://archive.news.softpedia.com/news/NASA-Study-Shows-039-Dramatic-039-Arctic-ice-Thinning-116091.shtml

in the dataset. Typically the standard deviation in both latitude and longitude for a set of measurements along a flight line is much smaller than that (order 0.01), as the samples are approximately 40m apart [Kurtz et al., 2015]. Cases where one collection ends and another starts result in values closer to 0.5 or 1, hence the threshold being set in the middle. Any sets of measurements exceeding that threshold are omitted from the analysis. This threshold was used only to automate the process of selecting the clusters of observations.

Once the set of measurements is determined, the ice thickness distribution is calculated by fitting a gamma distribution to the set of ice thickness measurements. The gamma distribution was chosen as the best fitting distribution for most of the ice thickness measurements: the asymmetrical distribution captures the steep increase to the peak of thermodynamic

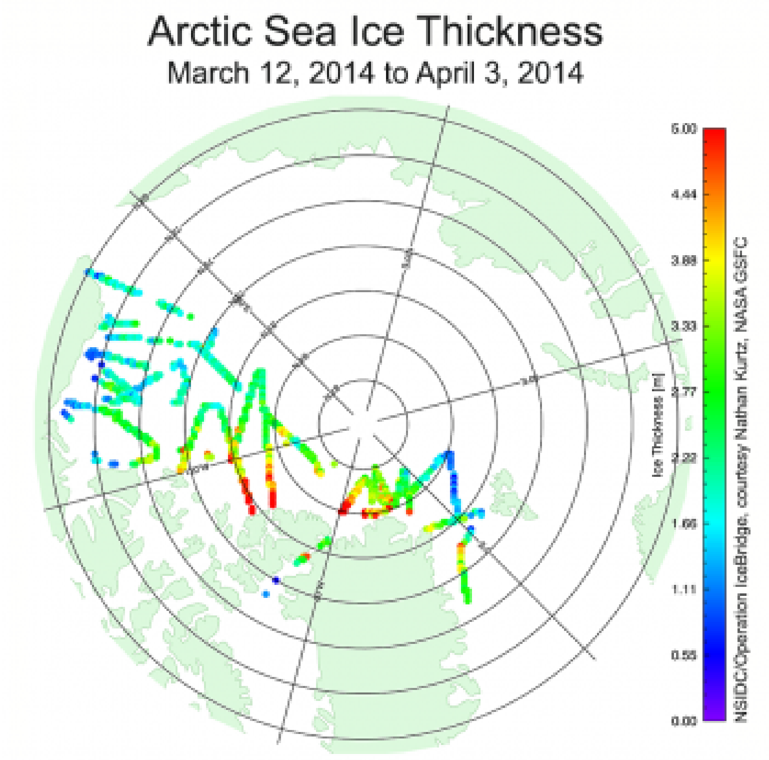

Figure 6.4: Ice thickness measured on the IceBridge campaign corresponding to fall 2013 freeze-up. There is significant variability between ice thicknesses in regions dominated by FYI (though most of the flights are mostly over older ice); whether this is strongly correlated with timing of freeze-up is to be determined. Reproduced from http://nsidc.org/arcticseaicenews/files/2014/06/Figure4a1.png.

growth and the long, thick tail of mechanically deformed ice thicker than the median ice thickness. Figure 6.5 is a histogram of the median ice thicknesses for each set of 100 original measurements over 2012-2014. The gamma distribution (red) fits far better than a normal distribution (shown in yellow). The median ice thickness of 1.67m is almost exactly matched by the gamma distribution (1.674m), but not by the normal distribution (1.75m).

6.2.1.3 First-year ice selection

In order to select first year ice, we used the Pathfinder Ice Age product [Tschudi and Fowler, 2013]. Each location of an IceBridge thickness measurement was checked against the ice age map. The ice age map was calculated by taking the ice age product [Tschudi et al.,

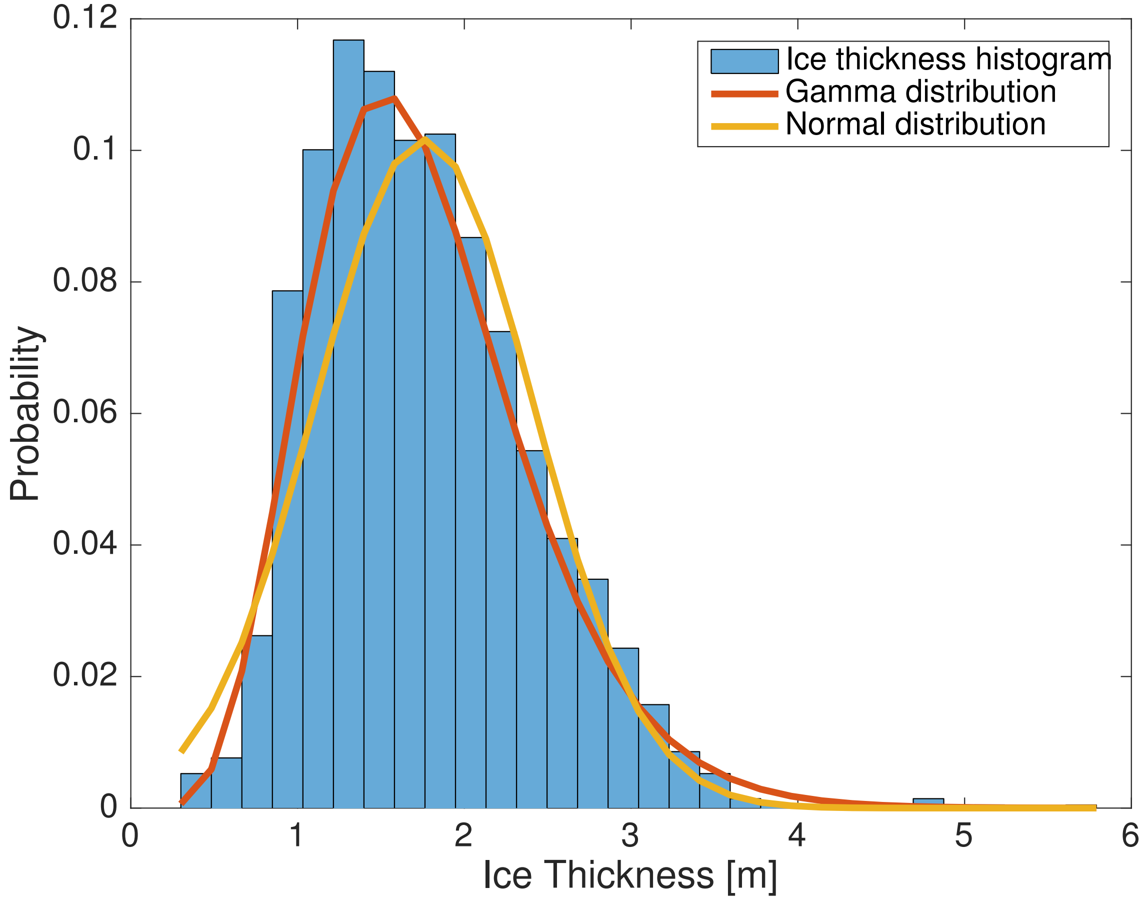

Figure 6.5: Ice thickness distribution for all local mean ice thickness measurements from 2012-2014

2015] for the weeks of the IceBridge campaign plus the week before and the week after. The ice age maps for these weeks were averaged together on a pixel-by-pixel basis. An average ice age of 1 year was used as the cutoff between first-year and multi-year ice, meaning that there was notable quantities of second year or older ice present in the grid cell for none of the 5 weeks surrounding the observations. This approach accounted for uncertainty in ice motion on a week-to-week scale, while maintaining a low likelihood of unintentionally including multiyear ice in the analysis. This approach does not guarantee that no multiyear floes will be included in the analysis, but it does minimize it in a computationally efficient manner with the available data products. Ice present at less than 15% concentration at the end of a summer melt season is not 'aged' in the ice age tracking system, so it is possible that the grid cells contain low concentrations of multi-year ice. It is also possible that there is error in the drift tracking algorithm used to find the ice age, and that some of these grid cells may be erroneously labeled as first-year ice.

6.2.1.4 Ice drift path

In order to link the ice thickness measurements at the end of the season to dates of ice formation, it is important to know where the ice came from. Ice motion tracks allow for backtracking from the end-of-season ice to the location where it formed.

Ice motion data is available from the NSIDC as the Polar Pathfinder ice motion dataset [Fowler et al., 2013]. On a daily timescale, it calculates the trajectory of ice parcels using a combination of feature tracking in passive microwave satellite products, assimilated drifting buoy tracks, and wind estimates from atmospheric reanalysis products. The combined product is shown in Figure 6.6, where gridded vectors indicate the mean daily motion of the ice pack. Initially this analysis was done using a prior version (2) of the dataset and weekly averaged ice motion gridded vectors, but the drift tracks were less accurate when compared to buoys.

In order to determine where the ice being measured in the IceBridge record drifted from and when it froze, the floe motion is traced back though time in the ice motion data products. If ice thickness is measured at point a on date w, the prior day's mean drift vector corresponding to that location can be subtracted off to get the floe's location the day before (date $d{-}1$, point a_{d-1}). This is then applied successively until the date when the ice formed is reached, creating a virtual, backwards-in-time ice tracking buoy. This analysis used the daily ice motion data, as that time scale has vectors for all points. The daily product likely misses small variations in ice motion and does not include estimates of convergence or divergence in a single grid cell, but it does offer some estimate of ice motion at all points in the Arctic sea ice pack each day (ice motion is not defined where there is no ice). This method keeps track of the floe locations, which can be used to interpolate through reanalysis data in space

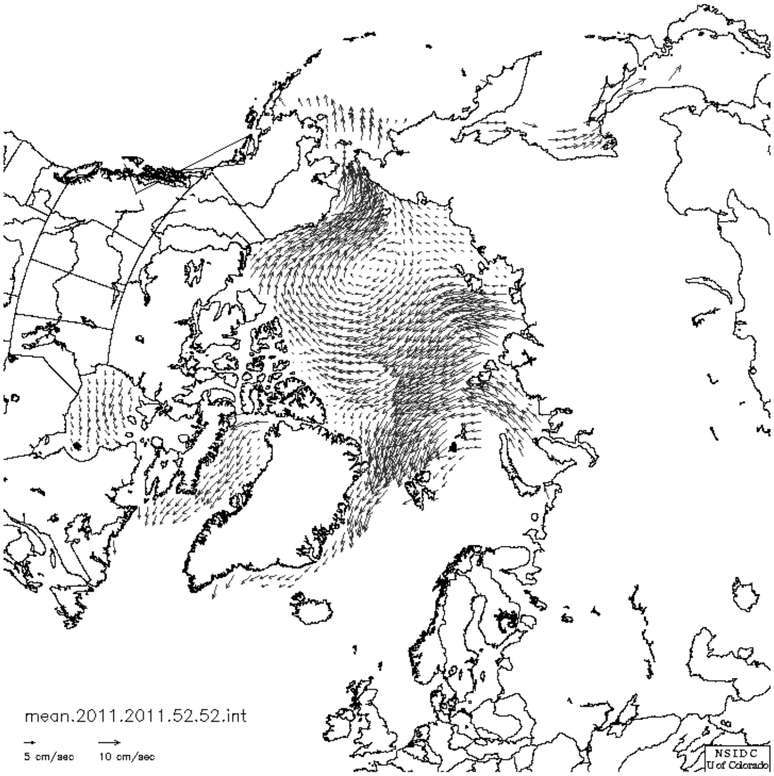

Figure 6.6: Image copied from the NSIDC hosted data, Fowler et al. [2013]. Weekly mean motion of the pack ice is shown with the gridded vectors.

and time to get some estimate of the conditions under which the ice grew.

The ice motion grid is referenced to the EASE-grid, so the first step in tracking ice motion was to convert EASE-grid referenced u- and v- vectors to north ($N^{\rightarrow}$) and east ($E^{\rightarrow}$) referenced vectors. The conversion factors are based on the grid cell longitude (λ).

$$N^{\rightarrow} = u \cos \lambda + v \sin \lambda \tag{6.4}$$

$$E^{\rightarrow} = u \sin \lambda + v \cos \lambda \tag{6.5}$$

From these corrected vectors, each ice parcel measured by the IceBridge flight can be tracked backwards along the drift trajectory in order to back out the seasonal drift of ice that ended at that location.

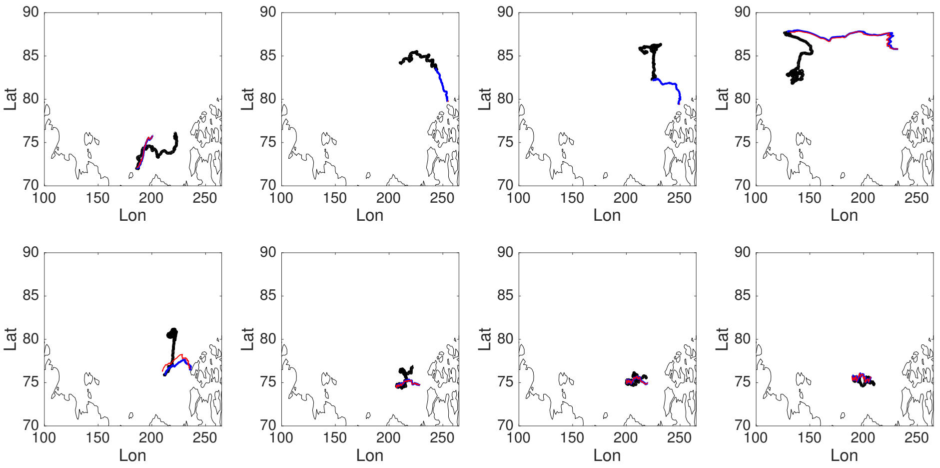

Figure 6.7: Ice drift paths estimated backwards (blue, starting with the end of season location and date and tracking back through the winter) and forwards (red, starting with the freeze-up location and time identified in the backwards track and followed forward in time to the end of season). Each panel contains one IMB track (black) and the estimated tracks. The location where the black and blue paths meet is the end-of-winter location for the IMB in question.

Figure 6.7 shows the testing for the ice drift tracking method. End-of-season locations from nine Ice Mass Balance buoys [Perovich et al., 2014] were used to start the backwards tracking algorithm, shown in blue. The beginning of season location was then used to start the tracking algorithm again, this time running forwards in time and shown in red.

The two major exceptions are the second and third buoys, which were deployed at relatively high latitudes. The tracking ended up with these two virtual buoys in the area of highly deformed ice near the Canadian Archipelago. When run forward from that location though, the virtual buoys hardly moved and did not retrace the path of the backwards-drifting virtual buoys. Fortunately, buoys at lower latitudes performed much better. The locations where there is significant first year ice are most similar to the lower latitude buoy locations.

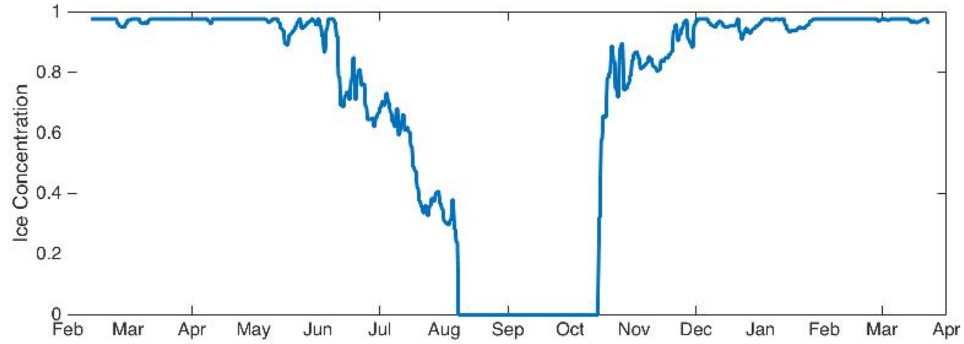

Figure 6.8: Ice concentration along the drift track of an ice parcel. The freeze-up date is selected as the time when the ice concentration goes above 15%, in this case mid-October.

6.2.1.5 Freeze up date

The freeze-up date corresponding to each measured ice thickness location is estimated by following the drift track backwards through the ice concentration data set, looking for the time when ice concentration drops below 15%, the typical threshold for "ice-free" in passive microwave retrievals. Ice concentration data comes from the SSMI-based product [Cavalieri et al., 1996a]. Ice concentration is sampled at each time step along the drift path, resulting in an ice concentration history of the parcel. Beyond this time, the drift track typically does not move as the ice motion product is not defined where there is no ice. Figure 6.8 shows a sample ice concentration history along the drift track of one sea ice parcel. The freeze-up date is selected as the first date (moving backwards in time) that the ice concentration dips below 15%. Because this approach is tracking ice floes as they move, advection of already-formed ice is theoretically not an issue. There were a few parcels that could not be traced back to a freeze up date in the preceding year. For these it was assumed that either the drift path was erroneous or the ice age classification was incorrect, and the parcels were omitted from further analysis.

6.2.1.6 Atmospheric forcing of thermodynamic growth

In order to compare two ice parcels that have formed at different dates in the season and drifted through different routes to the point where ice thickness is ultimately measured, some accounting for the different over-winter growth conditions is necessary.

With a record of positions and times interpolated from the ice motion data, the track (in latitude, longitude, and time) can be used to determine to some degree the meteorological conditions encountered by the drifting flow throughout the winter. Reanalysis products such as MERRA, NCEP, and ERA solve numerical weather prediction models at high time resolution while assimilating available global meteorological observations and any additional observations (i.e. sea ice concentration) that may help the analysis. The result estimates basic weather parameters at many different pressure levels in the atmosphere (including at the surface) at 3 or 6-hourly time steps all over the Arctic and worldwide [Rienecker et al., 2011, Kalnay et al., 1996].

Given that there are so few in situ observations in the Arctic to assimilate, the estimates are far from perfect. Analyses of the accuracy of the various reanalysis products over different timescales and parameters have concluded that all products have some error in the Arctic, but MERRA is one of the better performing ones [Lindsay et al., 2014]. For the accumulated growth of the sea ice though, the small, local errors should not be too much of a problem for the analysis. Precipitation is unfortunately the most unreliable but also perhaps the most important in modeling ice growth.

The atmospheric forcing data does little good without a method for translating it into ice thickness. A one-dimensional thermodynamic ice growth model can map atmospheric forcing into a theoretical ice thickness. This allows us to control for atmospheric forcing of sea ice growth over the course of the winter in the statistical analysis of the driving factors of first-year ice thinning.

It may be possible use satellite-based observations of sea ice temperature (i.e., Hall et al.

[2004]) to further constrain sea ice growth rates. The MODIS ice surface temperature product is not complete in coverage (clouds may obscure images), but if used to supplement the reanalysis products, incomplete coverage is not necessarily a problem. The One-dimensional Thermodynamic Ice Model approach estimates ice thickness from surface flux parameters derived from satellite observations [Wang et al., 2016]. This approach could supplement the HB balance analysis in estimating the seasonal growth, though it is not a direct integrator of the atmospheric forcing because the real ice growth is subject to other factors like oceanic heat flux.

6.2.1.7 1-D ice growth model

The primary purpose of the simple model used in this analysis is to integrate atmospheric forcing over the season while weighting the early season (when ice is thin) more than the later season, as with actual ice growth. Two models were used: a simple degree day model from Weeks [2010], Maykut [1986] and a slightly more complicated energy balance model based (roughly) on Wagner and Eisenman [2015].

At each time step, three equations determine the ice growth: surface fluxes relate the forcing conditions (air temperature, wind, etc) to the surface temperature of the ice, the resulting heat loss is balanced by ice growth at the bottom of the ice, and then the surface temperature is updated based on the current ice thickness. This is not a completely physically accurate model - it does not track heat within the ice or allow for melt (which is not a significant factor when looking at wintertime growth)- but it does capture the variability in sea ice growth better than the degree day model. I used this model as opposed to finding a more elaborate model in order to keep things simple. Since the one real requirement was to keep a metric of atmospheric forcing over the course of the winter, it did not seem necessary to use a particularly sophisticated model. Tracking heat content within the ice and the effect of insulating the ice cover are both normal components of sea ice growth models that are omitted here, because without snowfall forcing information the model would be introducing an extra source of error.

Surface Fluxes The forcing is applied as heat fluxes at the surface:

$$F(t) = F_{solar} + F_{netLW} + F_{turbulent} + F_{ocean} \tag{6.6}$$

F_{solar} is the downwelling shortwave, assumed to be 0 throughout the growth season. In March the sun comes up, so this assumption does not hold for the last few weeks, but at this point the sun angle is so low and the snow albedo so high that the difference is negligible [Persson, 2012].

F_{netLW} is the long wave radiation emitted by the ice minus the long wave radiation emitted by the atmosphere. This is calculated using the Stefan-Boltzmann equation, σT^4 where T is the radiating body temperature. The net upwelling longwave radiation is then the surface emitted radiation, σT_{surf}^4 minus the downwelling component of the radiation from the atmosphere, σT_{air}^4.

$F_{turbulent}$ is the sum of the turbulent sensible and latent heat flux. The latent heat flux is assumed to be near zero because of the sea ice preventing any evaporation from the ocean and the cold air temperatures [Weeks, 2010]. The turbulent heat flux is then the sensible heat flux, which is

$$F_{sensible} = -C * \rho_{air} * C_{p_{air}} * v_{wind} * (T_{air} - T_{surf}) \tag{6.7}$$

Finally, the oceanic heat flux is included in the surface fluxes. For tracking the atmospheric contribution to sea ice growth over the winter in the ice thickness analysis, the oceanic heat flux was set to zero.

Ice growth In this model, it is assumed that all heat flux off the surface of the ice is matched by ice growth at the base. In actual sea ice some of this heat is drawn from changing the ice temperature and from the melting or freezing of ice in brine pockets, but this must be parameterized in the thermal conduction equations. This effect is relatively small compared to the total seasonal growth [Bitz and Lipscomb, 1999]. The resulting equation is

$$\frac{dh_{ice}(t)}{dt} = \frac{F(t)}{L_f \rho_{ice}} \tag{6.8}$$

Where L_f is the latent heat of freezing ($3.34 \times 10^5\,\mathrm{J\,kg^{-1}}$) and ρ_{ice} is the density of sea ice ($900\,\mathrm{kg\,m^{-3}}$). For the purposes of this analysis, it is assumed that the total amount of heat that goes to changing the temperature of the ice rather than growing ice is small (less than 2 cm ice equivalent in calculating the thermal capacity of the ice) and that this approach will make it easier to compare modeled ice thicknesses with different atmospheric forcing.

Surface temperature Surface temperature is where the ice thickness feeds back into the surface flux calculation. The surface temperature is recalculated for each time step, with

$$T_{surf}(t) = T_f - (\frac{h(t)}{k_{ice}} + \frac{h_{snow}}{k_{snow}}) \times F(t) \tag{6.9}$$

k_{ice} and k_{snow} are the thermal diffusivity terms for ice ($2.28\,\mathrm{W\,m^{-1}\,K^{-1}}$, [Pringle et al., 2007]) and snow (approximately $0.2\,\mathrm{W\,m^{-1}\,K^{-1}}$) respectively. h_snow is the snow thickness (fixed), and $h(t)$ is the ice thickness as it grows over time.

The ice growth rate variable was limited in their range in order to tune the model to observed ice thicknesses. The ice growth rate limit was determined from the polynya growth analysis (Section 5.4) at 12 cm/day. This is consistent with growth rates measured in the Barrow polynya as well in [Hirano et al., 2016].

6.2.1.8 Degree-day model

There is an additional form of sea ice growth model that has been commonly used [Weeks, 2010] and can be fairly accurate in many cases. Given the uncertainty about snow cover and upwelling heat, it may be informative to try a simplified model that just considers the difference between the atmospheric surface temperature and the ocean temperature in order to calculate ice growth.

$$P_i^{DD} = c * \left(\int_0^t (T_f - T_a) dt \right)^n \tag{6.10}$$

Which when the coefficients (following Maykut [1978]) are used, reduces to

$$H^2 + (13.1H_s + 16.8)H = 12.9\Theta \tag{6.11}$$

where H is the ice thickness, H_s is snow depth assumed to be 15 cm [Webster et al., 2015] added over the season, and Θ is the degree days for the winter. Degree-days are the cumulative days with air temperatures below a reference temperature (the freezing temperature of sea water) weighted by the amount below the reference temperature. For example, 3 days at 5 degrees below freezing and 2 days at freezing would be 15 degree-days.

Still, the simplified form omits the parameters which are estimated with the least confidence and does a moderately reasonable job of estimating ice thickness [Weeks, 2010]. It is meant for first year ice growth (in that it assumes ice thickness begins at zero), which makes it applicable to this study.

6.2.1.9 Model comparison

The two models show high correlation, though the degree-day model does tend to result in thicker end-of-season ice cover than the heat balance model. Figure 6.9 illustrates this: the spread between the two is due to the degree-day model not taking into account variable wind speeds. The degree-day model is usually higher because the heat-balance model discounts colder temperatures later in the season when ice is thicker and growth slower, while the degree-day model weights cold temperatures equally throughout the season.

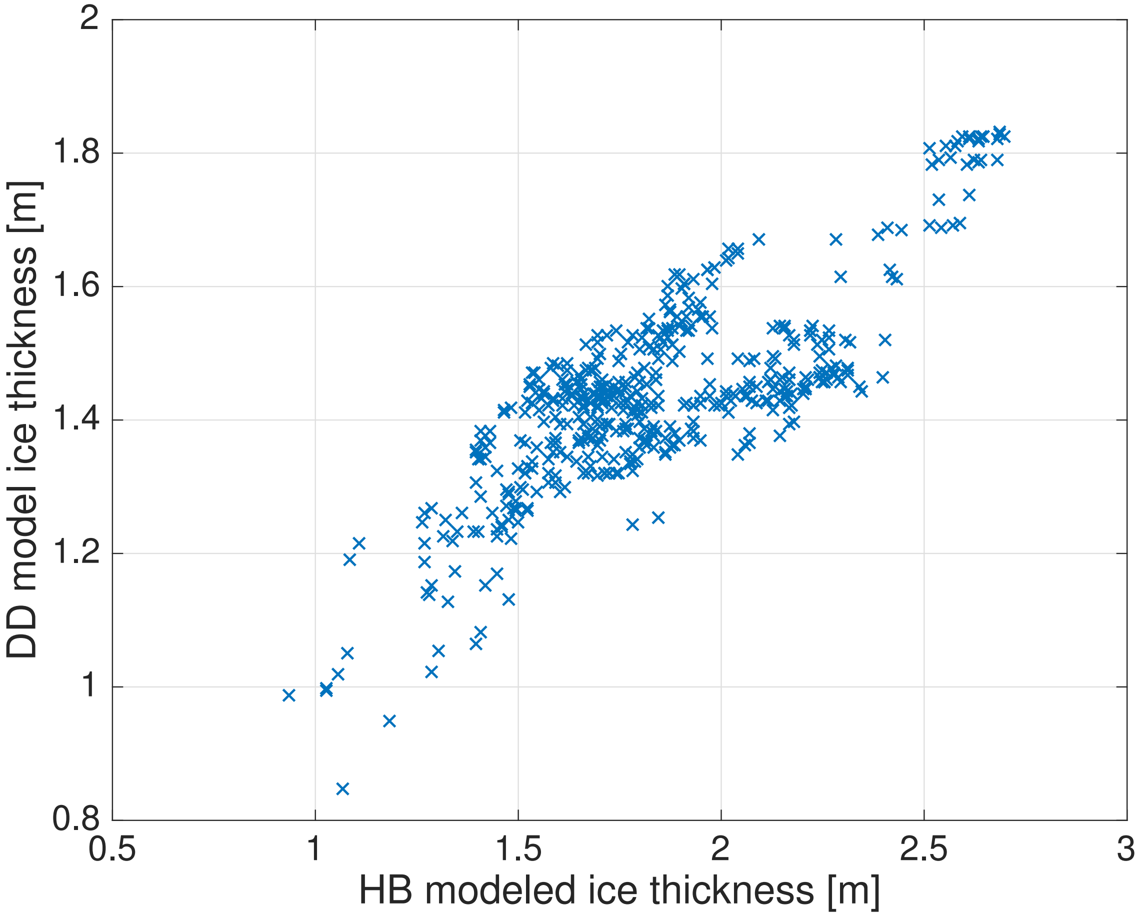

Figure 6.9: A comparison of the degree-day (DD) model and the heat balance (HB) model for integrating the atmospheric forcing over the season. Each point is one ice drift track as modeled using the two approaches.

6.2.2 Data set

Ultimately, for each cluster of sea ice thickness observations (100 samples along a flight track), the following parameters were retrieved. Each is listed with the data source and how it is retrieved.

(1) End of season:

   (a) Freeboard (histogram, fit gamma distribution, see Section 6.2.1.2): Freeboard measurements (snow plus ice) from the IceBridge campaigns are binned and then a gamma distribution is fit to the distribution. The histogram and the distribution parameters are saved.

   (b) Snow depth: similar to the freeboard measurements, snow depths retrieved from the IceBridge campaigns are binned into a histogram and then a gamma distribution is fit to the data. Both the bin values and the distribution parameters are saved.

   (c) Thickness: likewise, ice thicknesses retrieved from the IceBridge campaigns are binned into a histogram and then a gamma distribution is fit to the data. Both the bin values and the distribution parameters are saved.

   (d) Latitude: each set of 100 samples is checked for a minimal spread (standard deviation in latitude less than 0.1 degree) to make sure that the cluster of samples is along a single flight line with no breaks. Then the mean latitude for the cluster is calculated and saved.

   (e) Longitude: The mean longitude for the cluster is calculated and saved. Checking the Latitude spread is adequate to determine that the samples are all on the same flight track.

   (f) Date: The date of the fight is logged. Time precision is not required as the next steps have much coarser time resolution.

(2) Drift path

   (a) Latitude (time series): The drift path is estimated from the reverse-ice motion method described in Section 6.2.1.4. Latitudes along this drift track are logged at the original daily time steps and then linearly interpolated to 12-hour time steps. Both time series are saved.

   (b) Longitude (time series): Longitudes along this drift track are logged at the original weekly time steps and then interpolated to 12-hour time steps. Both time series are saved (weekly and twice-daily).

- (c) Date (time series): The original weekly time steps are logged and then subsampled to 12-hour time steps. Both sets of time steps are saved.

(3) Meteorology:

- (a) Air temperature (time series): Surface (2m) air temperatures from the MERRA2 reanalysis product are sampled via 3-D linear interpolation in latitude, longitude, and time at each point along the estimated drift track at the 12-hour time steps.
- (b) Wind speeds (u, v) (time series): Surface (2m) wind speeds in the u and v (eastward and northward directions) from MERRA2 reanalysis product are sampled via 3-D interpolation in latitude, longitude, and time at each point along the estimated drift track. Wind speed is calculated from the vector magnitude of the two components at each sample location.

(4) Freeze-up

- (a) Drift path ice concentration (time series): Ice concentrations are sampled along the drift track at daily intervals.
- (b) Freeze-up date: The date corresponding to the first (moving backwards in time) minimum in ice concentration below 15% ice concentration.
- (c) Freeze-up latitude: The latitude corresponding to the position of the ice drift track at the time of the freeze-up.
- (d) Freeze-up longitude: The longitude corresponding to the position of the ice drift track at the time of the freeze-up.

(5) Modeled growth

- (a) Degree-day (DD) model thickness (time series): At each 12-hour time step, the cumulative model thickness calculated by the degree day model is saved.

(b) Degree-day (DD) model EOS thickness: The last time step in the degree-day time series is saved as the end of season thickness.

(c) Thermodynamic (HB) model thickness (time series): Heat balance model results are saved at the 12-hour time steps of the atmospheric forcing data.

(d) Thermodynamic (HB)model EOS thickness: The last time step in the heat balance model record is stored as the end of season thickness.

6.3 Error analysis

In order to quantify the error in the drift tracking method, Ice Mass Balance buoys [Perovich et al., 2014] were used to track the motion of ice floes through the Arctic. The backwards tracking algorithm is run from the April 1 location of the buoys to evaluate the approach. These buoys carry air temperature sensors which are used to verify the meteorological data estimation along the drift route as well.

6.3.1 Ice Mass Balance buoys

The error analysis used ten ice mass balance buoys operated by CRREL [Perovich et al., 2014]. They are installed in ice floes early in the winter season where they can measure ice growth and melt over the following years. IMBs carry a suite of sensors above the ice, including meteorological sensors (air temperature and pressure), sounding sensors that measure the height of the snow surface relative to the buoy, and GPS and communication electronics. The mast of the buoy is outfitted with temperature sensors every few centimeters vertically, which extend down through the sea ice upper ocean and into the snow and air above. The profile of measurements is used to determine the ice thickness. Figure 6.10 shows two different types of IMBs with different packaging but largely similar sensors.

Ten IMBs from the central Arctic and Beaufort Sea regions were selected for this error analysis. They recorded ice growth over a full winter (starting prior to December 1 and

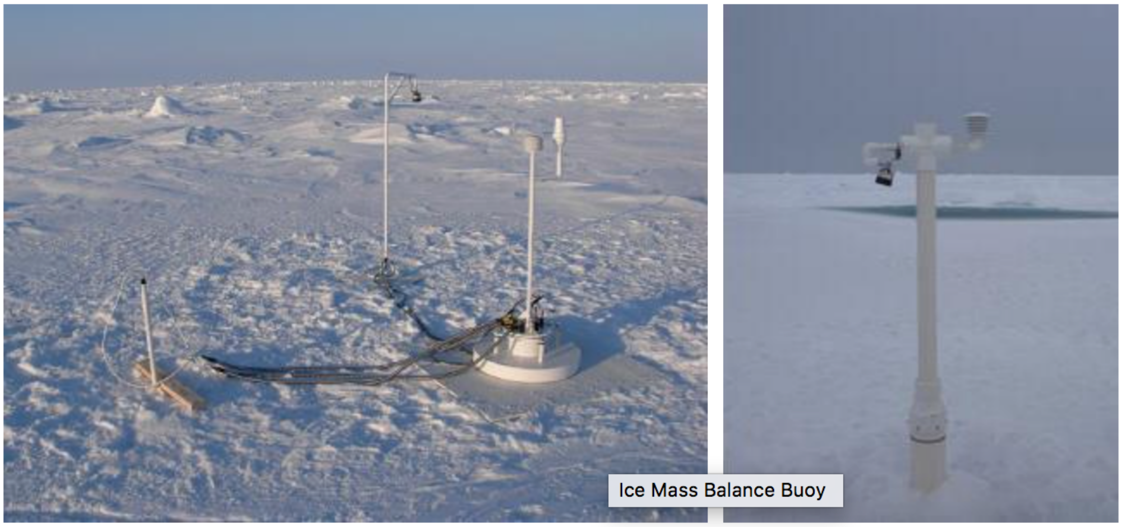

Figure 6.10: Two ice mass balance buoys installed in ice in the Arctic. Reproduced from http://imb.erdc.dren.mil/index.htm

ending after April 1) while drifting freely with the sea ice. Buoys were selected from 2011-2015, with the bulk of these buoys active in the winter of 2012-2013. A limitation with using IMBs for this analysis is that they are typically installed in multi-year ice, or at least ice that forms very early in the fall season. The modeling part of the ice thickness accounting is therefore hard to compare, since the models (both the energy balance and the degree-day) assume starting the season with little or no sea ice cover.

6.3.2 Buoy tracking

Buoy records were cut off on April 1 of their year of drift in order to make them comparable to the ice parcels. From IMB positions on these dates, the ice motion product and the parcel tracking algorithm were used to trace the buoy's ice parcel in the same manner as the ice parcels described previously. This creates two drift tracks that can be compared: the actual IMB drift track from the logged GPS locations and the 'estimated' drift track from the ice motion tracking algorithm. These tracks can then be sampled in the MERRA2 reanalysis data to get the reanalysis air temperatures for comparison to the measured temperature logged on the IMB.

6.3.2.1 Drift tracks

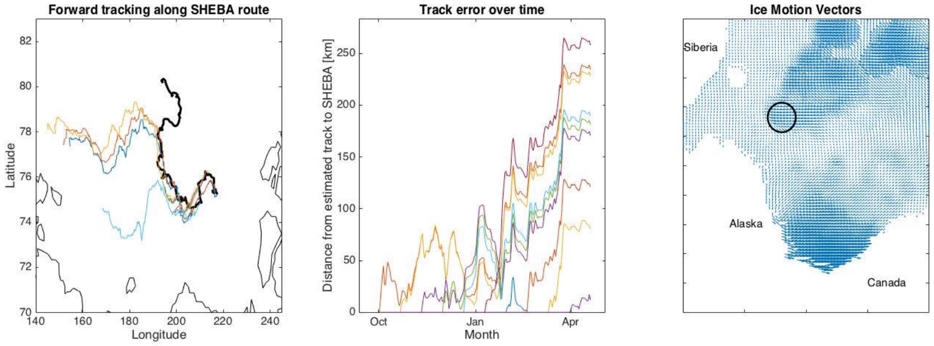

Figure 6.11: Left: The black line is the SHEBA drift track through the northern Chukchi and Beaufort Seas. Each colored line is an estimated track based on the ice motion product, started at a different point in the overwinter drift. Center: The distance between the estimated track and the actual track for each of the colored tracks. Left: An example of the ice motion vector field for the time in late March where all estimated tracks diverged notably from the actual track. The region in the black circle is where the tracks are located.

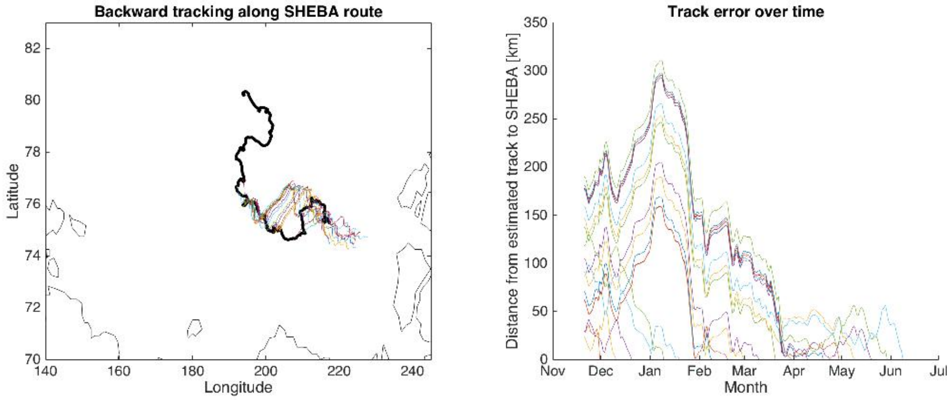

Figure 6.12: Left: The black line is the SHEBA drift track through the northern Chukchi and Beaufort Seas. Each colored line is an estimated track calculated by moving backwards through time, started at a different point on the SHEBA track. Right: The distance between the estimated track and the actual track over time, for each of the tracks initiated over the winter drift season.

The ice motion tracking offers only a moderately effective means of tracing ice back through its drift history. The ice motion product [Fowler et al., 2013] is first evaluated using forward tracking and compared against the SHEBA drift track from 1997-1998. Figure 6.11 shows the forward tracking results, where the estimated tracks follow the SHEBA drift path reasonably well for a while until the ice motion data diverges from the actual track and the estimated paths diverge abruptly. These cases appear to be because of the influence of wind in the ice motion algorithm ? the locations where the estimated tracks diverge from the actual tracks are often in areas where there are large regions of ice moving in the same direction in the ice motion product, which would suggest a large-scale influence that is not directly calculated from actual ice motion. In general, once the estimated track has diverged from the actual track, it is more likely to diverge further over time as it is being moved with the ice motion estimates from a different location.

When switching to backwards tracking, it is possible that additional error is introduced in places where there is converging flow of ice floes. The test of the SHEBA drift path performed reasonably well though, as shown in Figure 6.12. There was a period in January when the ice motion product diverged from the SHEBA track and all of the existing tracks turned northwards, rather than continuing south and east for another 150 km. In this particular case, these tracks converged again slightly with the actual track, getting to the beginning of the season with less than 200km of total path error distance.

Figure 6.13 shows how this tracking process can be applied to other drift tracks. In this case, ten Ice Mass Balance buoy tracks were used to see the spatial variability in how well the ice tracking algorithm follows the observed drift patterns. Buoys in the Chukchi and mid- to southern Beaufort tracked reasonably well, with relatively small deviations from the drift track. Buoys further north or tucked in near the dense ice areas north of the Canadian Archipelago did not perform as well, with sometimes very substantial divergences right at the beginning of the season. Ice motion vectors near the North Pole are known to be less reliable as the feature tracking from passive microwave satellite retrievals that underlies the dataset is not available in this region.

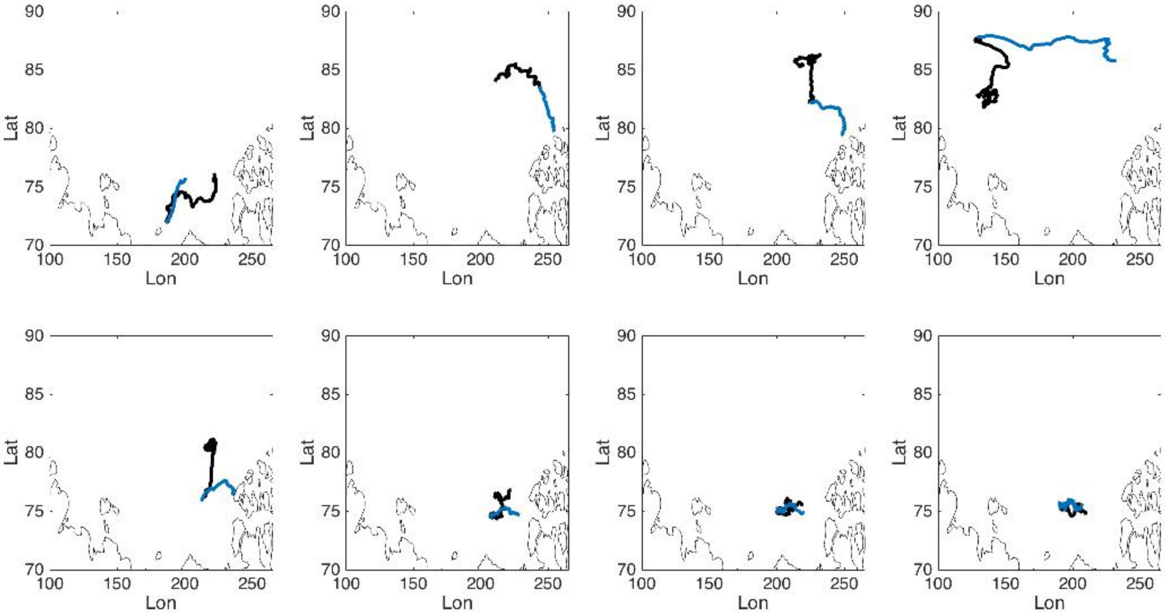

Figure 6.13: Maps of IMBs from 2011-2014 that were evaluated as the error analysis for this project. Each black line is the actual buoy drift track and the blue line is the estimated track traced backwards from the end-of-winter (April 1) buoy location.

Buoys at higher latitudes were not tracked as well as the buoys at lower latitudes, with extremely large errors (>500km distance between the buoy and the estimated drift track) on some of these. Fortunately most first-year ice growth does not occur at or even particularly near the North Pole or Canadian Archipelago, so increased error near the pole has less of an impact on this analysis than it might otherwise. Because the buoys in the Beaufort and Chukchi areas were more closely tracked, this analysis can move forward. The IceBridge observations come primarily from the Beaufort Sea and the area north of the Canadian Archipelago, but there is very little first year ice (and what there is is usually highly deformed) in the latter region. For the buoys in the relevant region, the beginning-of-winter location estimated by the tracking method falls within 3 degrees in latitude and/or longitude of the actual location.

Error in the drift path shows up two ways in the analysis: as error in the meteorological forcing (which becomes error in the modeled ice growth) and as error in the location and therefore timing of freeze-up.

6.3.2.2 Air temperatures

Because the IMBs carry air temperature sensors, it is possible to calculate the error in air temperature over the course of the winter season and to determine the components of that error attributable to the path error and using the MERRA2 reanalysis product.

Figure 6.14 shows the air temperatures measured by the IMB (yellow), sampled from the reanalysis product along the drift track (red), and sampled from the reanalysis product along the estimated (ice motion tracing method) drift track (in blue). The estimated track extends back before the ice mass balance buoy was installed in October and can therefore retrieve the temperature history of the floe prior to the installation of the IMB.

The air temperature estimates both along the actual drift path and the estimated drift path were fairly accurate. This suggests that drift path error had relatively little impact on the sampling of atmospheric state.

Figure 6.15 shows the mean temperature error for these buoy records over the winter season. The error is decomposed into two components: the path error (red x's) is the difference between the reanalysis temperatures along the actual drift track and the reanalysis temperatures along the estimated drift track, and the reanalysis error (yellow circles) is the difference between the reanalysis temperatures and the measured air temperatures by the IMB. The blue diamonds indicate the mean of the total temperature error on a time-step by time step basis between the reanalysis temperature along the estimated drift path and the measured air temperature at the IMB. In some cases (buoys 2,3,8,10), a warm-biased reanalysis error is balanced slightly by a cold-biased path error, though often the two error sources are both positively biased and add together for a larger warm bias.

The IMB temperature sensors are approximately two meters above the sea ice surface, so they are directly comparable to the 2m reanalysis temperatures.

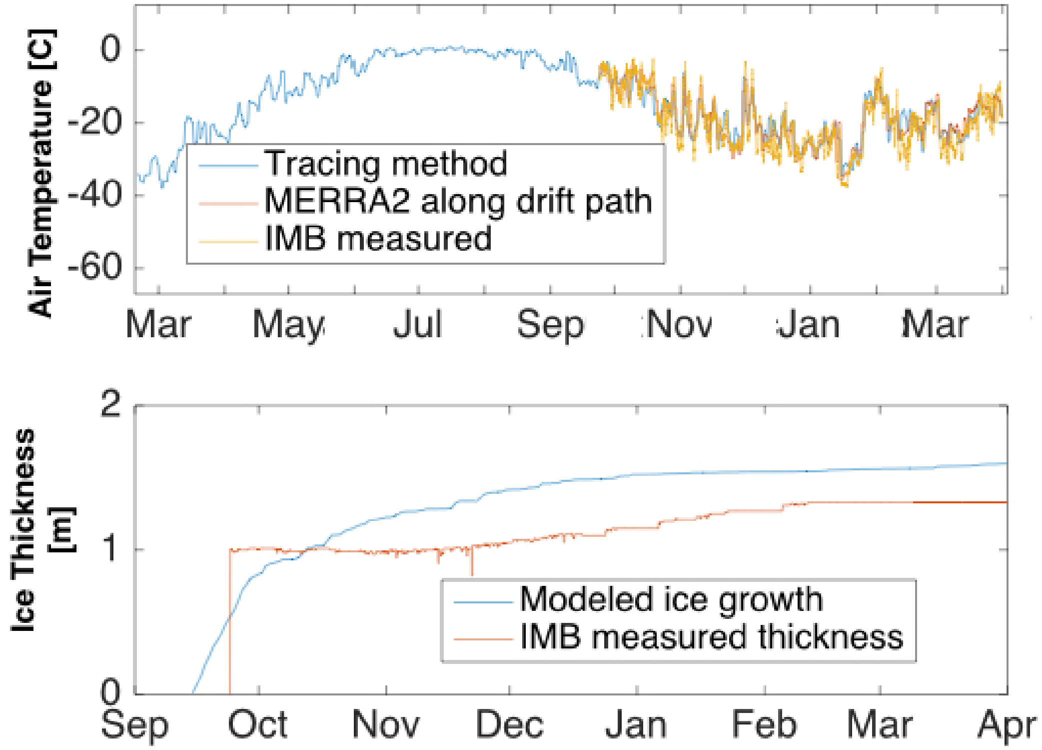

Figure 6.14: Top: Air temperatures (in °C) as measured by a drifting IMB (yellow), sampled from the MERRA2 reanalysis product along the IMB drift track (red), and sampled from the reanalysis product along the estimated drift track (blue). Bottom: Ice thickness measurements with the modeled growth superimposed.

Figure 6.16 shows the same error study, but in terms of percentages of the net error, where the two error sources do not cancel each other out. The path error tends to be quite low relative to the reanalysis error component, except in two cases.

The reanalysis temperature error is more of a concern in integrating the atmospheric forcing than the drift tack error is. MERRA is just one of several reanalysis data products available, and another product may do a marginally better job of capturing the temperature patterns in this part of the Arctic. That said, the Lindsay et al. [2014] study showed that there was little difference in most of the reanalysis products in this region, and that none of them were especially adept at capturing the wind variability.

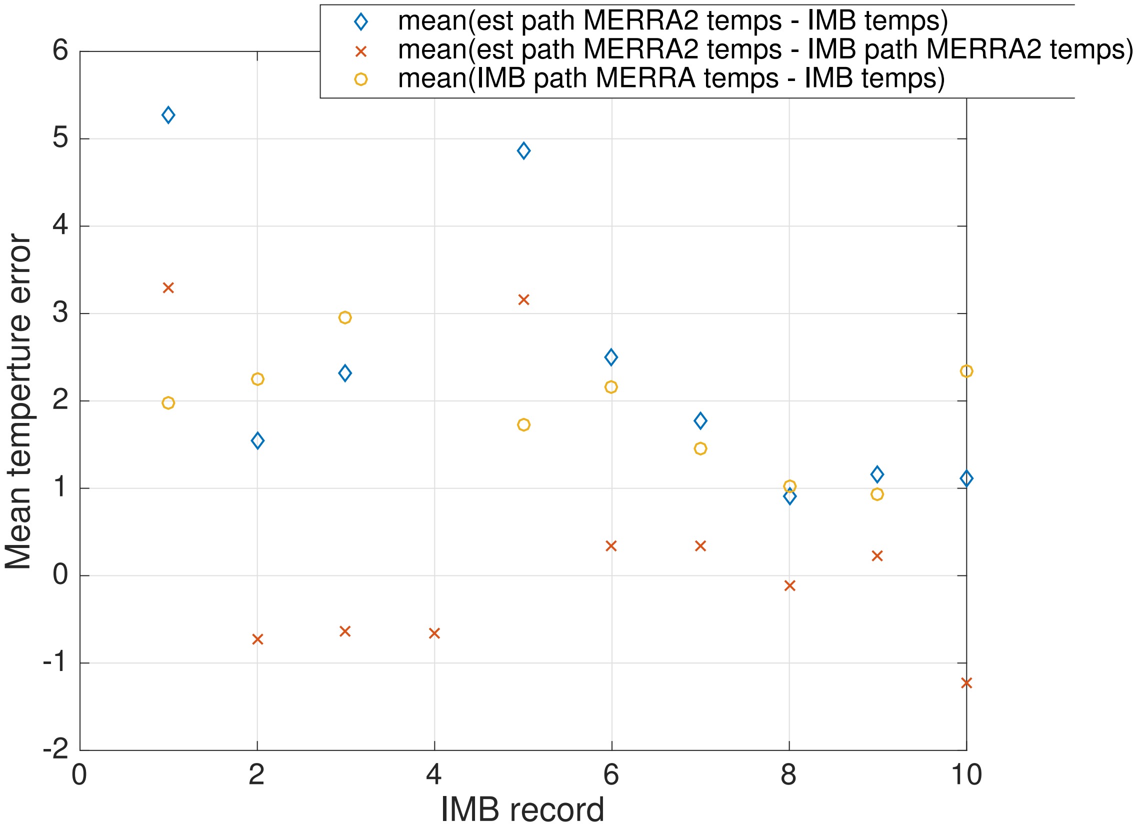

Figure 6.15: Mean temperature error over the winter season as measured for total error (blue), the drift error (red), and the reanalysis error (yellow).

6.3.2.3 Path error

The path error could be mitigated if there were a better method for estimating the drift path of the sea ice. There are several ice motion products that have been produced at various points, and another comparison of these may prove fruitful though there is no immediate evidence that a different product would necessarily perform better [Sumata et al., 2014].

6.3.2.4 Reanalysis error

While reanalysis error is the largest source of error in the temperature measurements, there is little that can be done about it. Reanalysis products could be improved in the Arctic by the inclusion of more measurements into the reanalysis products. Short of putting

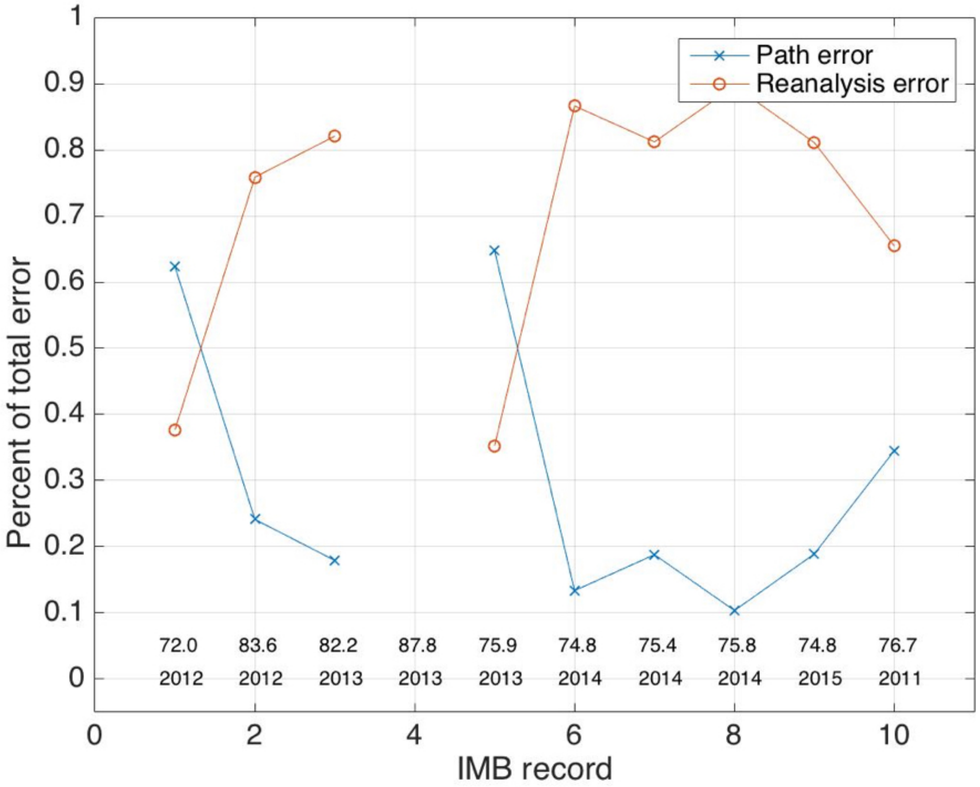

Figure 6.16: Path and reanalysis contributions to the surface air temperature error over the course of the winter drift. The numbers at the bottom indicate the mean latitude of the IMB (top row) and the last year they were active (bottom row).

more instruments in the field to increase observations available for the data assimilation procedures, reanalysis estimates of meteorological conditions in the Arctic will always be limited in accuracy. Near-surface meteorology is particularly challenging to capture with remote sensing measurements and the presence of sea ice, clouds, and darkness further complicate the process.

6.3.3 Freeze-up error

Figure 6.17 shows in the top panel the mean error in freeze-up date for one degree of error in either latitude or longitude of location. This is calculated by taking the expected value of the error in freeze-up date if the location is 1 degree in latitude or longitude in any direction off from the actual location. Without a known bias towards being too far north or too far south, the error typically averages out to zero. The exceptions are along the ice edge in the north Atlantic, or in areas (like between islands in the Canadian Archipelago) that have highly staggered ice growth because of the interactions of ice and land. The bottom panel looks at the mean magnitude of error for the surrounding 1 degree in latitude and longitude (note that the color scale has changed). In the Beaufort, the error is typically less than one week for 1 degree of position error.

The IMB drift analysis do show somewhat more error in location than 1 degree, sometimes as much as 4 degrees in longitude. The error in freeze-up dates for the IMBs cannot be tested directly, as the IMBs were all installed in multi-year ice and did not have a fall freeze-up date prior to the overwinter drift. This error can add up to as much as 4 weeks of uncertainty in the freeze-up date. With only a 120 day growth season in many locations, this error is very large compared to the total growth period.

Freeze-up timing must therefore be considered with some suspicion in this analysis. Given the geographic spread of the IceBridge observations, there is a fairly large spread in estimated freeze-up dates. Locations that saw freeze-up in December can be confidently distinguished from locations that experienced freeze-up in October, but more subtle nuance than that would requite a more reliable ice tracking method.

6.4 Results

6.4.1 Inter-annual variability

The first analysis looks at the variation in first year ice thickness distribution between years. Each panel is a histogram of ice thickness measurements from the IceBridge campaigns in spring of 2012-2015 [Kurtz et al., 2015]. First-year ice was found using the ice age product [Tschudi et al., 2015]. The bar on the far right of the histogram represents the fraction of ice thickness measurements that were more than 4 meters thick. This represents heavily

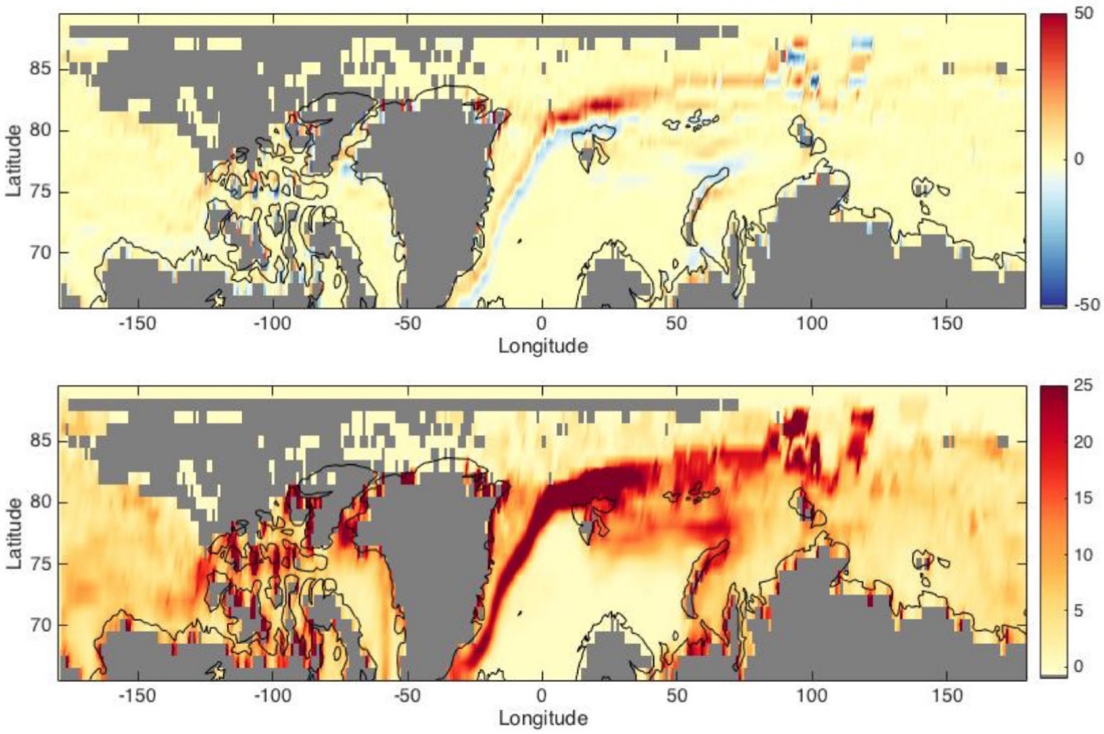

Figure 6.17: Error in freeze-up for a 1 degree (in latitude and longitude) radius error in location. The top panel shows the mean error in freeze-up date (in days), and the bottom panel shows the mean magnitude of the error (also in days). Both color bars are in days.

deformed ice, where ice is more than twice as thick as thermodynamically-grown ice. Figure 6.18 did not use any of the ice tracing algorithms or models and is just comparing the observations between years.

The summer of 2012 stands as the record for minimum sea ice extent. Large storms in the Chukchi combined with generally warm summer temperatures combined to beat the 2007 record for minimum ice extent. Spring 2013, the following winter growth season, shows a markedly thinner ice cover than the other years of IceBridge data: 1.1m for the mode of the distribution (an estimate of the thermodynamically grown ice thickness for the area) as opposed to 1.5m, 1.6, or 1.7m (2014, 2015, 2012 respectively).

The profile in the spring of 2012 is particularly interesting, where the mode is at 1.7m, but there is also a substantial area of sea ice that is significantly thinner at 0.5m, as if two ice

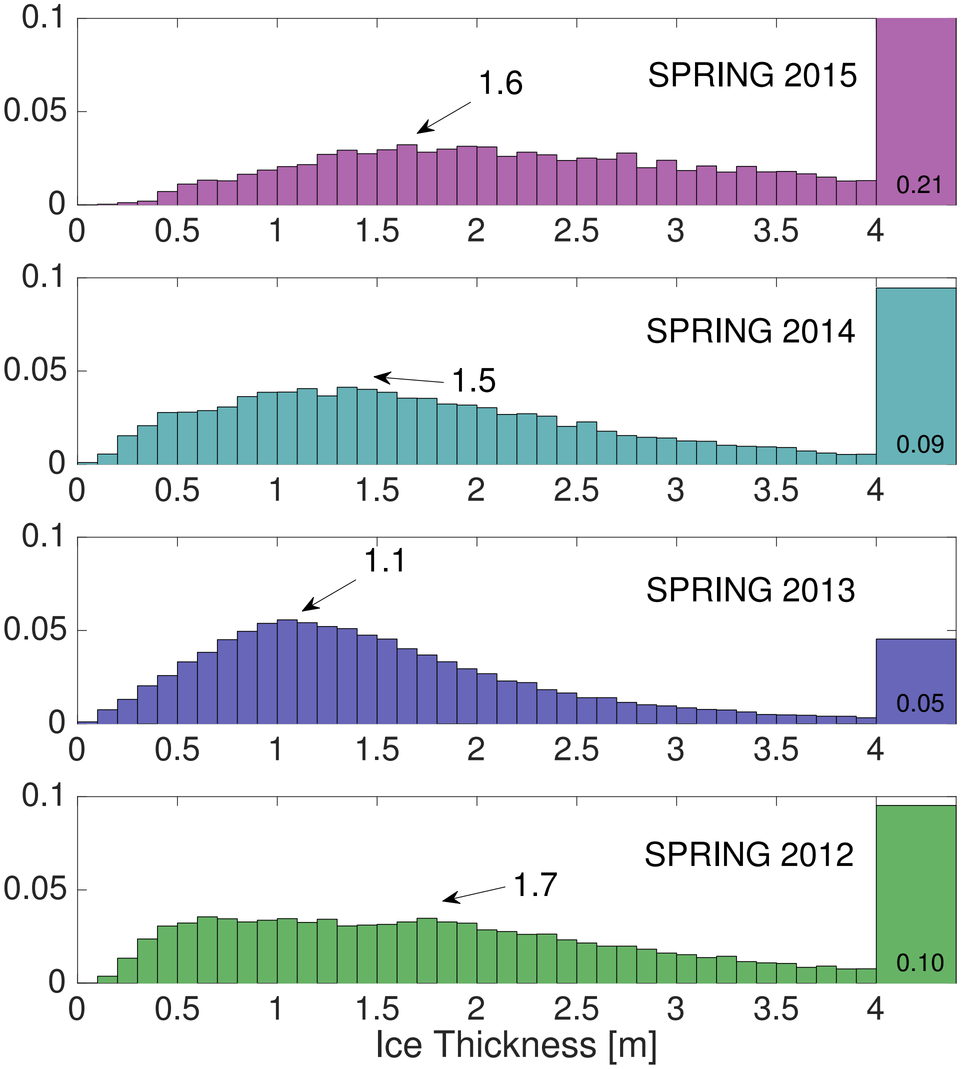

Figure 6.18: First-year sea ice thickness distributions by year for 2012-2015.

thickness distributions were superimposed. The relatively large amounts of slightly deformed ice suggests that this year experienced large amounts of deformation midway through the season, or that there was systematic bias in the measurement of ice thickness in certain regions, perhaps due to the snow thickness retrieval process based on climatological snow densities.

Spring 2015 shows substantially more heavily deformed ice than any other year. 2012 and 2014 are similar at 0.09 or 0.1 of the total ice cover, while 2013 was approximately 50% lower at 0.05 and 2015 was approximately 100% higher at 0.21. This high fraction may mean that some areas of MY ice made it through the ice age filter, as 4m of ice is much more common in areas of MY ice than FY ice. The ice age filter could possibly be improved by integrated additional datasets that estimate ice age using approaches other than ice tracking.

There could be some inter-annual variability in the accuracy of the thickness measurements: the snow depth is retrieved from the snow radar, which assumes a snow density from climatology for calculating the depth of snow and in the buoyancy assumption that goes into converting freeboard to ice thickness. If snow in the areas of the IceBridge flights (Beaufort Sea, mostly) was notably more or less dense than the climatology, it could bias the ice thickness estimates. Particularly light snow is $100\mathrm{g\,m^{-3}}$ while dense, heavily windblown snow can be as high as $450\ \mathrm{g\,m^{-3}}$. How this translates to error in the snow thickness and mass retrieval and then the buoyancy calculation to find ice thickness is not straightforward, but an error on the order of a few centimeters in ice thickness would be expected.

6.4.2 Latitude dependence

Generally, freeze-up dates are earliest further north and gradually later moving south. To investigate this, we combine all years of IceBridge ice thickness measurements into one analysis to see if there are significant trends with latitude. Figure 6.19 is a 2-D histogram of ice thickness measurements and latitude. The left panel shows the number of observations in each half-degree latitude band. There were nearly five times as many observations in the

70-72 N band than at any other latitude band due to the flight patterns during the campaigns and where first-year ice tends to end up.

Generally, there is an increase in ice thicknesses measured with increasing latitude. This could come from one or more of several different factors: earlier freeze-up dates (more time for ice to grow over the course of the winter), colder air temperatures (higher heat fluxes over the winter), or less ice-free time in the summer resulting in lower oceanic heat fluxes during the ice growth season. These factors will be investigated over the next few sections.

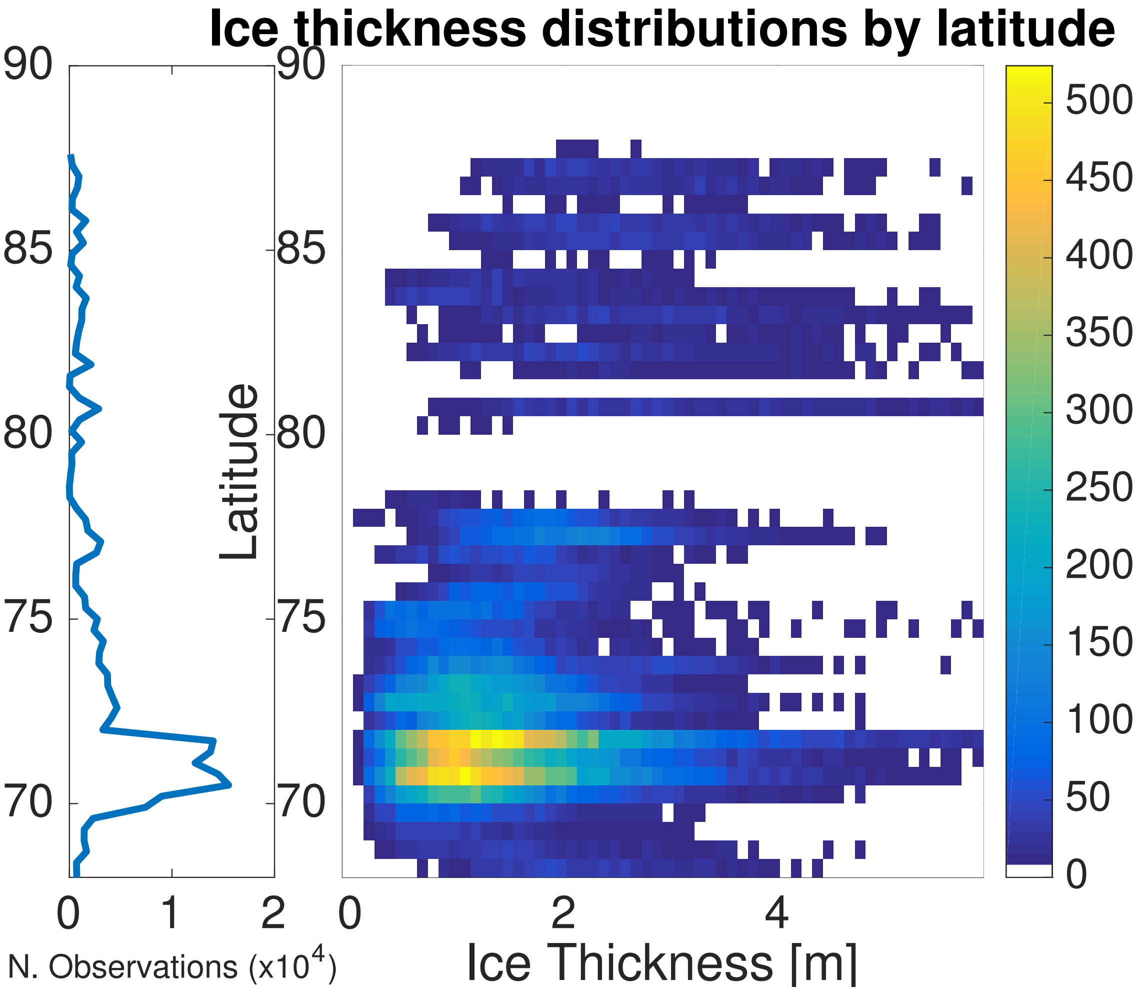

Figure 6.19: First-year ice thickness with latitude at the end-of-winter observation location. The right panel shows the number of observations by latitude - there were substantially more flights at lower latitudes, but there does still seem to be a slight trend of increasing ice thickness at the end of the season with higher latitudes, especially above 73N.

6.4.3 Relation with freeze-up

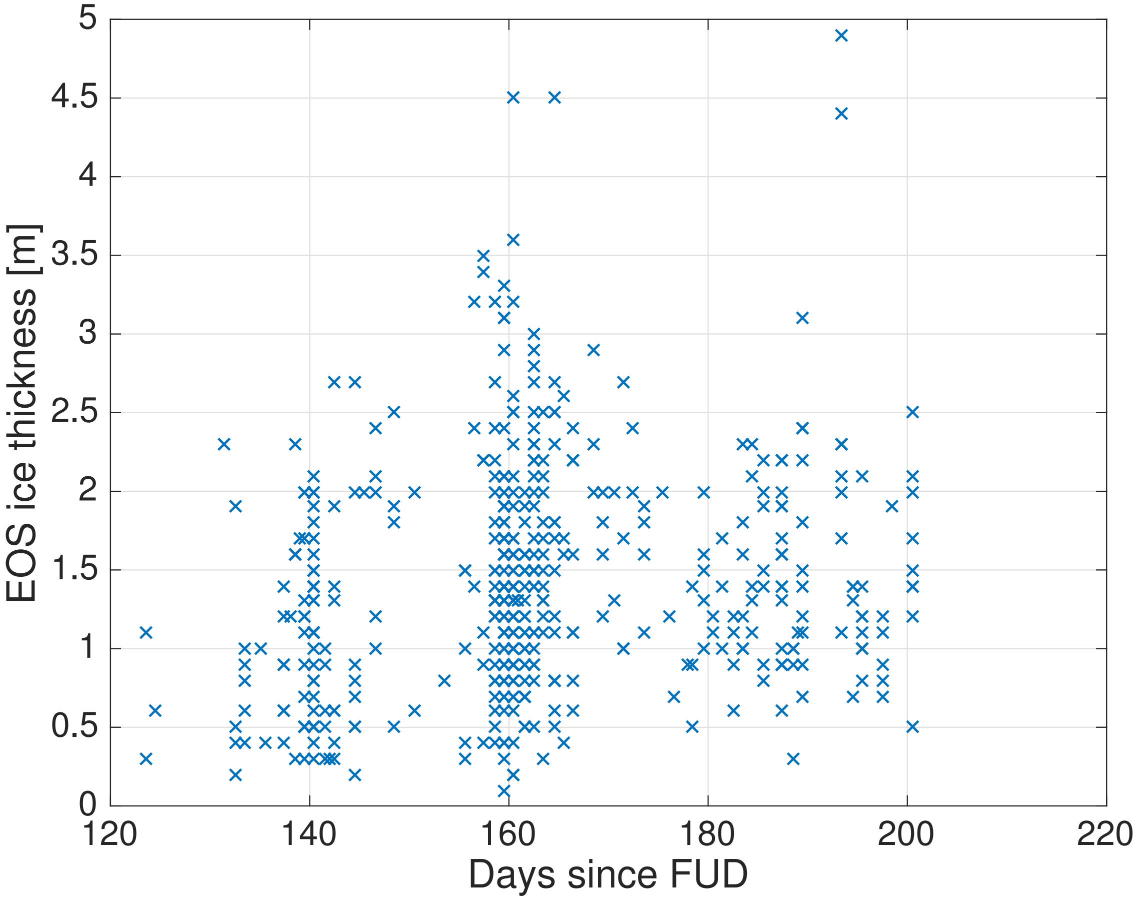

Figure 6.20: FYI thickness versus days since freeze-up. There is a very slight positive trend towards increased ice thickness with longer growth seasons, but this is partly because of areas of highly deformed ice.

Figure 6.20 shows median ice thickness measurements from the IceBridge campaigns plotted against their respective freeze-up dates, found using the ice-tracing algorithm described earlier. The median ice thickness is used to avoid deformed ice as much as possible. The correlation coefficient is low (0.18), but the p-value is 5×10^{-5}, indicating that the relationship is statistically significant.

Areas of thicker, mechanically deformed ice contribute to the spread, as there is no way that 3m thick ice could have grown thermodynamically. Separating mechanically thickened ice areas from thermodynamically grown ice is not a straightforward task. This result suggests that freeze-up date may have an impact on the end-of-season ice thickness, though the effect is much smaller than the variability in ice thickness from deformation and other forcings and it is not statistically significant.

6.4.4 Relation to atmospheric forcing

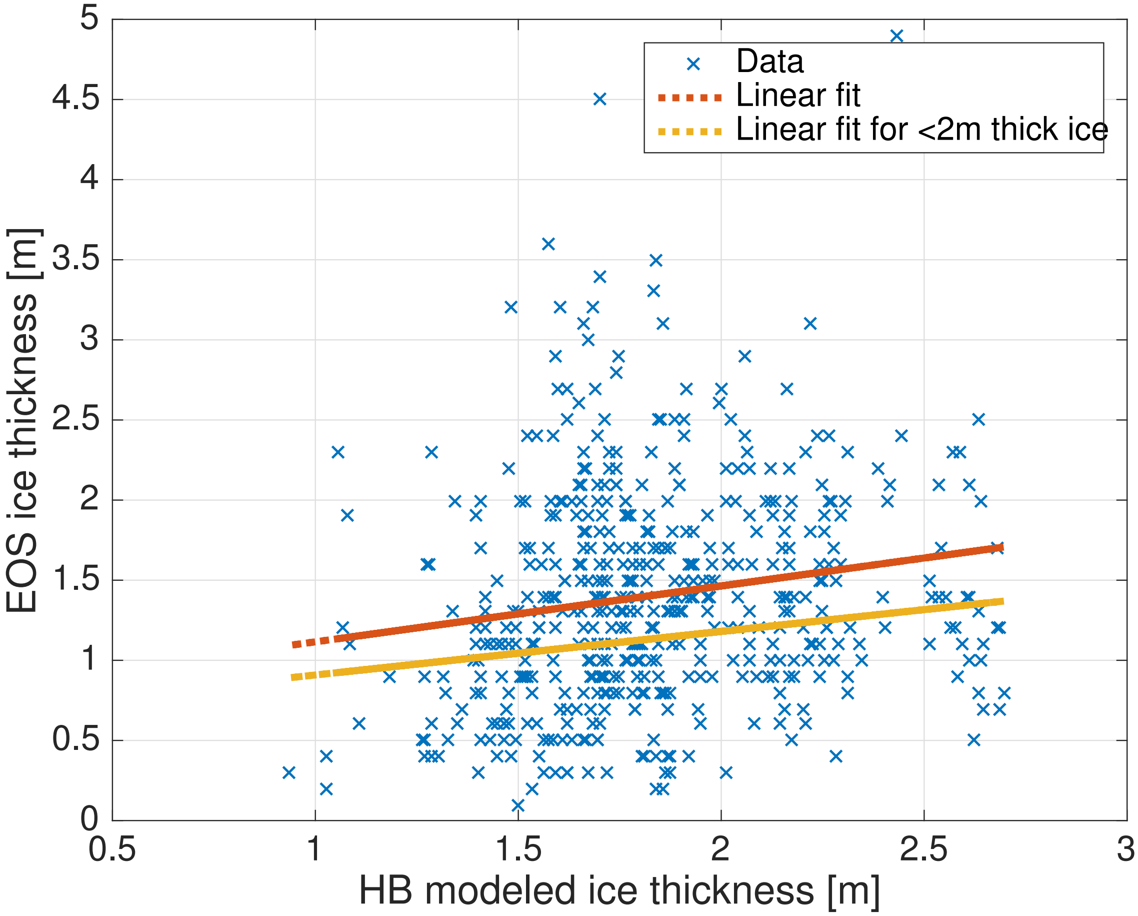

Figure 6.21: Observed FYI thickness versus modeled ice thickness for the corresponding drift path. The two lines indicate the linear fit for the whole dataset and the subset that only considers ice thicknesses less than two meters (a general estimate for first-year undeformed ice thickness).

The integrated atmospheric forcing (modeled ice thickness) captures some of the variability in ice thickness, with a correlation coefficient of 0.16. This relationship, despite the spread, is statistically significant at p = 0.0002.

The modeled ice thickness is meant to be an integrator of atmospheric forcing over the course of the winter and not a perfect model of the ice growth. This suggests that colder, windier winters do result in thicker ice growth, though this figure does not distinguish between rapid growth and a longer ice growth season.

The degree-day model (not pictured) does not do a better job of capturing the variability. Where the energy balance model results in the bulk of the ice ending the season between 1.2 and 2 meters thick, the degree-day model clusters most of the ice between 1.7 and 2.1 meters.

Once you control for the date of freeze-up (and therefore the length of the ice growth season in the model), the relationship between the modeled ice thickness and the measured ice thickness mostly breaks down. This is true for both the heat balance and the degree-day models. Figure 6.22 shows the modeled ice growth (x-axis) versus the measured ice growth (y-axis) for each the heat balance model (left column) and the degree-day model (right column). The rows are three different ages of first year ice, with the latest freeze-up dates (the youngest ice) in the top row and the earliest freeze-up dates in the bottom row. The correlations are consistently low, with the only statistically significant relationships (at the 5% level, not significant at the 1% level) are in the cases with early freeze-up and long growth seasons. This suggests that overwinter atmospheric conditions have at most a small effect on the end-of-winter ice thickness.

6.4.5 Relation with snow cover

Snow cover insulates sea ice from the atmosphere, slowing growth. Snow does tend to fall early in the winter season in the Arctic, so ice that has had a longer growth season (earlier freeze-up date) will tend to have thicker snow cover. Areas of sea ice with otherwise identical growth parameters (timing of freeze-up, oceanic heat flux, and atmospheric forcing) but with deeper (or shallower) snow cover than average will end the season with thinner (or thicker) ice than average. Wind across the sea ice moves snow around throughout the winter, with

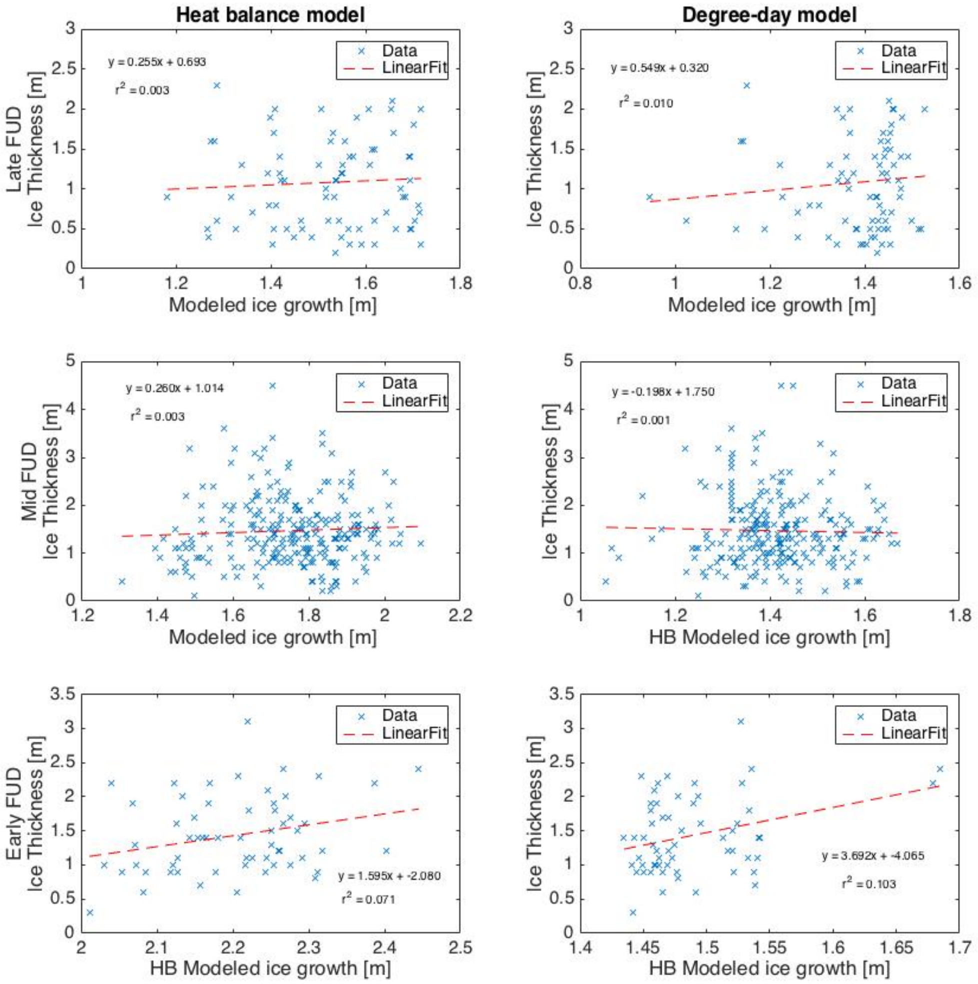

Figure 6.22: Ice thickness and model comparisons for early, middle, and late freeze-up dates.

drifts accumulating in areas with rougher surfaces and deformed ice. In this case, thicker (deformed) ice causes thicker snow. Finally, because the snow thickness measurements are part of the ice thickness retrieval, the two parameters are not observed independently. Snow thickness is therefore not considered as one of the driving factors in the ice thickness analysis later in this chapter, despite the significant role that snow plays in ice growth.

Greater ice thicknesses (especially above 2m of ice) means areas of highly deformed ice. That these correspond to areas of thicker snow cover is unsurprising - heavily deformed ice

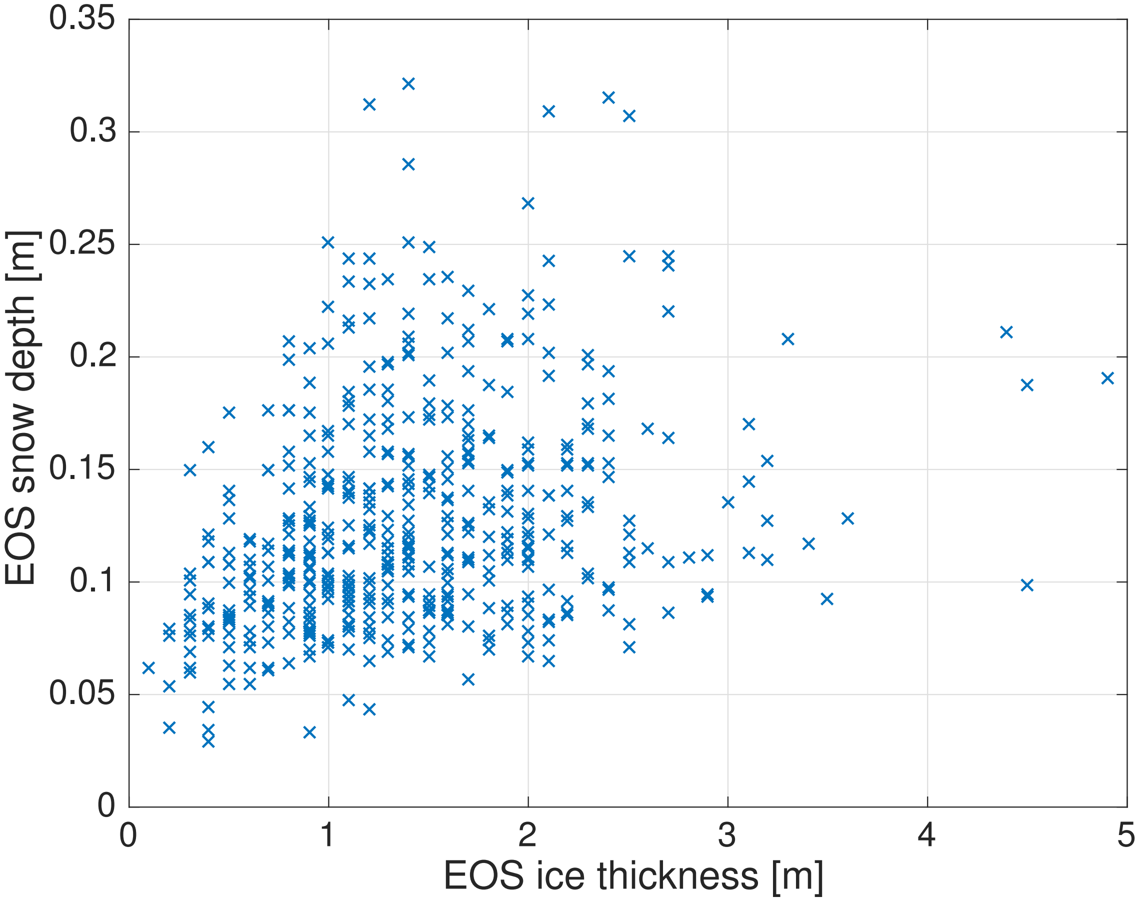

Figure 6.23: Median FYI thickness versus the snow depth as measured by the IceBridge flights.

captures the snow blowing in the wind, amassing snow drifts that are sheltered from further redistribution. Complicating this is that the snow radar system used to retrieve the snow depth suffers from decreased accuracy in areas of deformed ice with rough surfaces. These locations tend to be areas with greater ice thicknesses, so the increase in variability in 6.23 with increasing ice thickness may be related to retrieval error.

At first glance, there is little correlation between the time since freeze-up and the snow depth at the end of the season unless the years are separated (Figure 6.24). For each year, there is a slight positive trend in snow depth with the age of the ice. But because snowfall occurred at different times in the fall, the timing of the increased snow cover changes from year to year. There is significant variability that comes with having only a few snow thickness measurements corresponding to some freeze-up dates (e.g., the spike in the 20115 (purple) record around 150 days).

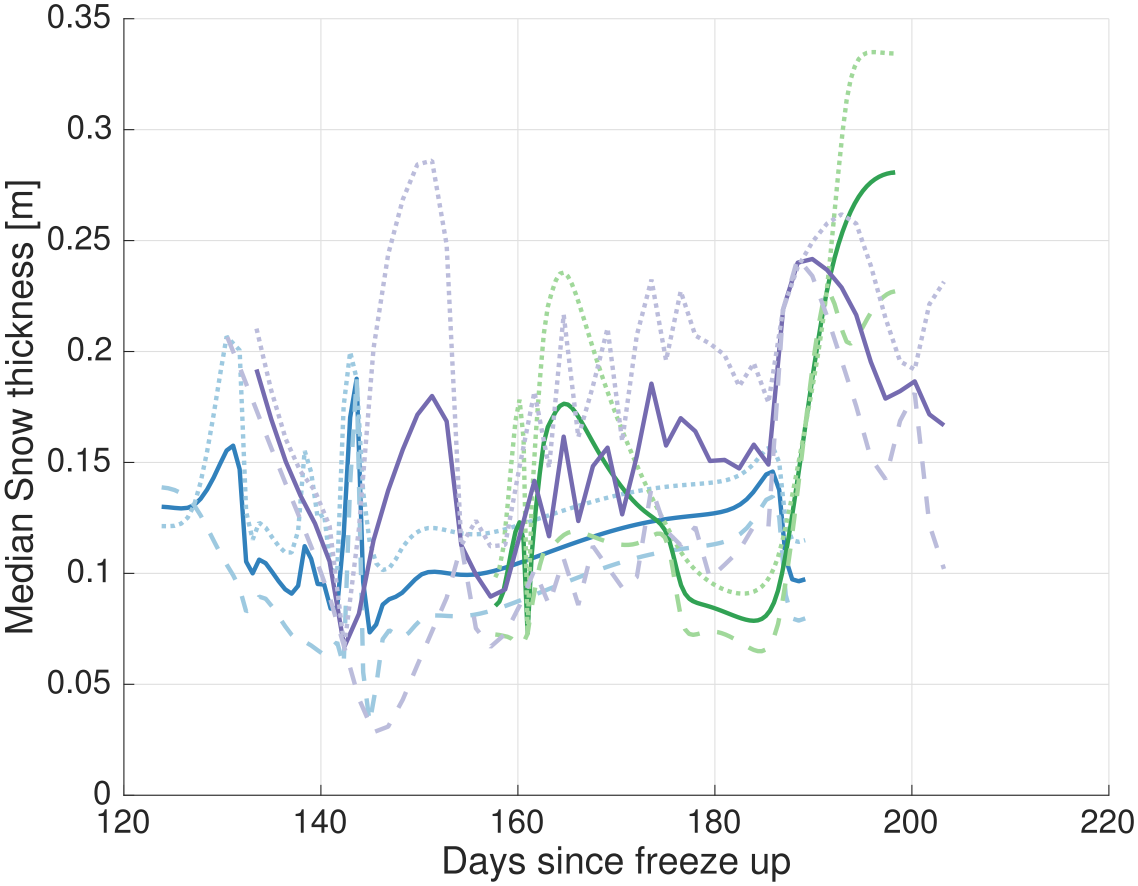

Figure 6.24: Time since freeze-up versus median snow thickness for each ice parcel, shown by the mean snow depth corresponding to each freeze-up date by year. Purple is the season ending in 2014, blue is 2013, and green is 2012. The dotted and dashed lines corresponding to each color represent + and - 1 standard deviation from the mean respectively.

Figure 6.25 shows this same data, but controlling for the timing of freeze-up and the amount of atmospheric forcing in the same manner as Figure 6.22. In these cases, the relationship between snow depth and freeze-up date is more consistent. There is still significant amounts of spread largely due to redistribution of snow over the course of the season. In all cases snow depth increases with increasing ice thickness, regardless of atmospheric forcing or timing of freeze-up. Snow is a much more effective insulator than sea ice, and so one might expect that when length of growth season and the atmospheric forcing is controlled for, thicker snow cover would result in thinner sea ice. Instead, thicker snow cover is consistently found on thicker sea ice.

When looking at the relationship between snow depth and ice thickness, the shorter growth seasons resulted in a statistically significant correlation (at the 5% level) under both the high and low atmospheric forcing cases. Still, their is significant spread and the correlation coefficients are low, suggesting that at least the end of winter snow cover is not a dominant factor in determining the ice thickness at the end of the season.

There are a few possible explanations for this:

There could also be some measurement error in the IceBridge measurements. If there was pointing error that introduced during the flight that was not fully accounted for in post-processing, both the snow depth and the ice thickness would be artificially thick. Underestimating the snow density would also result in erroneously low ice and snow measurements.

Snowfall in the Arctic is not a simple process: wind-blown snow accounts for a substantial fraction of snow in the Arctic, and redistribution exceeds direct snowfall in many locations [Barry et al., 1993]. Ice surface roughness catches snow as it is blown across the relatively smooth surface of the sea ice cover, creating drifts behind features. Areas with deformed ice have particularly rough surfaces, with sheltered areas for snow to accumulate.

6.4.6 Relation with summertime ocean temperatures

Summertime ocean temperatures are considered at two locations in this analysis: the end-of-season IceBridge measurement location, and the location of freeze-up identified in the drift track analysis. Summer surface temperatures from the NOAA optimal interpolation SST product [Reynolds et al., 2002] are used. This product is described in more detail in Section 4.2.4.

Figure 6.26 shows the median ice thickness as a function of the summer sea surface temperature from the September before freeze-up at the location of freeze-up. Often this

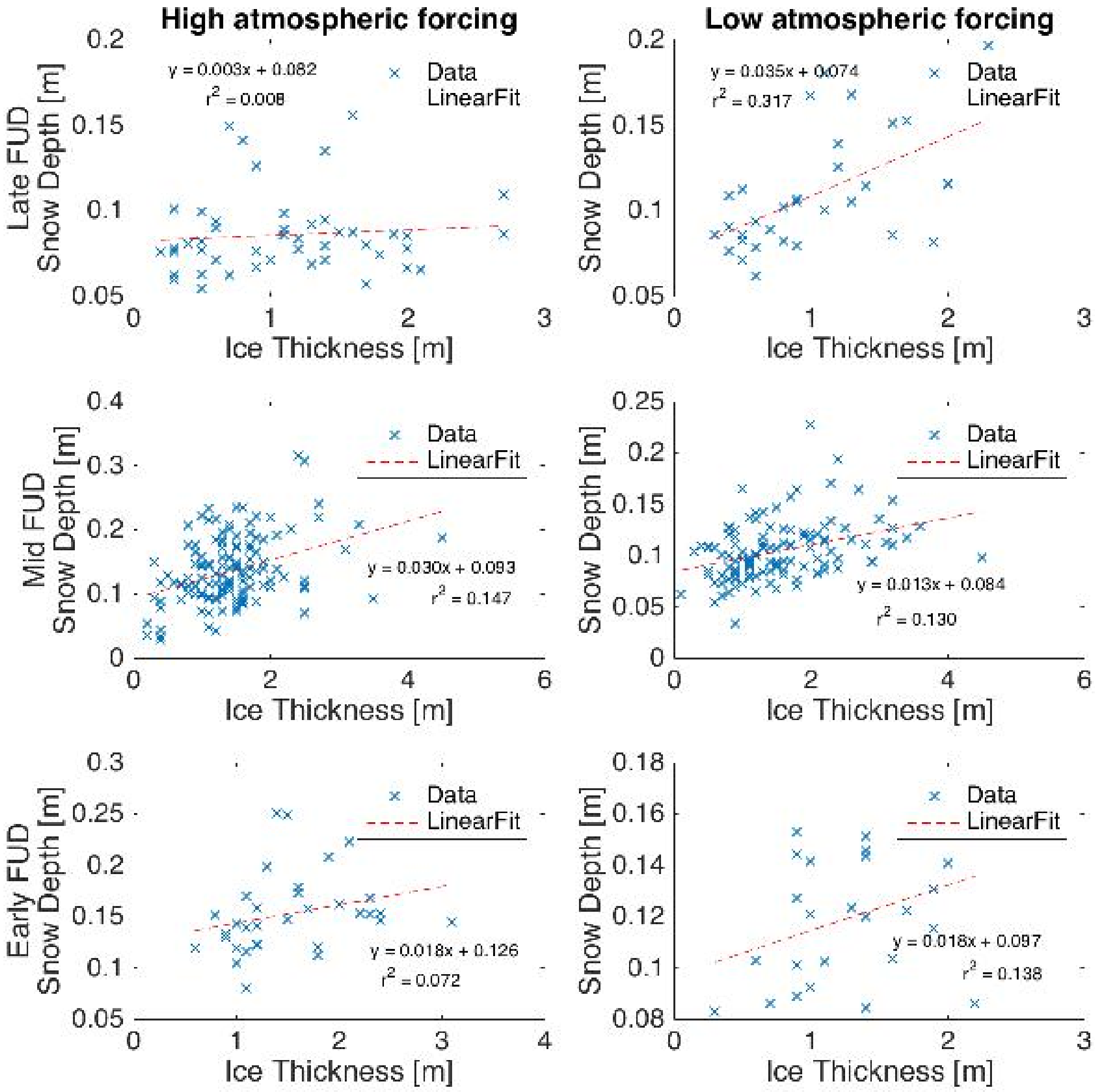

Figure 6.25: End of season ice thickness versus median snow thickness for each ice parcel, controlling for time since freeze up (rows) and the amount of atmospheric forcing (columns).

has to do with oceanic heat flux: warm SSTs are found in locations that tend to have heat trapped in the summer halocline layers (see Chapter 3). There is a very slight correlation (p $= 2 \times 10^{-4}$) between the summer water temperature and the median ice thickness: locations with low summer water temperatures are more likely to have areas of very thick (likely highly deformed) ice. The difference is trumped by the variability in ice deformation. This may also be a consequence of multi-year ice getting through the initial filter - where there is multiyear ice, surface temperatures are colder and then the end of season ice thickness is thicker.

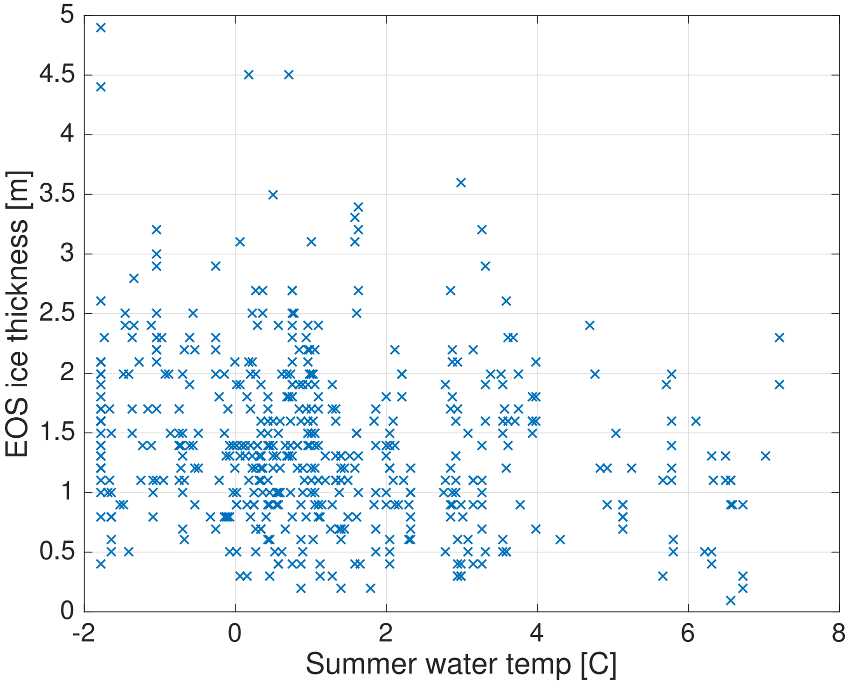

Figure 6.26: Median FYI thickness versus summertime (Sept 1) Sea Surface Temperature at the location of the end-of-season measurement.

Figure 6.27 is the same as as Figure 6.26, but with the summer surface temperatures sampled at the locations of freeze-up rather than the end of season measurement. There is no significant correlation between these, even though summer temperatures influence freeze-up dates, which are somewhat correlated with the end-of-season thickness.

Figure 6.28 shows how the end-of-season location and freeze-up location summer surface temperature measurements compare for each track. The freeze-up locations were consis-

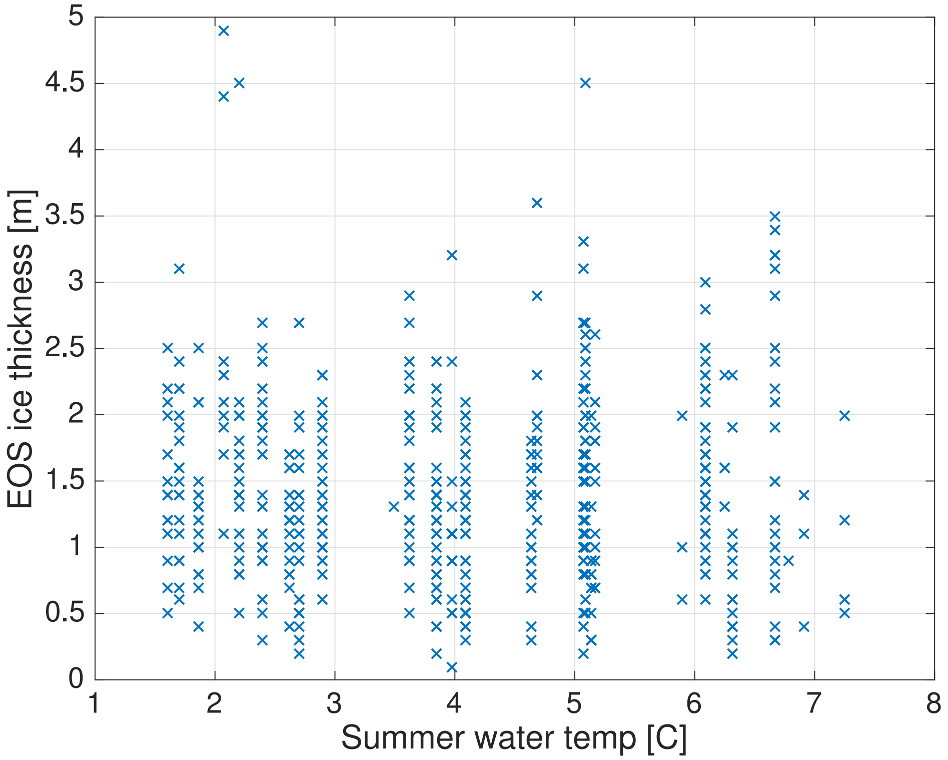

Figure 6.27: Median FYI thickness versus summertime (Sept 1) Sea Surface Temperature at the location of freeze-up.

tently at warmer locations than the end-of-season measurements. This is partly because of the locations of the IceBridge flights: areas north of Greenland and the Canadian Archipelago tend to accumulate multi-year ice, and first-year ice that moves towards that area generally froze in warmer waters.

6.5 Multi-factor analysis

Figure 6.29 shows the results of a linear regression between the summer SST (at the end-of-winter location), the freeze-up date, and the integrated atmospheric forcing and the observed sea ice thicknesses. The full spread of ice thickness is not captured because of ice deformation, but the regression seems to capture some of the non-deformation related variability. The right panels show the relationship between each of the constituent factors and the ice thickness, with the other factors held constant. The effects of freeze-up date and

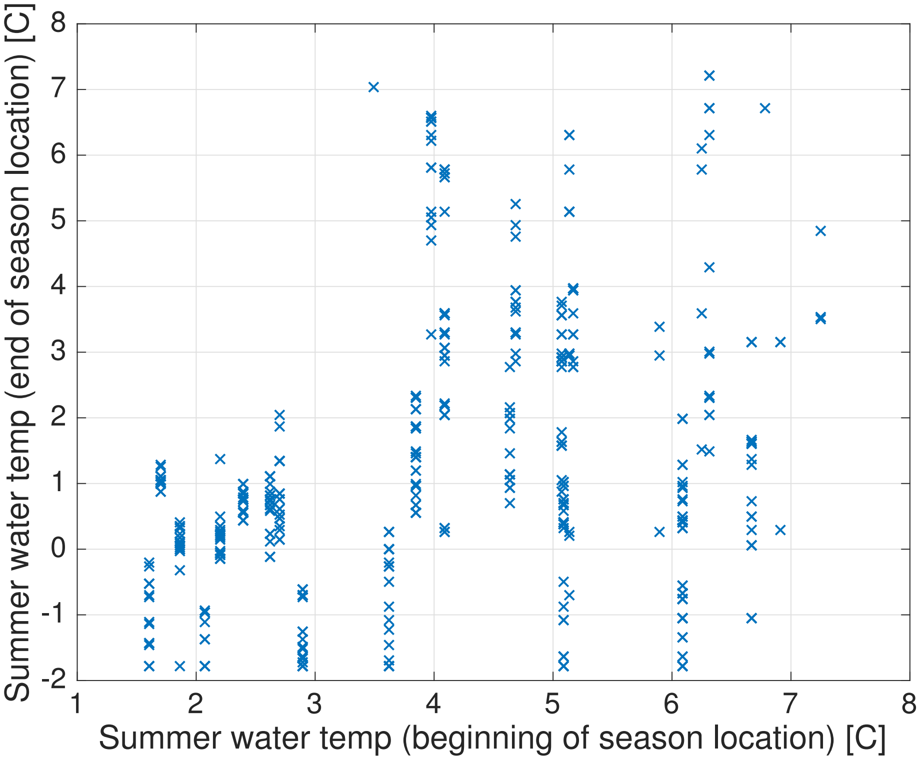

Figure 6.28: Previous summer surface temperatures at the locations of freeze-up and the end-of-season ice thickness observation. These suggest that ice predominantly moves from areas of warmer summer temperatures to areas with cooler summer temperatures.

summer SST are statistically significant at the 1% level, while the atmospheric forcing effect is not.

This statistical model supports the hypotheses that warmer summer water temperatures and later freeze-up dates both result in thinner end-of-season sea ice thickness, but because of the large uncertainty in the freeze-up dates and the low statistical power in the multiple regression overall, this is not shown conclusively. With that in mind, within this model 1 day of delay in the freeze-up date leads to ice thickness at the end of the season roughly 1 cm thinner. Warmer summer temperatures (via trapped heat in the halocline and overwinter oceanic heat flux) have a slight negative effect beyond the delay in freeze-up: for each degree warmer water in the summer, ice at the end of the season will be 7 cm thinner.

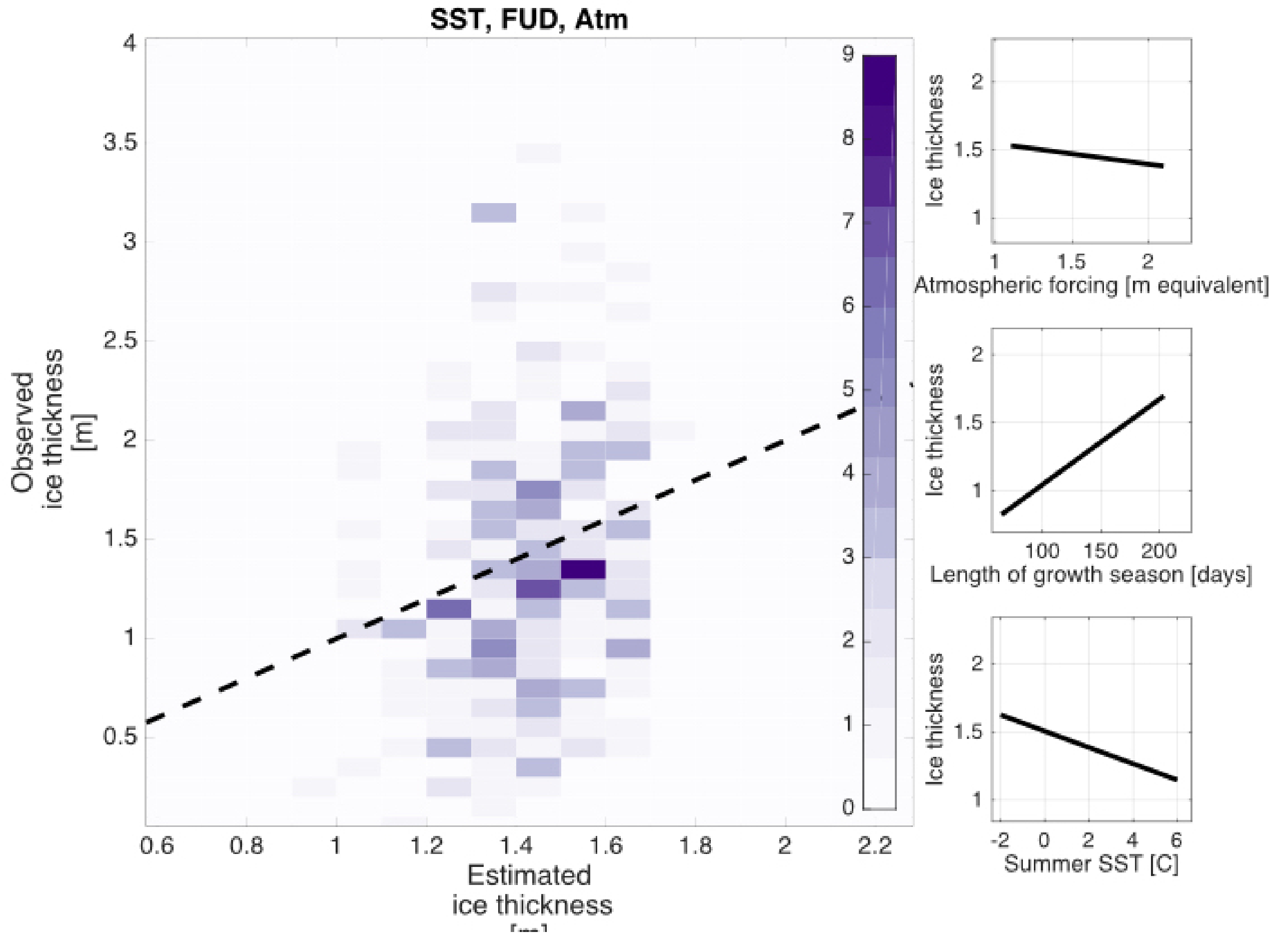

Figure 6.29: The result of a linear regression between summer SST (end of season location), freeze-up date, and atmospheric forcing and the end of season ice thickness.The left figure is estimated ice thickness from the forcing parameters (integrated atmospheric forcing, length of growth season, and summer ocean temperature as a proxy for oceanic heat flux) against the observed ice thickness, shown as a 2-D histogram. The panels on the right show the relative contributions of each parameter with the others held constant.

6.6 Summary

Ice thickness at the end of the growth season may be influenced by the freeze-up date, but this analysis is limited by uncertainty in drift paths, corresponding freeze-up dates, and overwinter atmospheric forcing. This analysis suggests that even moderate changes in the timing of freeze-up (10 days) could result in substantial changes in the end of season ice thickness (≈10 cm), but further improvements to the ice tracking approach will be necessary to prove this conclusively. In addition to causing a delay in freeze-up, warmer ocean temperatures seem to have further impacts on the ice cover, where a 1°C increase in the summer ocean temperature results in a 7 cm decrease in the ice thickness at the end of the season. The relationship between summer ocean temperatures and end-of-winter ice thickness at a particular location is statistically significant, but in order to control for the effects of delayed freeze-up, more accurate freeze-up timing and ice tracking estimates will be necessary. The hypothesis set forth in this chapter have been supported, but not confirmed, by this analysis.

A follow-up study to this analysis using CryoSat-2 ice thickness measurements would be appropriate. During the course of this dissertation work, there have been marked improvements in the quality and availability of CryoSat-2 thickness products, which cover the full Arctic at moderate spatial resolutions (6-25 km) at monthly or better time steps [Tilling et al., 2016]. The SMOS passive microwave instrument has been used to measure sea ice growth up to 0.5m with some success, though it requires ideal conditions (cold air temperatures and high ice concentrations) that are not always available during the freeze-up period [Kaleschke et al., 2012]. These could supplement CryoSat-2 observations in the early season.

Chapter 7

Conclusions

The seasonal cycle of heat and ice growth in the Arctic is undoubtably changing. Arctic amplification has accelerated the loss of summer sea ice cover, and feedback effects during the melt season are extending the area and time of open water.

Chapter 3 shows how the oceanic heat cycle differs in areas that are seasonally ice-free as compared to perpetually ice-covered, through the analysis of temperature and salinity profiles. The increasing area and length of the ice-free season in the lower latitudes of the Arctic seems to be allowing the upper ocean to absorb more heat than ever before, with summertime mixed layer temperatures warming in response. Heat also accumulates in the summer halocline layer, where it is trapped by the strong density gradient during freeze-up and can slow ice growth during the winter. Buoy records show that most of the net cooling in the upper ocean is due to heat loss during storms in the fall, suggesting that increases in storminess may mitigate some of the delays in freeze-up.

Considering the summer halocline as a layer rather than a single depth improves our ability to understand the seasonal cycle of heat storage in the upper ocean, providing a viable explanation for the observations of warm layers persisting in the upper ocean during the fall cooling season. Heat trapped in the vulnerable summer halocline layer should be expected to leak out over the course of the winter as the summer halocline is eroded, slowing ice growth throughout the season.

Chapter 4 uses empirical relationships based on physically-relevant parameters to estimate the mixed layer depth in locations where we do not have direct observations. These parameterizations are consistent with other reviews of mixed layer depths in the region [Peralta-Ferriz and Woodgate, 2015], and can be used to estimate heat content. Trends in upper ocean heat content must be considered with mixed layer depth in mind. Different methods for estimating the mixed layer depth can result in substantial differences in the magnitude of the trends in heat content. These estimates show significant warming trends in upper ocean heat content over the last two decades, especially in August-October and in the Chukchi and southeast Beaufort.

Maps of heat content derived from this approach correlate moderately well with October ice concentration in the Western Arctic, indicating that increasing summer upper ocean heat content plays a role in the delay of freeze-up. There is not yet statistical significance in the direct relationship between summer heat content and the timing of freeze-up because of high interannual variability and a short period during which there have been ice-free summers in many locations.

Chapter 5 investigates the upper limit to ice growth rates. Ice production in Antarctic coastal polynyas occurs under extreme sensible and latent heat fluxes, is a likely scenario for the upper limit to ice growth rates worldwide. Analysis of ice growth rates from surface temperature measurements in the Terra Nova Bay polynya in September 2012 show maximum ice growth rates of 12cm/day, which is comparable to the growth rates measured in leads and an order of magnitude higher than the growth rates measured under existing ice floes Perovich et al. [2003]. This suggests that there may be an upper limit to the rate of ice growth that occurs under most conditions. If the growth rate was unbounded, it would be more possible for ice that forms later in the season to “catch up” in thickness to ice that formed earlier. Instead, the freeze-up date is more likely to have an effect on the end of season thickness as it moves later in the season in response to warming summertime temperatures.

Chapter 6 considers the impact of changing seasonal cycles on the growth of first-year sea ice. End of winter ice thickness distributions are related to freeze-up dates, summer mixed layer temperatures, and overwinter atmospheric forcing by tracing the ice drift path back through the season. There are notable uncertainties in this analysis stemming from the ice tracking method, where freeze-up dates are particularly uncertain. This, combined with a lack of statistical significance in relating overwinter atmospheric forcing to the end-of-winter sea ice thickness, indicates that these results are not conclusive. The analysis suggests that while delayed freeze-up may have an impact on the thermodynamically-grown ice thickness, the summer mixed layer temperatures also factor in to the end-of-season thickness in other ways. Controlling for a delay in freeze-up, a degree warmer water in the summer results in a few centimeters thinner ice cover at the end of the winter while delaying freeze-up results in approximately one centimeter less end-of-season thickness per day of delay. This would suggest that trapped heat, as discussed in Chapter 3, is contributing to the thinning of first-year ice cover in the Arctic.

Because of these processes, first year ice is likely to continue to thin as climate change continues to warm the Arctic. Warmer summer ocean temperatures and longer ice-free seasons result in both delayed ice growth and seasonally-trapped heat. Delayed ice growth results in less time for ice to grow and generally thinner ice cover, and trapped heat slows ice growth over the shortened season.

Appendix A

UpTempO Analysis

A.1 UpTempO Observations

UpTempO buoys measure temperature in the upper 60 meters of the ocean, with temperature and pressure sensing elements unevenly spaced, starting at 2.5 meters below the sea surface [Steele, 2012]. The drifting buoys use GPS to measure position and an Iridium satellite link for data retrieval. These buoys float independently of any ice support and operate mostly in open water, unlike many of the systems deployed in the Arctic. The UpTempO buoy schematic is shown in Figure A.1, some carry surface meteorological sensors and/or salinity probes in addition to the ocean temperature sensors. Data is freely available from Steele et al. [2014].

UpTempO buoys have recorded the evolution of the seasonal ice zone mixed layer prior to freeze up on five occasions, four in 2013 and one in 2014 (04-Ukpik, 16-, 17-, 18-Healy, and 14-Mirai). Using these temperature profiles (thousands of hours of data each), the first major theme can be addressed. In addition to the UpTempO buoys, CTD profiles from the Sea State DRI and other campaigns during the late summer and fall will be considered.

A.2 UpTempO profiles before freeze up

There are five UpTempO profiles that have recorded measurements of the surface mixed layer cooling prior to the onset of freeze-up, from early September to sometime in October or early November in the regions of interest.

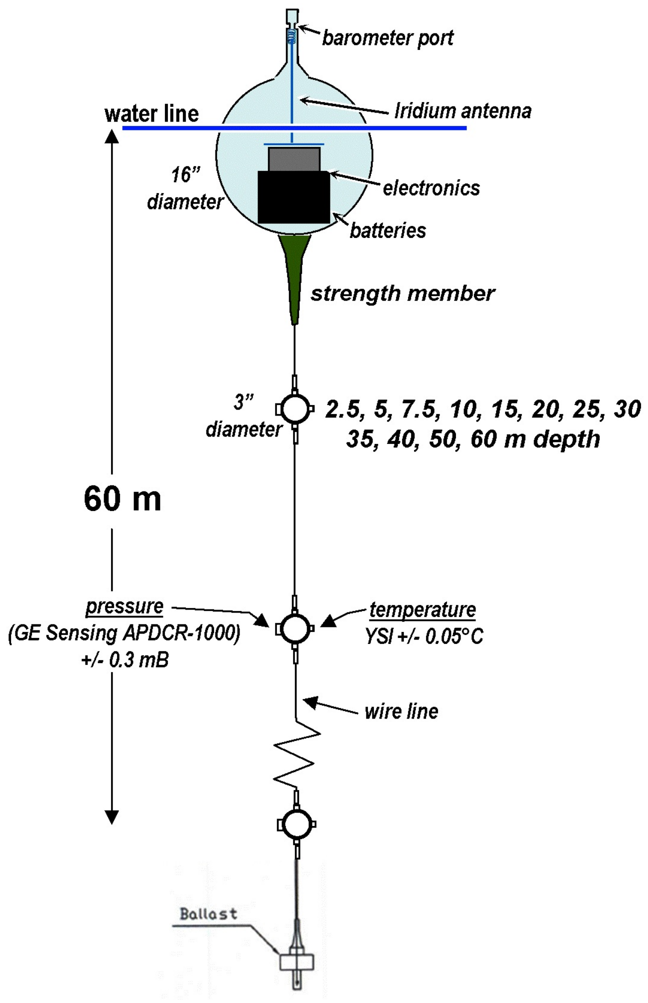

Figure A.1: Schematic of the UpTempO buoy from Temperature sensors are accurate to 0.05°C C and are fixed to the line extending down from the surface.

For the moment, the working assumption is that the UpTempO buoys were killed during freeze-up by ice growth/deformation. The likelihood of a buoy randomly ceasing operation shortly before the ice formed is assumed to be small, as no traumatic events are expected before the onset of ice growth and all of the buoys ceased operation after mixed layer temperatures reached a reasonable freezing point for the region. Once processing of the ice extent data products is complete, it will give a more clear picture as to when ice formation happened in the locations where the buoys were recording temperature profiles.

This assumption about the cause-of-death will be confirmed with the timing estimates of the onset of growth.

The following subsections show two figures for each buoy profile: the first is two color plots, with the top being the temperature as measured by the thermistor string on the buoys and the bottom being the difference between the temperature and the 2.5 meter (2m in some cases) temperature at the same time step. Inspection of the profiles show that the 2.5m thermistor temperature is consistently the best measure of the mixed layer temperature, as only in the rare case when there is no appreciable mixed layer is the 2.5 meter sensor below the thermocline. The surface is more variable, as it is influenced by solar heating and pooling of meltwater from nearby ice floes [Bradley et al., 2015]. This shows the relative temperatures in the water column as the surface layer cools.

The second is a series of line plots, showing the daily mean profile as it evolves from summer conditions to winter. The color of the lines transitions from the light green to dark blue as freeze-up approaches. The buoy profiles are named according to the year of deployment and the deploying vessel or campaign. An additional number (1, 6, 7, 8, 16) has beed assigned for reference to my own code and because it is easier than writing out the whole name each time.

A.2.0.1 2013 04 Ukpik (1)

Buoy 1, deployed in August 2013 in conjunction with the MIZOPEX campaign [Bradley et al., 2015], shows a mixed layer that reaches a maximum temperature of over 2 early September, though at the same time there is a deeper layer (10m to a depth that varies between 30 and 40) that is extremely warm (up to +6 temperatures that were observed nearby at the surface in early August [Bradley et al., 2015]. The bulk of cooling occurs very quickly, between 9/15 and 9/21, before it slows. On 9/25 a very warm layer (+1 to +1.5 etween 20 and 40 m depth emerges and persists for the remainder of the lifetime of the buoy (until 10/13). Between 9/29 and 10/2, there is some warming that comes down from the surface. This warms the mixed layer from around -0.6 0 efore the cooling resumes and the mixed layer makes its final cooling towards freeze-up.

The relative temperature figure (A.2) shows the significant amount of stored heat below the mixed layer at the onset of freeze up. Temperatures well above freezing (+1.5 re sustained until the last day and a half of the record, when they cool slightly but still are more than 1.5 ove the mixed layer temperature which is presumably at the freezing point corresponding to local salinity. This is a more extreme example of the NSTM described in Jackson et al. [2010].

In this profile, the mixed layer gradually deepens over the course of the fall, from a very shallow 2m mixed layer, which appears in the daily profile as the lightest green trace in figure A.3 to be a strongly warm thermal gradient, similar to that observed in Bradley et al. [2015]) to about 20 meters and well-mixed around freeze-up. There are several points when warmer incursions in the lower layers are present, including a period in mid-August when an intermittent very warm (+2 ayer appears over about two weeks, followed by an extremely warm period for another week and a half. There is some possibility that these may be remnants of a NSTM formed early in the summer.

A.2.0.2 2013 16 Healy (6)

Buoy 6 was deployed at the same time as 7 and 8, but slightly later in the season than 1, starting data collection on 9/1/2013 at the peak of warm summer temperatures. This profile doesn't have quite the temperature extremes measured in the Buoy 1 profile, with a steady temperature throughout the season in the winter mixed layer.

The second panel of Figure A.4 does indicate heat trapped below the mixed layer between 9/29 and 10/13. This happens when the cooling starts from the surface but doesn't make it all the way down to the bottom of the mixed layer, leaving a band of approximately 0 ter in between.

This profile also has a layer between 15 and 45 meters that is clearly defined and a pretty constant thickness throughout the season. This would seem to correspond to the winter mixed layer but will require more thought.

The profile towards the end gets particularly interesting: temperatures of the summer mixed layer get far cooler than the layer below, suggesting that the summer halocline persists and the summer mixed layer cools to freezing with relatively little thermal mixing with the deeper water, but also that the deeper water is above the freezing temperature. The picture of the winter mixed layer with freezing-temperature water the whole way down to the winter halocline is not apparent in this profile.

A.2.0.3 2013 17 Healy (7)

This buoy suffered failure of the lower thermistors in mid-September. The mixed layer evolution (mostly above the 20m depth) was captured for the most part, but for a period in mid-October it seems to extend below 20 meters that marked the lowest operational sensor towards the end of the campaign.

Cooling from above 2 ppened quite abruptly, but the rest of the cooling took much longer. At the end of the season in late October, there seemed to be a short pulse of slightly warmer water that preceded the cooling at all depths down to 20m. This is one of the cases where substantial cooling starts at the surface and gradually moves down, again providing evidence for lack of entrainment into the mixed layer as being a process for creating the NSTM-like temperature signatures.

A.2.0.4 2013 18 Healy (8)

Buoy 8 had the most frequently poorly-mixed surface mixed layer of the set. In early September, there were several occasions when the surface was 1 more above the 2m temperature. This is similar to what was observed during the MIZOPEX campaign [Bradley et al., 2015].

This profile had an interesting characteristic in that there were sometimes a second layer of warm water. From the surface down (i.e. Sept 22), there is slightly above 0 ter in the mixed layer, then a slightly warmer layer below that, a thin and inconsistent layer around 20m depth that is somewhat below 0, and then another warm layer +0.5 ing below the thin cool layer. This happens on several occasions in this profile and for a two-week period in Buoy 1's profile. As suggested in that discussion, this seems like it could be remnants of a previously existing NSTM, perhaps formed on more than one occasion.

Between Sept 29 and Oct 05, there is a cold layer just at the surface that does not extend down even to the two-meter temperature sensor. This cold, negative temperature gradient was observed on several occasions in Bradley et al. [2015] and likely corresponds to fresh meltwater from ice floes pooling at the surface.

A.2.0.5 2014 14 Mirai (16)

There was one buoy during fall 2014 that operated through freeze-up. This buoy frequently observed warm layers getting trapped below the cooling mixed layer (Sept 18, Sept 22, Oct 1). This profile also has a clear layer that fits the description of the winter mixed layer (as described in Figure 2.6), with the Pacific Shelf Water being the temperature maximum around 50m depth.

This profile lends more support for the idea that heat in the NSTM is trapped there when subsequent cooling at the surface mixes down only so far, leaving the warm layer behind underneath. Each of the occasions that a significant NSTM shows up in the profile, there is a corresponding dramatic cooling at the surface.

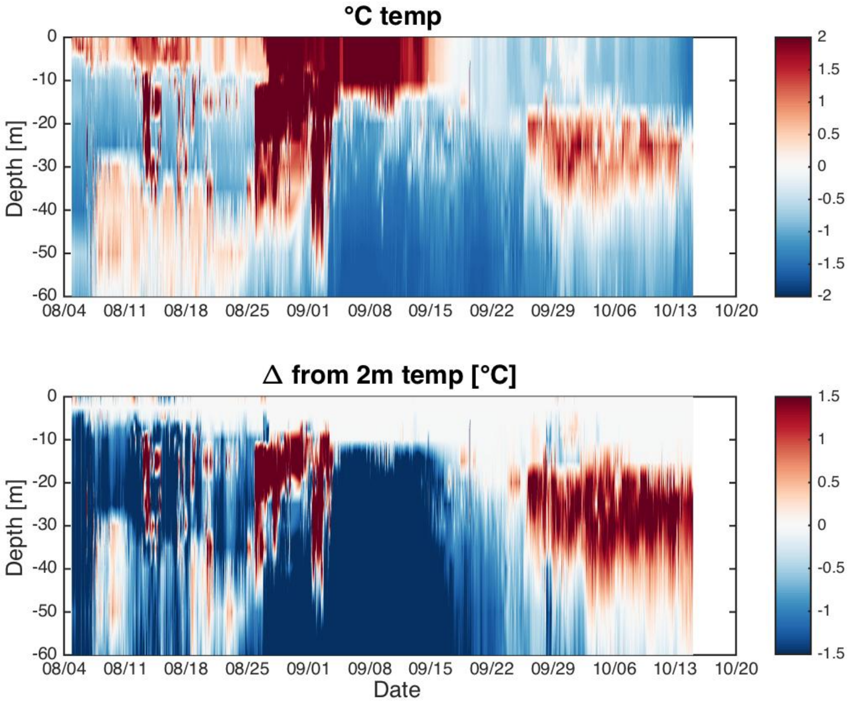

Figure A.2: Evolution of the upper ocean prior to freeze up as measured by UpTempO buoy 2013-04-Ukpik (1) during the fall of 2013.

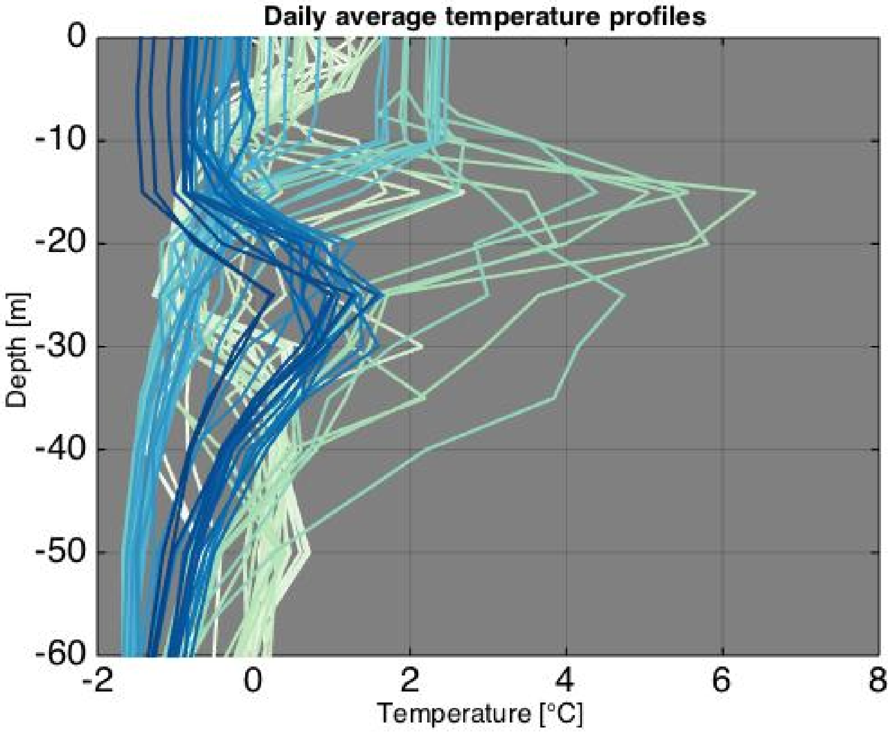

Figure A.3: Evolution of the upper ocean prior to freeze up as measured by UpTempO buoy 2013-04-Ukpik (1) during the fall of 2013, as shown by line plots for each day of the fall season. The line colors indicated the progression throughout the days of the record, with light green corresponding to late summer and dark blue corresponding to the period immediately before the onset of ice growth.

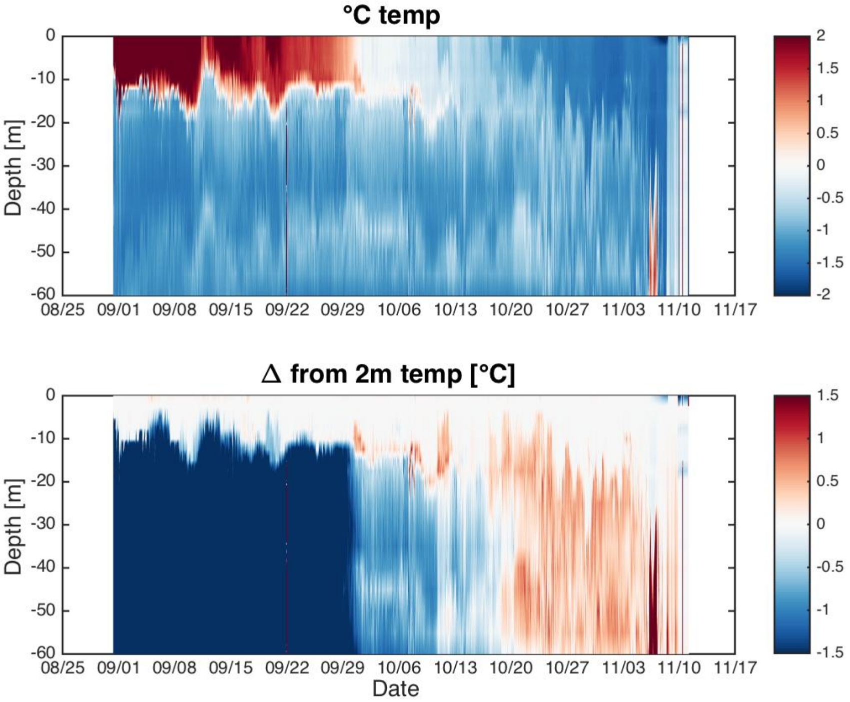

Figure A.4: Evolution of the upper ocean prior to freeze up as measured by UpTempO buoy 2013-16-Healy (6) during the fall of 2013.

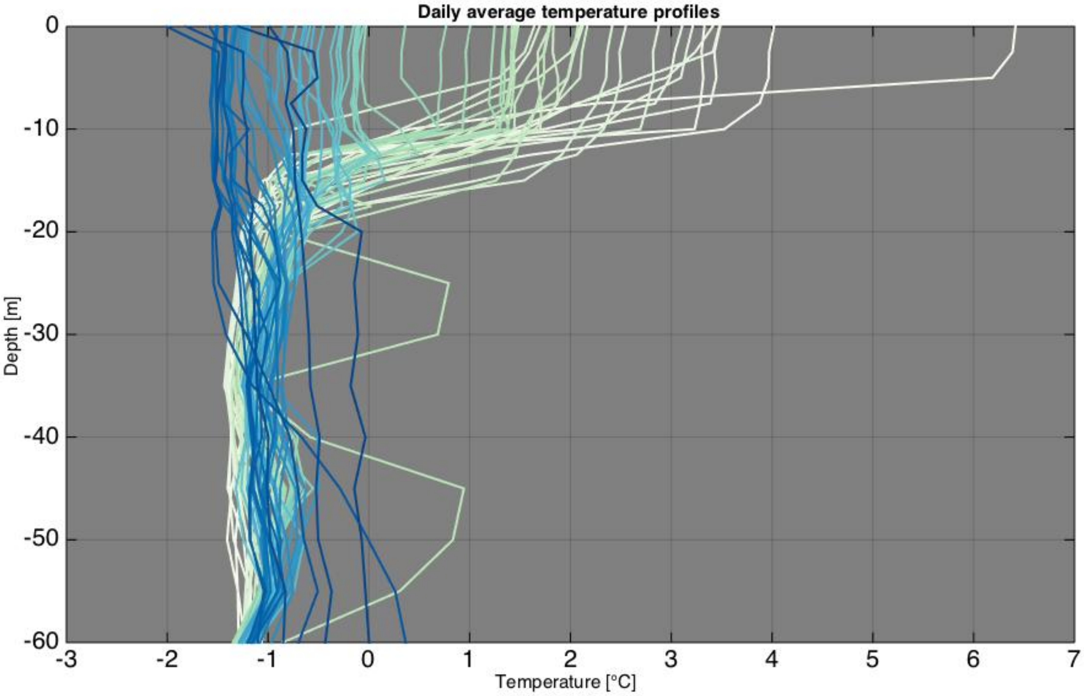

Figure A.5: Evolution of the upper ocean prior to freeze up as measured by UpTempO buoy 2013-16-Healy (6) during the fall of 2013, as shown by line plots for each day of the fall season.

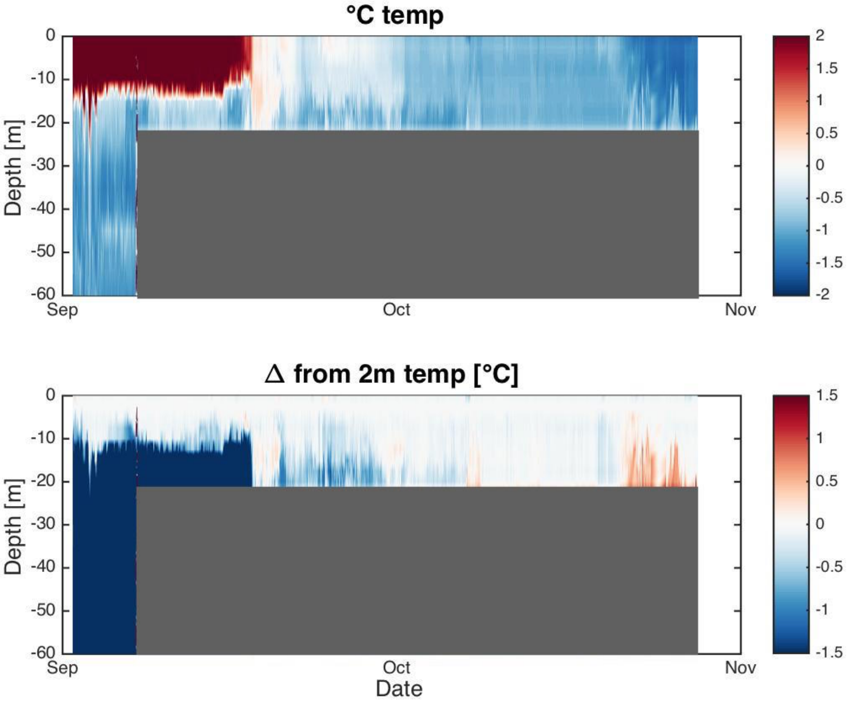

Figure A.6: Evolution of the upper ocean prior to freeze up as measured by UpTempO buoy 2013-17-Healy (7) during the fall of 2013.

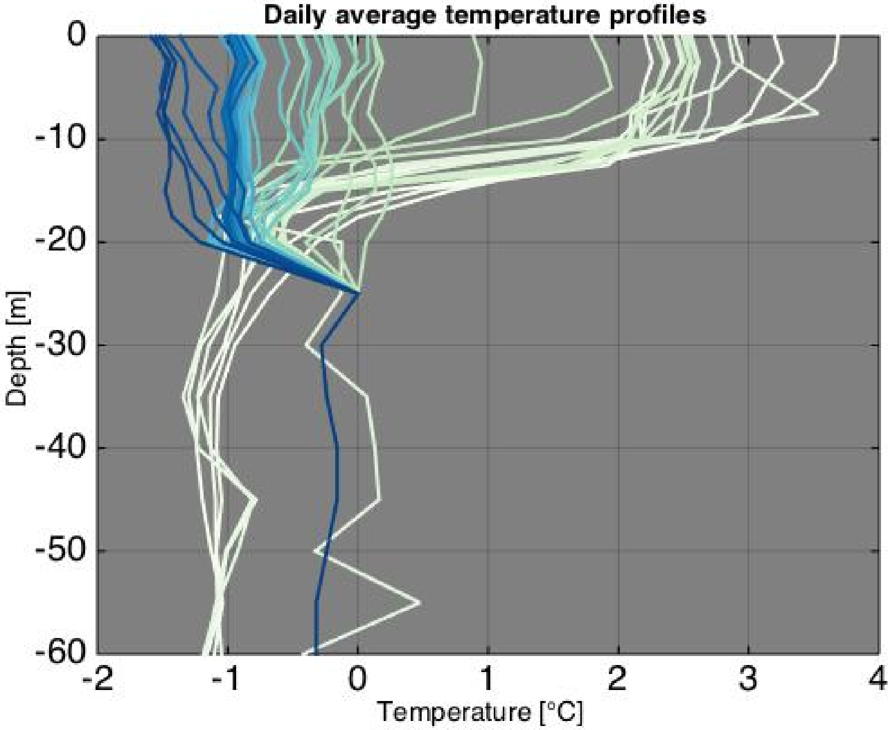

Figure A.7: Evolution of the upper ocean prior to freeze up as measured by UpTempO buoy 2013-17-Healy (7) during the fall of 2013, as shown by line plots for each day of the fall season.

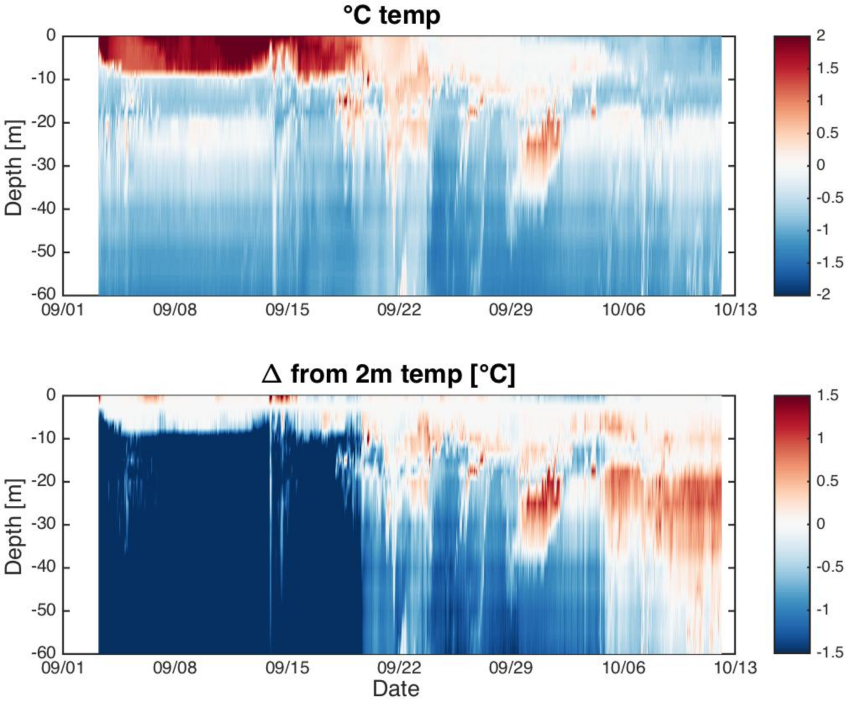

Figure A.8: Evolution of the upper ocean prior to freeze up as measured by UpTempO buoy 2013-18-Healy (8) during the fall of 2013.

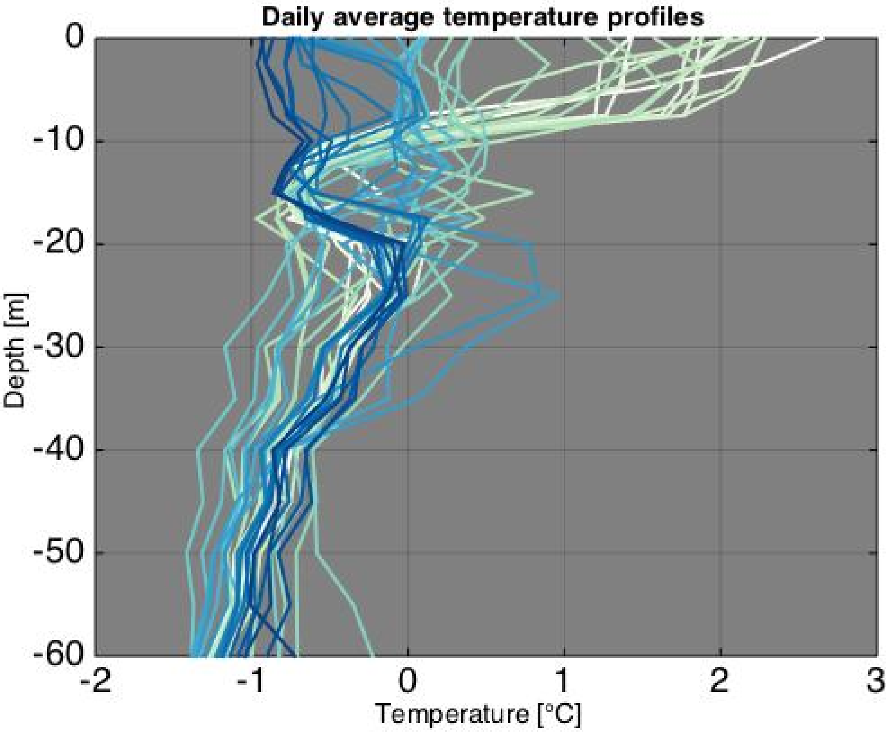

Figure A.9: Evolution of the upper ocean prior to freeze up as measured by UpTempO buoy 2013-18-Healy (8) during the fall of 2013, as shown by line plots for each day of the fall season.

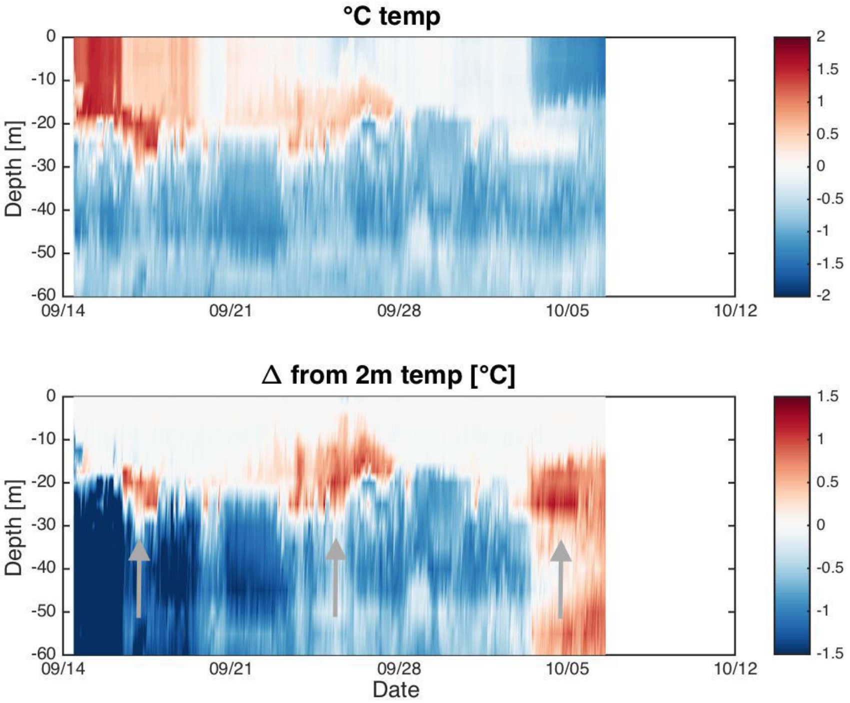

Figure A.10: Evolution of the upper ocean prior to freeze up as measured by UpTempO buoy 2014-14-Mirai (16) during the fall of 2014.

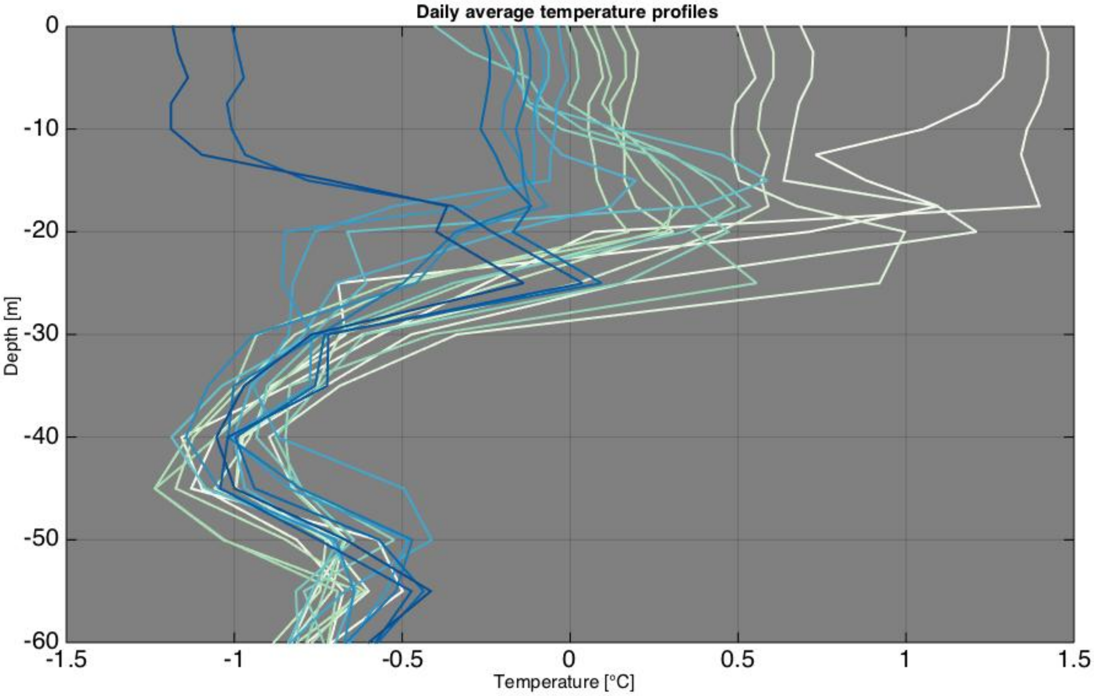

Figure A.11: Evolution of the upper ocean prior to freeze up as measured by UpTempO buoy 2014-14-Mirai (16) during the fall of 2014 as shown by line plots for each day of the fall season.

A.3 Discussion

At the end of the fall season, the temperatures measured below the surface mixed layer are consistently warmer than the summer mixed layer. This suggests that the summer mixed layer continues to cool independently from the rWML previously described. The summer halocline persists until ice growth begins and brine is rejected from the growing ice. This supports the relative thermal independence of the surface layer from the winter mixed layer below. However, the fact that this winter mixed layer is so warm suggests that perhaps it isn't that much of a winter mixed layer after all and rather a remnant of when the ice cover was more persistent. The layers observed in these profiles are significantly above freezing (by +0.5°C or so), and the amount of heat content that deeper column represents is non-trivial.

The summer halocline shown in Figure 2.6 persists into the early winter because the ice has not yet formed and released the brine necessary to fill the salinity void in the upper ocean. What is remarkable here is not that the summer halocline persists, but that, in at least the profile for buoys 6 and 16 (Figures A.4 and A.10, cools to temperatures lower than the winter halocline.

CTD profiles extending well past the onset of ice formation might address this: does the summer mixed layer persist when ice is present and the salinity deficit of the summer mixed layer is filled in? The increasing stratification of the upper ocean, especially in the Beaufort sea [Jackson et al., 2010] is likely a contributing factor to this. The summer mixed layer is buoyantly stable in part because it is fresher than the winter mixed layer. This means that the freezing point of the water contained in this layer would be lower than the freezing point of saltier water in the winter mixed layer. The winter mixed layer temperature then must be significantly (on the order of 0.5 bove the freezing point for the more saline water. This heat, if the summer halocline erodes with the release of brine from the surface and, could contact the sea ice and would severely limit growth rates late into the season. If the warmer winter mixed layer does not impact the ice growth, it means that the summer halocline is not disappearing over the winter. This suggests that the winter mixed layer may be a relic of the old Arctic with permanent ice cover and will likely continue to warm due to heat entrained in NSTMs.

Appendix B

WOD data sources

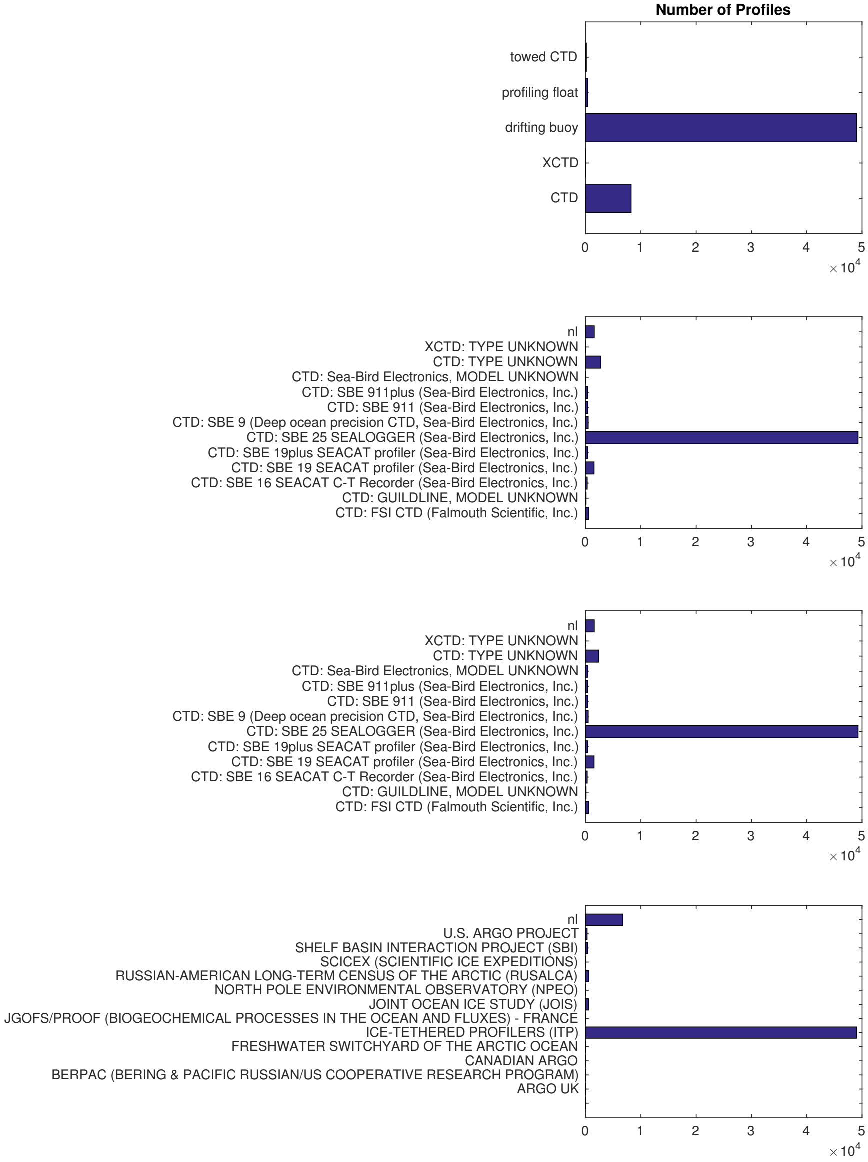

Figure B.1: WOD profiles sorted by type (top figure), temperature sensor (middle figure), and salinity sensor (bottom figure).

Figure B.2: Complete list of WOD projects supplying data to the analysis.

Bibliography

Knut Aagaard, L.K. Coachman, and Eddy Carmack. On the halocline of the Arctic Ocean*. Deep Sea Research, 28(6):529–545, 1981.

ABS. Low Temperature Operations Guidance for Arctic Shipping. Technical report, American Bureau of Shipping, Houston, TX, 2009. URL `www.eagle.org`.

Kevin R. Arrigo. Phytoplankton dynamics within 37 Antarctic coastal polynya systems. Journal of Geophysical Research, 108(C8):3271, 2003. ISSN 0148-0227. doi: 10.1029/2002JC001739. URL `http://doi.wiley.com/10.1029/2002JC001739`.

R G Barry, M C Serreze, J A Maslanik, and R H Preller. THE ARCTIC SEA ICE-CLI MATE SYSTEM : OBSERVATIONS AND. Reviews of Geophysics, 31(4):397–422, 1993.

C.M. Bitz and William H. Lipscomb. An energy-conserving thermodynamic model of sea ice. Journal of Geophysical Research, 104:15699–15677, 1999. ISSN 1098-6596. doi: 10.1017/CBO9781107415324.004.

BOEM. Report to the Secretary of the Interior: Review of Shell's 2012 Alaska Offshore Oil and Gas Exploration Program. Technical report, Bureau of Environmental Management, 2013. URL `http://www.doi.gov/news/pressreleases/upload/Shell-report-3-8-13-Final.pdf`.

Michael Bosilovich, Santha Akella, Lawrence Coy, Richard Cullather, Clara Draper, Ronald Gelaro, Robin Kovach, Quing Liu, Andrea Molod, Peter Norris, Krzysztof Wargan, Winston Chao, Rolf Reichle, Lawrence Takacs, Yury Vikhliaev, Steve Bloom, Allison Collow, Stacey Firth, Gordon Labow, Gary Partyka, Steven Pawson, Oreste Reale, Siegfried D. Schubert, and Max Suarez. MERRA-2 : Initial Evaluation of the Climate. NASA Technical Report Series on Global Modeling and Data Assimilation, 43(September), 2015.

P. Bourgain and J.C. Gascard. The Arctic Ocean halocline and its interannual variability from 1997 to 2008. Deep Sea Research Part I: Oceanographic Research Papers, 58(7):745–756, jul 2011. ISSN 09670637. doi: 10.1016/j.dsr.2011.05.001. URL `http://linkinghub.elsevier.com/retrieve/pii/S0967063711000884`.

T.P. Boyer, J. I. Antonov, O. K. Baranova, C. Coleman, H. E. Garcia, A. Grodsky, D. R. Johnson, R. A. Locarnini, A. V. Mishonov, T.D. O'Brien, C.R. Paver, J.R. Reagan, D. Seidov, I. V. Smolyar, and M. M. Zweng. World Ocean Database 2013, 2013.

Alice C Bradley, Scott Palo, Gabriel LoDolce, Doug Weibel, and Dale Lawrence. Air Deployed Micro Buoy measurement of temperatures in the marginal ice zone upper ocean during the MIZOPEX campaign. Journal of Atmospheric and Oceanic Technology, mar 2015. ISSN 0739-0572. doi: 10.1175/JTECH-D-14-00209.1. URL `http://dx.doi.org/10.1175/JTECH-D-14-00209.1`.

David H Bromwich. An Extraordinary Katabatic Wind Regime at Terra Nova Bay, Antarctica. Monthly Weather Review, 117:688–695, 1989.

David H Bromwich. The katabatic wind regime near Terra Nova Bay, Antarctica. Antarctic Journal, pages 1988–1990, 1990.

G. Budillon and G. Spezie. Thermohaline structure and variability in the Terra Nova Bay polynya, Ross Sea. Antarctic Science, 12(04):493–508, may 2000. ISSN 0954-1020. doi: 10.1017/S0954102000000572. URL `http://www.journals.cambridge.org/abstract_S0954102000000572`.

Giorgio Budillon, Giannetta Fusco, Emanuela Rusciano, and Giancarlo Spezie. Terra Nova Bay Polynya: A small coastal area affecting basin scale oceanic conditions. Ocean Observations 2009, 2009.

G. Buffoni, A Cappelletti, and P Picco. An investigation of thermohaline circulation in Terra Nova Bay. Antarctic Science, 14(I):83–92, 2002.

John J. Cassano, James Maslanik, Chris Zappa, Arnold L. Gordon, and Shelley L. Knuth. Observations of Antarctic Polynya With Unmanned Aircraft Systems. EOS, 91(28):2009–2010, 2010.

John J Cassano, Mark W Seefeldt, Scott Palo, Shelley L Knuth, Alice C Bradley, Paul D Herrman, Peter A Kernebone, and Nick J Logan. Observations of the atmosphere and surface state over Terra Nova Bay, Antarctica, using unmanned aerial systems. Earth System Science Data, 8(1):115–126, mar 2016. ISSN 1866-3516. doi: 10.5194/essd-8-115-2016. URL `http://www.earth-syst-sci-data.net/8/115/2016/`.

D. J. Cavalieri, C. L. Parkinson, P. Gloersen, and H. J. Zwally. Sea Ice Concentrations from Nimbus-7 SMMR and DMSP SSM/I-SSMIS Passive Microwave Data, Version 1., 1996a.

D. J. Cavalieri, C. L. Parkinson, P. Gloersen, and H. J. Zwally. Sea Ice Concentrations from Nimbus-7 SMMR and DMSP SSM/I-SSMIS Passive Microwave Data, Version 1, 1996b.

Achille Ciappa and Giorgio Budillon. The Terra Nova Bay (Antarctica) polynya observed by MODIS ice surface temperature imagery from May to June 2009. International Journal of Remote Sensing, 33(14):4567–4582, jul 2012. ISSN 0143-1161. doi: 10.1080/01431161.2011.652314. URL `http://www.tandfonline.com/doi/abs/10.1080/01431161.2011.652314`.

Lawrence K Coachman, Knut Aagaard, and Richard B Tripp. Bering Strait: the regional physical oceanography. University of Washington Press, 1975.

Josefino C Comiso, Donald J Cavalieri, Claire L Parkinson, and Per Gloersen. Passive Microwave Algorithms for Sea Ice Concentration: A Comparison of Two Techniques. Remote Sensing of Environment, 4257(96), 1997.

RI Cullather, DH Bromwich, and MC Serreze. The Atmospheric Hydrologic Cycle over the Arctic Basin from Reanalyses. Part I: Comparison with Observations and Previous Studies*. Journal of Climate, 13:923–937, 2000.

JA Curry, JL Schramm, and EE Ebert. Sea ice-albedo climate feedback mechanism. Journal of Climate, 8, 1995.

Yanni Ding, James A. Carton, Gennady A. Chepurin, Michael Steele, and Sirpa Hakkinen. Seasonal heat and freshwater cycles in the Arctic Ocean in CMIP5 coupled models. Journal of Geophysical Research: Oceans, 121(4):2043–2057, apr 2016. ISSN 21699275. doi: 10.1002/2015JC011124. URL `http://doi.wiley.com/10.1002/2015JC011124`.

Yu. P. Doronin and D. E. Kheisin. Sea Ice. Gidrometeoizdat Publishers, Leningrad, translated edition, 1975.

Robert Drucker. Observations of ice thickness and frazil ice in the St. Lawrence Island polynya from satellite imagery, upward looking sonar, and salinity/temperature moorings. Journal of Geophysical Research, 108 (C5):3149, 2003. ISSN 0148-0227. doi: 10.1029/2001JC001213. URL `http://www.agu.org/pubs/crossref/2003/2001JC001213.shtml`.

Hajo Eicken. From the microscopic, to the macroscopic, to the regional scale: growth, microstructure and properties of sea ice. Sea ice: an introduction to its physics, chemistry, biology and geology, pages 22–81, 2003.

WJ Emery, WG Lee, and L Magaard. Geographic and Seasonal Distributions of Brunt-\vaisala Frequency and Rossby Radii in the North Pacific and North Atlantic. Journal of Physical Oceanography, 14:294–317, 1984.

S L Farrell, N Kurtz, L N Connor, B C Elder, C Leuschen, T Markus, D C McAdoo, B Panzer, J Richter-Menge, and J G Sonntag. A First Assessment of IceBridge Snow and Ice Thickness Data Over Arctic Sea Ice. IEEE Transactions on Geoscience and Remote Sensing, 50(6):2098–2111, 2012.

Ilker Fer. Weak Vertical Diffusion Allows Maintenance of Cold Halocline in the Central Arctic. Atmospheric and Oceanic Science Letters, 2(3):148–152, 2009.

F. Fetterer, K. Knowles, W. Meier, and M. Savoie. Sea Ice Index, updated daily, 2002.

N. P. Fofonoff. Physical properties of seawater: A new salinity scale and equation of state for seawater. Journal of Geophysical Research, 90(C2):3332, 1985. ISSN 0148-0227. doi: 10.1029/JC090iC02p03332. URL `http://doi.wiley.com/10.1029/JC090iC02p03332`.

C. Fowler, W. Emery, and M. Tschudi. 2013. Polar Pathfinder Daily 25 km EASE-Grid Sea Ice Motion Vectors. Version 2., 2013.

Giannetta Fusco, Giorgio Budillon, and Giancarlo Spezie. Surface heat fluxes and thermohaline variability in the Ross Sea and in Terra Nova Bay polynya. Continental Shelf Research, 29(15):1887–1895, aug 2009. ISSN 02784343. doi: 10.1016/j.csr.2009.07.006. URL `http://linkinghub.elsevier.com/retrieve/pii/S0278434309002131`.

R. J. Galley, D. Babb, M. Ogi, B. G. T. Else, N.-X. Geilfus, O. Crabeck, D. G. Barber, and S. Rysgaard. Replacement of multiyear sea ice and changes in the open water season duration in the Beaufort Sea since 2004. Journal of Geophysical Research: Oceans, 121(3):1806–1823, mar 2016. ISSN 21699275. doi: 10.1002/2015JC011583. URL `http://doi.wiley.com/10.1002/2015JC011583`.

Katharine A Giles, Seymour W Laxon, Andy L Ridout, Duncan J Wingham, and Sheldon Bacon. Western Arctic Ocean freshwater storage increased by wind-driven spin-up of the Beaufort Gyre. Nature Geoscience, 5(3):194–197, 2012. ISSN 1752-0894. doi: 10.1038/ngeo1379. URL `http://dx.doi.org/10.1038/ngeo1379`.

Adrian E Gill. Atmosphere-ocean dynamics, volume 30. Academic press, 1982.

Global Modeling and Assimilation Office (GMAO). MERRA-2 instU_2d_asm_Nx: 2d,diurnal,Instantaneous,Single-Level,Assimilation,Single-Level Diagnostics V5.12.4, 2015.

Mats A. Granskog, Alexey K. Pavlov, Slawomir Sagan, Piotr Kowalczuk, Anna Raczkowska, and Colin A. Stedmon. Effect of sea ice melt on inherent optical properties and vertical distribution of solar radiant heating in Arctic surface waters. Journal of Geophysical Research: Oceans, 120:7028–7039, 2015. doi: 10.1002/2014JC010632.

John D. Guthrie, James H. Morison, and Ilker Fer. Revisiting internal waves and mixing in the Arctic Ocean. Journal of Geophysical Research: Oceans, 118(8):3966–3977, aug 2013. ISSN 21699275. doi: 10.1002/jgrc.20294. URL `http://doi.wiley.com/10.1002/jgrc.20294`.

Dororthy K. Hall, Jeffrey R. Key, Kimberly A. Casey, George A. Riggs, and Donald J. Cavalieri. Sea ice surface temperature product from MODIS. IEEE Transactions on Geoscience and Remote Sensing, 42(5):1076–1087, 2004. URL `http://ieeexplore.ieee.org/xpls/abs_all.jsp?arnumber=1298977`.

Øistein Harsem, Knut Heen, J.M.P. Rodrigues, and Terje Vassdal. Oil exploration and sea ice projections in the Arctic. Polar Record, 51(01):91–106, oct 2013. ISSN 0032-2474. doi: 10.1017/S0032247413000624. URL `http://journals.cambridge.org/abstract_S0032247413000624`.

P. J. Hezel, X. Zhang, C. M. Bitz, B. P. Kelly, and F. Massonnet. Projected decline in spring snow depth on Arctic sea ice caused by progressively later autumn open ocean freeze-up this century. Geophysical Research Letters, 39 (17):L17505, sep 2012. ISSN 0094-8276. doi: 10.1029/2012GL052794. URL `http://www.agu.org/pubs/crossref/2012/2012GL052794.shtml`.

D. Hirano, Y. Fukamachi, E. Watanabe, K. I. Ohshima, K. Iwamoto, A. R. Mahoney, H. Eicken, D. Simizu, and T. Tamura. A wind-driven, hybrid latent and sensible heat coastal polynya off Barrow, Alaska. Journal of Geophysical Research : Oceans, 121:1–14, 2016. ISSN 2169-9291. doi: 10.1002/2015JC011486.Received.

Marika M. Holland, Cecilia M. Bitz, and Bruno Tremblay. Future abrupt reductions in the summer Arctic sea ice. Geophysical Research Letters, 33(23): L23503, dec 2006. ISSN 0094-8276. doi: 10.1029/2006GL028024. URL `http://doi.wiley.com/10.1029/2006GL028024`.

Greg Holloway and Andrey Proshutinsky. Role of tides in Arctic ocean/ice climate. Journal of Geophysical Research: Oceans, 112(4):1–10, 2007. ISSN 21699291. doi: 10.1029/2006JC003643.

J. K. Hutchings and I. G. Rigor. Role of ice dynamics in anomalous ice conditions in the Beaufort Sea during 2006 and 2007. Journal of Geophysical Research: Oceans, 117(5): 1–14, 2012. ISSN 21699291. doi: 10.1029/2011JC007182.

J. M. Jackson, E. C. Carmack, F. a. McLaughlin, S. E. Allen, and R. G. Ingram. Identification, characterization, and change of the near-surface temperature maximum in the Canada Basin, 19932008. Journal of Geophysical Research, 115 (C5):C05021, may 2010. ISSN 0148-0227. doi: 10.1029/2009JC005265. URL `http://doi.wiley.com/10.1029/2009JC005265`.

Jennifer M. Jackson, William J. Williams, and Eddy C. Carmack. Winter sea-ice melt in the Canada Basin, Arctic ocean. Geophysical Research Letters, 39(3):2–7, 2012. ISSN 00948276. doi: 10.1029/2011GL050219.

E Peter Jones, Leif G Anderson, and James H Swift. Distribution of Atlantic and Pacific waters in the upper Arctic Ocean : Implications for circulation distinguish between oceanic waters of Pacific. Geophysical Research Letters, 25(6):765–768, 1998.

L. Kaleschke, X. Tian-Kunze, N. Maaß, M. Mäkynen, and M. Drusch. Sea ice thickness retrieval from SMOS brightness temperatures during the Arctic freeze-up period. Geophysical Research Letters, 39(5):1–5, 2012. ISSN 00948276. doi: 10.1029/2012GL050916.

E Kalnay, M Kanamitsu, R Kistler, W Collins, D Deaven, L Gandin, M Iredell, S Saha, G White, J Woollen, Y Zhu, M Chelliah, W Ebisuzaki, W Higgins, J Janowiak, K C Mo, C Ropelewski, J Wang, A Leetmaa, R Reynolds, Roy Jenne, and Dennis Joseph. The NCEP/NCAR 40-year reanalysis project. Bulletin of the American Meteorological Society, 77(3):437–471, 1996.

Vladimir M. Kattsov and John E. Walsh. Twentieth-century trends of Arctic precipitation from observational data and a climate model simulation. Journal of Climate, 13(8):1362–1370, 2000. ISSN 08948755. doi: 10.1175/1520-0442(2002)015¡0800:COTCTO¿2.0.CO;2.

Vladimir M. Kattsov, Vlarimir E. Ryabinin, James E. Overland, Mark C. Serreze, Martin Visbeck, John E. Walsh, Walt Meier, and Xiangdong Zhang. Arctic sea-ice change: a grand challenge of climate science. Journal of Glaciology, 56(200):1115–1121, dec 2010. ISSN 00221430. doi: 10.3189/002214311796406176.

S. L. Knuth, J. J. Cassano, J. a. Maslanik, P. D. Herrmann, P. a. Kernebone, R. I. Crocker, and N. J. Logan. Unmanned aircraft system measurements of the atmospheric boundary layer over Terra Nova Bay, Antarctica. Earth System Science Data, 5(1):57–69, feb 2013. ISSN 1866-3516. doi: 10.5194/essd-5-57-2013. URL `http://www.earth-syst-sci-data.net/5/57/2013/`.

Shelley L. Knuth and John J. Cassano. An Analysis of Near-Surface Winds, Air Temperature, and Cyclone Activity in Terra Nova Bay, Antarctica, from 1993 to 2009. Journal of Applied Meteorology and Climatology, 50(3):662–680, mar 2011. ISSN 1558-8424. doi: 10.1175/2010JAMC2507.1. URL `http://journals.ametsoc.org/doi/abs/10.1175/2010JAMC2507.1`.

R. Krishfield, J. Toole, a. Proshutinsky, and M-L. Timmermans. Automated Ice-Tethered Profilers for Seawater Observations under Pack Ice in All Seasons. Journal of Atmospheric and Oceanic Technology, 25(11):2091–2105, nov 2008. ISSN 0739-0572. doi: 10.1175/2008JTECHO587.1. URL `http://journals.ametsoc.org/doi/abs/10.1175/2008JTECHO587.1`.

R. A. Krishfield, A. Proshutinsky, K. Tateyama, W. J. Williams, E. C. Carmack, F. A. McLaughlin, and M.-L. Timmermans. Deterioration of perennial sea ice in the Beaufort Gyre from 2003 to 2012 and its impact on the oceanic freshwater cycle. Journal of Geophysical Research: Oceans, 119(2):1271–1305, feb 2014. ISSN 21699275. doi: 10.1002/2013JC008999. URL `http://doi.wiley.com/10.1002/2013JC008999`.

DD Kurtz and DH Bromwich. Satellite Observed Behavior of the Terra Nova Bay Polynya. Journal of Geophysical Research: ..., 88:9717–9722, 1983. URL `http://onlinelibrary.wiley.com/doi/10.1029/JC088iC14p09717/full`.

N. Kurtz, M. S. Studinger, J. Harbeck, V. Onana, and D. Yi. IceBridge L4 Sea Ice Freeboard, Snow Depth, and Thickness, Version 1 (subset: Arctic 2012-2015), 2015.

R. Kwok and G. F. Cunningham. ICESat over Arctic sea ice: Estimation of snow depth and ice thickness. Journal of Geophysical Research, 113(C8): C08010, aug 2008. ISSN 0148-0227. doi: 10.1029/2008JC004753. URL `http://doi.wiley.com/10.1029/2008JC004753`.

R Kwok and G F Cunningham. Variability of Arctic sea ice thickness and volume from CryoSat-2. Philosophical Transactions of the Royal Society of London A: Mathematical, Physical and Engineering Sciences, 373(2045):20140157, 2015. ISSN 1364-503X, 1471-2962. doi: 10.1098/rsta.2014.0157.

R. Kwok and D. a. Rothrock. Decline in Arctic sea ice thickness from submarine and ICESat records: 1958-2008. Geophysical Research Letters, 36(15): n/a–n/a, aug 2009. ISSN 00948276. doi: 10.1029/2009GL039035. URL `http://doi.wiley.com/10.1029/2009GL039035`.

Seymour W. Laxon, Katharine A. Giles, Andy L. Ridout, Duncan J. Wingham, Rosemary Willatt, Robert Cullen, Ron Kwok, Axel Schweiger, Jinlun Zhang, Christian Haas, Stefan Hendricks, Richard Krishfield, Nathan Kurtz, Sinead Farrell, and Malcolm Davidson. CryoSat-2 estimates of Arctic sea ice thickness and volume. Geophysical Research Letters, 40(4):732–737, 2013. ISSN 00948276. doi: 10.1002/grl.50193.

M.J. Lewis, J.L. Tison, B. Weissling, B. Delille, S.F. Ackley, F. Brabant, and H. Xie. Sea ice and snow cover characteristics during the winterspring transition in the Bellingshausen Sea: An overview of SIMBA 2007. Deep Sea Research Part II: Topical Studies in Oceanography, 58(9-10):1019–1038, may 2011. ISSN 09670645. doi: 10.1016/j.dsr2.2010.10.027. URL `http://linkinghub.elsevier.com/retrieve/pii/S096706451000305X`.

Sigrid Lind, Randi B. Ingvaldsen, and Tore Furevik. Arctic layer salinity controls heat loss from deep Atlantic layer in seasonally ice-covered areas of the Barents Sea. Geophysical Research Letters, pages 5233–5242, 2016. ISSN 00948276. doi: 10.1002/2016GL068421. URL `http://doi.wiley.com/10.1002/2016GL068421`.

R. Lindsay, M. Wensnahan, a. Schweiger, and J. Zhang. Evaluation of Seven Different Atmospheric Reanalysis Products in the Arctic*. Journal of Climate, 27(7): 2588–2606, apr 2014. ISSN 0894-8755. doi: 10.1175/JCLI-D-13-00014.1. URL `http://journals.ametsoc.org/doi/abs/10.1175/JCLI-D-13-00014.1`.

Camille Lique and Michael Steele. Seasonal to decadal variability of Arctic Ocean heat content: A model-based analysis and implications for autonomous observing systems. Journal of Geophysical Research: Oceans, 118(4):1673–1695, apr 2013. ISSN 21699275. doi: 10.1002/jgrc.20127. URL `http://doi.wiley.com/10.1002/jgrc.20127`.

G E Liston, M Sturm, and Fort Collins. The role of winter sublimation in the Arctic moisture budget *. (August 2003):25–29, 2004.

Ricardo Alejandro Locarnini. Water masses and circulation in the Ross Gyre and environs. Texas A&M University, Office of Graduate Studies, 1994.

V I Lytle and S.F. Ackley. Heat flux through sea ice in the western Weddell Sea: Convective and conductive transfer processes. Journal of Geophysical Research, 101(C4):8853–8868, 1996.

Marko Mäkynen, Bin Cheng, and Markku Similä. On the accuracy of thin-ice thickness retrieval using MODIS thermal imagery over Arctic first-year ice. Annals of

Glaciology, 54(62):87–96, 2013. ISSN 02603055. doi: 10.3189/2013AoG62A166. URL `http://www.igsoc.org/annals/54/62/a62A166.html`.

S Martin. Frazil Ice in Rivers and Oceans. Annual Review of Fluid Mechanics, 13(1):379–397, 1981. doi: 10.1146/annurev.fl.13.010181.002115. URL `http://dx.doi.org/10.1146/annurev.fl.13.010181.002115`.

J. A. Maslanik, C. Fowler, J. Stroeve, S. Drobot, J. Zwally, D. Yi, and W. Emery. A younger, thinner Arctic ice cover: Increased potential for rapid, extensive sea-ice loss. Geophysical Research Letters, 34(24):L24501, dec 2007. ISSN 0094-8276. doi: 10.1029/2007GL032043. URL `http://doi.wiley.com/10.1029/2007GL032043`.

James Maslanik, Julienne Stroeve, Charles Fowler, and William Emery. Distribution and trends in Arctic sea ice age through spring 2011. Geophysical Research Letters, 38(13):2–7, jul 2011. ISSN 0094-8276. doi: 10.1029/2011GL047735. URL `http://www.agu.org/pubs/crossref/2011/2011GL047735.shtml`.

G. a. Maykut and Miles G. McPhee. Solar heating of the Arctic mixed layer. Journal of Geophysical Research, 100(C12):24691, 1995. ISSN 0148-0227. doi: 10.1029/95JC02554. URL `http://doi.wiley.com/10.1029/95JC02554`.

Gary A Maykut. Energy Exchange Over Young Sea Ice in the Central Arctic by theoretical calculations Fe. Journal of Geophysical Research, 83(8):3646–3658, 1978.

Gary A Maykut. An Introduction to Ice in the Polar Oceans. Technical report, University of Washington, Department of Atmospheric Sciences/Geophysical Program, Seattle, WA, 1985.

Gary A Maykut. The surface heat and mass balance. In The geophysics of sea ice, pages 395–463. Springer, 1986.

F. McLaughlin, E. Carmack, A. Proshutinsky, R.A. Krishfield, C. Guay, M. Yamamoto-Kawai, J.M. Jackson, and B. Williams. The rapid response of the Canada Basin to climate forcing: From bellwether to alarm bells. Oceanography, 24(3), 2011. doi: http://dx.doi.org/10.5670/oceanog.2011.66.

Miles G McPhee, Timothy P Stanton, James H Morison, and Douglas G Martinson. Freshening of the upper ocean in the Arctic: Is perrenial sea ice disappearing? Geophysical Research Letters, 25(10):1729–1732, 1998.

Humfrey Melling, David A. Riedel, and Z. Gedalof. Trends in the draft and extent of seasonal pack ice, Canadian Beaufort Sea. Geophysical Research Letters, 32(24):1–5, 2005. ISSN 00948276. doi: 10.1029/2005GL024483.

Peter N. Mikhalevsky, Alexander N. Gavrilov, and Arthur B. Baggeroer. Transarctic acoustic propagation experiment and climate monitoring in the Arctic. IEEE Journal of Oceanic Engineering, 24(2):183–201, 1999. ISSN 03649059. doi: 10.1109/48.757270.

F J Millero and F Huang. The density of seawater as a function of salinity (5 to 70 g kg-1) and temperature (273.15 to 363.15K). Ocean Science, 5:91–100, 2009.

Keisuke Mizuno and Tomowo Watanabe. Preliminary Results of in-situ XCTD / CTD Comparison Test. Journal of Oceanography, 54:373–380, 1998.

James Morison, Ron Kwok, Cecilia Peralta-Ferriz, Matt Alkire, Ignatius Rigor, Roger Andersen, and Mike Steele. Changing Arctic Ocean freshwater pathways. Nature, 481(7379):66–70, jan 2012. ISSN 1476-4687. doi: 10.1038/nature10705. URL `http://www.ncbi.nlm.nih.gov/pubmed/22222749`.

M. Nicolaus, C. Katlein, J. Maslanik, and S. Hendricks. Changes in Arctic sea ice result in increasing light transmittance and absorption. Geophysical Research Letters, 39(24):1–6, 2012. ISSN 00948276. doi: 10.1029/2012GL053738.

S. J. Norris, I. M. Brooks, B. I. Moat, M. J. Yelland, G. de Leeuw, R. W. Pascal, and B. Brooks. Near-surface measurements of sea spray aerosol production over whitecaps in the open ocean. Ocean Science, 9(1):133–145, feb 2013. ISSN 1812-0792. doi: 10.5194/os-9-133-2013. URL `http://www.ocean-sci.net/9/133/2013/`.

Alejandro H. Orsi and Christina L. Wiederwohl. A recount of Ross Sea waters. Deep Sea Research Part II: Topical Studies in Oceanography, 56(13-14): 778–795, jun 2009. ISSN 09670645. doi: 10.1016/j.dsr2.2008.10.033. URL `http://linkinghub.elsevier.com/retrieve/pii/S0967064508003597`.

J. Ovadnevaite, a. Manders, G. de Leeuw, D. Ceburnis, C. Monahan, a. I. Partanen, H. Korhonen, and C. D. O'Dowd. A sea spray aerosol flux parameterization encapsulating wave state. Atmospheric Chemistry and Physics, 14(4): 1837–1852, feb 2014. ISSN 1680-7324. doi: 10.5194/acp-14-1837-2014. URL `http://www.atmos-chem-phys.net/14/1837/2014/`.

James E. Overland and Muyin Wang. When will the summer Arctic be nearly sea ice free? Geophysical Research Letters, 40(10):2097–2101, 2013. ISSN 00948276. doi: 10.1002/grl.50316.

W Scott Pegau. Inherent optical properties of the central Arctic surface waters. Journal of Geophysical Research, 107(C10), 2002. doi: 10.1029/2000JC000382.

P. Pemberton and J. Nilsson. The response of the central Arctic Ocean stratification to freshwater perturbations. Journal of Geophysical Research: Oceans, 121(1):792–817, jan 2016. ISSN 21699275. doi: 10.1002/2015JC011003. URL `http://doi.wiley.com/10.1002/2015JC011003`.

Cecilia Peralta-Ferriz and Rebecca A. Woodgate. Seasonal and interannual variability of pan-Arctic surface mixed layer properties from 1979 to 2012 from hydrographic data, and the dominance of stratification for multiyear mixed layer depth shoaling. Progress in Oceanography, 134:19–53, 2015. ISSN 00796611. doi: 10.1016/j.pocean.2014.12.005. URL `http://dx.doi.org/10.1016/j.pocean.2014.12.005`.

DK Perovich, JA Richter-Menge, K.F. Jones, Bonnie Light, Bruce Elder, Christopher Polashenski, Daniel Laroche, Thorsten Markus, and Ronald Lindsay. Arctic sea-ice melt in 2008 and the role of solar heating. Annals of Glaciology, 52(57):355–359, may 2011. ISSN 02603055. doi: 10.3189/172756411795931714.

Don Perovich, Jaqueline Richter-Menge, Chris Polashenski, Bruce Elder, Todd Arbetter, and Owen Brennick. Sea ice mass balance observations from the North Pole Environmental Observatory. Geophysical Research Letters, 41:2019–2025, 2014. doi: 10.1002/2014GL059356.Received. URL `http://www.sgmeet.com/osm2012/viewabstract2.asp?AbstractID=10081` `http://onlinelibrary.wiley.com/doi/10.1002/2014GL059356/full`.

Donald K. Perovich and Christopher Polashenski. Albedo evolution of seasonal Arctic sea ice. Geophysical Research Letters, 39(8):n/a–n/a, apr 2012. ISSN 00948276. doi: 10.1029/2012GL051432. URL `http://doi.wiley.com/10.1029/2012GL051432`.

Donald K. Perovich, Thomas C Grenfell, Jacqueline A Richter-Menge, Bonnie Light, Walter B Tucker III, and Hajo Eicken. Thin and thinner: Sea ice mass balance measurements during SHEBA. Journal of Geophysical Research, 108(C3):8050, 2003. ISSN 0148-0227. doi: 10.1029/2001JC001079. URL `http://doi.wiley.com/10.1029/2001JC001079`.

Donald K. Perovich, Bonnie Light, Hajo Eicken, Kathleen F. Jones, Kay Runciman, and Son V. Nghiem. Increasing solar heating of the Arctic Ocean and adjacent seas, 19792005: Attribution and role in the ice-albedo feedback. Geophysical Research Letters, 34(19):L19505, oct 2007. ISSN 0094-8276. doi: 10.1029/2007GL031480. URL `http://doi.wiley.com/10.1029/2007GL031480`.

Donald K. Perovich, Jacqueline a. Richter-Menge, Kathleen F. Jones, and Bonnie Light. Sunlight, water, and ice: Extreme Arctic sea ice melt during the summer of 2007. Geophysical Research Letters, 35(11):L11501, jun 2008. ISSN 0094-8276. doi: 10.1029/2008GL034007. URL `http://doi.wiley.com/10.1029/2008GL034007`.

P. Ola G Persson. Onset and end of the summer melt season over sea ice: Thermal structure and surface energy perspective from SHEBA. Climate Dynamics, 39(6):1349–1371, 2012. ISSN 09307575. doi: 10.1007/s00382-011-1196-9.

Bruce J Peterson, Robert M Holmes, James W McClelland, Charles J Vörösmarty, Richard B Lammers, Alexander I Shiklomanov, Igor a Shiklomanov, and Stefan Rahmstorf. Increasing river discharge to the Arctic Ocean. Science (New York, N.Y.), 298(5601):2171–2173, 2002. ISSN 00368075. doi: 10.1126/science.1077445.

Robert S. Pickart, Thomas J. Weingartner, Lawrence J. Pratt, Sarah Zimmermann, and Daniel J. Torres. Flow of winter-transformed Pacific water into the Western Arctic. Deep-Sea Research Part II: Topical Studies in Oceanography, 52(24-26):3175–3198, 2005. ISSN 09670645. doi: 10.1016/j.dsr2.2005.10.009.

Chris Polashenski, Donald Perovich, and Zoe Courville. The mechanisms of sea ice melt pond formation and evolution. Journal of Geophysical Research, 117 (C1):C01001, jan 2012. ISSN 0148-0227. doi: 10.1029/2011JC007231. URL `http://doi.wiley.com/10.1029/2011JC007231`.

Igor V. Polyakov, Andrey V. Pnyushkov, Robert Rember, Laurie Padman, Eddy C. Carmack, and Jennifer M. Jackson. Winter Convection Transports Atlantic Water Heat to the Surface Layer in the Eastern Arctic Ocean *. Journal of Physical Oceanography, 43: 2142–2155, 2013. doi: 10.1175/JPO-D-12-0169.1.

a. Preußer, S. Willmes, G. Heinemann, and S. Paul. Thin-ice dynamics and ice production in the Storfjorden polynya for winter seasons 2002/20032013/2014 using MODIS thermal infrared imagery. The Cryosphere, 9(3):1063–1073, 2015. ISSN 1994-0424. doi: 10.5194/tc-9-1063-2015. URL `http://www.the-cryosphere.net/9/1063/2015/`.

D. J. Pringle, Hajo Eicken, H. Joe Trodahl, and L. G E Backstrom. Thermal conductivity of landfast Antarctic and Arctic sea ice. Journal of Geophysical Research: Oceans, 112 (4):1–13, 2007. ISSN 21699291. doi: 10.1029/2006JC003641.

Andrey Proshutinsky, Richard Krishfield, Mary-louise Timmermans, John Toole, Eddy Carmack, Fiona Mclaughlin, William J Williams, Sarah Zimmermann, Motoyo Itoh, and Koji Shimada. Beaufort Gyre freshwater reservoir : State and variability from observations. Journal of Geophysical Research, 114:1–25, 2009. doi: 10.1029/2008JC005104.

Luc Rainville and Rebecca A. Woodgate. Observations of internal wave generation in the seasonally ice-free Arctic. Geophysical Research Letters, 36(23):1–5, 2009. ISSN 00948276. doi: 10.1029/2009GL041291.

Richard W. Reynolds, Nick A. Rayner, Thomas M. Smith, Diane C. Stokes, and Wanqiu Wang. An improved in situ and satellite SST analysis for climate. Journal of Climate, 15(13):1609–1625, 2002. ISSN 08948755. doi: 10.1175/1520-0442(2002)015¡1609:AIISAS¿2.0.CO;2.

Michele M. Rienecker, Max J. Suarez, Ronald Gelaro, Ricardo Todling, Julio Bacmeister, Emily Liu, Michael G. Bosilovich, Siegfried D. Schubert, Lawrence Takacs, Gi-Kong Kim, Stephen Bloom, Junye Chen, Douglas Collins, Austin Conaty, Arlindo da Silva, Wei Gu, Joanna Joiner, Randal D. Koster, Robert Lucchesi, Andrea Molod, Tommy Owens, Steven Pawson, Philip Pegion, Christopher R. Redder, Rolf Reichle, Franklin R. Robertson, Albert G. Ruddick, Meta Sienkiewicz, and Jack Woollen. MERRA: NASA's Modern-Era Retrospective Analysis for Research and Applications. Journal of Climate, 24(14):3624–3648, jul 2011. ISSN 0894-8755. doi: 10.1175/JCLI-D-11-00015.1. URL `http://journals.ametsoc.org/doi/abs/10.1175/JCLI-D-11-00015.1`.

Ignatius Rigor and Wendy Ermold. International Arctic Buoy Programme, 2008. URL `http://iabp.apl.washington.edu/`.

Ignatius G Rigor and Andreas Heiberg. International Arctic Buoy Program data report. NASA, (19980021246), 1997.

B. Rudels, L. G. Anderson, and E. P. Jones. Formation and evolution of the surface mixed layer and halocline of the Arctic Ocean. Journal of Geophysical Research, 101(C4):8807, 1996. ISSN 0148-0227. doi: 10.1029/96JC00143. URL `http://doi.wiley.com/10.1029/96JC00143`.

Karen Schwartz. As Global Warming Thaws Northwest Passage, a Cruise Sees Opportunity, jul 2016.

James a Screen and Ian Simmonds. The central role of diminishing sea ice in recent Arctic temperature amplification. Nature, 464(7293):1334–7, apr 2010. ISSN 1476-4687. doi: 10.1038/nature09051. URL `http://www.ncbi.nlm.nih.gov/pubmed/20428168`.

Joseph Sedlar, Michael Tjernström, Thorsten Mauritsen, Matthew D. Shupe, Ian M. Brooks, P. Ola G. Persson, Cathryn E. Birch, Caroline Leck, Anders Sirevaag, and Marcel Nicolaus. A transitioning Arctic surface energy budget: the impacts of solar zenith angle, surface albedo and cloud radiative forcing. Climate Dynamics, 37 (7-8):1643–1660, nov 2010. ISSN 0930-7575. doi: 10.1007/s00382-010-0937-5. URL `http://link.springer.com/10.1007/s00382-010-0937-5`.

Mark C. Serreze and Roger G. Barry. The Arctic Climate System. Cambridge University Press, New York, 2005.

Mark C. Serreze and Jennifer a. Francis. The Arctic Amplification Debate. Climatic Change, 76(3-4):241–264, mar 2006. ISSN 0165-0009. doi: 10.1007/s10584-005-9017-y. URL `http://link.springer.com/10.1007/s10584-005-9017-y`.

Mostafa H. Sharqawy, John H. Lienhard, and Syed M. Zubair. Thermophysical properties of seawater: a review of existing correlations and data. Desalination and Water Treatment, 16(1-3):354–380, aug 2012. ISSN 1944-3994. doi: 10.5004/dwt.2010.1079. URL `http://www.tandfonline.com/doi/abs/10.5004/dwt.2010.1079`.

W. J. Shaw, T. P. Stanton, M. G. McPhee, J. H. Morison, and D. G. Martinson. Role of the upper ocean in the energy budget of Arctic sea ice during SHEBA. Journal of Geophysical Research, 114(C6):1–21, 2009. ISSN 0148-0227. doi: 10.1029/2008JC004991.

William J Shaw and Timothy P Stanton. Vertical diffusivity of the Western Arctic Ocean halocline. Journal of Geophysical Research: Oceans, 119(8): 5017–5038, aug 2014. ISSN 21699275. doi: 10.1002/2013JC009598. URL `http://doi.wiley.com/10.1002/2013JC009598`.

Koji Shimada, Eddy C. Carmack, Kiyoshi Hatakeyama, and Takatoshi Takizawa. Varieties of shallow temperature maximum waters in the Western Canadian Basin of the Arctic Ocean. Geophysical Research Letters, 28(18):3441–3444, sep 2001. ISSN 00948276. doi: 10.1029/2001GL013168. URL `http://doi.wiley.com/10.1029/2001GL013168`.

Koji Shimada, Motoyo Itoh, Shigeto Nishino, Fiona McLaughlin, Eddy Carmack, and Andrey Proshutinsky. Halocline structure in the Canada Basin of the Arctic Ocean. Geophysical Research Letters, 32(3):1–5, 2005. ISSN 00948276. doi: 10.1029/2004GL021358.

Gunnar Spreen, Ron Kwok, and Dimitris Menemenlis. Trends in Arctic sea ice drift and role of wind forcing: 1992-2009. Geophysical Research Letters, 38 (19):n/a–n/a, oct 2011. ISSN 00948276. doi: 10.1029/2011GL048970. URL `http://doi.wiley.com/10.1029/2011GL048970`.

Gunnar Spreen, Ron Kwok, Dimitris Menemenlis, and An T. Nguyen. Sea Ice Deformation in a Coupled Ocean-Sea Ice Model and in Satellite Remote Sensing Data. The Cryosphere Discussions, (February):1–37, feb 2016. ISSN 1994-0440. doi: 10.5194/tc-2016-13. URL `http://www.the-cryosphere-discuss.net/tc-2016-13/`.

Michael Steele. UpTempO Buoys for Understanding and Prediction. Technical report, Polar Science Center, APL, University of Washington, Seattle, WA, 2012. URL `http://oai.dtic.mil/oai/oai?verb=getRecord&metadataPrefix=html&identifier=ADA572576`.

Michael Steele, James Morison, and Wendy Ermold. Circulation of summer Pacific halocline water in the Arctic Ocean. Journal of Geophysical Research: Oceans, 109:1–18, 2004. doi: 10.1029/2003JC002009. URL `http://onlinelibrary.wiley.com/doi/10.1029/2003JC002009/full`.

Michael Steele, Wendy Ermold, and Jinlun Zhang. Arctic Ocean surface warming trends over the past 100 years. Geophysical Research Letters, 35(2):L02614, jan 2008. ISSN 0094-8276. doi: 10.1029/2007GL031651. URL `http://doi.wiley.com/10.1029/2007GL031651`.

Michael Steele, Wendy Ermold, and Jinlun Zhang. Modeling the formation and fate of the near-surface temperature maximum in the Canadian Basin of the Arctic Ocean. Journal of Geophysical Research, 116(C11):C11015, nov 2011. ISSN 0148-0227. doi: 10.1029/2010JC006803. URL `http://doi.wiley.com/10.1029/2010JC006803`.

Mike Steele, Ignatius G. Rigor, Kristina Colburn, Wendy Ermold, and Mark Ortmeyer. UpTempO Preliminary Data, 2014. URL `http://psc.apl.washington.edu/UpTempO/Data.php`.

J. C. Stroeve, T. Markus, L Boisvert, J. Miller, and A. Barrett. Changes in Arctic melt season and implications for sea ice loss. Geophysical Research Letters, 41:1216–1225, 2014. doi: 10.1002/2013GL058951.Received.

Julienne C. Stroeve, Vladimir Kattsov, Andrew Barrett, Mark Serreze, Tatiana Pavlova, Marika Holland, and Walter N. Meier. Trends in Arctic sea ice extent from CMIP5, CMIP3 and observations. Geophysical Research Letters, 39 (16):n/a–n/a, aug 2012. ISSN 00948276. doi: 10.1029/2012GL052676. URL `http://doi.wiley.com/10.1029/2012GL052676`.

Matthew Sturm. Thermal conductivity and heat transfer through the snow on the ice of the Beaufort Sea. Journal of Geophysical Research, 107 (C10):1–17, 2002. ISSN 01480227. doi: 10.1029/2000JC000409. URL `http://www.agu.org/pubs/crossref/2002/2000JC000409.shtml`.

Hiroshi Sumata, Thomas Lavergne, Fanny Girard-Ardhuin, Noriaki Kimura, Mark Tschudi, Frank Kauker, Michael Karcher, and Rüdiger Gerdes. An intercomparison of Arctic ice drift products to deduce uncertainty estimates. Journal of Geophysical Research : Oceans, 119:4887–4921, 2014. doi: 10.1002/2013JC009724.

Takeshi Tamura, Kay I. Ohshima, Alexander D. Fraser, and Guy D. Williams. Sea ice production variability in Antarctic coastal polynyas. Journal of Geophysical Research: Oceans, 121(5):2967–2979, may 2016. ISSN 21699275. doi: 10.1002/2015JC011537. URL `http://doi.wiley.com/10.1002/2015JC011537`.

Torbjørn Taskjelle, Stephen R. Hudson, Mats A. Granskog, Marcel Nicolaus, Ruibo Lei, Sebastian Gerland, Jakob J. Stamnes, and Børge Hamre. Spectral albedo and transmittance of thin young Arctic sea ice. Journal of Geophysical Research: Oceans, 121:540–553, 2015. doi: 10.1002/2014JC010338.Received.

H Tennekes. The Logarithmic Wind Profile. Journal of the Atmospheric Sciences, 30:234–238, 1972.

J Thomson, V Squire, S F Ackley, W Rogers, A Babanin, P Guest, T Maksym, P Wadhams, S Stammerjohn, C Fairall, O Persson, M Doble, and Et Al. Sea State and Boundary Layer Physics of the Emerging Arctic Ocean. Technical report, Applied Physics Laboratory, University of Washington, Seattle, WA, 2013. URL `http://www.ice-ocean.com/unlockedPDFs/SeaStateDRI_SciencePlan.pdf`.

R. L. Tilling, a. Ridout, and a. Shepherd. Near Real Time Arctic sea ice thickness and volume from CryoSat-2. The Cryosphere Discussions, (February):1–15, 2016. ISSN 1994-0440. doi: 10.5194/tc-2016-21. URL `http://www.the-cryosphere-discuss.net/tc-2016-21/`.

M-L. Timmermans, J. Toole, a. Proshutinsky, R. Krishfield, and a. Plueddemann. Eddies in the Canada Basin, Arctic Ocean, Observed from Ice-Tethered Profilers. Journal of Physical Oceanography, 38(1):133–145, 2008. ISSN 0022-3670. doi: 10.1175/2007JPO3782.1.

M. L. Timmermans, A. Proshutinsky, E. Golubeva, J. M. Jackson, R. Krishfield, M. McCall, G. Platov, J. Toole, W. Williams, T. Kikuchi, and S. Nishino. Mechanisms of Pacific Summer Water variability in the Arctic's Central Canada Basin. Journal of Geophysical Research C: Oceans, 119(11):7523–7548, 2014. ISSN 21699291. doi: 10.1002/2014JC010273.

Mary-Louise Timmermans. The impact of stored solar heat on Arctic sea ice growth. Geophysical Research Letters, 42(15):6399–6406, 2015. ISSN 00948276. doi: 10.1002/2015GL064541. URL `http://doi.wiley.com/10.1002/2015GL064541`.

J. M. Toole, M.-L. Timmermans, D. K. Perovich, R. a. Krishfield, a. Proshutinsky, and J. a. Richter-Menge. Influences of the ocean surface mixed layer and thermohaline stratification on Arctic Sea ice in the central Canada Basin. Journal of Geophysical Research, 115(C10):C10018, oct 2010. ISSN 0148-0227. doi: 10.1029/2009JC005660. URL `http://doi.wiley.com/10.1029/2009JC005660`.

J. M. Toole, R. A. Krishfield, M.-L. Timmermans, and A. Proshutinsky. The Ice-Tethered Profiler: Argo of the Arctic. Oceanography, 24(3):126–135, 2011. doi: http://dx.doi.org/10.5670/ oceanog.2011.64.

Kevin E. Trenberth and Julie M. Caron. Estimates of Meridional Atmosphere and Ocean Heat Transports. Journal of Climate, 14(16):3433–3443, 2001. ISSN 08948755. doi: 10.1175/1520-0442(2001)014¡3433:EOMAAO¿2.0.CO;2.

M. Tschudi, C. Fowler, and J. Maslanik. EASE-Grid Sea Ice Age. Version 2., 2015.

Mark Tschudi and Charles Fowler. Polar Pathfinder Daily 25 km EASE-Grid Sea Ice Motion Vectors, Version 2, 2013. URL `http://nsidc.org/data/NSIDC-0116`.

Peter Wadhams. Ice in the Ocean. CRC Press, 2000.

Till J.W. Wagner and Ian Eisenman. How Climate Model Complexity Influences Sea Ice Stability. Journal of Climate, 28:3998–4014, 2015. doi: 10.1175/JCLI-D-14-00654.1.

Masaaki Wakatsuchi and Nobuo Ono. Measurements of salinity and volume of brine excluded from growing sea ice. Journal of Geophysical Research, 88 (C5):2943, 1983. ISSN 0148-0227. doi: 10.1029/JC088iC05p02943. URL `http://doi.wiley.com/10.1029/JC088iC05p02943`.

Yu Wang, Benjamin Holt, W. Erick Rogers, Jim Thomson, and Haley H. Shen. Wind and wave influences on sea ice floe size and leads in the Beaufort and Chukchi Seas during the summer-fall transition 2014. Journal of Geophysical Research: Oceans, 121:1502–1525, 2016. doi: doi:10.1002/ 2015JC011349.

SG Warren and IG Rigor. Snow depth on Arctic sea ice. Journal of Climate, 12:1814–1829, 1999.

Eiji Watanabe. Linkages among halocline variability , shelf-basin interaction , and wind regimes in the Beaufort Sea demonstrated in pan-Arctic Ocean modeling framework. Ocean Modelling, 71:43–53, 2013. ISSN 1463-5003. doi: 10.1016/j.ocemod.2012.12.010. URL `http://dx.doi.org/10.1016/j.ocemod.2012.12.010`.

Melinda A. Webster, Ignatius G. Rigor, Son V. Nghiem, Nathan T. Kurtz, Sinead L. Farrell, Donald K Perovich, and Matthew Sturm. Interdecadal changes in snow depth on Arctic sea ice. Journal of Geophysical Research: Oceans, 119:5395– 5406, 2014. ISSN 21699275. doi: 10.1002/2014JC009985. URL `http://doi.wiley.com/10.1002/2014JC009985`.

Melinda A Webster, Ignatius G Rigor, Donald K Perovich, Jacqueline A. Richter-Menge, Christopher M Polashenski, and Bonnie Light. Seasonal evolution of melt ponds on Arctic sea ice. Journal of Geophysical Research: Oceans, 120 (9):5968–5982, sep 2015. ISSN 21699275. doi: 10.1002/2015JC011030. URL `http://doi.wiley.com/10.1002/2015JC011030`.

W F Weeks, S F Ackley, and Norbert Untersteiner. The Geophysics of Sea Ice, chapter The Growth, pages 9–164. Springer US, Boston, MA, 1986. ISBN 978-1-4899-5352-0. doi: 10.1007/978-1-4899-5352-02. URL `http://dx.doi.org/10.1007/978-1-4899-5352-02`.

Willy Weeks. On Sea Ice. University of Alaska Press, 2010. ISBN 160223101X. URL `http://books.google.com/books?id=9S55O6WzuL8C&pgis=1`.

Thomas J. Weingartner, Donald J. Cavalieri, Knut Aagaard, and Yasunori Sasaki. Circulation, dense water formation, and outflow on the northeast Chukchi Shelf. Journal of Geophysical Research, 103(C4):7647, 1998. ISSN 0148-0227. doi: 10.1029/98JC00374.

Karl Weyprecht and A T GRAZ. Fundamental principles of scientific Arctic investigation. publisher not identified, 1875.

Rebecca A. Woodgate, Knut Aagaard, James H. Swift, Kelly K. Falkner, and William M. Smethie. Pacific ventilation of the Arctic Ocean's lower halocline by upwelling and diapycnal mixing over the continental margin. Geophysical Research Letters, 32(18):1–5, 2005. ISSN 00948276. doi: 10.1029/2005GL023999.

Rebecca A Woodgate, Tom Weingartner, and Ron Lindsay. The 2007 Bering Strait oceanic heat flux and anomalous Arctic sea-ice retreat. Geophysical Research Letters, 37:1–5, 2010. doi: 10.1029/2009GL041621.

Woods Hole Oceanographic Institution Upper Ocean Processes Group. Technical note: Oceanscience Underway CTD. Technical report, Woods Hole Oceanographic Institution, Woods Hole, MA, 2007.

M. Yamamoto-Kawai, F. A. McLaughlin, E. C. Carmack, S. Nishino, K. Shimada, and N. Kurita. Surface freshening of the Canada Basin, 2003-2007: River runoff versus sea ice meltwater. Journal of Geophysical Research: Oceans, 114(4):2003–2007, 2009. ISSN 21699291. doi: 10.1029/2008JC005000.

Mengnan Zhao, Mary-Louise Timmermans, Sylvia Cole, Richard Krishfield, Andrey Proshutinsky, and John Toole. Characterizing the eddy field in the Arctic Ocean halocline. Journal of Geophysical Research: Oceans, 119(12):8800–8817, dec 2014. ISSN 21699275. doi: 10.1002/2014JC010488. URL `http://doi.wiley.com/10.1002/2014JC010488`.

M. Zygmuntowska, P. Rampal, N. Ivanova, and L. H. Smedsrud. Uncertainties in Arctic sea ice thickness and volume: New estimates and implications for trends. Cryosphere, 8(2): 705–720, 2014. ISSN 19940424. doi: 10.5194/tc-8-705-2014.